Raman Memory for Entanglement in Diamonds and Light Storage in Optical Fibres

Michael Roger Sprague
St Edmund Hall, Oxford

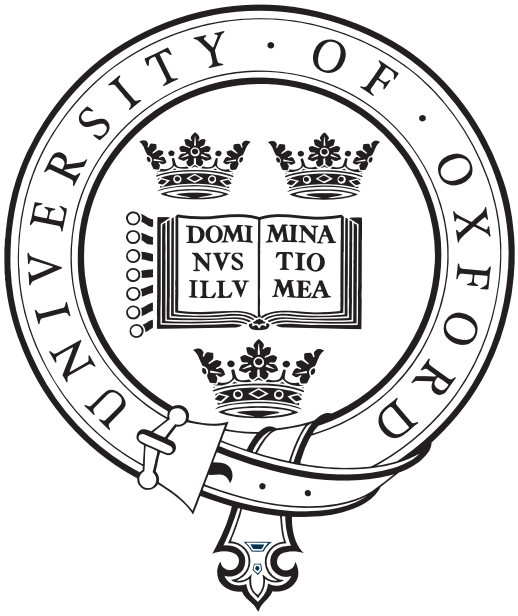

A thesis submitted for the degree of
Doctor of Philosophy
Hilary term 2014

Raman Memory for Entanglement in Diamonds and Light Storage in Optical Fibres

Michael Roger Sprague

St Edmund Hall, Oxford

Submitted for the degree of Doctor of Philosophy, Hilary term 2014

Abstract

Light, when reduced to the level of individual quanta, can possess, besides its familiar properties of frequency, direction, and polarization, a set of correlations irreducible to classical correlations, among other peculiar behaviour. These correlated states are intrinsically interesting, and are also useful for quantum-enhanced information processing. In this thesis I use a high-bandwidth, far-off-resonant Raman memory to implement two quantum information primitives – entanglement generation and light storage – at room temperature and ambient conditions. Specifically, I show, for the first time, the entanglement of two solid-state objects at room temperature and, also, the storage of light in a hollow-core optical fibre.

In the first part, I show that the optical phonon modes of two diamonds can be *entangled* – the prototypical non-classical correlation – at room temperature. The entanglement was generated by spontaneous Raman scattering with projective measurements using single-photon detectors. The degree of entanglement was rigorously quantified by measuring the concurrence – an entanglement monotone – of the joint state of the scattered optical fields. In the second part, I store light in the ground-state coherence of cesium atoms confined within a kagome-structured hollow-core photonic crystal fibre at room temperature using a far-off-resonant stimulated Raman interaction. The storage efficiency of the memory was $27\pm1\%$ and the noise level was sufficiently low such that single-photon-level pulses could be stored. Taken together, these results highlight the potential of Raman memories for quantum information processing in noisy systems with short coherence times.

This thesis is dedicated to my parents

Acknowledgments

The Large Blue (*Phengaris arion*), in its larval form, feeds on the flowers of thyme and marjoram plants. Once satiated and having reached its fourth instar, the caterpillar drops to the floor and secretes a sweet substance that attracts the red ant *Myrmica sabuleti*. The red ants carry the larva back to their nest, where the ants feed on the caterpillar's secretions. Once inside the nest, the caterpillar mimics the scent and sound of the red ants. The caterpillar hibernates and, upon awakening, begins eating the red ant larvae and eggs. After three weeks, the caterpillar pupates. The adult imago emerges from the chrysalis after another period of three weeks, at which point it leaves the ant nest. As the butterfly unfurls its wings, the red ants form a protective perimeter to ward off predators until the Large Blue flies away.

During my time here, Oxford has graded from a name and a dot on a map to a memory-bright home: see the white hydrangeas at Magdalen College cast yellow by the setting sun. See the swifts circling at dusk over the Natural History Museum, rising in expansive helices and dissolving against the dark cinereous sky. And see the crimson flash of the *Vanessa atalanta* circling three times before landing on my forehead.

I would like to thank my supervisor, Ian Walmsley, for his support of my work in the ultrafast group. His keen framing of the group's research direction was kindly appreciated. A special thanks to the members of the ultrafast group: Josh Nunn affected a very charming act of 'one-downsmanship' that blended displays of humility and self-parody. I will miss his quick and enthusiastic replies to every email, which were like the little *beeps* received from a satellite orbiting overhead, indicating everything was exactly as it should be. Thanks for reading through my whole thesis! KC Lee's genial, good-humoured

disposition made my first year (lights off, headlamps, arms hovering over the optics, the slightest adjustment of a mirror knob, silence, the steady flicker of photon counts) a pleasure. Duncan England was affable and always keen to help out in the lab. Patrick Michelberger and Tessa Champion were my brother- and sister-in-arms. Xian-Min Jin helped steer me toward the hollow-core-fibre experiments and Amir Abdolvand expertly drew the fibres. I appreciated Nathan Langford's enthusiastic help and Animesh Datta's laconic words of wisdom. I was always entertained by Mihai Dorian Vidrighin's stories. The support staff at the physics department (Matt, Simon Moulder, Alan Francis, Mike Tacon, and others) helped me out at key moments. Finally, it was a pleasure working with Kris Kaczmarek – rising star of the ultrafast lab – as I was writing my thesis.

I was fortunate that the Oxford University Press funded my studies through a Clarendon Fund Scholarship. I would also like to thank St Edmund Hall for supporting me with a graduate scholarship and Jeff Tseng, my college advisor, for kindly taking an interest in my studies.

I can detect, warmly suffused throughout my thesis (and all my endeavours), the support and encouragement of my family. For this, for everything, I want to thank my parents and my brothers. And above all, I want to thank *You*, your eyes flickering up from the screen, laughing in anticipation of what you are now about to tell me.

Michael Sprague

January 2014

Contents

Contents vii

List of Figures xiii

1 Introduction 1

1.1 General motivation 1

1.2 Structure of thesis 4

1.3 Publications 6

2 Review of Quantum Memories 9

2.1 Definition of a quantum memory 9

2.2 Applications of quantum memories 11

2.2.1 Synchronizing single-photon sources 11

2.2.2 Long-distance quantum communication 12

2.3 State of the art in quantum memories 15

2.3.1 Delay lines 15

2.3.2 Adiabatic memories 16

2.3.3 Photon-echo memories 20

2.4 Summary 24

I Entanglement Between Diamonds 25

3 Spontaneous Raman Memory with Optical Phonons 27

3.1 Description of the DLCZ protocol 28
3.1.1 Entanglement between two atomic ensembles 31
3.1.2 Read out of the entanglement between the ensembles 32
3.2 Optical Phonon in Diamond 35
3.2.1 Simple derivation of the phonon dispersion 36
3.2.2 Raman scattering in diamond 37
3.2.3 Phase-matching conditions 41
3.3 Non-classical light from diamond 45
3.3.1 Correlation functions for photon statistics 45
3.3.2 Violation of the Cauchy-Schwarz inequality 46
3.3.3 Experimental setup 48
3.3.4 Non-classical $g^{(2)}$ in diamond 49
3.3.5 Coherence time and lifetime of the optical phonon 52
3.4 Summary 54

4 Entanglement of Diamonds at Room Temperature 55
4.1 Motivation 55
4.1.1 The Importance of being entangled 55
4.1.2 In the context of other approaches 57
4.2 Quantifying entanglement in the number basis 58
4.2.1 Definition of the concurrence 60
4.2.2 Density matrix in the number basis 61
4.2.3 Calculation of the concurrence 64
4.2.4 Cross-correlation and visibility 64
4.3 Experimental setup 68
4.3.1 Oscillator and optical modes 68
4.3.2 Diamond properties and selection rules 70
4.4 Stokes and anti-Stokes interferometers 71
4.4.1 Polarization indistinguishability 71
4.4.2 Spectral overlap of the modes 72
4.4.3 Spatial-mode overlap 72

4.4.4 Temporal delay between the modes . . . 73
4.4.5 Phase stability of the interferometer . . . 75
4.4.6 Phase control of the interferometer . . . 78
4.4.7 Detection of single photons . . . 79
4.5 Experimental results . . . 80
4.5.1 Interference of heralded anti-Stokes photons . . . 80
4.5.2 Limit on the interference visibility . . . 82
4.5.3 Reconstruction of the density matrix . . . 83
4.5.4 Calculation of the concurrence . . . 84
4.5.5 Quantum state tomography . . . 88
4.6 Significance of the time ordering of the experiment . . . 91
4.7 Summary . . . 92

II Storage of Light in a Hollow-Core Photonic Crystal Fibre 95

5 Stimulated Raman Memory in Cesium 97

5.1 Light-matter interaction . . . 98
5.1.1 Dipole operator . . . 99
5.1.2 Three-level-system equations . . . 102
5.2 Raman memory interaction . . . 104
5.2.1 Optical fields . . . 104
5.2.2 Hamiltonian for multi-mode light-matter interaction . . . 105
5.2.3 Continuous atomic operators . . . 105
5.2.4 Propagation of the signal field . . . 106
5.2.5 Equations of motion for the Raman memory . . . 107
5.2.6 Raman storage and retrieval . . . 108
5.2.7 Raman coupling . . . 108
5.2.8 Raman interaction as a beam splitter . . . 110
5.2.9 Summary of theoretical derivation . . . 111
5.3 Summary of past memory results . . . 111
5.3.1 Storage of bright coherent pulse . . . 112

5.3.2 Storage of single-photon-level coherent pulse . . . 113
5.3.3 Storage of a polarization state . . . 114
5.3.4 Current research goals . . . 115
5.4 Frequency-offset lock for oscillator . . . 116
5.4.1 Motivation . . . 116
5.4.2 Operating principle . . . 116
5.4.3 Experimental implementation . . . 117
5.4.4 Results . . . 121
5.5 Solid-state etalons for control-field filtering . . . 122
5.5.1 Motivation . . . 122
5.5.2 Design considerations . . . 124
5.5.3 Experimental implementation . . . 125
5.5.4 Results . . . 126
5.6 Summary . . . 128

6 Hollow-Core Photonic Crystal Fibre 129

6.1 Motivation . . . 129
6.2 Microstructured photonic crystal fibres . . . 132
6.2.1 Photonic crystal fibres . . . 132
6.2.2 Hollow-core photonic crystal fibres . . . 132
6.2.3 Kagome-structured hollow-core photonic crystal fibres . . . 133
6.3 Vacuum System . . . 136
6.3.1 General design principles . . . 137
6.3.2 Fibre mount and viewports . . . 137
6.3.3 Vacuum pumps and gauges . . . 139
6.3.4 Cesium reservoir . . . 140
6.3.5 Buffer gas . . . 140
6.3.6 Vacuum bake . . . 142
6.4 Laser System . . . 143
6.4.1 External-cavity diode laser . . . 143
6.4.2 Locking laser via sub-Doppler spectroscopy . . . 145

6.5 Linear absorption in hollow-core fibre . . . 150
6.5.1 Optical depth . . . 150
6.5.2 Light-induced atomic desorption . . . 153
6.6 Spectroscopy in hollow-core fibre . . . 157
6.7 Optical pumping . . . 161
6.8 Summary . . . 164

7 Light Storage in a HC-PCF 167
7.1 Setup for memory experiment . . . 169
7.1.1 Oscillator and pulse preparation . . . 169
7.1.2 Optical pumping . . . 170
7.1.3 LIAD . . . 172
7.1.4 HC-PCF optical setup . . . 172
7.1.5 Filtering and detection . . . 174
7.1.6 Data acquisition and control system . . . 175
7.2 Optical depth measurements . . . 178
7.3 Classical memory results . . . 184
7.3.1 Comparison to Raman theory . . . 186
7.4 Single-photon-level measurements . . . 189
7.5 Memory lifetime . . . 193
7.6 Summary . . . 197

8 Conclusion 199
8.1 Summary of thesis . . . 199
8.2 Future work . . . 201
8.2.1 Optimize memory in HC-PCF . . . 201
8.2.2 Storage of heralded single photons . . . 202
8.2.3 Heralded single-photon source in HC-PCF . . . 203
8.2.4 Magnetic-field sensing in HC-PCF . . . 203
8.2.5 Rydberg atoms in HC-PCF . . . 204

Appendix A 207

Appendix B **217**

Appendix C **225**

Appendix D **231**

References **233**

List of Figures

2.1 Synchronization of heralded single-photon sources with a quantum memory 12

2.2 Entanglement swapping for long-distance quantum communication 13

2.3 Illustration of electromagnetically-induced transparency 17

2.4 Illustration of the stimulated Raman memory 18

2.5 Illustration of the three-level gradient echo memory 21

2.6 Illustration of the atomic frequency comb memory 23

3.1 Illustration of four-wave mixing via spontaneous Raman scattering 29

3.2 Illustration of the DLZC protocol used to establish entanglement between two remote atomic ensembles 33

3.3 Illustration of the vibration of the optical phonon mode in diamond and the Raman scattering process 37

3.4 Diagram of the phonon dispersion for the acoustic and optical branches in diamond 38

3.5 Polarization of the optical phonons as a function of the scattering angle of the Stokes photon 41

3.6 The phase-matching function and joint spectral probability distribution versus the Stokes and anti-Stokes wavelength 43

3.7 Square of phase-matching function showing angular correlations between the Stokes and anti-Stokes fields relative to the collinear pump fields . . . 44

3.8 Optical layout for the Raman-scattering measurements of the optical phonons in diamond 50

3.9 Non-classical correlations between Stokes and anti-Stokes fields in the quantum memory based on optical phonons in diamond 51
3.10 Population and coherence lifetimes of the optical phonons in diamond . . 53

4.1 Interference visibility as a function of the second-order cross-correlation between the Stokes and anti-Stokes fields 66
4.2 Maximum interference visibility as a function of the second-order cross-correlation of the two diamonds 67
4.3 Schematic of the experimental setup for generating entanglement between two diamonds. The insets show the vibrational motion of the diamond, the energy level diagram, and a photograph of the diamond sample 68
4.4 Optical layout of diamond entanglement experiment 70
4.5 Maximizing the temporal overlap of the pulses in the Stokes and anti-Stokes interferometers 74
4.6 Phase stabilization of the Stokes and anti-Stokes interferometers 77
4.7 Coincidence counts between the herald Stokes photons and the read-out anti-Stokes photons 81
4.8 Density matrix of the heralded anti-Stokes modes used to calculate the concurrence of the state 84
4.9 Quantum state tomography of the post-selected joint state of the Stokes/anti-Stokes fields 90

5.1 Diagram of the three-level Λ-system with signal and control optical fields 98
5.2 The Raman interaction as a beam splitter between the optical and atomic modes 109
5.3 Raman memory efficiency as function of the storage time and interference of a retrieved pulse with an input pulse 113
5.4 Raman memory storage at the single-photon level 114
5.5 The process matrix for polarization state storage using a Raman memory 115
5.6 Group delay and group velocity dispersion of the GTI as a function of the optical frequency and the length of the interferometer 118

5.7 Frequency stability setup showing the mode-locked oscillator, the laser diode locked to the atomic transition, the SFPI, and the associated electronics . . . 120
5.8 Frequency stability of the oscillator relative to the laser diode . . . 121
5.9 Frequency error relative to the lock position for four different scenarios . . 122
5.10 Transmission spectrum of etalon for the signal, control, and anti-Stokes field as a function of the finesse and free spectral range . . . 123
5.11 CAD drawing of the etalon with mount, temperature sensor, and thermoelectric cooler . . . 125
5.12 Measured transmission spectrum of the solid-state etalon . . . 126
5.13 Stability and temperature sensitivity of the etalon . . . 127

6.1 Images of the cross-section of the HC-PCF, the spatial mode in the fibre core, and the transmission of the fibre . . . 134
6.2 Ultra-high vacuum system for the HC-PCF experiments . . . 136
6.3 Cross-section of the fibre connector and holder . . . 138
6.4 Vacuum pressure and temperature during bake of the vacuum system . . 142
6.5 External-cavity diode laser power output and spatial mode . . . 143
6.6 Operating principle of ECDL, showing gain curves and an example of gain narrowing . . . 145
6.7 Schematic of saturated-absorption spectroscopy for locking the laser, along with error signals . . . 146
6.8 Saturated-absorption spectroscopy in a vapour cell . . . 147
6.9 Linear absorption in the HC-PCF . . . 152
6.10 Absorption and optical depth during light-induced atomic desorption . . . 154
6.11 Schematic of the layout for the LIAD beam and the output power from the tapered amplifier . . . 155
6.12 Illustration of the proposed mechanism by which LIAD operates . . . 156
6.13 Time-dependent optical depth induced by LIAD for a pulse repetition rate of one second . . . 157
6.14 Saturated-absorption spectroscopy in a HC-PCF . . . 160

6.15 Energy level diagram for the optical pumping in cesium 162
6.16 Optical pumping efficiency in a HC-PCF 164

7.1 Three-level Λ-system for memory showing the optical fields 168
7.2 Optical setup for signal and control fields 169
7.3 Optical setup for the Pockels cell used for the optical pumping 171
7.4 Optical layout for the HC-PCF memory experiment showing the four optical modes (signal, control, optical pumping, and LIAD) 173
7.5 Simplified optical layout of the memory experiment 175
7.6 Complete optical layout of the memory experiment 176
7.7 Pulse sequence for one run of the experiment and the acquisition sequence for memory experiment 177
7.8 Example of the segmentation of 10 000 data traces according to whether the control or optical pumping shutter was open or closed 179
7.9 Pulse delay as a function of the excited-state detuning with and without inhomogeneous broadening. Example showing the pulse delay extracted from an experimental trace 182
7.10 Storage of a classical, coherent-state pulse in a kagome-structured hollow-core fibre 185
7.11 Memory efficiency versus optical depth in a kagome-structured HC-PCF, and comparison to the theoretical prediction 187
7.12 Theoretical prediction of the Raman memory efficiency as a function of the optical depth and the Rabi frequency of control field 188
7.13 Storage of single-photon-level pulses in a HC-PCF 190
7.14 SNR at the single-photon level as a function of the memory efficiency (normalized to 1 input photon per pulse) 191
7.15 Memory lifetime in the hollow-core photonic-crystal fibre 194

1 Poissonian probability as a function of the parameters μ and X over a limited range. The continuous variable μ was calculated in discrete increments of 0.005 212

2 Ratio of the likelihoods used to rank the Poissonian probabilities when constructing the confidence intervals 214

3 Likelihood ordered confidence intervals for confidence level = 68.3% (1σ) and confidence level = 95% (2σ) 215

4 Front panel of the frequency-offset program showing the SFPI output, GTI voltage, frequency offset of the oscillator, PI feedback parameters, and the I/O settings. 226

5 Block diagram of the frequency-offset lock program. *Vanessa atalanta* calls the I/O initialize sub-VI, *Troides helena* calls the data output and channel close sub-VI, *Papilio* calls the save file sub-VI, and the Matlab icon calls the Matlab logic sub-VI. 227

6 Block diagram of the save file sub-VI for the frequency-offset lock program. 227

7 Block diagram of the I/O initialize sub-VI for the frequency-offset lock program. 228

8 Block diagram of the data output and channel close sub-VI for the frequency-offset lock program. 229

9 Block diagram showing the MATLAB implementation of the find-peak algorithm and the PI controller for the frequency-offset lock program. . . . 230

10 Front panel of the data acquisition and control program showing the oscilloscope trace from the APD, shutter status signal, and the I/O parameters. 231

11 Block diagram of the data acquisition and control program. The blue and grey icon calls the shutter control sub-VI. 232

12 Block diagram of the shutter control sub-VI for the data acquisition and control program. 232

1 Introduction

1.1 General motivation

When I consider the world (with interest, with curiosity, seldom with fear), my eye is invariably drawn to the way that light interacts with its surroundings: the pearl white iridescence on the wings of *Morpho sulkowskyi*; the retro-reflection of light from dew drops poised on the waxen needles of a Fraser fir; the flush of shimmering, multi-spectral light from the *setae* of *Aphrodita aculeata*; the lilac-hued sky moments after sunset; and, the pale eyespot on a butterfly that mimics the appearance of a drop of poison, the pattern imprinted on its chitinous scales carefully dislocated in order to mimic the refraction of light through the non-existent droplet [1]. That these effects are examples of photonic band-gap structures [2], sylvanshine [3], self-assembled hexagonal hollow-core photonic crystal fibres [4], and the Belt of Venus [5] does provide, I admit, a certain taxonomic thrill. However, these optical effects arise from the interplay of absorption, scattering,

diffraction, interference, and dispersion, which can be explained with clarity and concision by classical electromagnetism.

There are, however, more subtle optical effects that cannot be explained with reference to wave-based electromagnetism. When light is reduced to the level of individual quanta, or photons, it can possess a set of correlations irreducible to classical correlations. These quantum correlations give rise to a new set of quantum optical effects: the arrival of equally spaced, anti-bunched single photons [6]; the coalescence of two identical photons incident on a half-silvered mirror [7]; the existence of correlated states between two photons that violates the precepts of local realism [8]; and, the faithful teleportation of a quantum state of light using only classical communication and local operations [9].

These states are *intrinsically interesting* because of their rich structure of correlations; their study remains an active area of research and discovery. These states are also thought to be *useful* for certain quantum information tasks. The precise nature of their advantage in this regard is difficult to state simply. Certain applications, such as secure communication, rely on the fact that quantum states cannot be cloned [10, 11], or that certain quantum-correlated – *entangled* – states are monogamous [12]; a maximally entangled bipartite system cannot be simultaneously correlated with another system (no matter how hard they try). For quantum-enhanced computation (that mythical, many-hued firebird), the advantage lies in structuring a problem such that the probability amplitudes (which can be positive or negative) positively interfere for the right answer and negatively for the wrong one. For quantum-enhanced metrology, reducing the uncertainty in one observable quantity can improve the precision of a measurement at the cost of increasing the uncertainty in the complementary observable.

In order to study these states and, ultimately, realize these applications, we need to be able to reliably create these states on demand. The main source of quantum states of light, spontaneous parametric down-conversion [13], is inherently probabilistic; the generation of a correlated photon pair occurs rarely and at random intervals. The probability for success scales exponentially with the number of heralded single photons. While this approach is feasible for generating small numbers of photons (less than 10), for more complicated and interesting states the success probability rapidly vanishes.

Quantum memories can render probabilistic sources deterministic (that is, up to the efficiency of the memory) [14]. By storing single photons until all the memories are charged, many-particle quantum-correlated states of light can be created. This motivates the development of quantum memories that can be readily interfaced with single photons generated by existing single-photon sources such as spontaneous parametric down-conversion. These quantum memories should have a high efficiency and a long lifetime compared to the pulse duration – a quantity defined as the *time-bandwidth product*. For practical applications, it is desirable that a quantum memory be relatively simple to implement.

Quantum memories are also integral to *quantum repeaters* [15, 16], devices which can efficiently distribute entanglement for secure communication over long distances, in analogy with repeaters for classical fibre-optic-based communication. A primitive component of a quantum repeater is the establishment of entanglement between two remote atomic ensembles, which requires the ability to store information in stationary atomic states [17]. Further, proposals to implement efficient linear-optics quantum computation requires the storage of output states until other probabilistic components succeed [18].

The range of potential applications for quantum memories has spurred interest in a number of memory protocols and physical systems. Common to all these approaches is the dynamic modulation of the coupling between an optical mode and a stationary atomic mode. This can be done by modifying the susceptibility of the signal field with an auxiliary optical field, or by inducing the rephasing of the electric dipole. Some memory protocols are more suitable for specific physical systems or applications and, as yet, no one system has been shown to meet all the criteria for the above applications.

In this thesis, I describe my work to store light in *optical phonons* in diamond and in the spin-states of cesium atoms in a *hollow-core photonic crystal fibre*. These memories implement a far-detuned *Raman memory*, which is ideally suited for studying systems with short coherence times using high-bandwidth optical pulses. I show that two diamonds can be entangled at room temperature using a spontaneous Raman memory combined with projective measurements using single-photon detectors. In the second part, I show the storage and retrieval of GHz-bandwidth optical pulses in cesium atoms confined in

a hollow-core photonic crystal fibre. These experiments highlight the potential of Raman memories for quantum information tasks in room-temperature systems with short coherence times.

1.2 Structure of thesis

The thesis is divided into two parts prefaced by an introductory chapter that reviews the applications and the current state of development of quantum memories. Each part is relatively self-contained; the relevant theory and motivation are developed as required for each experiment. The details of the experimental system (optical setup, atomic system, experimental control system, data acquisition, etc...) are described alongside preliminary 'proof-of-principal' experiments performed to assess the viability of the proposed experiment. In the last chapter of each part, the results of the experiments are presented. The future extensions of the work are presented in chapter 8, section 8.2. A brief description of each chapter is given below.

Chapter 2 – Review of quantum memories: The applications of quantum memories for quantum information tasks are reviewed, and the relevant performance criteria for each application are introduced. The range of memory protocols and the attendant physical systems are reviewed. The Raman memories (both spontaneous and stimulated) are introduced in the context of other approaches, although a more detailed treatment is left for chapters 3 and 5.

Part I – Entanglement Between Diamonds:

Chapter 3 – Spontaneous Raman Memory with Optical Phonons in Diamond: The *DLCZ protocol* for long-distance quantum communication is reviewed. The protocol uses linear optics, atomic ensembles, and single-photon detectors in order to generate entanglement via Raman-scattered optical fields. We introduce optical phonons in diamond as a potential solid-state, room-temperature quantum memory. I discuss its Raman scattering properties, dispersion, and the phase-matching conditions. I show that non-classical-correlated Raman scattered light can be generated with the optical phonon acting as the intermediate material excitation.

Chapter 4 – Entanglement of Diamonds at Room Temperature: We describe

how a primitive of the DLCZ protocol can be used to establish entanglement between the optical phonon modes of two diamonds at room temperature. I summarize how entanglement is a resource for quantum information processing, and how it can be quantified in the number basis by measuring the *concurrence* of the joint optical state. I describe the experimental setup used, including: the oscillator, the optical mode overlap, and the phase stability and phase control of the interferometer. The reconstruction of the reduced density matrix is presented. The concurrence of the state is calculated along with its confidence level. Finally, polarization-based quantum state tomography is performed on the post-selected state.

Part II – Storage of Light in Hollow-Core Photonic Crystal Fibre:

Chapter 5 – Stimulated Raman Memory in Cesium: The equations of motion for the Raman memory are derived from the Hamiltonian of the atomic system, optical fields of the signal and control pulses, and the electric-dipole light-matter interaction. The optical Bloch equations are also derived. The Raman interaction is parameterized by a single coupling constant, and the implication of this on the memory performance is discussed. The previous demonstration, by our group, of a Raman memory in a vapour cell is summarized, and I present my contribution: the design and development of a new frequency-offset lock for the laser oscillator and a solid-state, temperature-stabilized etalon for filtering the control field.

Chapter 6 – Hollow-Core Photonic Crystal Fibre: The motivation for a memory in a guided-wave structure is given, and previous work using waveguides for non-linear optics is reviewed. Hollow-core photonic crystal fibres (HC-PCFs) are introduced, and a large-core kagome-structured HC-PCF is proposed as a promising candidate for the realization of an optical memory. An ultra-high vacuum system is designed and built in order to load cesium atoms in the HC-PCF. The optical depth is measured, and the phenomenon of *light-induced atomic desorption* (LIAD) is studied in order to increase the optical depth. The homogeneous linewidth and optical pumping efficiency are measured in order to assess the system's suitability for the storage of light.

Chapter 7 – Light Storage in a HC-PCF: I present the storage of light, for the first time, in a HC-PCF. I present the experimental setup of the four optical fields: the

signal, control, optical pumping and LIAD beams. I describe the filtering of the control field and the data acquisition and control system used to carry out the experiments. I developed a new method to monitor the optical depth during the measurements. The storage of classical, bright coherent pulses is presented and compared to the theory of the Raman memory interaction. The storage of single-photon-level pulses is also reported and, finally, I measure the storage lifetime of the memory.

1.3 Publications

The following publications directly arose from the work presented in this thesis:

1. K. C. Lee, B. J. Sussman, M. R. Sprague, P. Michelberger, K. F. Reim, J. Nunn, N. K. Langford, P. J. Bustard, D. Jaksch, I. A. Walmsley. Macroscopic non-classical states and terahertz quantum processing in room-temperature diamond. *Nature Photonics* **4**, 41-45 (2012).

2. K. C. Lee*, M. R. Sprague*, B. J. Sussman, J. Nunn, N. K. Langford, X.-M. Jin, T. Champion, P. Michelberger, K. F. Reim, D. England, D. Jaksch, I. A. Walmsley. Entangling macroscopic diamonds at room temperature. *Science* **334**, 1253 -1256 (2011) *equal contribution.

3. M. R. Sprague, D. G. England, A. Abdolvand, J. Nunn, X.-M. Jin, W. S. Kolthammer, M. Barbieri, B. Rigal, P. S. Michelberger, T. F. M. Champion, P. St.J. Russell, I. A. Walmsley. Efficient optical pumping and high optical depth in a hollow-core photonic-crystal fiber for a broadband quantum memory. *New Journal of Physics* **15**, 055013 (2013).

4. M. R. Sprague, P. S. Michelberger, T. F. M. Champion, D. G. England, J. Nunn, X.-M. Jin, W. S. Kolthammer, A. Abdolvand, P. St.J. Russell, I. A. Walmsley. Broadband single-photon-level memory in a hollow-core photonic crystal fibre. Accepted by *Nature Photonics.*

Chapter 3, in part, was adapted from publication 1, and Chapter 4 adapted from publication 2. This work was done in collaboration with another student, (now Dr.!) KC Lee.

I have emphasized in chapter 4 the parts of the experiment I led, such as the phase stabilization system, and the data and statistical analysis. The data acquisition was performed jointly.

Chapter 6 was adapted from publication 3, and Chapter 7 from publication 4. I led the hollow-core photonic crystal fibre project, including the design and construction of the experimental apparatus, as well as the data acquisition and analysis. Josh Nunn helped with the comparison of the data to the theoretical model, and various other postdocs and students lent a hand during the construction of the experimental apparatus. Amir Abdolvand from Philip Russell's group at the Max Planck Institute for the Science of Light in Erlangen Germany drew the hollow-core photonic crystal fibres used in the experiment.

2

Review of Quantum Memories

2.1 Definition of a quantum memory

Quantum memories can faithfully 'receive, retain, and recreate' [19], after a programmable delay, an unknown quantum state. Let's tackle these terms one at time. A programmable delay indicates that the stored state can be retrieved at an arbitrary time within the memory's lifetime. However, for most applications, storing a photon in an optical delay line with an active switch, which introduces a minimum timing resolution, is acceptable. 'Receive' means that the photon must be efficiently absorbed, requiring strong coupling of the light to the atomic medium (although see reference [20] for a different approach). The storage state must then 'retain' the coherence of the input state over an appreciable time. For long-distance quantum communication protocols, it would be desirable for the memory lifetime to exceed the lifetime of light in an optical fibre, which is $\sim$ 100 μs [21]. For synchronizing local quantum networks, the memory lifetime should exceed the

pulse repetition rate of the system. The state is then 'recreated' by mapping the stored excitation to an output state which, in the ideal case, is the time reverse of the absorption process. The total efficiency of the memory storage and retrieval process should exceed 50% for several quantum information applications, such as implementing error correction algorithms [22] and surpassing the no-cloning limit without post-selection [23]. Lower efficiency memories can still be useful for certain tasks, such as synchronizing multiple heralded single-photon sources [14]. Finally, the fidelity of the recreated state gives an indication as to the quantum character of the memory. In a general form, the fidelity,

$$F = \mathrm{Tr}\left(\sqrt{\sqrt{\rho_{\mathrm{in}}}\rho_{\mathrm{out}}\sqrt{\rho_{\mathrm{in}}}}\right)^2, \tag{2.1}$$

determines the 'overlap', or stability of the input state ρ_{in} as it evolves through the memory to the state ρ_{out}. As an example, a classical 'measure and prepare' strategy for storing the polarization state of a single photon has a maximum fidelity of 2/3. Consider one photon that is polarized in a linear combination of basis states. We then make a projective measurement along one basis, which annihilates the photon. The optimal guess is that the original polarization of the photon was along the direction associated with the measurement outcome, and the probability that this conjecture is true is 2/3 [24].[1] This is the classical limit; a fidelity greater than 2/3 indicates the memory is superior to the classical measurement strategy outlined above.[2] The process does not violate the 'no-cloning' theorem [10] because the original quantum state is destroyed.

At the heart of a quantum memory is the ability to synchronize events, acting as a buffer in time. Quantum memories have important applications: they are an essential component of a quantum repeater, and can help improve the generation rate of heralded single photons. We summarize these applications in the next section.

[1] $S_{\mathrm{avg}} = \frac{1}{4\pi}\int_0^{2\pi} d\phi \int_0^{\pi} \sin\theta d\theta P(\psi, H/V) S(H/V, \psi) = \frac{1}{4\pi}\int_0^{2\pi} d\phi \int_0^{\pi} \sin\theta d\theta 2\left(|\langle H|\psi\rangle|^2 + |\langle V|\psi\rangle|^2\right)\cos^2\theta = \int_0^{\pi}\sin\theta\cos^2\theta d\theta = \frac{2}{3}$, where $P(\psi, H/V)$ is the probability of outcome $|H\rangle$ or $|V\rangle$ given state $|\psi\rangle$, and $S(H/V, \psi) = \cos^2(\theta)$ is information gained about state $|\psi\rangle$ given a measurement along basis H/V.

[2] If an ensemble of N particles were measured then the maximum fidelity would scale as $(N+1)/(N+2)$ [24].

2.2 Applications of quantum memories

2.2.1 Synchronizing single-photon sources

Single photons, which are useful for quantum information applications, are generally produced with low probability via spontaneous parametric down-conversion.[3] Consider the production of heralded single photons with probability $p \ll 1$. N single-photon states will be produced with probability p^N, which rapidly vanishes as N increases. With a quantum memory, the generation rate of multiple single photons can be enhanced by storing the heralded single photons in a set of N memories. When all the memories are charged with a single photon, they can be read out to produce N single photons, as illustrated in figure 2.1**a**. The synchronization of two single-photon sources was demonstrated experimentally in reference [29]. If a quantum memory can store a single photon for 10 experimental runs, then there are 10 possible time bins when the generation of a second single photon will result in a two-photon state, as opposed to one time bin previously. The two-photon rate is, therefore, increased by $\eta\Gamma_{\mathrm{BW}}$, where η is the efficiency of the memory (storage and retrieval) and Γ_{BW}, the time-bandwidth product, is the number of pulses (time bins) that a memory can store a photon before it decoheres [14] (strictly this should be the ratio of the memory lifetime to the pulse repetition rate).

The exact enhancement in the rate of heralded single-photon generation was calculated in reference [14]. The success probability of generating N single photons is

$$\Theta_N = p^N \left\{ 1 + \frac{(1-R)(1-p)\eta\Gamma_{\mathrm{BW}}}{1 + (\Gamma_{\mathrm{BW}} - 1)\left[R(1-2p) + p\right]} \right\}^N , \tag{2.2}$$

where R is the probability that all the memories are ready to be read out. In the limit $\{R\Gamma_{\mathrm{BW}}, p\Gamma_{\mathrm{BW}}\} \ll 1$, the success probability asymptotes to $\Theta_N \approx (p\eta\Gamma_{\mathrm{BW}})^N$; the success probability is enhanced by the base factor of the product of the efficiency and the time-bandwidth product. In the opposite limit, $\{R\Gamma_{\mathrm{BW}}, p\Gamma_{\mathrm{BW}}\} \gg 1$, the success probability saturates to the value $\Theta_{\mathrm{N}} \approx \eta^N$; the success probability can be no higher than the memory efficiency (raised to the power N). Figure 2.1**b** shows the potential enhancement in multi-

[3] We note that the development of on-demand single-photon sources is an active area of research. Promising results have been achieved with single emitters such as quantum dots [25], nitrogen-vacancy centres in diamond [26], trapped ions [27], and atoms [28].

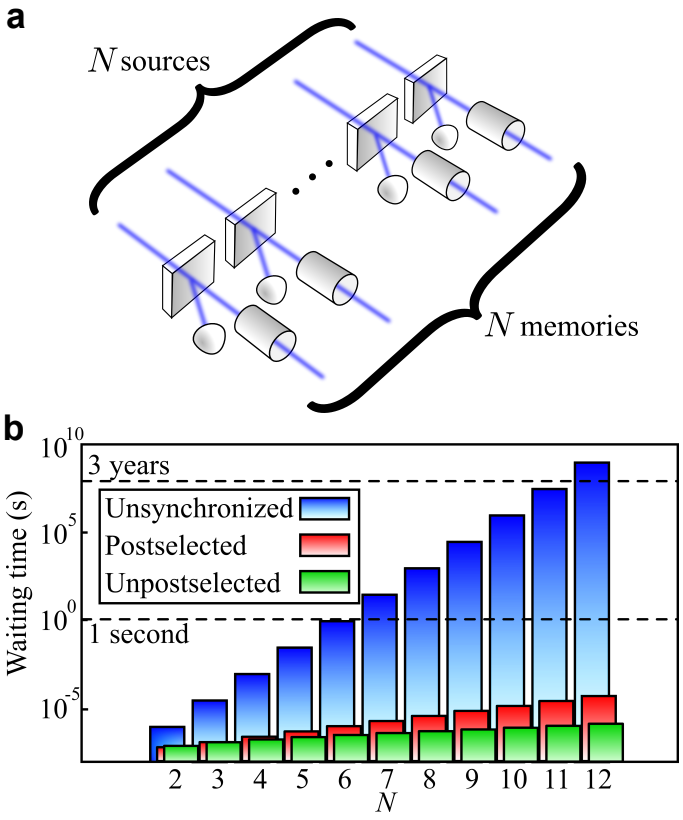

Figure 2.1: From reference [14]. **a** An array of N heralded single-photon sources with N quantum memories to enhance the rate of multi-photon generation. **b** Waiting time to produce N single photons with a threshold fidelity 90% without a quantum memory (blue bars), with a quantum memory with efficiency 56% (red bars), post-selected, and with a quantum memory with efficiency 99% (green bars), not post-selected. The time-bandwidth product is 1000 and the repetition rate is 1 GHz.

photon rates for a realistic quantum memory with time-bandwidth product $\Gamma_{\mathrm{BW}} = 1000$, and efficiency $\eta = 56\%$. For these parameters, the waiting time for $N = 12$ can be reduced by twelve orders of magnitude, from over 3 years down to 100 μs. The desirable properties of a quantum memory for this application are, therefore, a high time-bandwidth product and a high efficiency.

2.2.2 Long-distance quantum communication

Photons are exponentially attenuated in optical fibres by a minimum rate of 0.15 dB/km at 1.5 μm [30]. Classical communication relies on repeaters to amplify and rectify the attenuated signal. For quantum communication, which generally uses non-classical light in order to send information securely [31, 32], the situation is more complicated as a single quantum state cannot be cloned [10]. A solution to this problem is to use a quan-

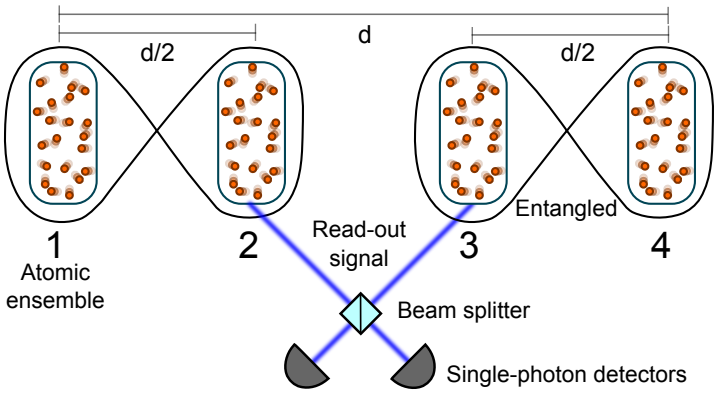

Figure 2.2: Entanglement swapping for long-distance quantum communication. Initially atomic ensembles 1 and 2 are entangled, as are ensembles 3 and 4. Conditional on the detection of only one photon from both detectors, entanglement is established between ensembles 1 and 4.

tum repeater [15] to distribute entanglement over long distances through 'entanglement swapping' with a quantum memory [33].

Entanglement swapping can transfer entanglement between remote atomic ensembles. If ensembles 1 and 2 are entangled, and ensembles 3 and 4 are entangled then ensembles 1 and 4 can be entangled through a joint measurement of ensembles 2 and 3, followed by local operations and classical communication [16]; this is illustrated in figure 2.2. Instead of transmitting an entangled state a distance d, the entangled state is transmitted a small fraction of this distance and linked together via a series of nested entanglement swapping operations. As an example, let ensembles 1 and 2 be in unnormalized state

$$|\psi\rangle = |0_1 1_2\rangle + \mathrm{e}^{\mathrm{i}\phi_1}|1_1 0_2\rangle, \tag{2.3}$$

and ensembles 3 and 4 be in the unnormalized state

$$|\varphi\rangle = |0_3 1_4\rangle + \mathrm{e}^{i\phi_2}|1_3 0_4\rangle, \tag{2.4}$$

where the arguments zero and one refer to the number of excitations and the subscript labels the ensembles. The total resulting state is $|\Psi\rangle = |\psi\rangle|\varphi\rangle$. Ensembles 2 and 3 are converted into optical modes, which are combined on a 50:50 beam splitter and then

measured with a single-photon detector, which implements the projection

$$\langle 0_2 0_3 | \hat{a}_\pm | \Psi \rangle = \left[|0_1 1_4\rangle \pm e^{i(\phi_1+\phi_2)} |1_1 0_4\rangle \right], \tag{2.5}$$

where $\mathrm{Tr}_{2,3}(...)$ is the partial trace over modes 2 and 3, and $\hat{a}_\pm = \hat{a}_2 \pm \hat{a}_3$ is the beam splitter transformation of modes 2 and 3. As a result of detecting a single photon, the joint system is now in an entangled state between ensembles 1 and 4. In this way, entanglement can be established between two remote nodes that contain quantum memories. Because the operation of each link is probabilistic, each with success probability p (whether from photon loss, detection, or from the process of entanglement generation), the success rate of N links scales as p^N. With quantum memories to synchronize these probabilistic events (assuming long enough lifetime), the success rate can scale sub-exponentially (i.e. polynomially) [16].

The canonical example of a quantum repeater is implemented via the DLCZ protocol [17], a proposal which showed that a quantum repeater could be implemented with linear optics, atomic ensembles, and single-photon detectors. The entanglement generation for this protocol is established via spontaneous Raman scattering and projective measurements; more details can be found in chapter 3. Since this proposal, a number of refinements to the original DLCZ protocol have been proposed [16]. A particularly favorable approach is to replace the entanglement generation process with single-photon sources and absorptive quantum memories [34] (that is, memories capable of storing and retrieving quanta of light, as defined in section 2.1). This approach can result in a higher rate of entanglement distribution [16]. This is critical as the memory storage time must exceed the entanglement creation time, which can be on the order of seconds. Therefore, a suitable quantum memory for a quantum repeater would have high efficiency and very long storage times. This is a slightly different set of parameters than is needed for synchronizing single-photon sources, where the time-bandwidth product is of paramount importance, as opposed to the absolute storage time.

2.3 State of the art in quantum memories

The broad applicability of quantum memories has spurred a concerted effort to develop new memory protocols and to identify suitable physical systems in which to store light. I will now briefly review the most recent quantum memory experiments. The protocols considered here can be divided into roughly two broad categories: adiabatic approaches (where the excited state is not populated, and can be adiabatically eliminated), and photon-echo approaches (and variants) [35] (with some degree of overlap). I restrict myself here to absorptive quantum memories, although we make note of transmissive memories that rely on, for example, slow light [36] or an off-resonant Faraday interaction [20, 37, 38]. We will also limit the discussion to ensemble-based memories, owing to their technical simplicity, although we note that many interesting and pioneering results have been demonstrated with single-emitters, such as trapped ions [39, 40, 41], neutral atoms in cavities [42, 43], defect centres in diamond[44, 45, 46, 47] and silicon vacancies [48, 49]. First, however, we consider the simplest implementation of an optical memory.

2.3.1 Delay lines

It is a source of mild amusement that an experimentalist considers the simplest memory to be an optical delay line [50] while a theorist considers the simplest memory to be a single atom with two energy levels [51]. Certainly the simplest memory to implement is an optical delay line with an optical fibre or free-space cavity. The optical pulse circulates in a traveling-wave cavity that can be switched out with an active optical element, such as a fast electro-optic modulator. This introduces a minimum timing resolution, which is not necessarily an impediment if the timing resolution can be matched to the pulse repetition rate of the oscillator. However, any losses within the cavity can severely limit the time-bandwidth product (here the ratio of the storage time to the round-trip time of the cavity); a total loss of even 1% limits the time-bandwidth product to 100. Currently, losses of on-chip switches are 13% [52, 53], resulting in a time-bandwidth product less than ten. Switches using cross-phase modulation in optical fibres are also limited to a loss on the order of 1 dB [54], although this may be improved in the future. Clearly, an optical memory based on a delay line is not suitable for long-distance quantum communication,

although it may have some scope for synchronizing single-photon sources [55, 56].

2.3.2 Adiabatic memories

Adiabatic quantum memories use a Λ-level system with two ground states ($|g\rangle$ and $|s\rangle$) coupled via an intermediate excited state $|e\rangle$. A strong control field dynamically modulates the coupling of a weak signal field to the atomic system. The term 'adiabatic' refers to the fact that the excited state is not occupied during the storage process, which is desirable in order to avoid spontaneous emission from the excited state. The adiabatic approach has two limits, on-resonant excitation via *electromagnetically-induced transparency* (EIT), and far-off-resonant excitation via a *Raman interaction* (Raman). These two techniques will be discussed below.

Electromagnetically-induced transparency

Electromagnetically-induced transparency is a near-resonant scheme with $\Delta \ll \Gamma d$, where d is the optical depth of the ensemble, Δ the excited-state detuning, and Γ the excited-state linewidth. A strong control pulse with Rabi frequency $\Omega \gg \Gamma$ creates two excitation pathways ($|g\rangle \rightarrow |e\rangle$ and $|g\rangle \rightarrow |e\rangle \rightarrow |s\rangle \rightarrow |e\rangle$), whose probability amplitudes destructively interfere, creating a transparency window [57].[4] The transparency window creates a highly dispersive feature and strong reduction in the group velocity; the incoming light is slowed and temporally compressed. If the control field is adiabatically reduced to zero,[5] the incoming light is transferred to a stationary atomic excitation, implementing a quantum memory.

Storage of classical light using electromagnetically-induced transparency was first demonstrated with a cold atomic ensemble [59] and, afterward, with a warm vapour [60]. EIT was also used to store a number-entangled single photon in an ensemble of laser-cooled atoms [61]. Storage of classical light was also demonstrated in a rare-earth doped solid (for over one second) [62]. Recently, a storage efficiency of 78% was demonstrated

[4] When the control and signal field are in two-photon resonance such that $\omega_s - \omega_c = \omega_{sg}$, where ω_{sg} is the frequency splitting between the ground and storage state. The transparency window ω_{trsp} is proportional to $|\Omega|^2/(L\sqrt{d})$, where L is the length of the ensemble [58].

[5] The adiabatic condition is that the entire pulse must fit inside the ensemble before the control field is reduced, and the pulse spectrum must fit within the transparency window [57].

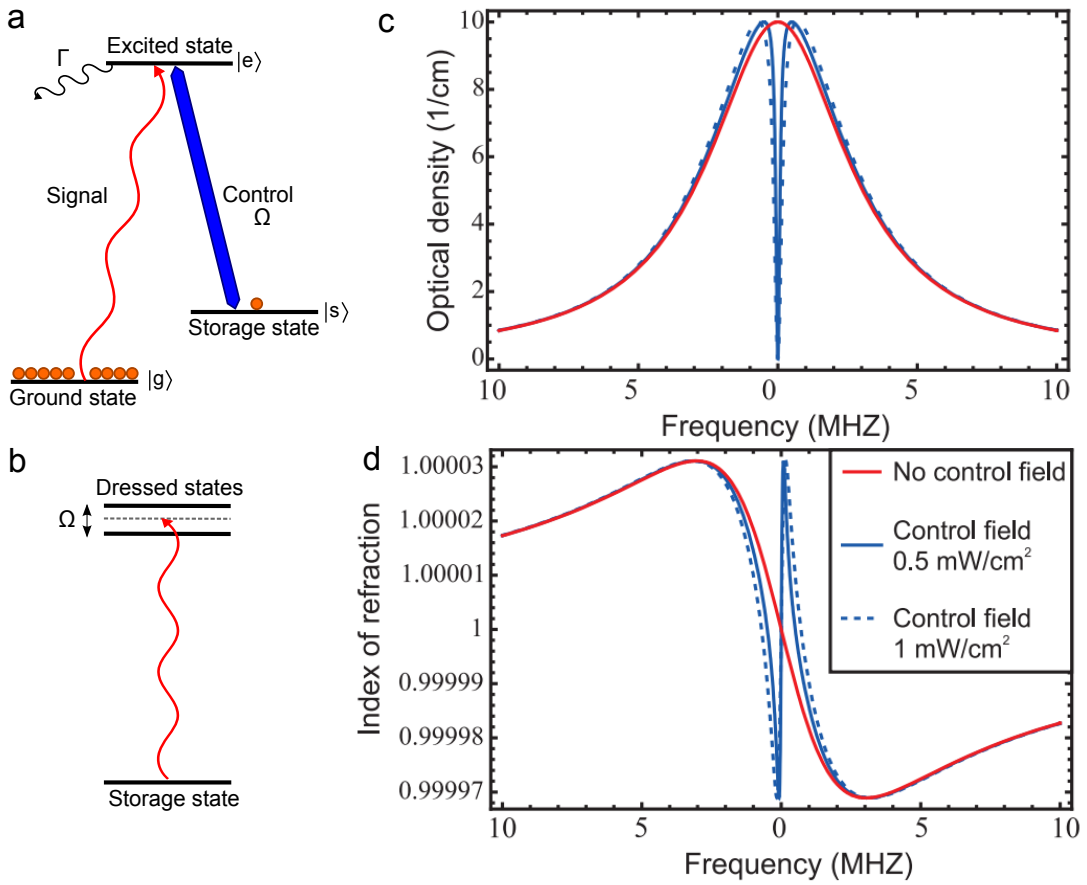

Figure 2.3: Electromagnetically-induced transparency. **a** Λ-level system showing the signal and control field. **b** Dressed-state picture where the energy levels are split by the Rabi frequency. **c** Real part of the susceptibility with the control field switched off (red line) and on (blue line), from reference [50] **d** Imaginary part of susceptibility in the presence and absence of the control field, from reference [50]

in a cold atomic ensemble [63] and, in separate experiments, a storage time on the order of one minute was achieved [64, 65]. Storage of a single photon, or a single-photon-level pulse has, so far, not been demonstrated with EIT at room temperature (although slow light has been demonstrated [66]) as the noise from spontaneous emission has prevented the faithful retrieval of single-photon-level pulses [67].

A theoretical treatment of EIT by Gorshkov *et al.* [35, 58, 68, 69] found the optical bandwidth of EIT similar to that of other memory protocols, such as the Raman memory. However, this ignores the presence of multiple energy levels in the excited-state manifold. These levels limit the bandwidth of EIT to be much less than the frequency splitting of the excited-state levels; typical storage bandwidths are on the order of several MHz, which is a bandwidth that is challenging to generate with single-photon sources. This motivates

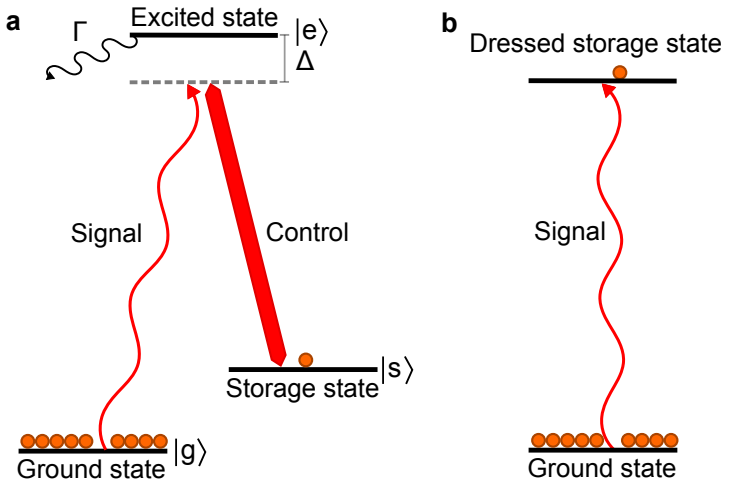

Figure 2.4: Stimulated Raman memory. **a** Λ-level system showing the signal and control field. **b** Dressed-state picture where the control field 'lifts' the storage state near the excited state in order to create a virtual level, coupling the ground state and storage state.

the development of a broadband quantum memory compatible with single-photon sources that is also robust to inhomogeneous broadening.

Raman memory

Conceptually, the Raman memory [70, 71, 58] is quite simple. As opposed to EIT, the Raman interaction is far-detuned from the excited-state manifold ($\Delta \gg \Gamma d$). A strong control pulse couples a weak signal pulse (the mode to be stored) to the storage state via a two-photon transition. The signal pulse is stored in a coherence between the storage state and the ground state. A second control pulse, with a programmable delay, converts the atomic coherence into an outgoing optical pulse. The equations governing the memory interaction are derived in chapter 5, and the memory operation is illustrated in figure 2.4. In the adiabatic regime, the occupation of the excited state is negligible[6] and the interaction can be thought of as directly coupling the ground and storage state (i.e. the virtual state is mainly comprised of the storage state). The bandwidth of the memory is determined by the control pulse bandwidth, unlike EIT, where the memory bandwidth is set by the Rabi frequency of the control field. The bandwidth is only limited by the splitting between the ground state and storage state, which can be several GHz in alkali atoms.

[6] A balance must be made between a strong control field (high Ω) for strong coupling to the storage state while avoiding high levels of noise due to spontaneous emission ($\propto \Omega^2/\Delta^2$) [58].

The memory lifetime is determined by the Raman linewidth, which can be very narrow, limited by diffusion and magnetic dephasing in warm vapours [72]. Therefore, the ratio of the memory lifetime to the pulse duration can be very high in alkali atoms, resulting in a time-bandwidth product greater than 1000 [72], the largest yet demonstrated in a quantum memory. An additional advantage of the Raman memory is that it is insensitive to inhomogeneous broadening or multiple levels in the excited state manifold. When the detuning is much larger than the broadening, the complete excited-state manifold can be treated as a single effective level. Finally, any fluorescence from the excited state can be easily filtered from the signal field both spectrally and temporally as the protocol is off-resonance and the signal pulse duration can be much shorter than the spontaneous emission decay time. This a distinct advantage of the Raman protocol over resonant memory protocols such as EIT.

Recently our group has demonstrated a broadband Raman memory (bandwidth 1.5 GHz) in a thermal vapour cell of cesium atoms [73] that is capable of operating at the single-photon level [72]. A detailed summary of these results is given in section 5.3. A Raman memory has also recently been demonstrated with THz-bandwidth pulses in a hydrogen gas [74] and diamond [75], although the memory lifetime is very short (1 ns and 10 ps, respectively). The stimulated Raman memory is the focus of the second part of this thesis. Chapters 6 and 7 demonstrate the first implementation of a Raman memory in a waveguide structure using a kagome-structured hollow-core photonic crystal fibre.[7]

An alternative approach is to use spontaneous Raman scattering to create a spin excitation without sending in a signal pulse. The Stokes-scattered light is then correlated with the material excitation. It is not obvious that this state would be particularly useful. However, the DLCZ protocol [17] showed that exactly this interaction can be used to implement a quantum repeater as discussed in section 2.2.2. A primitive of the DLCZ protocol is the establishment of entanglement between two remote atomic ensembles using spontaneous Raman scattering. We will use this technique in chapter 3 and 4 to demonstrate, for the first time, entanglement between two solid-state objects at room temperature.

[7] We note a conceptually similar memory protocol using stimulated Brillouin scattering was previously demonstrated in a standard single-mode fibre [76].

2.3.3 Photon-echo memories

An alternative approach to the adiabatic memories in section 2.3.2 are photon-echo protocols where the signal pulse is typically absorbed into the excited state. The coherence between the ground state and excited state rapidly dephases due to the inhomogeneous broadening of the transition; each atom i has a slightly different detuning δ_i, causing the atomic ensemble to rapidly decohere as $\sum_i \mathrm{e}^{-\mathrm{i}\delta_i t}$ [50]. If the phase evolution of each atom can be reversed at time τ, the coherence will then rephase, producing a photon echo at 2τ. This is a well-known technique in nuclear magnetic resonance spectroscopy [77], and has been implemented with classical optical pulses as well [78]. The first pulse creates a coherence (with a $\pi/2$-pulse) and the second pulse inverts the coherence (with a π-pulse). However, this technique is not suitable for a quantum memory as the inversion of the atomic population leads to spontaneous emission and amplification [79]. The key insight of the photon-echo memory protocol is that the excited-state rephasing can be induced non-optically by artificially altering the inhomegenous broadening in an ensemble. This eliminates the amplification from the optical pulse rephasing. Several variations on this theme have been proposed, such as applying a transverse or longitudinal gradient (controlled reversible inhomogeneous broadening (CRIB) [80, 81], and gradient echo memory (GEM) [82, 83, 84]), and atomic frequency combs (AFC) [85, 86, 87]. With the addition of a third atomic level, the excitation can be mapped onto a spin coherence and read out on demand. Finally, it has also been shown that the first photon echo can be suppressed and the atomic population can be mapped back into the ground state with a π-pulse, allowing the atoms to rephase with minimal noise (known as ROSE [88] or HYPER [89]). The modified photon-echo memory protocols will be reviewed in the following sections.

Gradient Echo Memory/Controlled Reversible Inhomogeneous Broadening

Gradient echo memory [90] and controlled reversible inhomogeneous broadening [91, 80] protocols artificially induce inhomogeneous broadening in the excited state along the transverse (CRIB) or longitudinal direction (GEM). First, a narrow absorption line is isolated in the excited state $|e\rangle$, typically by optical pumping. The isolated line is then inhomogeneously broadened by applying an external electric or magnetic field. The signal

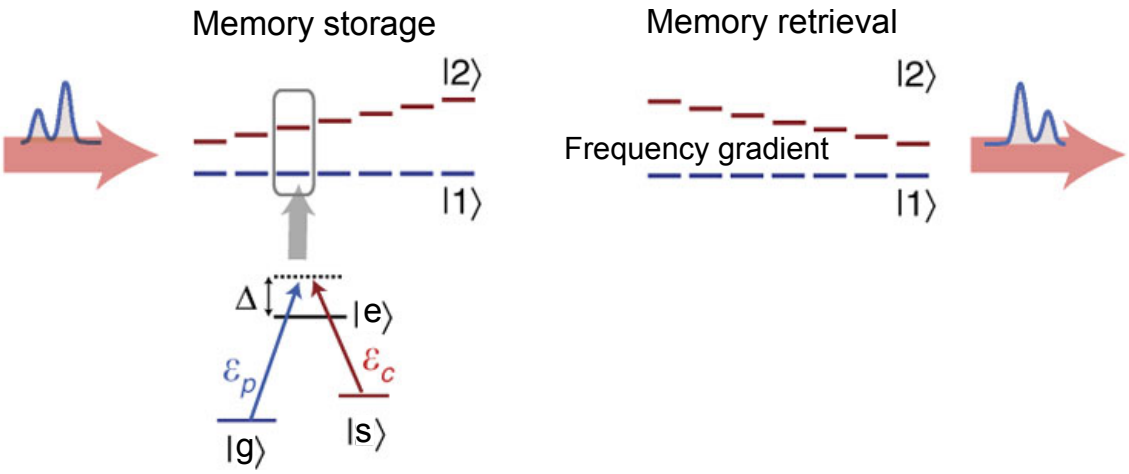

Figure 2.5: Three-level gradient echo memory, from reference [84]. Λ-level system showing the signal and control field. A magnetic field gradient causes the Raman resonance frequency to vary along the length of the atomic ensemble. Reversing the direction of the magnetic field retrieves the signal pulse.

pulse, resonant with the $|g\rangle \rightarrow |e\rangle$ transition, is absorbed by the broadened excited state and begins to dephase due to the frequency shift across the signal pulse. When the frequency detuning is reversed ($\delta_i \rightarrow -\delta_i$) by switching the direction of the electric or magnetic field, the atomic dipoles rephase, resulting in re-emission of the signal pulse. Broadening in the longitudinal direction (GEM) has the added advantage of suppressing re-absorption of the signal along the atomic ensemble. As the excited-state frequency varies along the ensemble, light retrieved at one end of the ensemble will not be resonant with atoms at the other end. With both these techniques, the excited-state coherence can be mapped onto a spin coherence after the signal is absorbed using a control field and storage state $|s\rangle$.

The CRIB protocol was first demonstrated in a rare-earth-doped solid, europium-doped Y_2SiO_5 [92]. In general, rare-earth-doped systems are promising for quantum memories because of their exceedingly long lifetimes, on the order of seconds to minutes [79].[8] The efficiency of CRIB was typically woeful, on the order of 1% [92], limited by the low optical depth; the isolation of a single absorption feature greatly reduced the number of atoms that could participate in the memory interaction. The limited optical depth motivated the development of the atomic frequency comb (AFC) protocol [93], which has

[8] This is due to a quirk in the electronic structure of rare-earth atoms. The tightly-bound valence $4f^N$-shell is closer to the atomic nucleus than the closed $5s^2$ and $5p^6$ shells. These closed shells shield the spin state of the valence electron, isolating it from the external environment.

largely supplanted the CRIB protocol.

The gradient echo memory was first demonstrated with praseodymium dopants in yttrium orthosilicate ($Pr^{3+} : Y_2SiO_5$) [90] and soon after in alkali atoms [94]. GEM was implemented in a two-level rare-earth-doped solid [83] with an efficiency of 69%. The highest memory efficiency was demonstrated in a three-level Λ-system in a warm alkali vapour (rubidium) where the total efficiency was 87% [95]. The Raman line was broadened with a magnetic field, as illustrated in figure 2.5. The three-level GEM memory is closely related to the Raman memory; the signal field is absorbed via a two-photon transition whereby the excited state is not occupied. However, the bandwidth of the three-level GEM protocol is determined by the applied broadening of the Raman line, unlike the Raman memory, where the bandwidth is determined by the control bandwidth. Single-photon-level storage has been demonstrated with 98% fidelity [84]. However, the storage of true heralded single photons has yet to be demonstrated. The main challenge is that the memory bandwidth is very low, typically less than 1 MHz [84]. To produce single photons with such a narrow bandwidth is technically challenging, requiring a cavity to enhance the emission rate [96]. Further, the time-bandwidth product of the memory was typically less than 10 (although this may be improved by using trapped laser-cooled atoms [97]).

Atomic Frequency Comb

Instead of using a single transition, multiple absorption lines with separation Δ_s form a spectral grating in the excited-state absorption profile, which has been termed an atomic frequency comb [93] and is illustrated in figure 2.6. Periodic spikes in the absorption spectrum with width γ results in periodic rephasing of the atomic coherence with a period $2\pi/\Delta_s$. Because a higher fraction of the inhomogeneously broadened excited state is retained, the effective optical depth is higher than the CRIB protocol. As with other photon-echo protocols, the signal is initially absorbed by the $|g\rangle \rightarrow |e\rangle$ transition. In the two-level AFC protocol, the signal is re-emitted at time $2\pi/\Delta_s$, the system acting only as a fixed delay. A control field can map the spectral grating onto a spin coherence, which can then be read out on demand as a true memory (the three-level AFC protocol). It

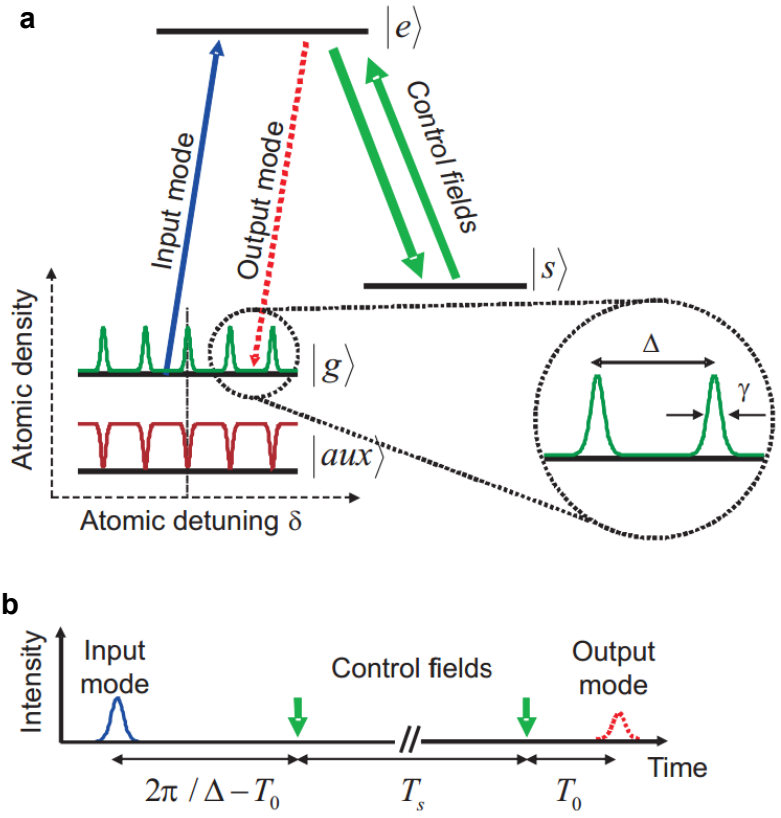

Figure 2.6: Atomic frequency comb memory, from reference [93]. **a** Energy levels for the three-level AFC protocol showing the signal pulse (input mode) and the control field that maps the spectral grating to the spin state $|s\rangle$. The atoms not used in the atomic frequency comb are shelved in the auxiliary state $|aux\rangle$. **b** Time-domain representation showing the input pulse and retrieved echo resulting from the rephased coherence.

may seem that only part of the signal pulse would be absorbed by the spectral grating. However, in the limit that the pulse bandwidth is much larger than Δ_s, the spectral grating is not resolvable during the absorption process and the entire pulse can be absorbed. An important advantage of the AFC protocol is its multi-mode capacity, which is not directly limited by the optical depth (rather limited by the number of absorption peaks that span the signal bandwidth) [93]. The ability to store multiple modes reduces the number of memories required for certain information processing tasks [16].

An atomic frequency comb memory was demonstrated initially in neodynium-doped YVO_4 [85]. Since then, high-efficiency storage with an impedance-matched cavity (56%) [98], high-bandwidth storage (4 GHz) [99], single-photon-level storage at telecommunication wavelengths [81], and the storage of entangled photons [87] has been implemented in a two-level system where the retrieval time is predetermined (i.e. on-demand read out

is not possible). The two-level implementation of AFC does not require a control field, so is simpler to demonstrate than the three-level version. Recently the three-level AFC protocol has been demonstrated at the single-photon level in europium-doped Y_2SiO_5, albeit so far with low efficiency ($< 1\%$) and a time-bandwidth product of 10 [100].

Other photon-echo techniques

There also have been several proposals to modify the original two-pulse photon-echo experiment introduced in section 2.3.3. As in the two-pulse protocol, the atomic population is inverted with a second pulse. The coherence is then allowed, however, to evolve beyond the rephasing point by suppressing the photon-echo. The population is reverted with a π-pulse, and can then be rephased with a third optical pulse without the presence of amplified spontaneous emission. The photon echo is supressed via a phase mismatch (Revival of Silenced Echo, or ROSE [88]) or via an applied electric field (Hybrid Photon-Echo Rephasing, or HYPER [89]). Initial proof-of-principle experiments have been performed to validate the ROSE and HYPER protocols and the storage efficiency of bright coherent states was 12% [88] and 2% [89], respectively. These new techniques do not require spectral shaping of the excited state, which is both technically challenging and limits the bandwidth of AFC/GEM/CRIB protocols.

2.4 Summary

We have reviewed the applications of quantum memories for quantum information processing. For synchronizing probabilistic single-photon sources, memories with a high bandwidth and efficiency are desirable. For quantum repeaters for long-distance quantum communication, memories with long absolute storage time and high efficiency are required. We reviewed absorptive quantum memories based on two broad approaches, adiabatic storage and photon-echo storage. The Raman protocol is well-suited for the storage of broadband pulses in systems with short coherence times because of its far-off-resonance nature and technical simplicity. In this thesis we implement two versions of the Raman memory (spontaneously-initiated and stimulated) in order to entangle two diamonds at room temperature (Part I) and store light in a hollow optical fibre (Part II).

Part I

Entanglement Between Diamonds

3

Spontaneous Raman Memory with Optical Phonons in Diamond

Luming Duan, Mikhail Lukin, Ignacio Cirac and Peter Zoller (DLCZ) in 2001 proposed a practical method to distribute entanglement for long distance quantum communication [17]. Long-distance communication based upon single-photon encoding is limited by the losses in optical fibres; the attenuation in fibres at telecommunication wavelengths is 0.15 dB/km, which sets a practical bound of approximately 100 km [101].[1] Their essential insight was that using atomic ensembles, spontaneous Raman scattering, linear optics, and standard single-photon detectors, the transmission probability can scale polynomially with distance instead of exponentially. These components are relatively simple to implement as

[1]The reason that a bound exists, as opposed to the case of a trade-off between distance and time taken for transmission of the message, is because of the presence of background noise in the single-photon detectors (known as 'dark counts'). The dark count rate must not exceed the product of the repetition rate and the transmission probability for secure communication with low error rates.

compared to single atoms trapped in high-finesse cavities [102]. The DLCZ protocol was first demonstrated by C.W. Chou *et al.* with a magneto-optical trap of alkali atoms [103]. Distilled down to its simplest level, the DLCZ protocol creates measurement-induced entanglement between two remote atomic ensembles. The atomic ensembles we study here are optical phonons in diamond. I now discuss the operation of the DLCZ protocol.

3.1 Description of the DLCZ protocol

The DLCZ protocol relies on spontaneous Raman scattering from an atomic ensemble of N atoms possessing a Λ-level structure. All the atoms are initially prepared in the ground state $|g\rangle^{\otimes N}$. A *write* pulse, detuned from the excited state $|e\rangle$, Raman-scatters one atom into the metastable storage state $|s\rangle_i$, which is dipole-decoupled from the ground state. The Stokes photon is said to herald the creation of an atomic excitation. The state of the atomic ensemble is then

$$\hat{b}^\dagger|0\rangle_\mathrm{b} = \frac{1}{\sqrt{N}}\sum_{i=1}^{N}|g\rangle_1|g\rangle_2\cdots|s\rangle_i\cdots|g\rangle_N = |1\rangle_\mathrm{b}, \tag{3.1}$$

where $|0\rangle_\mathrm{b} = |g\rangle^{\otimes N}$ is the initial state of the atomic ensemble, and the creation operator for collective the atomic mode is

$$\hat{b}^\dagger = \frac{1}{\sqrt{N}}\sum_{i=1}^{N}|s\rangle_i\langle g|. \tag{3.2}$$

This state corresponds to the coherent superposition of one atomic excitation spread over all N atoms, and is known as a symmetrical collective state [17]. Equation 3.1 also assumes that every atoms is equally likely to interact with the control pulse, which will not be the case in general, and can be modified by the spatial distribution of the atoms in the ensemble or the laser pulses.

The effective Hamiltonian for the Stokes interaction is

$$H_\mathrm{s} = \sqrt{\chi_\mathrm{s}}\hat{s}^\dagger\hat{b}^\dagger + (\sqrt{\chi_\mathrm{s}})^*\hat{s}\hat{b}, \tag{3.3}$$

where $\hat{s}$ and $\hat{b}$ are the annihilation operator for the Stokes photon and atomic-excitation

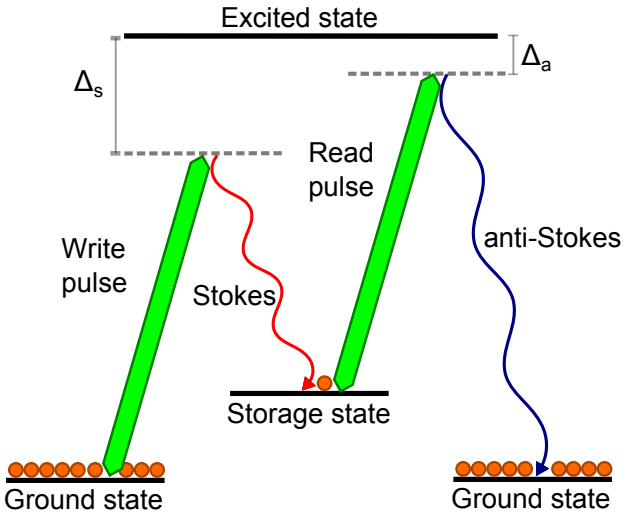

Figure 3.1: Illustration of the four-wave mixing interaction showing the write pulse, read pulse, Stokes pulse, and anti-Stokes pulse. The detuning of the Stokes Δ_{s} and anti-Stokes Δ_{a} differs by the splitting between the storage state and the ground state.

mode respectively and χ_{s} is the coupling parameter, which is a function of the control pulse energy, excited-state detuning, and optical depth. A second control pulse – the *read* pulse – absorbs the atomic excitation and scatters an anti-Stokes photon. The Hamiltonian of the complete Stokes and anti-Stokes interaction is then

$$H_{\mathrm{s,a}} = \left(\sqrt{\chi_{\mathrm{s}}}\hat{s}^{\dagger}\hat{b}^{\dagger} + (\sqrt{\chi_{\mathrm{s}}})^{*}\hat{s}\hat{b}\right) + \left(\sqrt{\chi_{\mathrm{a}}}\hat{a}^{\dagger}\hat{b} + (\sqrt{\chi_{\mathrm{a}}})^{*}\hat{a}\hat{b}^{\dagger}\right), \tag{3.4}$$

where $\hat{a}$ is the annihilation operator for the anti-Stokes mode and χ_{a} is the coupling parameter between anti-Stokes and atomic modes. The Stokes interaction is called a two-mode squeezing Hamiltonian, and the anti-Stokes interaction is known as a beam-splitter Hamiltonian. The interaction is illustrated in figure 3.1.

The coherent superposition of the probability amplitudes from all possible scatterers within the atomic ensemble, modulated by the spatial profile of the optical modes, results in strong coupling of the atoms with a well-defined, forward-propagating optical mode. This is analogous to superradiance as described by Dicke [104], where atoms spaced less than a wavelength exhibit an enhanced rate of spontaneous emission. Here Raman scattering produces a correlated Stokes-atom pair. The Stokes emission is not directional in the limit that the excitation probability is low, but rather the Stokes emission occurs in a dipolar pattern (contra [105]). The reason the Stokes emission is not directional

is that there is no quantum interference, as the final state (one atomic excitation) and initial state (no atomic excitation) are not the same. This is different than the case of a two-level system, where the spontaneous emission can be directional [106].

Conditional on the detection of a Stokes photon in the forward direction, the atomic ensemble is prepared into a collective spin state according to equation 3.1. Detection of a Stokes photon in another direction would prepare the atomic ensemble in another state that would not couple well with an optical mode in the forward direction. The anti-Stokes emission, however, is highly correlated with the spatial mode of the detected Stokes photon as the absorption of an atomic excitation and creation of an anti-Stokes photon leaves the final atomic state in the same state as the initial ($|g\rangle^{\otimes N}$). The collective enhancement occurs for the entire process, involving both Stokes and anti-Stokes modes, which is referred to as four-wave mixing **??**.

The initial vacuum state of the atomic $|0\rangle_{\mathrm{b}}$ and Stokes mode $|0\rangle_{\mathrm{s}}$ evolve according to the Hamiltonian in equation 3.3

$$|\psi\rangle = \mathrm{e}^{-\mathrm{i}H_s t}|0\rangle_{\mathrm{s}}|0\rangle_{\mathrm{b}}, \tag{3.5}$$

where $\exp(-\mathrm{i}H_s t)$ is the evolution operator. Substituting equation 3.3 into equation 3.5 in the limit that $\chi_s \ll 1$ gives

$$|\psi_{\mathrm{sb}}\rangle \simeq \sqrt{1-\chi}\left[|0\rangle_{\mathrm{s}}|0\rangle_{\mathrm{b}} + \sqrt{\chi}|1\rangle_{\mathrm{s}}|1\rangle_{\mathrm{b}} + \chi|2\rangle_{\mathrm{a}}|2\rangle_{\mathrm{b}} + \mathcal{O}(\chi^{3/2})...\right], \tag{3.6}$$

$$\simeq \sqrt{1-\chi}\sum_{n=0}^{\infty}\chi^{n/2}|n\rangle_{\mathrm{s}}|n\rangle_{\mathrm{b}}, \tag{3.7}$$

where $\sqrt{\chi_{\mathrm{s}}}t = \sqrt{\chi}$ as the product of the time and coupling parameter can be thought of as the coupling constant. A time-dependent Hamiltonian can be also be accommodated by integrating the Schrödinger equation with appropriate time ordering. We should note that this state is an entangled state in the number basis between the Stokes mode and the atomic mode. The state in equation 3.7 can be written down exactly as

$$|\psi_{\mathrm{sb}}\rangle = \frac{1}{\cosh(\sqrt{\chi})}\sum_{n=0}^{\infty}(-\mathrm{i})^n \tanh^n(\sqrt{\chi})|n\rangle_{\mathrm{s}}|n\rangle_{\mathrm{b}}. \tag{3.8}$$

The argument in the ket refers to the number of exciations and the subscript refers to the appropriate mode. This state is a two-mode squeezed state, which has the same form as the twin-beam states generated in spontaneous parametric down-conversion, where the detection of a photon in one mode heralds the presence of (ideally) a single photon in the other mode. Here the detection of a Stokes photon heralds the generation of the collective state given by equation 3.1. It is important to note that the total number of Stokes photons generated by a single control pulse may be much greater than one. The condition $\chi \ll 1$ applies only to the spatial mode defined by the collection and detection optics. As the Stokes scattering is not directional, there are many possible modes into which the Stokes photon can emerge. Only the probability that a Stokes photon scatters into this one particular mode must be small in order to avoid the generation of higher photon numbers.

3.1.1 Entanglement between two atomic ensembles

Entanglement between atomic ensembles in two remote locations (denoted here by subscripts l and r) is established by a projective measurement of a single photon, as illustrated in figure 3.2. The Stokes modes from the two ensembles are interfered on a beam splitter and then detected using an avalanche photodiode (APD). The wavefunction of the two atomic ensembles before the beam splitter is a tensor product of two wavefunctions given by equation 3.7,

$$|\Psi\rangle = |\psi_{\mathrm{sb}}\rangle_l \otimes |\psi_{\mathrm{sb}}\rangle_r, \tag{3.9}$$

which is, explicitly,

$$\begin{aligned} |\Psi\rangle \;=\; & \sqrt{1-\chi}[|0_{\mathrm{s}}0_{\mathrm{b}}\rangle_l|0_{\mathrm{s}}0_{\mathrm{b}}\rangle_r + \sqrt{\chi}\,[|0_{\mathrm{s}}0_{\mathrm{b}}\rangle_l|1_{\mathrm{s}}1_{\mathrm{b}}\rangle_r + |1_{\mathrm{s}}1_{\mathrm{b}}\rangle_l|0_{\mathrm{s}}0_{\mathrm{b}}\rangle_r] & (3.10)\\ & +\chi\,[1_{\mathrm{s}}1_{\mathrm{b}}\rangle_l|1_{\mathrm{s}}1_{\mathrm{b}}\rangle_r + |0_{\mathrm{s}}0_{\mathrm{b}}\rangle_l|2_{\mathrm{s}}2_{\mathrm{b}}\rangle_r + |2_{\mathrm{s}}2_{\mathrm{b}}\rangle_l|0_{\mathrm{s}}0_{\mathrm{b}}\rangle_r] + \mathcal{O}(\chi^{3/2})...]. & (3.11)\end{aligned}$$

The herald Stokes photons (mode s) from the two atomic ensembles interfere on a beam splitter with transmittance T_{s} and reflectance R_{s} – assumed to be lossless, i.e. $T_{\mathrm{s}} + R_{\mathrm{s}} = 1$ – and are detected with an APD. The average numbers of detected photons at the two output ports of the beam splitter are given by $\langle \hat{s}_+^\dagger \hat{s}_+ \rangle$ and $\langle \hat{s}_-^\dagger \hat{s}_- \rangle$ respectively, where the

annihilation operators for the output modes are related to the Stokes modes emerging from the two atomic ensembles by the beam splitter transformations $\hat{s}_+ = \sqrt{T_\mathrm{s}}\hat{s}_l + \sqrt{R_\mathrm{s}}\mathrm{e}^{i\phi_s}\hat{s}_r$ and $\hat{s}_- = \sqrt{R_\mathrm{s}}\hat{s}_l - \sqrt{T_\mathrm{s}}\mathrm{e}^{i\phi_s}\hat{s}_r$ (and similarly for the creation operator $\hat{s}_\pm^\dagger$). The phase ϕ_s is the phase difference for modes l and r (i.e. the differential length of the interferometer formed by beam splitters that separate and join together modes l and r before and after the ensembles, respectively) [107]. After detection of a photon in one of the two output modes, the atomic state is projected onto the state (with probability χ, which has been factored out)

$$\langle 0_{sl}0_{sr}|\hat{s}_+|\Psi\rangle = |\Phi^+\rangle = \sqrt{T_\mathrm{s}}|1_\mathrm{b}\rangle_l|0_\mathrm{b}\rangle_\mathrm{r} + \sqrt{R_\mathrm{s}}\mathrm{e}^{i\phi_s}|0_\mathrm{b}\rangle_l|1_\mathrm{b}\rangle_r + \mathcal{O}(\sqrt{\chi})... \tag{3.12}$$

$$\langle 0_{sl}0_{sr}|\hat{s}_-|\Psi\rangle = |\Phi^-\rangle = \sqrt{R_\mathrm{s}}|1_\mathrm{b}\rangle_l|0_\mathrm{b}\rangle_r - \sqrt{T_s}\mathrm{e}^{i\phi_s}|0_\mathrm{b}\rangle_l|1_\mathrm{b}\rangle_r + \mathcal{O}(\sqrt{\chi})... \tag{3.13}$$

Setting $T_\mathrm{s} = R_\mathrm{s} = 1/2$ gives the maximally entangled state and ignoring higher order photon number terms results in the maximally entangled state

$$|\Phi^\pm\rangle = \frac{1}{\sqrt{2}}\left[|1_\mathrm{b}\rangle_l|0_\mathrm{b}\rangle_r \pm \mathrm{e}^{i\phi_s}|0_\mathrm{b}\rangle_l|1_\mathrm{b}\rangle_r\right]. \tag{3.14}$$

This state is entangled in the number basis, and represents one atomic excitation delocalized over the two ensembles, which is depicted in figure 3.2**b**. The state is a superposition between the case of one atomic excitation in the left ensemble and none in the right ensemble *and* one atomic excitation in the right ensemble and none in the left ensemble. Converting this stationary entangled state into an optical mode will be discussed in the next section.

3.1.2 Read out of the entanglement between the ensembles

The delocalized atomic excitation can be mapped to an optical state by absorbing an atomic excitation from either l or r and creating a single anti-Stokes photon, as illustrated in figure 3.2**c**. This process is efficient when the phase-matching condition is met,

$$\mathbf{k}_\mathrm{s} + \mathbf{k}_\mathrm{a} = \mathbf{k}_\mathrm{p1} + \mathbf{k}_\mathrm{p2}, \tag{3.15}$$

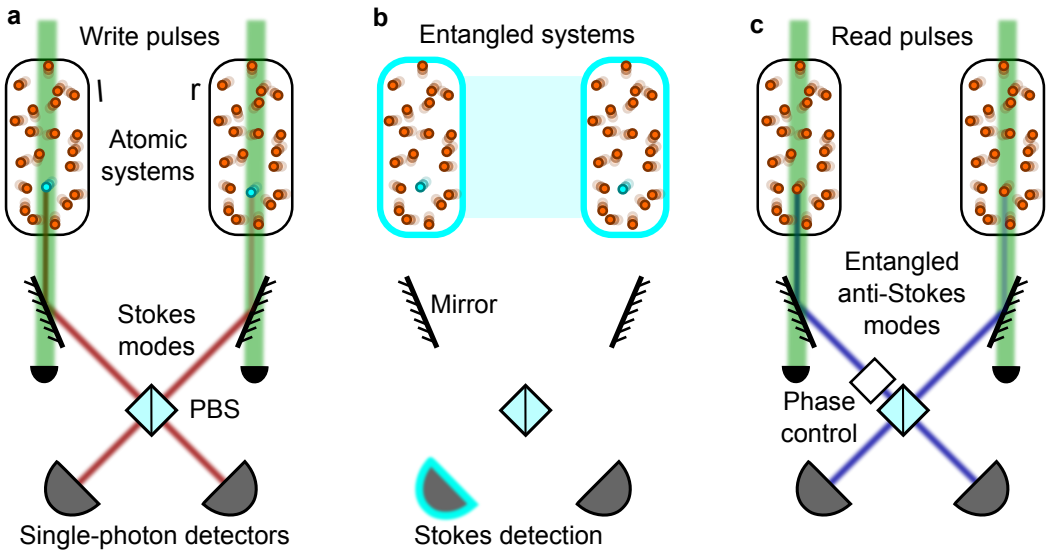

Figure 3.2: Triptych of the DLCZ protocol. **a** Two write pulses generate one Stokes photon with low probability. **b** Detection of the Stokes photon heralds the creation of an entangled state between the atomic ensembles as depicted by the shaded blue area connecting ensembles l and r. **c** The entangled atomic state is converted into an entangled state between the anti-Stokes optical fields, which exhibits phase-sensitive interference.

where the wave-vector subscript refers to the Stokes (s), anti-Stokes, write (p1) and read (p2) pulses. Given the success probability for creating an anti-Stokes photon χ_{a}, the wavefunction of the optical state is (c.f. equation 3.4)

$$\langle 0_{bl}0_{br}|\hat{a}^{\dagger}\hat{b}|\Phi^{\pm}\rangle = \frac{1}{\sqrt{2}}\left[|1_{\mathrm{a}}\rangle_l|0_{\mathrm{a}}\rangle_r \pm \mathrm{e}^{i\phi_s}|0_{\mathrm{a}}\rangle_l|1_{\mathrm{a}}\rangle_r\right]. \tag{3.16}$$

Therefore, with probability χ_{a} we retrieve a maximally entangled state between the anti-Stokes modes instead of the atomic modes. This is a feature of the DLCZ protocol, and is referred to as built-in entanglement purification [17]. Only successful events are detected, or post-selected, from the experimental runs and the unsuccessful events, where the output is vacuum, are ignored. This will be considered in more detail in section 4.2 on quantifying entanglement.

The anti-Stokes modes from the two ensembles can be likewise interfered on a beam splitter ($\hat{a}_+ = \sqrt{T_{\mathrm{a}}}\hat{a}_l + \sqrt{R_{\mathrm{a}}}\mathrm{e}^{i\phi_a}\hat{a}_r$ and $\hat{a}_- = \sqrt{R_{\mathrm{a}}}\hat{a}_l - \sqrt{T_{\mathrm{a}}}\mathrm{e}^{i\phi_a}\hat{a}_r$, where ϕ_a is the phase difference between the paths containing modes l and r) whose output is measured with an APD. The number of anti-Stokes photons detected at the output port of the beam

splitter $\langle \hat{a}_+^\dagger \hat{a}_+ \rangle$ or $\langle \hat{a}_-^\dagger \hat{a}_- \rangle$, conditioned on the detection of Stokes photon, is given by

$$\langle \hat{a}_\pm^\dagger \hat{a}_\pm \rangle = \sin^2 \left[(\phi_s + \phi_a + (\pi \mp \pi)/2)/2 \right] \tag{3.17}$$

where $T_s = T_a = R_s = R_a = 1/2$. This corrects a sign error in the same expression from [108]. The maximum interference visibility, as a function of beam splitter transmittance and reflectance, can be easily calculated as

$$V = \frac{2\sqrt{T_s T_a R_s R_a}}{T_s T_s + R_s R_a}, \tag{3.18}$$

which agrees with the classical case of coherent light incident on a Mach-Zehnder interferometer.

In this manner, the entanglement between two atomic ensembles, conditioned on the detection of a Stokes photon, is transferred to the entanglement between the anti-Stokes modes from the two ensembles, still conditioned (or heralded) on the detection of a Stokes photon. The entanglement is verified by measuring the interference of the heralded anti-Stokes photon. By varying the phase of either the Stokes interferometer ϕ_s, or the anti-Stokes interferometer ϕ_a (or both), the anti-Stokes photon can be directed to exit one of the output ports of the beam splitter where the two anti-Stokes modes are combined. The entanglement will be a function of the maximum visibility of the interference signal. High visibility alone is not, however, a sufficient condition, as described below.

Consider the case where anti-Stokes mode was, instead, a coherent state $|\alpha\rangle$, with photon number decomposition

$$|\alpha\rangle = \mathrm{e}^{-|\alpha|^2/2} \sum_{n=0}^{\infty} \frac{\alpha^n}{\sqrt{n!}} |n\rangle_{\mathrm{a}}. \tag{3.19}$$

The interference of the two phase-coherent anti-Stokes modes, with relative phase ϕ_c, will result in the mean photon number detected at the output ports $+$ and $-$

$$\langle \hat{n}_\pm \rangle = \mathrm{Tr} \left(\hat{B}^\dagger \hat{\rho} \hat{B} n_\pm \right) = \alpha^2 \sin^2 \left[(\phi_c + (\pi \mp \pi)/2)/2 \right], \tag{3.20}$$

where $\hat{B}$ is the beam splitter transformation, $\hat{B}^\dagger$ the Hermitian conjugate, $\hat{\rho} = |\alpha, \alpha \mathrm{e}^{\mathrm{i}\phi_c}\rangle\langle \alpha, \alpha \mathrm{e}^{\mathrm{i}\phi_c}|$

is the density operator for the two anti-Stokes modes, and $hatn_{\pm}$ is the photon number operator for the two ports. The interference in this case has the same functional form as equation 3.17, illustrating that high interference visibility is not sufficient to demonstrate entanglement if no assumption is made as to the nature of the scattering process. Entanglement can be verified without resort to any assumption regarding the physical processes. This requires measuring both the interference visibility and the probability of higher order photon number terms in order to estimate the density matrix of the two-photon subspace. The concurrence, an entanglement measure [109], of this restricted subspace quantifies the amount of entanglement. This will be discussed in the next chapter. Now we turn our attention to the material excitation of our atomic ensemble: optical phonons in diamond. The optical phonon is inherently a delocalized, collective excitation as compared to the single atomic spin excitation normally associated with the DLCZ protocol. However, the resulting behaviour is essentially the same.

3.2 Optical Phonon in Diamond

The properties of diamond are determined by the crystallographic properties of the diamond structure. The space group of diamond is $Fd3m$ (O_h^7) and the crystal group is $m3m$ (O_h). The dipole selection rules determine the allowed scattering processes: a process is allowed if the direct product of the initial state, final state, and transition operator equals the irreducible representation of the space group of the crystal structure [110]. This is in analogy to the calculation of Clebsch-Gordan coefficients for transitions between different angular momentum states in individual atoms.

Artificial diamonds were first reliably produced in 1954 [111] after many false claims, notably by Henri Lemoine, who convinced officers of the De Beers diamond company and numerous others, including Marcel Proust, to invest in his fraudulent scheme. The subsequent scandal in Parisian society was satirized by Proust in a series of pastiches entitled *L'affaire Lemoine* [112]. The diamond samples in our experiment were artificially produced using chemical vapour deposition. The sample contained < 5 parts per billion nitrogen impurity and a dislocation density of around 10^3 – 10^4 cm^{-2} [105].

3.2.1 Simple derivation of the phonon dispersion

The diamond structure is formed from two interlaced face-centred cubic lattices with two carbon atoms per unit cell. Two atoms per primitive cell gives rise to two phonon branches per polarization mode, of which there are three (two transverse and one longitudinal). The branches are defined by their dispersion relations, whose derivation will now be motivated following reference [113]. Consider the case of a set of planes that alternate between two atomic species with masses M_1 and M_2. The equation of motion for the atoms, given only nearest-neighbour interactions, is given by the coupled equations

$$M_1 \frac{\mathrm{d}^2 v_n}{\mathrm{d}t^2} = \Gamma(w_n + w_{n-1} - 2v_n), \tag{3.21}$$

$$M_2 \frac{\mathrm{d}^2 w_n}{\mathrm{d}t^2} = \Gamma(v_{n+1} + v_n - 2w_n), \tag{3.22}$$

where v_n and w_n are the displacement of the atoms from their equilibrium position indexed by the location of the atom, and Γ is the force constant between the nearest-neighbour atoms. The solution to equations 3.21 and 3.22 can be expressed in terms of plane waves of the form

$$v_\mathrm{n} = v \exp(inKa) \exp(-i\omega t), \tag{3.23}$$

$$w_\mathrm{n} = w \exp(inKa) \exp(-i\omega t), \tag{3.24}$$

where a is the lattice spacing between planes of the same atomic species and K is the phonon wave-vector. Substitution of equations 3.23 and 3.24 into equations 3.21 and 3.22 yields

$$\begin{bmatrix} \frac{2\Gamma}{M_1} - \omega^2 & -\Gamma[1 + \exp(-iKa)] \\ -\Gamma[1 + \exp(-iKa)] & \frac{2\Gamma}{M_2} - \omega^2 \end{bmatrix} \begin{bmatrix} v \\ w \end{bmatrix} = 0. \tag{3.25}$$

We can recognize a correspondence to the eigenvalue equation $\left|A - \lambda I\right| = 0$, where we associate $\lambda = \omega^2$. From Cramer's rule, this equation has a solution when the determinant vanishes. The roots of the equation are

$$\omega^2 = \left(\frac{\Gamma}{M}\right) \left[M \pm \sqrt{(M) - 2M_1 M_2 (1 - \cos Ka)}\right], \tag{3.26}$$

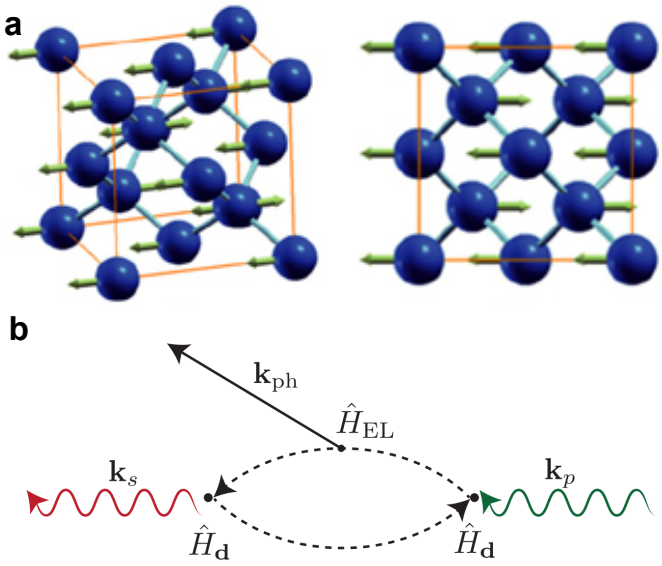

Figure 3.3: **a** Illustration of the vibration of the optical phonon in diamond showing the two interlaced face-centre cubic lattices, from reference [114]. On the right shows the plane [100]. **b** Illustration of Raman scattering process in diamond. The pump photon (green line) creates an exciton (dashed line), which scatters off the deformation potential, creating a phonon (solid black line) and a lower energy Stokes photon (red line).

where $M = M_1 + M_2$. Equation 3.26 is plotted in figure 3.4**a**, showing the two phonon branches corresponding to the + and − terms in equation 3.26. At the zone centre, the acoustic phonon dispersion is linear; the phonon propagates with velocity ω/K. The optical phonon dispersion is flat at the band edge; the optical phonons are non-propagating, delocalized excitations. Qualitatively, with acoustic phonons, neighbouring atoms move in phase and, with optical phonons, neighbouring atoms move out of phase. In diamond, there is only one atomic species, carbon, and the two phonon branches arise from the different force constants between the two sub-lattices; however, the behaviour is qualitatively similar, and is plotted in figure 3.4**b**. The term optical phonon refers to the fact that the lattice vibrations can be excited by photons at optical frequencies, which will be discussed in the next section.

3.2.2 Raman scattering in diamond

Raman scattering from crystals arises from the dependence of the electric polarizability on the crystal strain. The electric polarizability α has a term proportional to the displacement of the atoms from their equilibrium position $v(t) = v\cos(\omega_{pn}t)$ and the induced

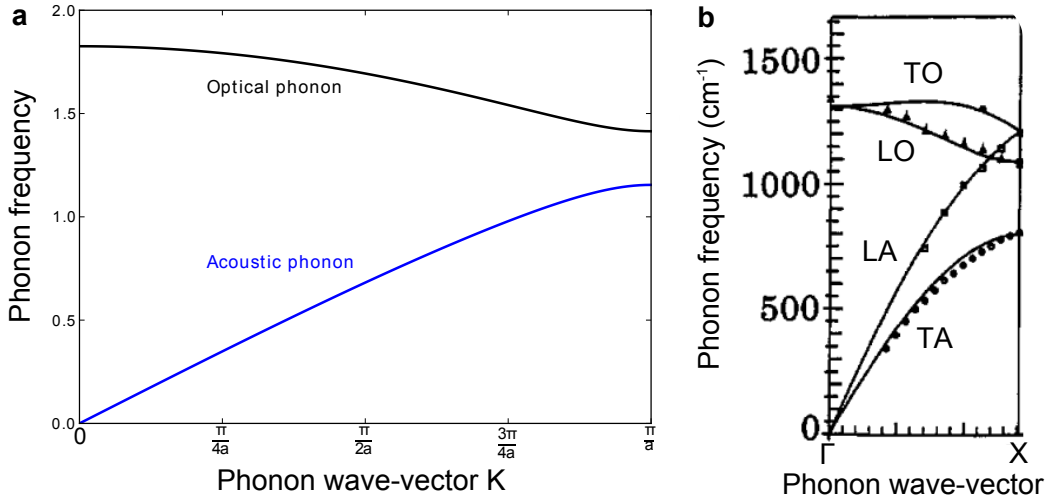

Figure 3.4: **a** Qualitative diagram of the phonon dispersion for the acoustic and optical branches from equation 3.26. **b** Dispersion of the optical and acoustic branches in diamond showing the transverse optical (TO), longitudinal optical (LO), transverse acoustic (TA), and longitudinal acoustic (LA) branches, from reference [115].

dipole moment in the crystal d_{Raman} is proportional to the polarizability and the optical field $E(t) = E_0 \cos(\omega_{\text{pt}} t)$,

$$d_{\text{Raman}} \propto v\alpha E_0 \cos(\omega_{\text{pn}} t)\cos(\omega_{\text{pt}} t) = \frac{1}{2} v\alpha E_0 \left[\cos(\omega_{\text{pt}} t + \omega_{\text{pn}} t) + \cos(\omega_{\text{pt}} t - \omega_{\text{pn}} t)\right], \tag{3.27}$$

where ω_{pn} is the phonon frequency and ω_{pt} is the photon frequency. The emission of a phonon generates a Stokes photon and the absorption of a phonon generates an anti-Stokes photon, which can be thought of as spectral sidebands at the carrier optical frequency. The intensity of the Stokes I_{S} relative to the anti-Stokes I_{AS} intensity is given by

$$\frac{I_{\text{S}}}{I_{\text{AS}}} = \frac{\langle n_{\text{K}} \rangle}{\langle n_{\text{K}} \rangle + 1} = \exp\left(-\frac{\hbar\omega_{\text{pn}}}{k_{\text{B}} T}\right), \tag{3.28}$$

where the phonon thermal population is n_{K}, and T is the temperature. As $T \to 0$ the Stokes and anti-Stokes lines become asymmetric in intensity. Indeed, several recent experiments have used this fact as a signature for demonstrating that optomechanical oscillators can be cooled to their mechanical ground state [116, 117, 118].

In dipolar Raman-active materials, the strain induced in a crystal causes the displace-

ment of charged ions, creating a dipole moment that couples directly to an optical field. Diamond is homopolar as it consists of only one atom, carbon, and the mechanism by which it couples to an optical field is slightly more complicated. The far-detuned pump pulse creates a virtual *exciton* – a bound state of an electron in the conduction band and hole in the valence band of diamond. The energy bands arise from coherent scattering of electrons with atoms in the crystal, and the energy of the bands is determined by the crystal geometry. Deformation of the crystal structure can change the energy of the excitons. In particular, the virtual exciton can scatter off an optical phonon, resulting in a virtual exciton recombining to form a photon with a different energy [119]. This process is illustrated in figure 3.3**b**.

The strength and polarization of Raman scattering is determined by the geometry of the crystal structure. The optical phonon mode in diamond is triply degenerate with vibrational symmetry T_{2g} (Γ_5^+) and has a first order Raman shift of 1332 cm^{-1} [119, 120, 121]. In our experiments, the diamond sample was cut along the [100] face, resulting in Raman-scattered light polarized orthogonal to the input field. In general, the Raman scattering efficiency in a crystal is given by [122]

$$S = A\left[\sum_{\sigma,\rho,\tau=x,y,z} e_i^\sigma R_{\sigma\rho}\xi_\tau e_s^\rho\right]^2 \tag{3.29}$$

where A is a constant, e_i^σ is the principal component of the polarization vector of the incident photon with wavevector k_i, e_s^ρ is the principal component of the polarization vector of the scattered photon with wavevector k_s, ξ_τ is the polarization vector of the phonon and $R_{\sigma\rho}$ is the Raman tensor for the relevant crystal symmetry class. Diamond has a cubic structure with a symmetry class of $m3m(O_h)$, which gives the three-fold degenerate Raman tensors for the Raman-active vibration (along [100]) [122]

$$R_{xy} = \begin{bmatrix} 0 & d & 0 \\ d & 0 & 0 \\ 0 & 0 & 0 \end{bmatrix}, \; R_{yz} = \begin{bmatrix} 0 & 0 & 0 \\ 0 & 0 & d \\ 0 & d & 0 \end{bmatrix}, \; R_{zx} = \begin{bmatrix} 0 & 0 & d \\ 0 & 0 & 0 \\ d & 0 & 0 \end{bmatrix}. \tag{3.30}$$

As an example, consider an incident photon with wavevector pointing in the z direction

and polarised in the y direction incident normal to the diamond sample, which produces a scattered Stokes photon at an angle ϕ to the incident photon and a phonon with angle $-\frac{\pi}{2} - \frac{\phi}{2}$ (in the limit $k_{pn} \ll k_i$). If we consider a diamond structure with two different atoms, we can decompose equation 3.29 into scattering contributions from transverse (ξ_x) and longitudinal (ξ_z) optical phonons

$$S_T = e_i^y A_T \sum_{\sigma,\rho=x,y} R_{\sigma\rho}\xi_x e_s^\rho = e_i^y A_T [R_{yx}\xi_x e_s^x + R_{yz}\xi_x e_s^z]^2, \tag{3.31}$$

$$S_L = e_i^y A_L \sum_{\sigma,\rho=x,y} R_{\sigma\rho}\xi_z e_s^\rho = e_i^y A_L [R_{yx}\xi_z e_s^x + R_{yz}\xi_z e_s^z]^2, \tag{3.32}$$

where $\xi_{x,y}$ and e_s^ρ are defined relative to the wave-vector direction, and need to be transformed to the basis defined by the crystal orientation (this is where the direction of the phonon wavevector is significant)

$$\xi_x = \begin{bmatrix} \cos\frac{\phi}{2} \\ 0 \\ \sin\frac{\phi}{2} \end{bmatrix}, \ \xi_z = \begin{bmatrix} \sin\frac{\phi}{2} \\ 0 \\ \cos\frac{\phi}{2} \end{bmatrix}, \tag{3.33}$$

$$e_s^x = \hat{\mathbf{x}}\cos\phi, \ e_s^y = \hat{\mathbf{y}}\sin\phi. \tag{3.34}$$

Therefore, the scattering contributions from the longitudinal and transverse optical phonons are

$$S_T = e_i^y A_T d^2 \cos^2\left(\frac{3\phi}{2}\right), \tag{3.35}$$

$$S_L = e_i^y A_L d^2 \sin^2\left(\frac{3\phi}{2}\right), \tag{3.36}$$

which are plotted in figure 3.5. For the case of diamond, the longitudinal and transverse optical phonons are degenerate ($A_T = A_L$) at the zone center, and the resulting emission is circularly symmetric. The optical phonon is not exactly at the zone centre as the small but finite phonon wavevector breaks the degeneracy. Each emission will be correlated to a particular combination of longitudinal and transverse optical phonons as in figure 3.5. In other words, Stokes photons can be generated in any direction, but the direction is

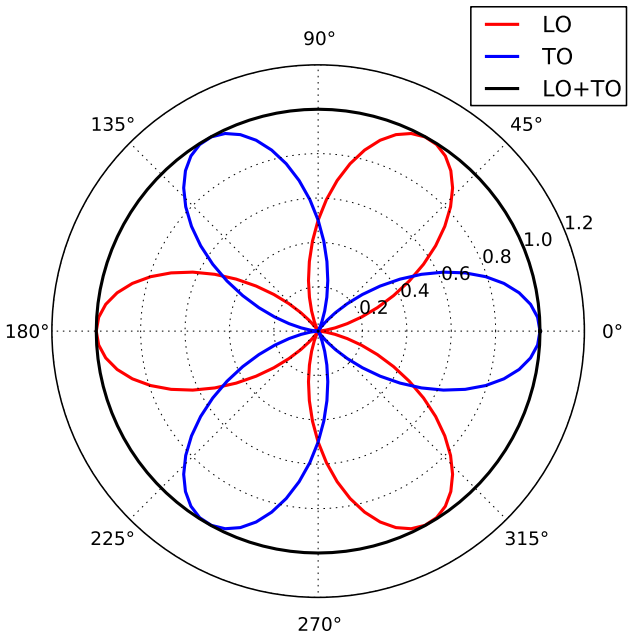

Figure 3.5: Polarization of the optical phonons as a function of the scattering angle of the Stokes photon relative to the pump photon. The transverse optical phonon (TO) is a blue line, the longitudinal optical phonon a red line and the black circle is $S_T + S_L$.

correlated to the polarization of the phonon, with no particular direction being forbidden. In addition, the Raman tensors in equation 3.30 enforce a key selection rule, the Stokes or anti-Stokes scattered light is orthogonally polarized to the input pump pulse when the wavevector is parallel to [001]. This will be important when discussing the experimental implementation of the DLCZ protocol with diamonds. We now turn to discussing the phase-matching condition for Raman scattering in diamond.

3.2.3 Phase-matching conditions

The conservation of energy and momentum underlie every physical process. The Raman interaction in a homogeneous medium must satisfy the following conditions[2]

$$\Delta\mathbf{k} = 2\mathbf{k}_\mathrm{p} - \mathbf{k}_\mathrm{s} - \mathbf{k}_\mathrm{a} = 0, \tag{3.37}$$

$$\Delta\omega = 2\omega_\mathrm{p} - \omega_\mathrm{s} - \omega_\mathrm{a} = 0, \tag{3.38}$$

[2]Birefringence here is ignored. A perfect diamond crystal will not have any birefringence. Although this is not entirely achieved in practice, the diamonds used in our experiment were manufactured to have low birefringence.

where we assume the first and second pulse have the same momentum and energy and the subscripts p, s, and a denote the pump pulse, Stokes photon and anti-Stokes photon. The frequency of the optical phonon is $\omega_{\mathrm{pn}} = (\omega_{\mathrm{a}} - \omega_{\mathrm{s}})/2$.

The magnitude of the wavevector mismatch ($\Delta\mathbf{k}$) is meaningful only when compared with the length of the material. The four-wave mixing efficiency S_{FWM} (the efficiency of the combined process of Stokes followed by anti-Stokes scattering) is proportional to the integral of the phase mismatch ($\Delta\phi = \Delta\mathbf{k}\cdot\mathbf{r}$) over the volume of the ensemble [123]

$$S_{\mathrm{FWM}} \propto \int_V \mathrm{d}V \mathrm{e}^{\mathrm{i}\Delta\mathbf{k}\cdot\mathbf{r}} = \tag{3.39}$$

$$\frac{1}{L}\int_0^L \exp(\mathrm{i}\Delta k_z z)\mathrm{d}z \int_{-\infty}^{\infty}\int_{-\infty}^{\infty} G(x,y)\exp\left[\mathrm{i}(\Delta k_x x + \Delta k_y y)\right]\mathrm{d}x\mathrm{d}y, \tag{3.40}$$

where $G(x,y) = 1/(2\pi\sigma_x\sigma_y)\exp(-(x^2/\sigma_x^2 + y^2/\sigma_y^2)/2)$ is the Gaussian spatial profile of the pump laser in the transverse direction, with standard deviation $\sigma_{x,y}$, and L is the length of the diamond in the longitudinal direction. It is assumed that the beam profile is independent of the z coordinate, indicating the Rayleigh length of the pump beam is much greater than the length of the diamond crystal. Evaluating equation 3.40 yields

$$\phi_{\mathrm{FWM}} = \exp\left(\frac{\mathrm{i}\Delta k_z L}{2}\right)\mathrm{sinc}\left(\frac{\Delta k_z L}{2}\right)\exp\left[-\frac{1}{2}\left(\sigma_x^2\Delta k_x^2 + \sigma_y^2\Delta k_y^2\right)\right], \tag{3.41}$$

where ϕ_{FWM} is termed the phase-matching function. We are interested in answering two questions when considering the phase-matching function. First, when looking on-axis ($\Delta k_x = \Delta k_y = 0$), what is the joint spectral probability distribution (square of the phasematching function) of the Stokes and anti-Stokes photons given the broadband pump pulse used in our experiments ($\nu_{\mathrm{pump}} = 8$ THz, FWHM)? Second, what is the angular dependance of the joint spectral probability distribution – for what emission angles of the Stokes and anti-Stokes photon is the four-wave mixing process phase matched?

The broadband pump pulses used in our experiments had a bandwidth of 8 THz FWHM or, equivalently, 17 nm at a central wavelength of 800 nm. The optical phonon has a fixed, well-defined frequency of 40 THz as the phonon linewidth is 100 GHz, which is an order of magnitude smaller than the optical pulse bandwidth. In our experiments, we used diamonds with thicknesses of 0.25 and 0.5 mm, but here we simply consider

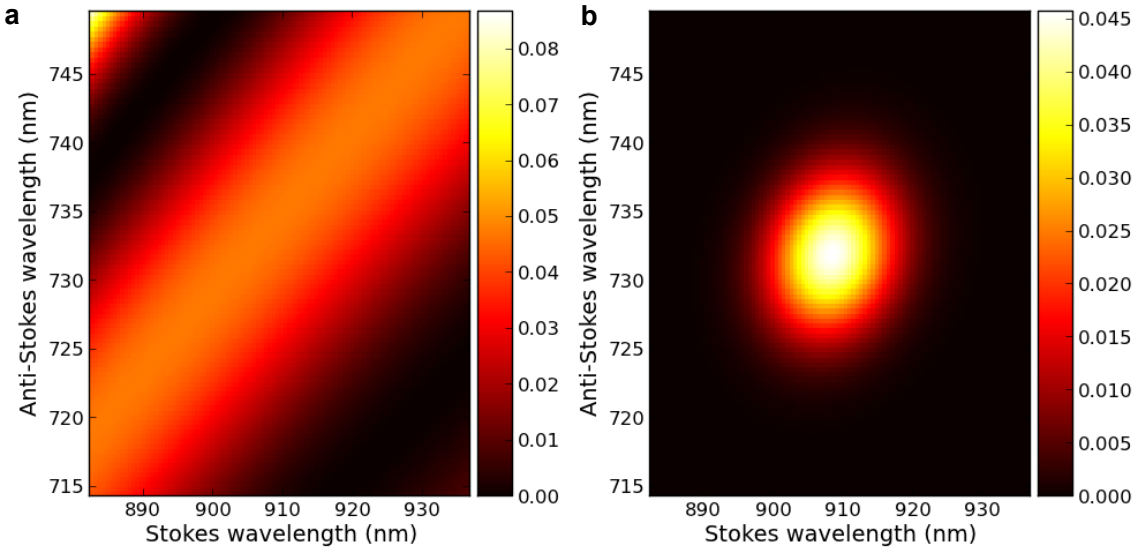

Figure 3.6: **a** The square of the phase-matching function plotted versus the Stokes and anti-Stokes wavelength. **b** Joint spectral probability distribution versus the Stokes and anti-Stokes wavelength, showing a maximum of 0.046 for $\lambda_s = 908.8$ nm and $\lambda_a = 732.2$ nm compared to a maximum wavelength due only to the pulse envelope of $\lambda_s = 909.1$ nm and $\lambda_a = 731.7$ nm

the thinner sample. In a normally dispersive regime (diamond, infrared), the index of refraction increases with increasing frequency, as does the rate of increase.[3] The increasing rate of dispersion means that the average index of refraction of the Stokes and anti-Stokes fields is higher than the index of refraction of the pump field. The dispersion is modelled by Sellmeir's equation, which for diamond is [124]

$$n(\lambda[\text{nm}]) = \sqrt{\frac{0.3306\lambda^2}{\lambda^2 - 175^2} + \frac{4.3356\lambda^2}{\lambda^2 - 106^2}}. \tag{3.42}$$

The modulus square of the phase-matching function is plotted in figure 3.6**a** for $L = 0.25$ mm for a parameter space of 20 THz, and expressed in terms of the Stokes and anti-Stokes wavelength. The pump, Stokes, and anti-Stokes beams are all collinear. Only when the difference in frequency between the two pump pulses is on the order of the frequency of the optical phonon does phase matching occur, which is outside the bandwidth of the pump pulse (8 THz). Multiplying the phase-matching function with the Gaussian envelope of the pump pulse ($\lambda_{\text{centre}} = 808$ nm, $\Delta\omega_{FWHM} = 8$ THz, $\Delta\lambda_{FWHM} = 17$ nm, and assuming that the spectrum is roughly Gaussian) gives the joint spectral amplitude

[3] Diamond is prized for its strong dispersion, lending it a multi-spectral glint known as its 'fire'.

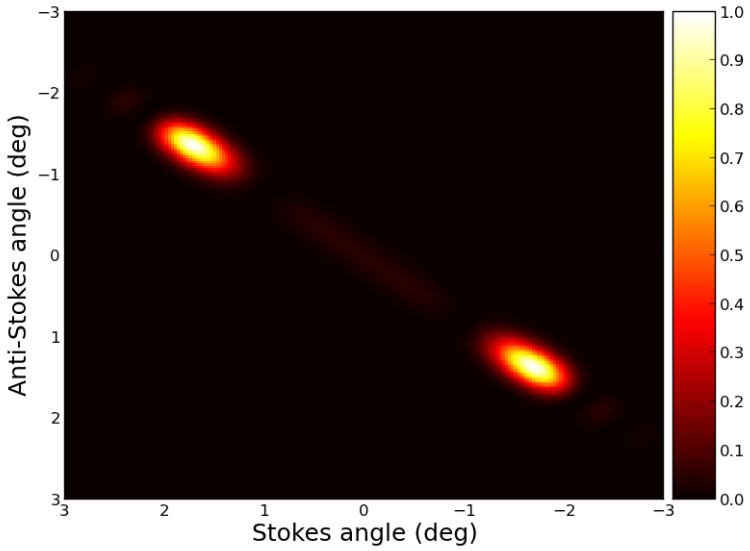

Figure 3.7: Square of phase-matching function showing angular correlations between Stokes and anti-Stokes fields, relative to the collinear pump fields. The phase-matching angles are $\theta_{\mathrm{s}} = \pm 1.70°$ and $\theta_{\mathrm{a}} = \mp 1.37°$.

$$f(\omega_{p_1}, \omega_{p_2}) = \phi(\omega_{p_1}, \omega_{p_2}) \cdot \exp(-\left[(\omega_{p_1} - \omega_c)^2/2\sigma^2 + (\omega_{p_2} - \omega_c)^2/2\sigma^2\right]), \tag{3.43}$$

where ω_{p1}, ω_{p2} are the frequency of the first and second pump pulse, $\omega_c = 2\pi \cdot 371\,\mathrm{THz}$ is the centre frequency of the pump, and $\sigma = 2\pi \cdot 3.6\,\mathrm{THz}$. The square of the joint spectral amplitude, the joint spectral probability distribution, is shown in figure 3.6**b**. The maximum value is 0.046, which occurs for $\lambda_{\mathrm{s}} = 908.8$ nm and $\lambda_{\mathrm{a}} = 732.2$ nm. The joint spectral probability distribution is circularly symmetric as the phase-matching bandwidth (≈ 100 THz) is much larger than the pulse bandwidth (8 THz) and therefore no frequency correlations will be present. Tracing over frequency correlations between the Stokes and anti-Stokes photons would reduce the interference visibility of the heralded anti-Stokes photons [123].

The preceding analysis considered the case where the pump, Stokes, and anti-Stokes fields were collinear. This condition can be relaxed to allow for an angle between the pump and the Stokes and anti-Stokes fields. The fact that the mean dispersion of the Stokes and anti-Stokes is higher than the dispersion of the pump means that the four-wave mixing process can be phase matched given a relative angle between the Stokes and anti-Stokes wave-vectors.

The square of the phase-matching function in equation 3.41 was plotted for $\sigma_x =$

$\sigma_y = 17\,\mu$m in figure 3.7 with the same pump parameters. As expected, phase matching occurs when the angle of the Stokes and anti-Stokes fields are anti-correlated such that $\theta_s = \pm 1.70°$ and $\theta_a = \mp 1.37°$. The approximate width of the phase-matching condition is 0.6°. On-axis, the value of the square of the phase-matching function is 0.046, consistent with figure 3.6.

To conclude this section, the joint spectral probability density sets a bound on the maximum retrieval efficiency of the phonon via anti-Stokes scattering. The four-wave mixing process is not phase matched on-axis, but is phase matched when a small angle of 3.07° is introduced between the Stokes and anti-Stokes fields. This angle needs to be compared to the numerical aperture of the detection optics to determine the coupling of the optical fields. Now that we have considered aspects of four-wave mixing, we move on to discuss the generation and quantification of non-classical light using four-wave mixing.

3.3 Non-classical light from diamond

3.3.1 Correlation functions for photon statistics

Non-classical light cannot be described by classical electrodynamics. A canonical example is the single-photon Fock state $|\psi\rangle = |1\rangle$. These states of light are uniquely useful for quantum-enhanced operations, as outlined in the introductory chapter. Ways to detect and quantify non-classical features form an ongoing research programme [125]. Two common approaches for detecting quantum signatures in light are with homodyne measurements, where the electric field quadratures are measured using a local oscillator, and photon counting measurements, where photon-number statistics are estimated. Here we consider the latter approach.

A light field can be characterized via its correlation functions. The k^{th}-order correlation function can be calculated via its generating function, and is given by

$$g^{(k)} = \frac{\langle : \hat{n}^k : \rangle}{\langle \hat{n} \rangle^k}, \tag{3.44}$$

where $\hat{n} = \hat{a}^\dagger \hat{a}$ is the photon number operator and $: \hat{n} :$ indicates the normal ordering of the creation and annihilation operators. For mixed states, N correlation functions

are needed to determine the occupancy of N modes [125]. For stationary states, the second-order correlation function is

$$g^{(2)}(\tau) = \frac{\langle : \hat{n}(0)\hat{n}(\tau) : \rangle}{\langle \hat{n}(0) \rangle^2}, \tag{3.45}$$

where τ is the relative time delay between the fields.

Often the second-order auto-correlation $g^{(2)}(\tau)$ suffices to demonstrate that light has non-classical features. Coherent states – states that are generated by lasers – have $g^{(2)}(\tau) = 1$ for all τ; the arrival times follow a Poissonian distribution where the arrival of each photon is statistically independent. For thermal states, which can be thought of as phase-averaged coherent states, $g^{(2)}(0) = 2$. Photons from thermal states are said to have super-Poissonian or bunched statistics; the arrival of one photon makes the arrival of a second photon more likely. Fock-states have $g^{(2)}(0) = 0$. Indeed, having $g^{(2)}(0) < 1$ is a sufficient but not necessary condition for non-classicality. A related, but not equivalent[4], measure for demonstrating non-classicality is the observation of anti-bunching, which is when the arrival of one photon makes the arrival of a second photon less likely. In this case, the signature of anti-bunching is $g^{(2)}(\tau) > g^{(2)}(0)$ [126]. Besides measuring the auto-correlation, non-classicality can be demonstrated by measuring the cross-correlation between two modes, as will now be discussed.

3.3.2 Violation of the Cauchy-Schwarz inequality

The Cauchy-Schwarz inequality, as originally stated, relates the norm of two vectors to the inner product of the vectors,

$$||\mathbf{a} \cdot \mathbf{b}|| \leq ||\mathbf{a}|| \cdot ||\mathbf{b}||. \tag{3.46}$$

It is clear that this inequality cannot be violated in geometric vector space. However, an analogous inequality in quantum optics has also been termed the Cauchy-Schwarz inequality. Classical optical intensities are square-integrable functions that can be thought of as forming a vector space, where the inner product is the integral of the product of the

[4]For instance, it is not meaningful to ask whether a single-photon and single-mode Fock state is anti-bunched. Anti-bunching only occurs in multi-mode states [107].

two fields (for real-valued fields). We can express equation 3.46 in terms of the photon-number operators for optical fields 1 and 2 as

$$\langle \hat{a_1}^\dagger \hat{a_2}^\dagger \hat{a_1} \hat{a_2} \rangle \leq \left[\langle (\hat{a_1}^\dagger)^2 (\hat{a_1})^2 \rangle \langle (\hat{a_2}^\dagger)^2 (\hat{a_2})^2 \rangle \right]^{1/2}. \tag{3.47}$$

This in turn can be expressed in terms of the second-order correlation functions,

$$[g_{12}^{(2)}(0)]^2 \leq g_{11}^{(2)}(0) g_{22}^{(2)}(0), \tag{3.48}$$

where

$$g_{12}^{(2)}(0) = \frac{\langle \hat{a_1}^\dagger \hat{a_2}^\dagger \hat{a_1} \hat{a_2} \rangle}{\langle \hat{a_1}^\dagger \hat{a_1} \rangle \langle \hat{a_2}^\dagger \hat{a_2} \rangle} \tag{3.49}$$

is the second-order cross-correlation between the two optical modes, and $\left\{ g_{11}^{(2)}, g_{22}^{(2)} \right\}$ are the second-order auto-correlation functions. This inequality can be violated for photon modes where the integral of the product of the optical intensities is not equal to the product of the integral of the individual fields, which is an indication that the light is non-classical. Loosely speaking, the Cauchy-Schwarz inequality can be violated for two functions that are better correlated with each other than with themselves.

One example of such a state is the two-mode squeezed state introduced earlier in equation 3.7. For this state, we can calculate the expectation value of the number of photons in the Stokes mode [127]

$$\langle \hat{s}^\dagger \hat{s} \rangle = (1-\chi) \sum_{n=1}^{\infty} n \chi^n = (1-\chi) \chi \frac{\partial}{\partial \chi} \sum_{n=1}^{\infty} \chi^n = \frac{\chi}{1-\chi}. \tag{3.50}$$

The first- and second-order moments of the number operator can be calculated in a similar

manner and are given by

$$\langle \hat{a}^\dagger \hat{a} \rangle = \frac{\chi}{1-\chi}, \tag{3.51}$$

$$\langle \hat{s}^\dagger \hat{a}^\dagger \hat{s} \hat{a} \rangle = \frac{\chi + \chi^2}{(1-\chi)^2}, \tag{3.52}$$

$$\langle \hat{s}^\dagger \hat{s}^\dagger \hat{s} \hat{s} \rangle = \frac{2\chi}{(1-\chi)^2}, \tag{3.53}$$

$$\langle \hat{a}^\dagger \hat{a}^\dagger \hat{a} \hat{a} \rangle = \frac{2\chi}{(1-\chi)^2}. \tag{3.54}$$

From these expressions, the second-order cross- and auto-correlations for the Stokes and anti-Stokes modes can be calculated as

$$g^{(2)}_{sa}(0) = 1 + \frac{1}{\chi}, \tag{3.55}$$

$$g^{(2)}_{ss}(0) = g^{(2)}_{aa}(0) = 2. \tag{3.56}$$

The auto-correlation of the fields signifies that the individual modes, traced over the other mode, are thermal in nature [126, 128]. The Cauchy-Schwarz inequality is therefore violated when $\chi < 1$. This seems trivial since we developed equation 3.7 in the regime $\chi \ll 1$. Indeed, the number of photons and, hence, the energy of the optical modes diverges to infinity as $\chi \to 1$. It may seem that we are guaranteed to violated a Cauchy-Schwarz inequality and generate non-classical light when we have a Hamiltonian that produces a two-mode squeezed state. The main challenge, however, is to ensure detection of the correct scattered mode and elimination of any spurious noise that could spoil the correlation measurement. Another challenge is to ensure it is a two-mode state and not a more multi-mode state. This is guaranteed as we are in the limit where the Raman linewidth (100 GHz) is much less than the pump bandwidth (8 THz) and, as a result, the pump pulse defines a single spectral mode. We will describe these efforts briefly in the next section.

3.3.3 Experimental setup

The generation of non-classical light using optical phonons in diamond is inherently interesting as a demonstration of the fact that non-classical correlations can persist in a

room-temperature, solid-state object. In addition, the visibility of the interference in the DLCZ protocol outlined earlier is contingent on the second-order cross-correlation, which sets the bound on the amount of entanglement between the two atomic ensembles. Therefore, measuring the non-classical correlation of Raman-scattered optical modes from diamond is an important milestone toward the goal of demonstrating entanglement between two objects, which is a fundamental component of the DLCZ protocol.

We measured the second-order cross-correlation between the Raman-scattered Stokes and anti-Stokes mode using the apparatus shown in figure 3.8. An 80-MHz repetition rate titanium-sapphire oscillator generated pulses with a wavelength of 800 nm and duration of 60 fs (FWHM) at an average power of 600 mW. The pulses were split into two time bins (the *write* and *read* control pulses) separated by up to 11 ps (spanning the coherence time of the phonon) using an unbalanced Mach-Zehnder interferometer. A 5-cm focal length achromatic lens focused the pulses through the diamond sample, which had a thickness of 0.5 mm. Given the crystal geometry, the Stokes and anti-Stokes beams were polarized orthogonal to the read and write pulses. The write pulses from the two spatial modes were, in turn, orthogonally polarized , as were the read pulses, which allowed for polarization-selective detection of the read or write pulse. The 800-nm-wavelength pump was removed by notch filters (Semrock RazorEdge), which provided a combined extinction ratio of 10^{-12} and a transmission of approximately 70% (total). The Stokes and anti-Stokes beams were separated with dichroic mirrors, coupled into single-mode fibres and detected with APDs (operating in Geiger mode). Coincidence counts were measured with a field-programmable gate array (FPGA) with a 5-ns synchronous coincidence window.

3.3.4 Non-classical $g^{(2)}$ in diamond

The second-order cross-correlation $g^{(2)}_{\mathrm{s,a}}$ was estimated from the probability of the joint detection of a Stokes and anti-Stokes photon $P_{\mathrm{s,a}}$, along with the unconditional probability of detecting a Stokes P_{s} and anti-Stokes photon P_{a}

$$g^{(2)}_{\mathrm{s,a}}(T) = \frac{P_{\mathrm{s,a}}(T)}{P_{\mathrm{s}}(T)P_{\mathrm{a}}(T)}, \tag{3.57}$$

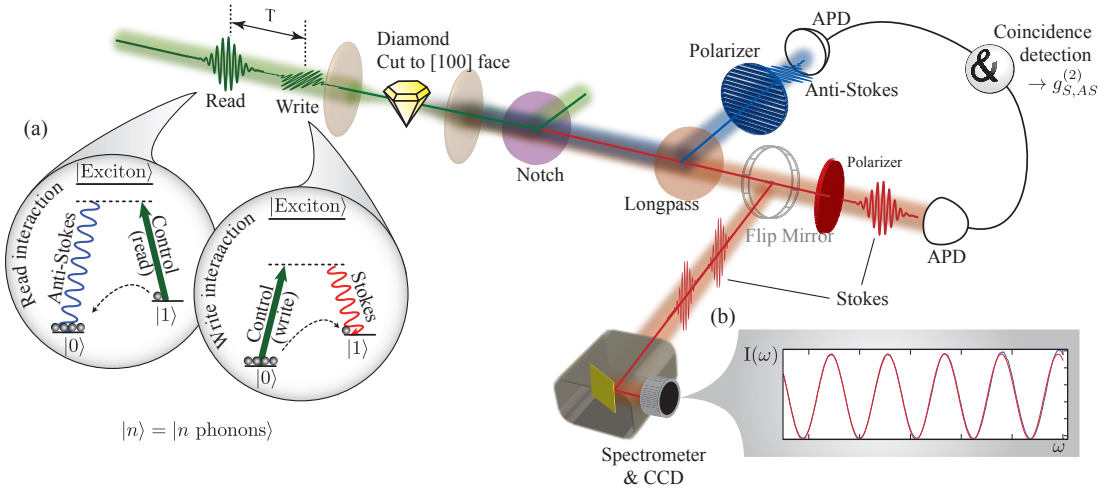

Figure 3.8: Optical layout for the Raman-scattering measurements of the optical phonons in diamond, from reference [129]. A Stokes photon and an optical phonon were created with a write pulse. A read pulse, delayed by a time T, created either a second Stokes photon (for the coherence measurement), or annihilated the phonon and created an anti-Stokes photon (for the quantum memory). For the quantum-memory correlation measurements, the read pulse was polarized orthogonal to the write pulse, allowing the write Stokes and read anti-Stokes photons to be isolated and detected with single-photon APDs. For the coherence measurement, the read- and write-pulse polarizations were aligned in the same direction and the Stokes photons were sent to a single-photon-sensitive spectrometer. **a** Level structure of the Raman interaction. **b** Interference of the Stokes spectrum, which was a measure of the coherence of the phonons.

where T is the delay between the write and read pulses (i.e. the storage time). We found that $P_{\mathrm{s}}(T)$ and $P_{\mathrm{a}}(T)$ were, to a good approximation, independent of T. Experimentally, we measured $P_{\mathrm{s,a}} \approx 10^{-8}$ and $P_{\mathrm{s}} \approx 10^{-3}$ for a storage time of $T = 3$ ps. The collection and detection efficiency of the Stokes and anti-Stokes modes was estimated to be $\eta \approx 1\%$ from which we can infer that the probability of creating a Stokes photon per pump pulse was $0.1 \ll 1$ in accordance with our earlier analysis. We can also infer that the retrieval efficiency from the memory was $P_{\mathrm{s,a}}/P_{\mathrm{s}}\eta \approx 0.1\%$. This could be improved by phase and mode matching. When the read and write pulses have the same energy, the retrieval efficiency will be limited to the Stokes creation probability (10%). This is a limitation of the DLCZ protocol and can be overcome by using read and write pulses with different energies or frequencies.

Figure 3.9 shows that we observed $g^{(2)}_{\mathrm{s,a}}(T = 1\,\mathrm{ps}) \approx 5.1$. This exceeds the Cauchy-

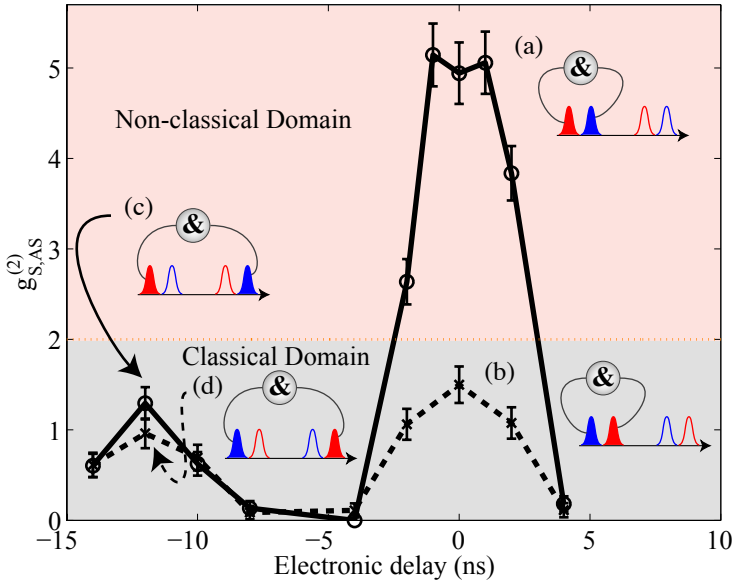

Figure 3.9: Non-classical correlations generated by the quantum memory as a function of the relative electronic delay between the Stokes and anti-Stokes APDs, from reference [129]. The black line shows the second-order cross-correlation $g^{(2)}_{\mathrm{s,a}}$ for a delay of 1 ps. (a) The Cauchy-Schwarz inequality $g^{(2)}_{s,a} < 2$ is violated, demonstrating non-classical correlation between Stokes photons from the write pulse and anti-Stokes photons from the read pulse. (b) The reverse time ordering: the correlation between anti-Stokes photons from the write pulse and Stokes photons from the read pulse (dashed line). (c) and (d) The experiment was repeated with a period of 12.5 ns. When the electronic delay was increased to 12.5 ns, accidental coincidences were measured between write and read pulses from separate read-write sequences, and no violation was observed. Note the width of non-classical peak was determined by the coincidence window of the detection electronics.

Schwarz bound,

$$\left[g^{(2)}_{\mathrm{s,a}}(T)\right]^2 \leq g^{(2)}_{\mathrm{s,s}}(0)g^{(2)}_{\mathrm{a,a}}(0), \tag{3.58}$$

as the auto-correlation of the Stokes and anti-Stokes fields were less than two for thermal states (see section 3.3.2). The second-order cross-correlation was measured as function of the electronic delay between the Stokes and anti-Stokes APDs; the signal from the two APDs were delayed with short lengths of coaxial cable before being input into the FPGA. Point (a) corresponds to the cross-correlation between the Stokes photons in the write time bin and the anti-Stokes in the read time bin. Other time orderings, including the Stokes from the read time bin and the anti-Stokes from the write time bin, or cross-correlation between successive read-write sequences, had $g^{(2)}_{\mathrm{s,a}} < 2$ as expected. We therefore conclude that optical phonons in diamond acted as a quantum memory capable of storing and

retrieving non-classical states of light.

3.3.5 Coherence time and lifetime of the optical phonon

Optical phonons in diamond are especially long lived relative to other optical phonons because the phonon transition is dipole-forbidden.[5] The dominant decay mechanism in diamond is the so-called *Klemens channel*, which arises from the anharmonicity of the lattice potential [130]. A zone-centre optical phonon decays into two counter-propagating acoustic phonons each with half the energy in order to conserve energy and momentum. We measured the lifetime T_1 and the coherence time T_2 of the optical phonon and compared it to the theoretical prediction from the Klemens channel.

The population lifetime of the optical phonon was determined by measuring $P_{\mathrm{s,a}} \propto g^{(2)}_{\mathrm{s,a}}$ as a function of the delay between the write and read pulse, as is shown in figure 3.10**a**. The population lifetime was measured to be $T_1 = 3.6 \pm 0.2$ ps. The coherence of the optical phonons was measured by sending the Stokes photons into a spectrometer, as shown in figure 3.8. Spectral fringes were a signature of the phonon coherence and could be quantified by measuring their visibility [131, 105]. This can be thought of as an instance of Feynman's rule, where any two processes that are indistinguishable can interfere quantum mechanically. The read and write time bins can be thought of as 'temporal double slits' which were indistinguishable given that the modes were engineered to overlap in time inside the spectrometer; the dispersion from the grating element induced the overlap of the pulses. Any decay process caused *'which-way'* information to leak into the environment, which rendered the two paths distinguishable and reduces the fringe visibility.

Figure 3.10**b** shows the spectral fringe visibility of the Stokes field as the delay T between the read and write pulse was varied. The lifetime of the fringe visibility directly determines the coherence lifetime $T_2 = 6.9 \pm 0.2$ ps. The ratio $T_2/T_1 \leq 2$ is a measure of how dominant pure dephasing mechanisms are compared to inhomogeneous broadening mechanisms. For example, if $T_2/T_1 = 2$ then there is no inhomogeneous broadening and the coherence time of the optical phonon is said to be 'lifetime limited'. If the

[5] This is due to the fact that diamond consists of only one atomic species, carbon.

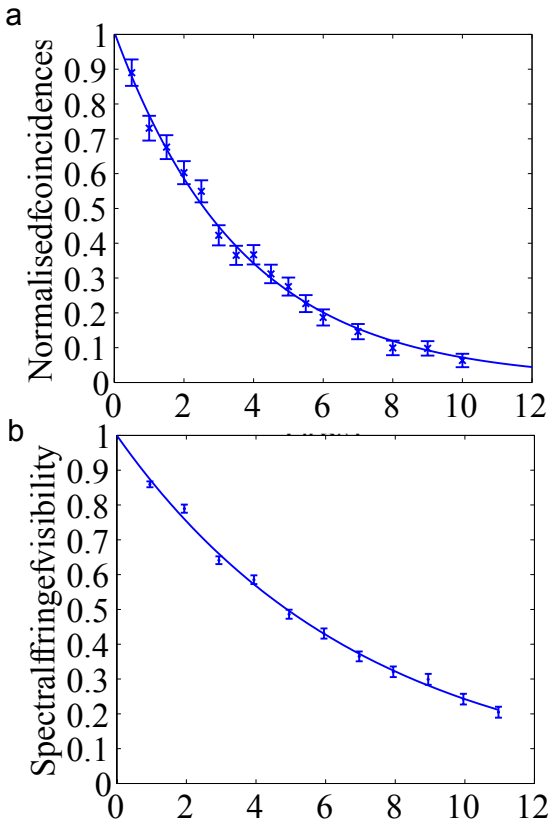

Figure 3.10: Population and coherence lifetimes of the optical phonons in diamond, from reference [129]. Solid lines are exponential fits. **a** Normalized coincidences between Stokes photons in the write time bin and anti-Stokes photons in the read time bin, which is a measure of the phonon population lifetime. **b** The decay of the spectral fringe visibility, which determines the phonon coherence time.

coherence time were much less than the lifetime, the different regions in the crystal would dephase relative to each other. We measured $T_2/T_1 = 1.9 \pm 0.1 \approx 2$ from which we concluded that the optical phonons in diamond were lifetime limited, and no significant inhomogeneous broadening existed. These results are consistent with theoretical [132] and experimental [133] work, which found that the dominant decoherence mechanism for the optical phonons in diamond was the Klemens channel [130]. The theoretical prediction of the coherence lifetime due to the Klemens channel is $T_2 \approx 10$ ps [132] at zero Kelvin, which is slightly higher than our measurement. However, our results are consistent with earlier experimental studies using a different technique, which measured a coherence time of 8 ps [132]. The discrepancy between our results and the theoretical prediction may be

due to dislocations or defects within the diamond structure, or contributions from other decay channels of the optical phonon [105].

While the phonon lifetime is short, the time-bandwidth product Γ_{BW} is still impressive: the pulse duration is 100 fs and the lifetime nearly 10 ps, giving $\Gamma_{\mathrm{BW}} = 100$. In practice, the prospects for practical applications are less promising. The potential of a quantum memory lies in the ability to perform conditional operations based on the successful completion of some task. This timescale is set by the operating speed of electronics, which is currently on the order of 100 ps to 1 ns, or at least an order of magnitude slower than the lifetime of optical phonons in diamond. There are some speculative ideas to extend the lifetime by making a phononic band gap to forbid propagation of the acoustic phonons generated by the Klemens decay channel [129]. We will leave this issue for now to focus on entangling the optical phonon modes from two diamonds at room temperature.

3.4 Summary

The DLCZ protocol blends several promising insights. First, a single atomic excitation can couple efficiently to an optical mode owing to a collective-enhancement effect. Second, measurement-induced entanglement using linear optics and single-photon detectors can perform entanglement swapping whose success probability scales polynomially with distance. Third, single quantum-entangled states can be joined together to form standard Bell-type two-particle entanglement (albeit by post-selection). It does, however, possess severe practical limitations, *inter alia*, the requirement for phase stability and a memory coherence time exceeding several minutes [16]. We will use the first two insights in the next chapter to demonstrate entanglement between two diamonds at room temperature.

As a preamble, we examined optical phonons in some detail, describing their emergence as a collective excitation between two sub-lattices. The optical phonons in diamond are Raman-active and the optical phonons scattered in the forward direction have a polarization transverse to the photon. The four-wave mixing process was not phase matched on axis and we considered the possibility of spectral and angular correlations. Finally, we demonstrated that non-classical light could be generated with optical phonons, which is a necessary condition for demonstrating entanglement between diamonds.

4

Entanglement of Diamonds at Room Temperature

4.1 Motivation

4.1.1 The Importance of being entangled

The definition of entanglement seems to be, at first glance, underwhelming. Consider a bipartite mixed state with density matrix ρ^{S}. The state is not entangled if the density matrix can be decomposed into a tensor product of states corresponding to the two individual subsystems A and B,

$$\rho^{\mathrm{S}} = \sum_i p_i \rho_i^{\mathrm{A}} \otimes \rho_i^{\mathrm{B}}, \tag{4.1}$$

where p_i are probabilities ($\sum_i p_i = 1$). Note that unentangled states are referred to as *separable* (in reference to the fact the sub-systems can be separated) and this is, in general, distinct from product states of the form $\rho = \bigotimes_n \rho_n$ as separable non-product

states possess classical correlations.[1]

This modest definition belies the wide-ranging importance of entanglement. Erwin Schrödinger called entanglement "*the* characteristic trait of quantum mechanics" [134]. In condensed matter systems, strongly interacting phenomena such as the fractional quantum Hall effect [135] and superconductivity [136, 137] involve states that are entangled [138]. The notions of long-range order, super-fluidity and entanglement are closely intertwined [139], and are all examples of quantum correlations. In addition, new topological insulators have topologically protected edge states that are entangled [140]. Entanglement is therefore intimately linked to the emergence of correlated behaviour in many-body condensed matter systems.

In quantum information science, entanglement is viewed as a resource for performing certain computational tasks. Entanglement is required for measurement-induced computation schemes such as the DLCZ protocol [17] and linear-optics quantum computing [18]. In these cases, separable state inputs can be simulated efficiently in a computation time that scales polynomially with the number of inputs. For gate-based quantum computation, the role of entanglement is still being elucidated. Entanglement above a certain level is needed for pure-state quantum computation to have an exponential advantage compared to classical computation [141, 142]. For mixed states, however, it is not known if entanglement, as opposed to other correlations, is required for exponentially faster computation [143]; recently it has been shown that quantum discord [144, 145], a more general type of non-classical correlation, can be used for a limited range of quantum algorithms [146, 147].

From a fundamental perspective, our intuition about the physical world is strongly informed by our experience that macroscopic solids move according to the laws of classical mechanics. The possibility of observing quantum correlations in the motion of an object therefore holds particular appeal. Further, and more speculatively, there is interest in exploring whether large-scale objects exhibit behaviour that deviates from conventional quantum mechanics [148]. The goal to entangle the motion of two objects, as a manifestly quantum mechanical phenomenon, is therefore well motivated based on the potential

[1] Indeed, separable non-product mixed states can also posses a particular type of quantum correlation known as quantum discord.

applications and fundamental interest. Before I present the details of the experiment, I will first orientate this work within the broader scope of the field of optomechanics.

4.1.2 In the context of other approaches

A principal goal of the field of cavity optomechanics is to demonstrate non-classical behaviour in the motion of engineered mechanical systems. The systems are designed to have well-defined normal modes of vibration that can be well isolated from the environment, thereby extending the coherence time. Cooling the vibrational modes is necessary to eliminate thermal noise that can mask signatures of non-classical motion. This can be accomplished either passively, with a cryostat or dilution refrigerator [116], or in combination with active cooling techniques [149, 150, 117, 118]. These mechanical structures can be further shielded from the environment by phononic shields – band-gap structures for phonons that forbid the transmission of certain frequencies of sound [118]. Recent experiments have shown that these structures can generate non-classical light [151, 152], and can also be cooled to their quantum ground state [116, 117, 118], however entanglement of two optomechanical objects remains, as yet, an unrealized goal.

A different approach is needed to observe non-classical motion of "ordinary" objects at ambient conditions. Without an artificially engineered system, measurements must be made on time-scales shorter than the typically fast decoherence times found in a real-world system. This can be achieved using ultra-short-duration optical pulses. In biology, studies of photosynthetic complexes have used interferometric methods to establish the presence of coherence in naturally occurring bulk systems [153, 154]. Researchers have also observed interference between complex molecules [155], demonstrating the wave-like behaviour of these systems. However, demonstration of entanglement between two solid-state objects at ambient conditions has been lacking.

Along these lines, optical phonons in diamond are a natural optomechanical system. Diamond has many superlative material properties, including the highest Debye temperature (2000 K), which ensures that the optical phonon mode occupies the ground state at room temperature and, therefore, no optical pumping is required.[2] The exceptional

[2]The occupation rate is given by the Boltzmann occupation probability $\exp(-\hbar\omega/k_{\mathrm{B}}T) = 1.7 \times 10^{-3}$, where ω is the frequency of the optical phonon and T is the ambient temperature of environment.

hardness of diamond, arising from strong internal interactions, means the optical phonons in diamond are very energetic; the carrier frequency of the optical phonon is 40 THz, as discussed in chapter 3. The optical phonon mode has a quality factor of several hundred and can therefore accommodate a high time-bandwidth product. We make use of these properties to entangle two diamonds at room temperature, which we discuss in the sections that follow.

4.2 Quantifying entanglement in the number basis

The modest definition of entanglement based on equation 4.1 also belies the challenging task of verifying and quantifying entanglement. For bipartite two-level quantum states – *qubits* – the maximally entangled states are the so-called Bell states

$$|\Phi^{\pm}\rangle = \frac{1}{\sqrt{2}}\left(|\alpha\rangle_1|\alpha\rangle_2 \pm |\beta\rangle_1|\beta\rangle_2\right), \tag{4.2}$$

$$|\Psi^{\pm}\rangle = \frac{1}{\sqrt{2}}\left(|\alpha\rangle_1|\beta\rangle_2 \pm |\beta\rangle_1|\alpha\rangle_2\right), \tag{4.3}$$

where the subscripts label the subsystems 1 and 2, and α and β are some orthogonal states, for example photon number or polarization. These states are equivalent up to local operations and classical communication (LOCC). Maximum entanglement of state $|\Phi^+\rangle$, for instance, means the partial trace over one subsystem – denoted by a subscript – is proportional to the identity operator $\mathrm{Tr}_1(|\Phi\rangle\langle\Phi|) = \mathbf{I}/2$. There is no information contained in the measurement of one subsystem, only in the correlation between the two subsystems. The entanglement can be quantified in terms of the von Neumann entropy of the reduced density matrix ρ_1 of one subsystem,

$$E(|\psi\rangle) = -\mathrm{Tr}(\rho_1 \log_2 \rho_1), \;\; \rho_1 = \mathrm{Tr}_2\left(|\psi\rangle\langle\psi|\right). \tag{4.4}$$

Conceptually entanglement is quantified in terms of units of maximally entangled states or *ebits*. The *entanglement of formation* $E_\mathrm{f}(\rho)$ is the number of ebits required to prepare some state ρ [156].[3] The reverse process, the number of copies of ρ needed

[3] A related concept is the *entanglement cost* $E_\mathrm{c}(\rho)$, which is the number of ebits needed per copy to prepare multiple copies of ρ. It is thought that $E_\mathrm{c}(\rho) = E_\mathrm{f}(\rho)$ [157].

to make a maximally entangled state, is known as the *distillable entanglement* $E_{\mathrm{d}}(\rho)$. For two-qubit pure states $E_{\mathrm{f}}(\rho) = E_{\mathrm{d}}(\rho)$ but, in general, $E_{\mathrm{f}}(\rho) \geq E_{\mathrm{d}}(\rho)$ [158].[4] These measures are difficult to calculate as they require evaluation of the minimum over all pure-state decompositions of the state,

$$E_{\mathrm{f}}(\rho) = \min_{\{|\psi_i\rangle\}} \sum_i p_i E(|\psi_i\rangle). \tag{4.5}$$

The length of this calculation scales exponentially with the dimension of the state and these measures are classified as NP-hard [9]. An alternative approach is to measure some observable whose expectation value $\langle W \rangle = \mathrm{Tr}(\rho W)$ is non-negative (by convention) for all separable states and negative for *some* entangled states. This can be thought of as partitioning the space of all density matrices. Witnesses cannot detect all entangled states [159], and some advanced knowledge of the state is required to choose a suitable witness. A special example of an entanglement witness is the violation of a Bell inequality. Bell inequalities are used to test the foundations of quantum mechanics, specifically whether a state obeys local realism [8]. The entanglement witness associated with a Bell test for a bipartite system is

$$W_{\mathrm{B}} = 1 - \frac{1}{2}\left(M_1^A M_2^A + M_1^A M_2^B + M_1^B M_2^A - M_1^B M_2^B\right), \tag{4.6}$$

where M_i^j is a measurement j of subsystem i with outcome ± 1. All bipartite entangled pure states violate a Bell inequality (the so-called Gisin theorem) [160],[5] however the degree of the violation cannot be used as a way to quantify the amount of entanglement in the presence of post-selection [162].

The full DLCZ protocol can be used to violate a Bell inequality by using four atomic ensembles, albeit in post-selection (i.e. only considering events where the expected number of detection events occurred). This can be simplified to two atomic ensembles by measuring entanglement in the photon-number basis. Measuring a violation of a Bell inequality is challenging in the number basis due to the difficulty of varying the phase

[4] States with $E_{\mathrm{f}}(\rho) > 0$ but $E_{\mathrm{c}}(\rho) = 0$ are said to have bound entanglement; the entanglement 'used' to create these states cannot be recovered.

[5] This is not true in general for $N > 2$, where some entangled states do not violate a Bell inequality [161].

between the vacuum $|0\rangle$ and single-photon $|1\rangle$ term [163], and another approach is needed in this case. One possibility is to calculate the concurrence, an entanglement monotone, over a restricted subspace in order to place a lower bound on the amount of entanglement. This approach was first realized experimentally by CW Chou *et al.* in 2005 [164]. We now define the concurrence of a bipartite system and show how it can be bounded experimentally.

4.2.1 Definition of the concurrence

The concurrence is a monotonic function of the entanglement of formation, from which it derives its physical significance. The concurrence C of state ρ is defined as [109]

$$C = \max(\lambda_1 - \lambda_2 - \lambda_3 - \lambda_4, 0), \tag{4.7}$$

where λ_i are the eigenvalues of the Hermitian matrix, ordered in descending order, $R = \sqrt{\sqrt{\rho}\tilde{\rho}\sqrt{\rho}}$, with $\tilde{\rho} = (\sigma_y \otimes \sigma_y)\,\rho^*\,(\sigma_y \otimes \sigma_y)$ and ρ^* is the complex conjugate of ρ. The concurrence can be related to the entanglement of formation by

$$E_{\mathrm{f}}(C) = h\left(\frac{1+\sqrt{1-C^2}}{2}\right), \tag{4.8}$$

where

$$h(x) = -x\log_2 x - (1-x)\log_2(1-x) \tag{4.9}$$

is the binary entropy function.

The concurrence has the following convenient properties:

1. The concurrence is a monotonic function of the entanglement of formation.

2. It has an explicit formula given by equation 4.7.

3. The concurrence provides an exact demarcation between entangled and separable states for the case of two qubits.

4. Finally, it has a simple interpretation where $C = 0$ for all separable states and $C = 1$ for all maximally entangled states.

Note the concurrence is defined only for pairs of qubits, although extensions to higher dimensional states have been explored [165]. In order to calculate the concurrence, the density matrix must be estimated, which we do here in the number basis.

4.2.2 Density matrix in the number basis

The wavefunction in equation 3.10 from chapter 3 can be expressed as the density matrix ρ_{lr}, truncated at a maximum of two photons spread over the two ensembles l and r (up to order χ in equation 3.7) [164]

$$\rho_{lr} = \begin{pmatrix} p_{00} & 0 & 0 & 0 & 0 & 0 \\ 0 & p_{10} & d_1 & 0 & 0 & 0 \\ 0 & d_1^* & p_{01} & 0 & 0 & 0 \\ 0 & 0 & 0 & p_{11} & d_2 & d_3 \\ 0 & 0 & 0 & d_2^* & p_{20} & d_4 \\ 0 & 0 & 0 & d_3^* & d_4^* & p_{02} \end{pmatrix}, \tag{4.10}$$

where p_{ij} are the the probabilities corresponding to having i photons from atomic ensemble l and j photons from atomic ensemble r in the anti-Stokes mode[6], conditioned on the detection of a photon in the mode s. The off-diagonal terms are set to zero between states with different total photon number (e.g. there is no coherence between the vacuum state and states with one photon, p_{01} or p_{10}). This assumption is conservative as the operation that would reduce these terms to zero cannot increase the amount of entanglement (as it involves only local operations and classical communication), making the estimate of the concurrence strictly a lower bound [127].

The anti-Stokes modes from the two atomic ensembles are interfered on a beam splitter, as discussed in the previous chapter. The beam splitter transformations between l,r

[6]Normalized such that $\mathrm{Tr}\,(\rho) = 1$.

and the +,− basis is given by [127]

$$B = \begin{pmatrix} 1 & 0 & 0 & 0 & 0 & 0 \\ 0 & \sqrt{R} & \sqrt{T}\mathrm{e}^{\mathrm{i}\phi} & 0 & 0 & 0 \\ 0 & \sqrt{T} & \sqrt{R}\mathrm{e}^{\mathrm{i}\phi} & 0 & 0 & 0 \\ 0 & 0 & 0 & (T-R)\mathrm{e}^{\mathrm{i}\phi} & \sqrt{R}\mathrm{e}^{\mathrm{i}\phi} & \sqrt{2TR}\mathrm{e}^{2\mathrm{i}\phi} \\ 0 & 0 & 0 & \sqrt{2TR}\mathrm{e}^{\mathrm{i}\phi} & -R & T\mathrm{e}^{2\mathrm{i}\phi} \\ 0 & 0 & 0 & \sqrt{2TtR}\mathrm{e}^{\mathrm{i}\phi} & T & -R\mathrm{e}^{2\mathrm{i}\phi}, \end{pmatrix}, \tag{4.11}$$

and the matrix elements of the density matrix in the number basis $\rho_{+-} = B\rho_{lr}B^{\dagger}$ is then

$$p_{00}^{\pm} = p_{00}, \tag{4.12}$$

$$p_{10}^{\pm} = Rp_{10} + Tp_{01} + 2\sqrt{RT}|d_1|\sin(\phi - \phi_d), \tag{4.13}$$

$$p_{01}^{\pm} = Tp_{10} + Rp_{01} - 2\sqrt{RT}|d_1|\sin(\phi - \phi_d), \tag{4.14}$$

$$p_{11}^{\pm} = (T-R)^2 p_{11}, \tag{4.15}$$

$$p_{20}^{\pm} = 2TRp_{11}, \tag{4.16}$$

$$p_{02}^{\pm} = 2TRp_{11}, \tag{4.17}$$

where $\phi_d = \arg d_1$. Ideally, the term p_{11}, which corresponds to the detection of one anti-Stokes photon from each arm detected conditioned on the detection of a single Stokes photon, should vanish when the beam splitter is balanced due to interference. The experimentally measured population probabilities P_{ij} will be affected by the coupling and

detector inefficiencies for the two ensembles (η_l and η_r)

$$\begin{aligned} P_{00} &= p^{\pm}_{00} + (1-\eta_l)p^{\pm}_{10} + (1-\eta_r)p^{\pm}_{01} + (1-\eta_r)(1-\eta_l)p^{\pm}_{11} \\ &\quad +(1-\eta_l)^2 p^{\pm}_{20} + (1-\eta_r)^2 p^{\pm}_{02} \end{aligned} \tag{4.18}$$

$$P_{10} = \eta_l p^{\pm}_{10} + (1-\eta_r)p^{\pm}_{11} + (1-\eta_l)p^{\pm}_{20} \tag{4.19}$$

$$P_{01} = \eta_r p^{\pm}_{01} + (1-\eta_l)p^{\pm}_{11} + (1-\eta_r)p^{\pm}_{20} \tag{4.20}$$

$$P_{11} = \eta_l \eta_r p^{\pm}_{11} \tag{4.21}$$

$$P_{20} = \eta_l^2 p^{\pm}_{20} \tag{4.22}$$

$$P_{02} = \eta_r^2 p^{\pm}_{02}. \tag{4.23}$$

The interference visibility V of the heralded anti-Stokes photons is given by the difference between the number of heralded anti-Stokes photons exiting the beam splitter ports as a function of the phase

$$V = \frac{(P_{01}-P_{10})_{\max} - (P_{01}-P_{10})_{\min}}{(P_{01}+P_{10})_{\max} + (P_{01}+P_{10})_{\min}} \tag{4.24}$$

$$= \frac{2\left(\eta_l+\eta_r\right)\sqrt{RT}|d|}{p_{01}\left(\eta_l R+\eta_r T\right)+p_{01}\left(\eta_r R+\eta_l T\right)+p_{11}\left[4\eta_l\eta_r\left(1-\eta_l\right)\left(1-\eta_r\right)\left(T-R\right)^2+4\eta_l\eta_r TR\left(4-\left[\eta_l+\eta_r\right]\right)\right]}, \tag{4.25}$$

which, for balanced beam splitters ($R = T = 1/2$) and identical inefficiencies $\eta_l = \eta_r = \eta$, results in a simplified expression for the magnitude of the coherence term d

$$|d| = \frac{V}{2}\left[p_{01} + p_{10} + p_{11}\left(2-\eta\right)\right]. \tag{4.26}$$

All the elements are in place to calculate the concurrence from the density matrix in equation 4.10. The density matrix is expressed in terms of the detection probabilities and the interference visibility, which can be measured with APDs. The exact expression for the concurrence is presented in the next section.

4.2.3 Calculation of the concurrence

The concurrence can be calculated with equations 4.10 and 4.7. The density matrix is truncated at p_{11} as the concurrence is defined here for a bipartite two-level system, and higher-order photon-number terms from each atomic ensemble were not considered.[7] The concurrence is therefore

$$C = \max(2|d| - 2\sqrt{p_{00}p_{11}}, 0), \tag{4.27}$$

where $|d|$ is given by equation 4.26, and p_{00}, p_{11} are given by equations 4.12, 4.15, 4.18, and 4.21. The condition on the visibility can, therefore, be written as

$$V \geq \frac{2\sqrt{p_{00}p_{11}}}{[p_{01} + p_{10} + p_{11}(2 - \eta)]}, \tag{4.28}$$

where $p_{11} \ll \{p_{10},\ p_{01}\}$ and can be neglected in the denominator (but not the numerator!). The interference visibility needed to demonstrate entanglement is dependent on the probability of generating two phonons (or anti-Stokes photons). In the limit where the probability χ of generating one atomic excitation is much less than one, the visibility must be on the order of unity, placing demanding requirements on the observation of entanglement. We now pause before moving on to the experimental details to derive how the maximum interference visibility is related to the second-order cross-correlation between the Stokes and anti-Stokes modes.

4.2.4 Cross-correlation and visibility

In the previous chapter we established that the intensity cross-correlation $g^{(2)}_{\mathrm{s,a}}$ between the Stokes and anti-Stokes modes witnesses the presence of non-classical correlations. The strength of the correlation between these two modes will place an ultimate limit on the visibility of the interference discussed in the preceding section. The visibility will clearly depend on the indistinguishability of the Stokes and anti-Stokes modes. It will also crucially depend on the ratio of the correlated to uncorrelated pairs of the Stokes/anti-Stokes photons, which is quantified by the intensity cross-correlation. Uncorrelated anti-

[7] Ignoring these higher order terms will give a lower bound on the concurrence as, in principle, whenever two photons are detected from one beam splitter output that information could be discarded, which is a local operation known not to increase the entanglement [127].

Stokes photons, produced by spontaneous emission of the anti-Stokes photon or phonon decay, will not interfere with a fixed phase, reducing the fringe visibility. Here we derive the relationship between the intensity cross-correlation and the visibility in equation 4.28.

From equation 3.44 the intensity cross-correlation $g^{(2)}_{s,a}$ is given by [107]

$$g^{(2)}_{\mathrm{s,a}} = \frac{\langle I_s I_a\rangle}{\langle I_s\rangle\langle I_a\rangle} = \frac{\langle \hat{s}^\dagger \hat{a}^\dagger \hat{s}\hat{a}\rangle}{\langle \hat{s}^\dagger\hat{s}\rangle\langle \hat{a}^\dagger\hat{a}\rangle}, \tag{4.29}$$

where $\hat{s}^\dagger$, $\hat{a}^\dagger$, $\hat{s}$, $\hat{a}$ are the respective creation and annihilation operators for the Stokes and anti-Stokes modes. The two modes from two atomic ensembles impinge on a beam splitter and the intensity cross-correlation at the two output ports, labelled by $+$ and $-$ respectively, are given by

$$\langle I_{s\pm} I_{a\pm}\rangle = \xi_s\xi_a\langle \hat{s}^\dagger_\pm \hat{a}^\dagger_\pm \hat{s}_\pm \hat{a}_\pm\rangle, \tag{4.30}$$

where $\xi_s\xi_a$ relate the photon number to intensity. Using the beam-splitter transformation $B^\dagger\rho B$, the output of the beam splitters can be related to the input. There are four sets of fringes formed by $\langle I_{s+}I_{a+}\rangle$, $\langle I_{s+}I_{a-}\rangle$, $\langle I_{s-}I_{a+}\rangle$, and $\langle I_{s-}I_{a-}\rangle$. The intensity of the coincidence counts for the first set is

$$\begin{aligned}\langle I_{s+}I_{a+}\rangle =& \xi_s\xi_a\langle \hat{s}^\dagger_+\hat{a}^\dagger_+\hat{s}_+\hat{a}_+\rangle \\ =& \xi_s\xi_a\langle\left(\sqrt{T_s}\hat{s}^\dagger_l + \mathrm{e}^{-\mathrm{i}\phi_s}\sqrt{R_s}\hat{s}^\dagger_r\right)\left(\sqrt{T_a}\hat{a}^\dagger_l + \mathrm{e}^{-\mathrm{i}\phi_a}\sqrt{R_a}\hat{a}^\dagger_r\right) && (4.31)\\ & \left(\sqrt{T_s}\hat{s}_l + \mathrm{e}^{i\phi_s}\sqrt{R_s}\hat{s}_r\right)\left(\sqrt{T_a}\hat{a}_l + \mathrm{e}^{i\phi_a}\sqrt{R_a}\hat{a}_r\right)\rangle. && (4.32)\end{aligned}$$

The sixteen inner products are then evaluated with the state given in equation 3.8. Evidently some of these inner products will be zero, and only the following terms need be considered

$$\begin{aligned}\langle I_{s+}I_{a+}\rangle = \xi_s\xi_a[&R_sR_a\langle \hat{s}^\dagger_r\hat{a}^\dagger_r\hat{s}_r\hat{a}_r\rangle + T_sT_a\langle \hat{s}^\dagger_l\hat{a}^\dagger_l\hat{s}_l\hat{a}_l\rangle + \mathrm{e}^{-\mathrm{i}(\phi_s+\phi_a)}\sqrt{T_sT_aR_sR_a}\langle \hat{s}^\dagger_r\hat{a}^\dagger_r\hat{s}_l\hat{a}_l\rangle \\ &+ \mathrm{e}^{\mathrm{i}(\phi_s+\phi_a)}\sqrt{T_sT_aR_sR_a}\langle \hat{s}^\dagger_l\hat{a}^\dagger_l\hat{s}_r\hat{a}_r\rangle + R_sT_a\langle \hat{s}^\dagger_r\hat{a}^\dagger_l\hat{s}_r\hat{a}_l\rangle + R_aT_s\langle \hat{s}^\dagger_l\hat{a}^\dagger_r\hat{s}_l\hat{a}_r\rangle].\end{aligned} \tag{4.33}$$

The inner products in equation 4.33 can be evaluated as a function of χ using equation 3.9

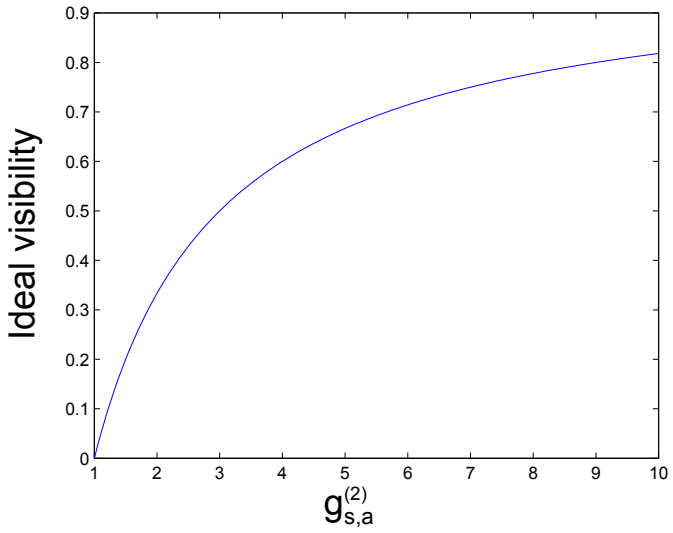

Figure 4.1: Interference visibility as a function of the second-order cross-correlation between the Stokes and anti-Stokes fields.

as was done in chapter 3 and reference [127].[8] The maximum visibility can be written as a function of the cross-correlation if we assume that the probability of excitation χ for the two atomic ensembles is identical and that the two beam splitters are balanced, $T_a = R_a = T_s = R_s = 1/2$. Then equation 4.33 can be rewritten as

$$\langle I_{s+} I_{a+} \rangle = \frac{1}{4}\left[2\langle \hat{s}^\dagger \hat{a}^\dagger \hat{s}\hat{a}\rangle + 2\langle \hat{s}^\dagger \hat{s}\rangle\langle \hat{a}^\dagger \hat{a}\rangle + 2\langle \hat{s}^\dagger \hat{a}^\dagger\rangle\langle \hat{s}\hat{a}\rangle \cos\left(\phi_s + \phi_a\right)\right]. \tag{4.34}$$

The interference visibility is then

$$\begin{aligned} V &= \frac{\langle I_{s+} I_{a+}\rangle_{\max} - \langle I_{s+} I_{a+}\rangle_{\min}}{\langle I_{s+} I_{a+}\rangle_{\max} + \langle I_{s+} I_{a+}\rangle_{\min}} = \frac{\langle \hat{s}^\dagger \hat{a}^\dagger\rangle\langle \hat{s}\hat{a}\rangle}{\langle \hat{s}^\dagger \hat{a}^\dagger \hat{s}\hat{a}\rangle + \langle \hat{s}^\dagger \hat{s}\rangle\langle \hat{a}^\dagger \hat{a}\rangle} \\ &= \frac{\langle \hat{s}^\dagger \hat{a}^\dagger \hat{s}\hat{a}\rangle - \langle \hat{s}^\dagger \hat{s}\rangle\langle \hat{a}^\dagger \hat{a}\rangle}{\langle \hat{s}^\dagger \hat{a}^\dagger \hat{s}\hat{a}\rangle + \langle \hat{s}^\dagger \hat{s}\rangle\langle \hat{a}^\dagger \hat{a}\rangle} = \frac{\frac{\langle \hat{s}^\dagger \hat{a}^\dagger \hat{s}\hat{a}\rangle}{\langle \hat{s}^\dagger \hat{s}\rangle\langle \hat{a}^\dagger \hat{a}\rangle} - 1}{\frac{\langle \hat{a}^\dagger \hat{b}^\dagger \hat{a}\hat{a}\rangle}{\langle \hat{s}^\dagger \hat{s}\rangle\langle \hat{a}^\dagger \hat{a}\rangle} + 1}. \end{aligned} \tag{4.35}$$

Comparing equation 4.35 with equation 4.29, we see that [166]

$$V = \frac{g^{(2)}_{\mathrm{s,a}} - 1}{g^{(2)}_{\mathrm{s,a}} + 1}. \tag{4.36}$$

Equation 4.36 is plotted in figure 4.1 in order to show the relationship between the inten-

[8] $\langle \hat{s}_i^\dagger \hat{a}_i^\dagger \hat{s}_j \hat{a}_j\rangle = \frac{\sqrt{\chi_i \chi_j}}{(1-\chi_i)(1-\chi_j)}$, $\langle \hat{s}_i^\dagger \hat{a}_j^\dagger \hat{s}_i \hat{a}_j\rangle = \frac{\chi_i \chi_j}{(1-\chi_i)(1-\chi_j)}$, $\langle \hat{s}_i^\dagger \hat{a}_i^\dagger \hat{s}_i \hat{a}_i\rangle = \frac{\chi_i + \chi_i^2}{(1-\chi_i)^2}$

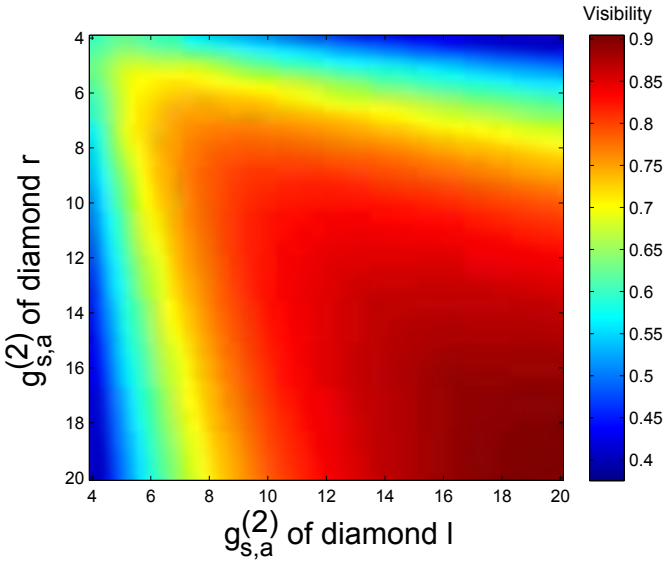

Figure 4.2: Maximum interference visibility as a function of the second-order cross-correlation of the two diamonds.

sity cross-correlation and the maximum ideal visibility. Equation 4.36 can be understood intuitively by considering that randomly correlated fields will have a Poissonian distribution with an intensity cross-correlation equal to one. The intensity cross-correlation can be thought of consisting in two parts, the uncorrelated signal, which will not interfere, and the correlated part, which will interfere. The maximum visibility will be determined by the ratio of the difference between correlated and uncorrelated photons to the sum, which is approximately equation 4.36.

For $\chi_r \neq \chi_l$, the maximum visibility is then

$$V_{\max} = \frac{\frac{\sqrt{\chi_r \chi_l}}{(1-\chi_r)(1-\chi_l)}}{\frac{1}{2}\left(\frac{\chi_r+\chi_r^2}{(1-\chi_r)^2} + \frac{\chi_l+\chi_l^2}{(1-\chi_l)^2}\right) + \frac{\chi_r\chi_l}{(1-\chi_r)(1-\chi_l)}}, \tag{4.37}$$

$$= \frac{(g_r^{(2)}-2)(g_l^{(2)}-2)\sqrt{(g_r^{(2)}-1)(g_l^{(2)}-1)}}{4+g_r^{(2)}g_l^{(2)}\left[\frac{1}{2}\left(g_r^{(2)}+g_l^{(2)}\right)-3\right]}, \tag{4.38}$$

where $\chi_r = \frac{1}{g_r^{(2)}-1}$ and $\chi_l = \frac{1}{g_l^{(2)}-1}$. The interference visibility as a function of the cross-correlation of the two diamonds is shown in figure 4.2. Interestingly, for a fixed cross-correlation from one diamond, the maximum visibility occurs for a slightly higher, but not too high, cross-correlation from the second diamond. Equation 4.38 simplifies to equation 4.36 when $g_r^{(2)} = g_l^{(2)}$.

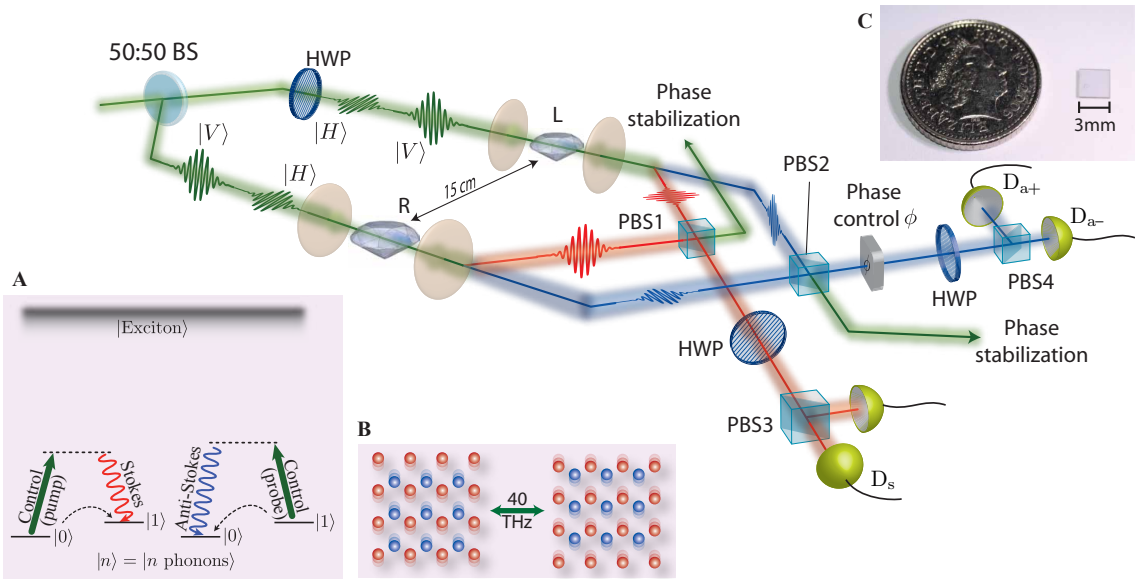

Figure 4.3: The optical layout of the experiment to generate entanglement between two diamonds, from reference [108]. A pump pulse, split by the beam splitter BS, was focused into two diamonds. Spontaneous Raman scattering created orthogonally polarized heralding Stokes fields s_l, s_r (see **A**: $|n\rangle$ represents the phonon number state in diamond). Polarization beam splitter PBS1 combined the Stokes spatial modes, and the half-wave plate HWP rotated and combined the fields on PBS3, which were then directed to the APD D_s. A second pulse, delayed by 350 fs relative to the first, coherently absorbed an optical phonon and created the orthogonally polarized anti-Stokes fields a_l, a_r (see **A**), which were similarly combined and mixed on PBS2, PBS4, and measured with the detectors D_{a+}, D_{a-}. The relative phase ϕ_a between the fields $a_{l,r}$ was adjusted outside the spatial interferometer via a geometric phase rotation. Pump beams exiting PBS1,2 were used to stabilize the spatial interferometer. Inset **B** shows the diamonds oscillating with a vibrational period of 25 fs. Inset **C** shows the diamond sample, with a 10-pence coin for scale.

4.3 Experimental setup

We now turn our attention to the experimental realization of entanglement between two diamonds. The details of the experimental apparatus will be described starting with the laser oscillator and ending with single-photon detection.

4.3.1 Oscillator and optical modes

A home-built, mode-locked titanium-sapphire oscillator generated a train of pulses with an 80-MHz repetition rate. The pulses were 80 fs (FWHM) in duration and centered at a wavelength of 808 nm with a bandwidth of 18 nm. The oscillator, affectionately known as Sapphy, was passively mode locked and pumped with a 5-W Verdi laser from Coherent

Inc. Mode locking was initiated by gently perturbing the translating stage holding one of the dispersion-compensating quartz prisms inside the laser cavity. At moments of desperation, we would initiate mode-locking by hitting the side of the optical table with the palm of one hand (often with painful results).

The output power of the laser was 600 mW. The pulses were focused using an anti-reflection-coated achromatic lens through a small circular aperture (or pinhole) 15 μm in diameter to filter out high-order transverse spatial modes. The focal spot was approximately 7 μm and the transmission through the pinhole was 75-80%. The pulse was also spectrally filtered to remove any pump photons at the Stokes (900 nm) and anti-Stokes (735 nm) wavelengths that could obscure the single-photon signal; a set of three bandpass filters with centre wavelength 830 nm and bandwidth 40 nm were angle-tuned to create a spectral window with transmission edges 795 nm and 820 nm. Finally, the pulses were linearly polarized using a half-wave plate (HWP), quarter-wave plate (QWP), and polarizing beam-splitter (PBS). The average power of the pulse train after spectral, spatial, and polarization filtering was 300 mW.

The entanglement experiment required two pulses in two time bins, the first to *write* the atomic excitation (i.e. phonon) into the two diamonds and the second to *read* the phonon out as an anti-Stokes photon. A single pulse from the laser was split into two time bins using a birefringent quartz crystal with its optical axis aligned at 45° with respect to the pump polarization. The pulses were split into a cross-polarized pump-probe pair separated by 350 fs, which could be adjusted by changing the thickness of the quartz plate. The time delay was chosen to be less than the coherence time of the diamond (7 ps) and greater than the pulse duration.

The pulses were then split into two beams by a non-polarizing 50:50 beam splitter (CVI BSNP-808-50-025), as shown in figure 4.3. The polarization of a set of pulses in one spatial mode was rotated by 90° with a HWP. This ensured the polarization of the write pulses for the two diamond samples were orthogonally polarized, as were the read and write pulses from the *same* diamond. The pump-probe pair in each arm of the interferometer was focused into the diamond with a 5-cm focal length achromatic lens. The diamond plate was 0.25 mm thick (half the width of sample used in the previous

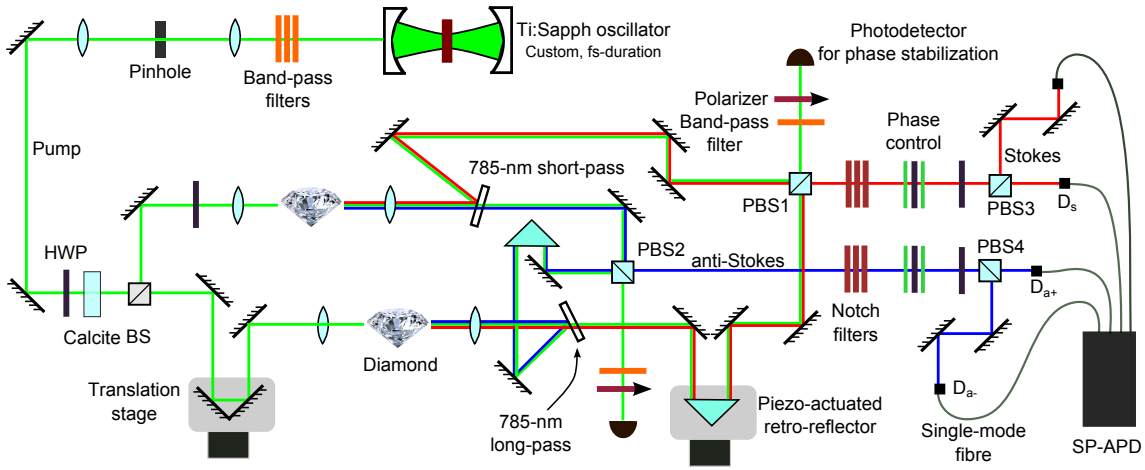

Figure 4.4: Optical layout of diamond experiment showing the pump (green line), Stokes (red line), and anti-Stokes (blue line) modes. The Stokes interferometer is between the BS and PBS3, and the anti-Stokes between the BS and PBS4. Between PBS1 and 3, and PBS 2 and 4, the two arms of the interferometer are in the same spatial mode, but orthogonal polarization modes.

chaptre) with transverse dimensions of 3 mm by 3 mm. The diamonds were mounted into standard lens mounts with the capability to adjust the tilt and position parallel to the optical beam axis.

4.3.2 Diamond properties and selection rules

The diamond samples (from Element 6 Ltd.) were synthetically grown by chemical vapor deposition. As discussed in chapter 3, the orientation and lattice symmetry of the crystal dictated that the Raman-scattered light was orthogonally polarized to the linearly polarized pump field [122]. The quality of the polarization selection rule in diamond was reduced by nitrogen impurities and crystal defects such as structural impurity arising from strain and grain boundaries [167, 168]. In our experimental geometry, the ratio of the intensity of the orthogonally polarized to the parallel polarized component (with respect to the pump) was 10:1 for the Stokes field and 4:1 for the anti-Stokes field. The detection of uncorrelated Stokes/anti-Stokes photons was reduced by detecting only the heralding Stokes photon scattered from the *write* pulse and the anti-Stokes photon scattered from the *read* pulse. This was achieved by using cross-polarized pump-probe pulses followed by the polarizing beam splitters PBS1, PBS2 in figure 4.3. This was necessary to isolate the relevant Raman signals as electronic time gating was not possible given that the pulse

separation was only 350 fs.

4.4 Stokes and anti-Stokes interferometers

The Stokes photons, with wavelength 900 nm, and the anti-Stokes photons, with wavelength 735 nm, were separated into two spatial modes using a 780-nm long-pass and short-pass filter (Semrock RazorEdge®). A more detailed schematic of the experiment is shown in figure 4.4. The Stokes and anti-Stokes modes from the two diamonds were combined on PBS1 and PBS2, respectively, as shown in figure 4.4. The pump pulses were extinguished by a set of notch filters that provided a total extinction of ∼120 dB.

4.4.1 Polarization indistinguishability

The output of the interferometers were then passed through a HWP with angle θ between the axis of the HWP and the photon polarization, which results in the rotational transformation

$$U_{\mathrm{HWP}}(\theta) = \begin{pmatrix} \cos(2\theta) & -\sin(2\theta) \\ -\sin(2\theta) & -\cos(2\theta) \end{pmatrix}, \tag{4.39}$$

where 2θ is the phase between the linear components of the polarization. When $\theta = \pi/16$ the polarization of the Stokes and anti-Stokes modes became

$$U_{\mathrm{HWP}}|H\rangle_L = \frac{1}{\sqrt{2}}\left(|H\rangle - |V\rangle\right)_l \quad \text{and} \quad U_{\mathrm{hwp}}|V\rangle_r = \frac{1}{\sqrt{2}}\left(|H\rangle + |V\rangle\right). \tag{4.40}$$

The rotated polarization state was then mixed on beam splitters PBS3, PBS4, and the transmitted mode was

$$U_{\mathrm{PBS}}U_{\mathrm{HWP}}|H\rangle_l = \frac{1}{\sqrt{2}}|H\rangle_l \quad \text{and} \quad U_{\mathrm{PBS}}U_{\mathrm{HWP}}|H\rangle_r = \frac{1}{\sqrt{2}}|H\rangle_r. \tag{4.41}$$

This step erased the *'which path'* information because the light from the two modes have the same polarization. High interference visibility requires removing any information that could label the photons from the two arms of the interferometer; the Stokes and anti-Stokes photons from the two diamonds must exit the interferometer at the same

time, they must have the same spectrum, and they must have been produced in the same volume inside the diamond. These degrees of freedom are discussed in the next few sections.

4.4.2 Spectral overlap of the modes

The spectrum of the Stokes and anti-Stokes photons from the two diamonds were matched in order to ensure high interference visibility. The pulse carrier frequencies were identical for both arms of the interferometer, as was the phonon frequency. The spectral filtering, however, could result in a mismatch between the spectra of the Raman scattering light. Although we used the same filters in both arms, the transmission edges of the filters were sensitive to the angle of the filter relative to the optical beam. We measured the Stokes and anti-Stokes spectra from both diamonds using a spectrometer with a single-photon-sensitive camera (ANDOR), which we judged by eye to be excellent. The possibility of frequency correlations in the joint spectrum of the Stokes/anti-Stokes light was explored in chapter 3 and calculated to be negligible.

4.4.3 Spatial-mode overlap

Good spatial overlap between the Stokes and anti-Stokes light from the two arms was enforced by coupling the two modes into the same single-mode fibre. It was important that the coupling efficiency from the two arms was roughly equal to ensure that there was no distinguishing information encoded in the intensity of the fields. It was also important that the same volume inside the crystal was sampled by the Stokes and anti-Stokes fibres. The detection of Raman-scattered light from different regions within the diamond would be uncorrelated, reducing the cross-correlation and, hence, the maximum visibility according to equation 4.36.

The experimental sequence was as follows. First, the pump filters were removed and the pump field from one of the arms of the Stokes or anti-Stokes interferometer was coupled into a single-mode fibre using an aspheric lens. By adjusting the collimating lens after the diamond and the tilt of two mirrors *inside* the other of arm of the interferometer, the pump beam from that arm was coupled into the single-mode fibre with equal efficiency

(approximately 60%).

Next, the position of the diamond was set using a confocal imaging technique. The pump light was first coupled into the free-space spectrometer using an achromatic lens. The focal position of this lens was adjusted such that the maximum pump signal was coupled through the 10-μm-wide entrance slit. The focal position of the achromatic lens was left fixed as the Stokes light shares the same focal point. Spectral filters blocked the pump light, and the Stokes light was measured using the spectrometer. The intensity of the Stokes light was optimized by adjusting the angle and position of the diamond within the telescope. At this point, the Stokes light was directed towards a single-mode fibre. Small adjustments were needed to optimize the coupling as the focal position of the aspheric fibre coupling lens differed by several μm between the pump and Stokes light. This procedure was then repeated for the other diamond sample in the other telescope.

The anti-Stokes signal was maximized by adjusting the position of the fibre tip. I also tried to improve the coupling by maximizing the number of Stokes/anti-Stokes coincidences, which resulted in a fibre tip location similar to that found by maximizing solely the number of anti-Stokes photons. Therefore optimization on the singles counts, which was much quicker, was used to maintain alignment.

4.4.4 Temporal delay between the modes

The length of the Stokes and anti-Stokes interferometers, which were 1 m long, were matched to within the coherence length of the pulses, which was 25 μm. The path lengths were first matched to within 2 or 3 mm using a piece of string. In order to find the zero delay between the corresponding Stokes and anti-Stokes photons from the two diamonds, we mounted retro-reflectors on two translation stages (Newport) to form 'trombones' in the interferometer beam path. One was located between the BS and diamond r in figure 4.4, and a second located between the long-pass filter and PBS2. The delay stages were carefully aligned so that the movement of the translation state induced no lateral shift or angle in the optical beam path. I found that good coupling to a single-mode fibre 1.5 meters downstream could be maintained over the full 5 mm travel of the translation stage.

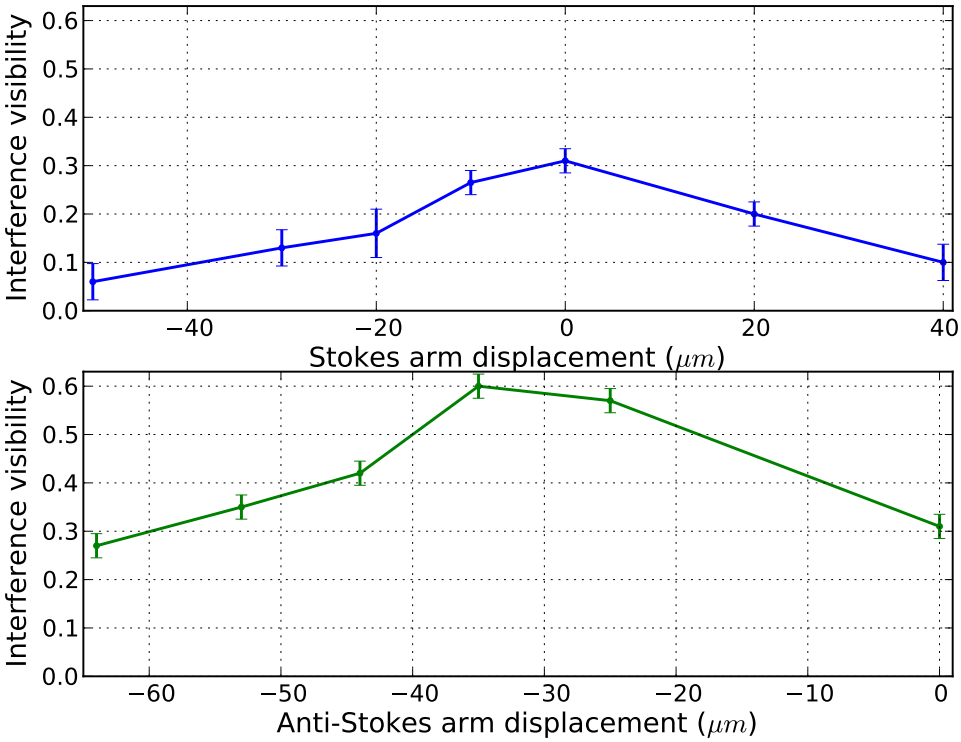

Figure 4.5: Maximizing the temporal overlap of the Stokes and anti-Stokes interferometers. At each point, a full interference fringe was measured and the visibility extracted by fitting the data to a sinusoidal function. For the first plot, the Stokes delay was scanned while keeping the anti-Stokes fixed at the nominal zero delay. For the second plot, the Stokes interferometer was fixed at the nominal (and actual) zero delay and the anti-Stokes delay was scanned.

The band-pass filters on the pump were removed in order to be able to detect leakage from the pump at the Stokes and anti-Stokes wavelengths. All the filters and optical components inside the interferometer were left unchanged. The light was sent onto the spectrometer, where the presence of spectral fringes was used to measure the relative distance of the two paths in the interferometer. The translation stage was adjusted until the period of the spectral fringes diverged, which indicated ideal temporal overlap.

Let's pause now to add a historical gloss. The maximum interference visibility of the quantum interference was initially low, on the order of 20%. We spent several months investigating the cause. I stayed late on Monday May 23$^{\text{rd}}$ 2011, intent on crossing out one last possibility before a group meeting the next day. I wanted to check the temporal delay of the Stokes and anti-Stokes modes by measuring the maximum interference visibility at

a few positions about the nominal zero delay point we found using the method described above. I measured a set of complete ($> 2\pi$) fringes in 15 μm increments from -45 μm to +45 μm about the zero delay point. I found the best visibility occurred at the nominal zero delay point for the Stokes mode, indicating that our method worked as expected. For completeness, I tried changing the anti-Stokes delay and started 45 μm from the nominal zero delay point. I was blissfully shocked to measure a visibility of 45%; I was to later spill out of the Clarendon Laboratory at 3 a.m. slightly delirious. We later measured a maximum visibility of 60% when displaced 35 μm from the nominal zero delay. The maximum interference visibility as a function of Stokes and anti-Stokes delay is plotted in figure 4.5.

4.4.5 Phase stability of the interferometer

The phase of the interferometer needed to be stabilized and then varied in a controllable manner. The interferometers for the Stokes and anti-Stokes modes (in figure 4.4 from the 50:50 BS to PBS1 and PBS2, respectively) had to be stabilized to much less than the wavelength of the optical modes for the duration of the experiments (several hours). This exceeded the passive stability of the setup, which drifted by 101° over five hours, with root-mean-square error (RMSE) of 33°, as shown in figure 4.6**a**. As a consequence, I built a control system to actively stabilize the phase of the two interferometers.

The phase of the interferometers was measured with the residual pump light exiting the interferometers at PBS1 and PBS2 in figure 4.4. The pump light from the two arms was orthogonally polarized. An interference pattern was formed with a polarizer (made with a HWP and PBS) that mixed the modes, as described in section 4.4.1. Good temporal overlap of the Stokes and anti-Stokes modes did not necessarily lead to good temporal overlap of the pump pulses; the dispersion characteristics of the two arms of the interferometer were different. This was likely due to differences in the spectral characteristics of the pump filters and the two filters separating the Stokes and anti-Stokes modes. The difference could be attributed to small differences in the tilt angle or different properties of the short- and long-pass filters. I used a narrow-band filter (5 nm bandwidth) to increase the duration of the two pump pulses to ensure good temporal overlap. The interference

signal was detected using a silicon photodiode (Thorlabs DET10A/M), as depicted in figure 4.4. These detectors have a fast temporal response (1 ns) and were sensitive to the 80-MHz pulse repetition frequency of the laser. The photodetector response was slowed down by connecting it in parallel to a high-impedance 1-MΩ resistor. As the photodetector acted as a capacitor (with capacitance 6 pF), the combined circuit was a low pass filter with a bandwidth of 26 kHz, eliminating the fast pulse modulation.

The intensity of the interference signal $e(t)$ varied sinusoidally with the relative phase ϕ_{lr} between the two arms, $e(t) \propto \sin(\phi_{\mathrm{lr}})$. The signals were digitized with a data acquisition card (DAQ, National Instruments PCI-6602) interfaced with a computer. In software, a proportional-integral (PI) feedback loop generated an output signal $s(t)$ from the input error signal $e(t)$,

$$s(t) = K_{\mathrm{p}} e(t) + K_{\mathrm{i}} \int_0^t e(\tau)\mathrm{d}\tau, \tag{4.42}$$

where K_{p} is the proportional gain and K_{i} is the integral gain. The proportional term controlled the sensitivity of the loop response and the integral term drove the output signal to the set point with a timescale determined by K_i.[9] The PI gains were tuned heuristically using the Ziegler-Nicols method [169]. The program was written in MATLAB with the Data Acquisition Toolbox V2.13 and NI DAQ driver V9.0.[10] The output signal was converted to an analog signal (with the DAQ card), which was sent to a voltage driver (Thorlabs MDT94A and Piezomechanik PosiCon.an150) to modulate the length of a piezoelectric crystal (Thorlabs AE0505D08F). The piezoelectric actuator was mounted on a custom-built retro-reflector located in one arm of each of the interferometers to provide feedback to the differential path length. The loop bandwidth was 5 Hz, which was fast enough to counter the slow phase drift arising from thermal fluctuations in the laboratory. See Appendix B for details of the program.

Figure 4.6 shows the phase stability before and after active phase stabilization. With stabilization, the RMSE was 0.6° for the Stokes interferometer and 1.3° for the anti-Stokes

[9] The integral term increases the sensitivity of the control loop at low frequencies and introduces a $\pi/2$ phase shift between $s(t)$ and $e(t)$. An intuitive and necessary (but not sufficient) condition for loop stability is that the gain is less than one when the phase lag is greater than π.

[10] My experience with LABVIEW, with its tangle of wires, remains that of the overeager neighbour plugging one too many Christmas light strings into the same electrical socket.

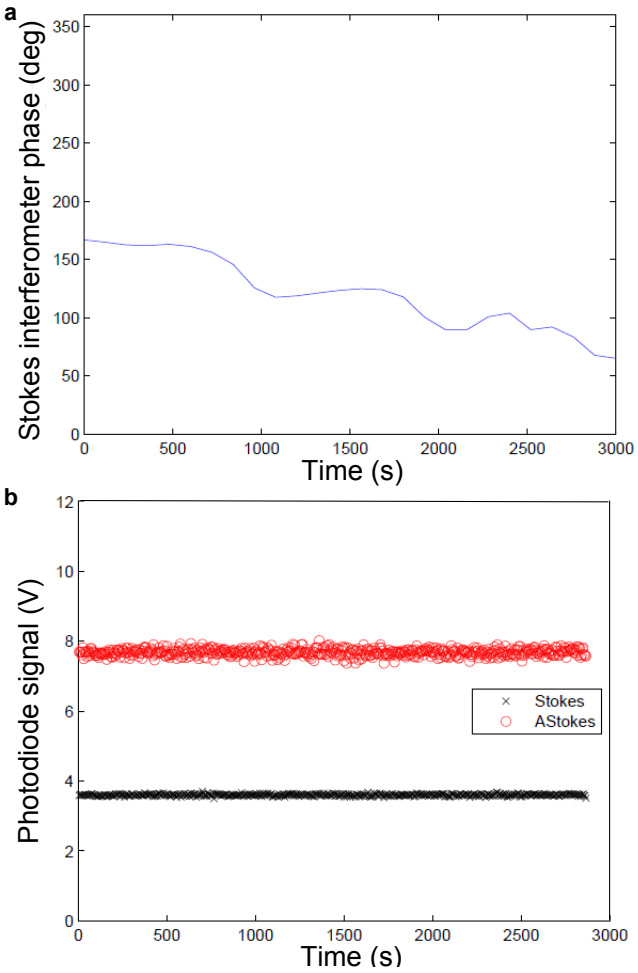

Figure 4.6: Phase stabilization of the Stokes and anti-Stokes interferometers. **a** Relative phase of the Stokes interferometer without active stabilization. The phase drift was 101°, and the RMSE was 33°. **b** Interference signal from the Stokes and anti-Stokes interferometers. The voltage fluctuations were proportional to phase fluctuations (in the limit that they are small). The voltage range for the Stokes signal was 2.7 V and 4.57 V for the anti-Stokes signal. With phase stabilization, the RMSE was 0.6° for the Stokes interferometer and 1.3° for the anti-Stokes interferometer over 45 minutes.

interferometer, compared to a passive phase drift of 101° for the Stokes interferometer over the same period (the anti-Stokes channel was not measured here). The length of the phase stability was limited by the stability of the laser oscillator.

A change in laser power would be erroneously interpreted as a phase change within the interferometer. With the construction of a new box for the laser oscillator (and removing all vestiges of duct tape), I found that the laser power output was sufficiently stable over the course of the measurements. For the interference and quantum state tomography measurements (sections 4.5.1 and 4.5.5), a program was written to dynamically scan the piezoelectric voltage to determine the midpoint voltage prior to, in between, and after

the measurements to ensure that the laser power had not changed.

4.4.6 Phase control of the interferometer

Scanning the phase over a range greater than 2π was required to measure the visibility of the quantum interference. The phase stabilization circuit in section 4.4.5 only functioned when the error signal was approximately linear (i.e. near $\phi_{lr} = n \pm \pi$, where n is an integer) and failed where the gradient went to zero at the maxima and minima of the interference pattern (e.g. $\phi_{lr} = \pi/2$). As an alternative approach, the phase of the anti-Stokes interferometer ϕ_{a} can be varied by introducing a birefringent delay between the orthogonally polarized anti-Stokes fields while keeping the phase of the spatial interferometer fixed.

After PBS2 in figure 4.4, the anti-Stokes photons from the two arms of the interferometer were cross polarized, but in the same spatial mode. Varying the phase of the interferometer was accomplished by delaying one polarization component relative to the other. An elegant way to implement a birefringent delay is via the Pancharatnam-Berry phase [170] by using two quarter-wave plates and a half-wave plate [171, 172] outside the (spatial) interferometer, as shown in figure 4.4.

The geometric phase is a general phenomenon where a system subject to an adiabatic cyclic process can acquire a phase due to the geometric structure of the phase space. This occurs in both classical and quantum mechanics. Changing the polarization of a photon along a closed trajectory on the Poincaré sphere results in a geometric phase given by the solid angle subtended by the enclosed area.[11] In this way, a phase between $|H\rangle$ and $|V\rangle$ can be implemented without changing the polarization states for an arbitrary state, exactly as desired. This was implemented by the combination of a quarter-wave plate,

[11] There is no condition that the rate of change must be slow compared to some energy scale as the polarization states of light all have the same energy.

half-wave plate, and quarter-wave plate in the following manner [172],

$$S(\phi) = U_{\mathrm{QWP}}\left(\frac{\pi}{4}\right) U_{\mathrm{HWP}}\left(-\frac{\pi}{4}-\frac{\phi}{4}\right) U_{\mathrm{QWP}}\left(\frac{\pi}{4}\right) \tag{4.43}$$

$$= \begin{pmatrix} \mathrm{e}^{-\mathrm{i}\frac{\phi}{2}} & 0 \\ 0 & \mathrm{e}^{\mathrm{i}\frac{\phi}{2}} \end{pmatrix} = \mathrm{e}^{-\mathrm{i}\frac{\phi}{2}} \begin{pmatrix} 1 & 0 \\ 0 & \mathrm{e}^{-\mathrm{i}\phi} \end{pmatrix}, \tag{4.44}$$

where, for $U_{\mathrm{WP}}(...)$, the term in the brackets indicates the physical angle between the axis of the wave plate and the polarization vector. The global phase outside the matrix in equation 4.44 can be ignored as it is the same for both polarizations. Therefore, according to equations 4.43 and 4.44, a physical rotation of the half-wave plate by an angle ϕ will result in a birefringent phase change of 4ϕ. To summarize, the phase of the anti-Stokes interferometer was varied by introducing a delay between orthogonally polarized light in the same spatial mode using two quarter-wave plates and one half-wave plate.

4.4.7 Detection of single photons

The Stokes and anti-Stokes photons were coupled into single-mode fibres (Thorlabs 780HP for the Stokes light and Thorlabs SM600 for the anti-Stokes light) with a metal articulated jacket to eliminate ambient light scattering into the fibre mode. One output port from PBS3 (Stokes) and two output ports from PBS4 (anti-Stokes) were detected with APDs (Perkin Elmer SPCM-AQ4C), as shown in figure 4.4. The coincidence detection was performed by a custom field-programmable gate array[12] and controlled through a Labview interface. The coincidence detection window was 5 ns and the dead time 20 ns, compared to a pulse separation of 12 ns. Due to the low probability of excitation (10^{-3} probability of Stokes creation per pulse), we assumed that the dead time of the detector had a negligible effect on the count rates.

[12] Designed by Alan Strummer at the University of Toronto.

4.5 Experimental results

4.5.1 Interference of heralded anti-Stokes photons

As discussed in section 3.1.1, detecting a Stokes-scattered photon at detector D_s (from figure 4.3) projected the diamonds into the (unnormalized) entangled phonon state (equation 3.14)

$$|\Phi^+\rangle = \left[b_l^\dagger + e^{-\mathrm{i}\phi_\mathrm{s}} b_r^\dagger\right] |\mathrm{vac_{vib}}\rangle, \tag{4.45}$$

where $|\mathrm{vac_{vib}}\rangle = |0_\mathrm{b}\rangle_l |0_\mathrm{b}\rangle_r$ is the initial vacuum state of the phonon mode, $b_{l,r}^\dagger$ is the creation operator for the phonon mode in diamond l or r, and we have adopted the Schrödinger interaction picture, where the quantum states evolve.

This state was mapped onto a Raman-scattered anti-Stokes optical field with probability $|\xi_\mathrm{a}|^2$ by directing pump pulses into the crystals a time $T = 350$ fs after the phonon was created, which was short compared to the coherence lifetime of 7 ps. The combined state of the diamonds and anti-Stokes modes was (cf. section 3.1.2, equation 3.16)

$$\begin{aligned} |\Psi_\mathrm{a}\rangle \quad = \quad & \{b_\mathrm{l}^\dagger + e^{-\mathrm{i}\phi_\mathrm{s}} b_\mathrm{r}^\dagger \\ & + \xi_\mathrm{a}[a_\mathrm{l}^\dagger + e^{-\mathrm{i}\phi_\mathrm{s}} a_\mathrm{r}^\dagger]\}|\mathrm{vac}\rangle. \end{aligned} \tag{4.46}$$

The anti-Stokes modes were combined on a polarizing beam splitter, and interfered with a controllable phase ϕ_a implemented via a geometric phase as described in section 4.4.6, equation 4.44. The number of anti-Stokes photons, $N_\pm$, that detected emerging from the two output ports of PBS4 in figure 4.3 is given by (cf. section 3.1.2, equation 3.17)

$$N_\pm = |\langle \mathrm{vac}|\hat{a}_\pm|\Psi_\mathrm{a}\rangle|^2 \propto \xi_\mathrm{a}^2 \sin^2\left[(\phi_s + \phi_a + (\pi \mp \pi)/2)/2\right], \tag{4.47}$$

where $\hat{a}_\pm = \left[\hat{a}_\mathrm{l} \pm e^{\mathrm{i}\phi_\mathrm{a}} \hat{a}_\mathrm{r}\right]/\sqrt{2}$. The relative phases ϕ_s and ϕ_a were actively stabilized separately, as described in section 4.4.5 such that the entanglement generation and verification processes were independent [162].

The number of heralded anti-Stokes photons $N_\pm$ is plotted as a function of ϕ_a in figure 4.7. The interference visibility was $V = 61 \pm 3\%$ for N_+ and $V = 55 \pm 3\%$ for N_-.

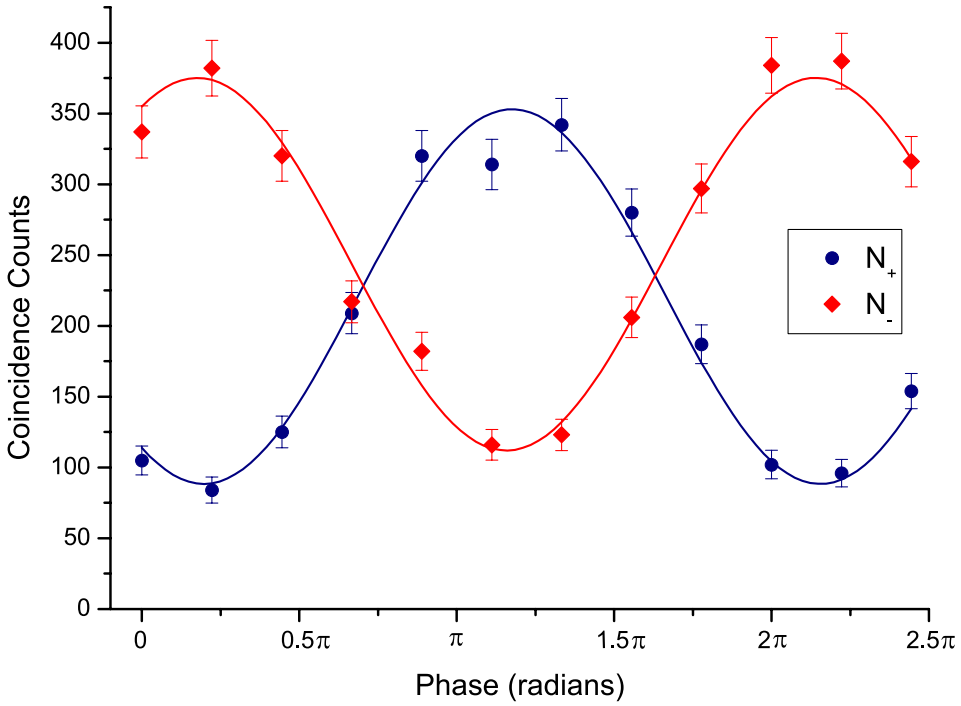

Figure 4.7: Coincidence counts between the herald Stokes photons and the read-out anti-Stokes photons, from reference [108]. The interference visibility for $N_+ = D_+ \& D_s$ was $V = 61 \pm 3\%$, and was $V = 55 \pm 3\%$ for N_- . The error bars on the y-axis were calculated from the standard deviation of the counts, which followed a Poissonian distribution.

The difference in visibility between the two detectors could be attributed to the different rates of accidental coincidences between the two detectors. Subtraction of the accidental coincidences (dominated by dark counts of the anti-Stokes detectors randomly coincident with the detection of a Stokes photon), gave an estimated visibility of 63 $\pm$ 3% for N_+ and 60 $\pm$ 3% for N_-, showing that the visibility measured with the two detectors agreed to within experimental uncertainty. The acquisition time was five minutes per data point as approximately one heralded anti-Stokes signal was detected per second.

The sinusoidal oscillations indicate that the coherence between the two diamond modes has been preserved; the probability amplitudes of two indistinguishable events – phonon in ensemble r and phonon in diamond l – interfered with a stabilized and controllable phase. We note that, although the coincidence rate of heralded anti-Stokes photons was sensitive to the relative phase of the anti-Stokes interferometer, the rate of heralded anti-Stokes photons when the modes were not interfered was independent of the geometric phase, as expected [164].

To show that the phonon mode was entangled, the interference visibility must be

compared to the higher-order photon number contributions to show that the interference was not classical in origin, as discussed in section 3.1.2. Before we do so, we first consider what limits the visibility of the interference in figure 4.7 with reference to the second-order cross-correlation discussed in section 4.2.4.

4.5.2 Limit on the interference visibility

Uncorrelated anti-Stokes photons, produced by spontaneous emission of an anti-Stokes photon or phonon decay, will not interfere with a fixed phase, reducing the fringe visibility. If both diamonds have the same second-order cross-correlation, the maximum visibility is given by equation 4.36. In the case of unequal cross-correlations for the two diamond samples, the maximum visibility is given by equation 4.38. In our experiment, we measured the cross-correlation ($g^{(2)}_{\mathrm{s,a}} = P_{\mathrm{s,a}}/P_{\mathrm{s}}P_{\mathrm{a}}$) between the Stokes and anti-Stokes fields for each of the two diamonds. The second-order cross-correlation was 11.4 ± 0.1 and 7.2 ± 0.1 for the right and left diamond, respectively. The maximum visibility is $75 \pm 1\%$ according to equation 4.38 for the measured cross-correlations. This is nearly the same as the visibility predicted by equation 4.36 if both diamonds have a cross-correlation of $g^{(2)}_{\mathrm{s,a}} = 7.2$. Comparing this to our experimental results in figure 4.7 implies good overlap between the optical fields; the product of the Stokes and anti-Stokes mode overlap was $75 - 80\%$ and $\sim 85 - 90\%$ individually.

Causes of decorrelation include spontaneous emission of anti-Stokes photons from thermally excited phonons; however, the spontaneous emission of anti-Stokes photons was suppressed compared to Stokes photons by a ratio of $2.5{\times}10^{-3}$ (owing to the low thermal occupation of the optical phonon state at room temperature). In addition, the Stokes/anti-Stokes correlation could be limited by the coupling efficiency as a result of scattering into higher order spatial modes, placing a lower bound on the correlation between the phonons. Note that the above analysis assumes the visibility was limited by high-photon number contributions in equation 3.8. If the noise source was assumed to be thermal or coherent light, the combined cross-correlation could be reconstructed from the correlation functions of the individual fields [125].

4.5.3 Reconstruction of the density matrix

The entanglement of the two phonon modes of the diamonds was verified by examining the entanglement between the heralded anti-Stokes photons (here we consider only N_+ from figure 4.7). The fact that local operations and classical communication (LOCC) cannot increase the amount of entanglement [173] forms the logical basis of this approach. Local in this context means that an operation is applied to each of the two subsystems (the diamond samples and the associated optical fields) independent of the other subsystem (e.g. Raman scattering in one diamond is *local*, interfering the Raman-scattered modes from the two diamonds on a beam splitter is *non-local*).

The conversion of a phonon into an anti-Stokes photon is a local operation and, therefore cannot increase the amount of entanglement [164]; the entanglement of the optical fields is a strict lower bound on the entanglement of the phonon. By examining the probability of generating higher photon numbers, we can show that the phonon state is incompatible with any separable state (e.g. of the form $|\Psi_\mathrm{a}\rangle = (1+\xi_\mathrm{a} a_l^\dagger)(1+\xi_\mathrm{a} a_r^\dagger)|\mathrm{vac}\rangle$). That is, the probability of twin anti-Stokes read-out detection events ($a_l^\dagger a_r^\dagger|\mathrm{vac}\rangle$) is sufficiently small compared to the probability of detecting a single anti-Stokes photon.

We reconstructed the density matrix in the number basis as developed in section 4.2.2. We limited the density matrix to a maximum of one heralded anti-Stokes per ensemble (including the case of one photon from both ensembles), which is a local operation (limiting to one total photon over the two ensembles is a non-local operation as both subsystems need to be examined in concert [162]). The density matrix over the restricted subspace is

$$\rho_{lr} = \begin{pmatrix} p_{00} & 0 & 0 & 0 \\ 0 & p_{10} & d_1 & 0 \\ 0 & d_1^* & p_{01} & 0 \\ 0 & 0 & 0 & p_{11} \end{pmatrix}. \tag{4.48}$$

The on-diagonal terms p_{mn} are the probability of detecting m and n anti-Stokes in ensembles l and r conditioned on detecting a Stokes photon with detector D_s. These probabilities were measured experimentally by measuring the anti-Stokes photons from the ensembles directly, without interference, heralded by the detection of a Stokes photon

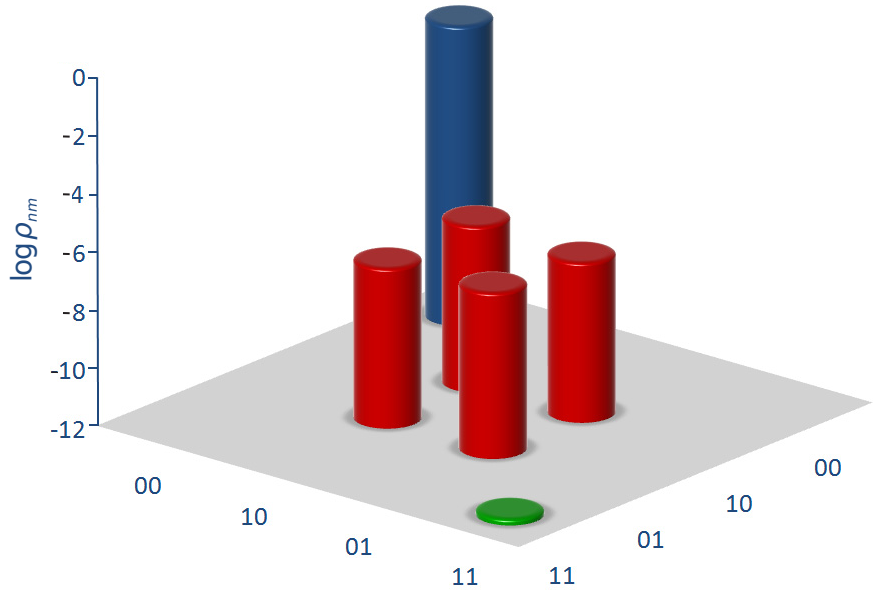

Figure 4.8: Density matrix of the heralded anti-Stokes modes, from reference [108]. The elements of the density matrix are $p_{00} = 1 - 2.3\times10^{-5}$, $p_{01} = 1.2\times10^{-5}$, $p_{10} = 1.1\times10^{-5}$, $d = 7.0 \pm 0.3\times10^{-6}$, and $p_{11} = 2.0 \pm 1.1\times10^{-11}$. The errors on the first three terms were negligible and have been omitted. The population terms were measured without interference between the anti-Stokes modes of the two diamonds. Note that there were no corrections made for any accidental coincidences. The large vacuum component was caused by the inefficiency of the anti-Stokes read-out and detection processes.

via detector D_s. The off-diagonal term $d_1 = V(p_{01} + p_{10})/2$ was determined by the interference visibility, as derived in section 4.2.2, and given by equation 4.2.2 in the limit $p_{11} \ll \{p_{01}, p_{10}\}$. All other terms were set to zero, which cannot increase the amount of entanglement as this action corresponds to a local operation.

The experimentally measured density matrix is plotted in figure 4.8 on a logarithmic scale. The individual elements were $p_{00} = 1 - 2.3\times10^{-5}$, $p_{01} = 1.2\times10^{-5}$, $p_{10} = 1.1\times10^{-5}$, $d = 7.0 \pm 0.3\times10^{-6}$, $p_{11} = 2.0 \pm 1.1\times10^{-11}$. The error in the coherence was dominated by the error in the visibility in figure 4.7, while the error in p_{11} arises from the statistical error of the Poissonian process, and the other errors are negligible. This will be discussed in more detail in the next section, where we evaluate the concurrence of the reduced density matrix in figure 4.8.

4.5.4 Calculation of the concurrence

As defined in section 4.2.3, the concurrence is an entanglement monotone for two-qubit entanglement that is zero for all separable states and positive for all entangled states

[156]. The concurrence here is defined over a subspace that consists of detecting zero or one anti-Stokes photon at the two detectors heralded on the detection of a Stokes photon. Higher-order photon-number contributions were neglected, as discussed previously. With these assumptions, the concurrence provides a strict lower bound to the entanglement between the diamonds [164]. According to equation 4.27, the concurrence of ρ is therefore [164, 156]

$$C = \max(2|d| - 2\sqrt{p_{00}p_{11}}, 0). \tag{4.49}$$

For the state in figure 4.8, the concurrence was $5.2 \pm 2.6\times10^{-6}$. This value approaches the maximum value of the concurrence, which, for perfect interference visibility and no higher order terms ($V = 1$, and $p_{11} = 0$), is given by $C_{\max} = p_{01} + p_{10} = 2.3 \times 10^{-5}$. The maximum value of the concurrence was limited by the coupling and detector efficiencies, and the read-out probability – that is the probability of converting a phonon into an anti-Stokes photon, conditioned on detecting a Stokes photon, which was approximately 10^{-3}. The read-out probability could be increased by ensuring the four-wave mixing interaction was phase-matched (see section 3.2.3) or increasing the Raman coupling with a higher pulse energy or smaller detuning.

The concurrence was positive by two standard deviations. The standard deviation ΔC of the concurrence is

$$(\Delta C) = \sqrt{\left(\frac{\partial C}{\partial |d|}\Delta|d|\right)^2 + \left(\frac{\partial C}{\partial p_{00}}\Delta p_{00}\right)^2 + \left(\frac{\partial C}{\partial p_{11}}\Delta p_{11}\right)^2}, \tag{4.50}$$

where ΔX denotes the error on the quantity X, and ΔC is dominated by Δp_{11}. The confidence level cannot be calculated directly from the standard deviation when the number of counts is small (< 10) as the Poisson distribution is not, in this case, well-approximated by a normal distribution. To determine our confidence in concluding that the diamonds were entangled, I calculated the Poissonian confidence level [174] at which the concurrence is positive.

I compared the measured probability p_{11} of detecting twin read-out events ($a_l^\dagger a_r^\dagger|\text{vac}\rangle$) to the maximum probability of detecting twin read-out events given a concurrence of zero, $p_{11}^0 = d^2/p_{00} \approx d^2 = 4.9 \times 10^{-11}$. The null hypothesis is that the measured p_{11} was a

statistical fluctuation from p_{11}^0. It is simpler to cast the discussion in terms of expected events, where the probabilities are multiplied by the number of Stokes photons, which is the product of the number of experimental runs $R = 1.9 \times 10^{14}$ and the probability of detecting a Stokes photon $p_s = 10^{-3}$.[13] Expressed in these terms, we measured $X = 3$ twin read-out events when we would expect to see a minimum of $\mu_0 = 9.1 \pm 0.9$ events were the concurrence zero and the diamonds not entangled. The problem reduces to estimating the confidence level for detecting $X = 3$ events given an expected mean number of events μ_0 consistent with zero concurrence $\mu_0 = 9.1$. There are two approaches: the frequentist approach calculating $P(X|\mu)$, and the Bayesian approach calculating $P(\mu|X)$.[14]

Rare events, that occur independent of the previous event, follow a Poissonian distribution and are defined by a single parameter μ, which is both the mean and variance, with probability

$$P(X|\mu) = \frac{\mu^X \mathrm{e}^{-\mu}}{X!}. \tag{4.51}$$

For the frequentist approach, we calculate the confidence level α given X observations such that the confidence interval is $0 \leq \mu \leq \mu_0$, where μ_0 is the smallest value consistent with zero concurrence. The confidence level is given by [174]

$$P(\mu \in [0, \mu_0]) = \alpha. \tag{4.52}$$

This was found by calculating $P(X|\mu)$ from equation 4.51 for each value of μ (a continuous variable) and each value of X (a non-negative integer). For a given observation X, the Poisson distribution is integrated with respect to μ at that value of X until the confidence level in equation 4.52 is met. In the case of an upper limit, the expression is

$$\int_0^{\mu_0} P(X|\mu)\mathrm{d}\mu = \sum_{x=X+1}^{\infty} P(x|\mu) = \alpha. \tag{4.53}$$

For $X = 3$ and $\mu_0 = 9.1$ the confidence level is 98%.

[13] Even with a pulse repetition frequency of 80 MHz, several days of continuous measurement were required to see one event, and the total measurement time was over 2 weeks.

[14] A frequentist confidence interval encompasses a belief in a single, fixed, value for the parameter μ_t and, for a given confidence level, gives the fraction of experiments that the confidence interval will contain μ_t. This is in contrast to the Bayesian approach, where the credible level indicates the 'degree of belief' that μ_t is within the credible interval $0 \leq \mu \leq \mu_0$ [174]. The distinction is valid.

For the Bayesian approach, we calculate the posterior distribution $P(\mu|X)$ from the likelihood function $L(X|\mu) = \mu^X \mathrm{e}^{-\mu}/X!$ and the prior distribution of $P(\mu)$

$$P(\mu|X) = \frac{L(X|\mu)P(\mu)}{\int L(X|\mu)P(\mu)\mathrm{d}\mu}. \tag{4.54}$$

The choice of prior is a delicate matter. The simplest is a uniform, flat prior that is constant over the real line (or some part of it). Another common prior, doted on by statisticians, is a Jeffreys prior, based on minimizing the Fisher information [175].[15] Here we consider only a flat prior, see Appendix A for consideration of the Jeffreys prior. The Bayesian credible level is given by integrating all $\mu \leq \mu_0$,

$$\begin{aligned} P(\mu \leq \mu_0|X) &= \int_0^{\mu_0} \frac{\mu'^X \mathrm{e}^{-\mu'}}{\int_0^\infty \mu'^X \mathrm{e}^{-\mu'}\mathrm{d}\mu'}\mathrm{d}\mu' \\ &= 1 - \frac{\Gamma(X+1,\mu_0)}{\Gamma(X+1,0)}, \end{aligned} \tag{4.55}$$

where Γ is the incomplete Gamma function. For $X = 3$ and $\mu_0 = 9.1$ the credible level is 98.0% (a Jeffreys prior $\mu^{-1/2}$ gives a 99% credible level). In summary, both approaches, whether Bayesian (flat prior) or frequentist, give the same confidence level for positive concurrence, 98%.

Our results ($X = 3$, $N = 1.9 \times 10^{14}$, and $\mu_0 = 9.1 \pm 0.9$) indicate positive concurrence at a confidence level of $98 \pm 1\%$. The confidence interval for positive concurrence was $98 \pm 1\%$ for N_+ (between detectors D_s and D_{as+}) and $94 \pm 2\%$ for N_- (betweeen detectors D_s and D_{as-}). The concurrence estimate from N_- was $(3.8 \pm 2.6)\times 10^{-6}$. Subtraction of accidental coincidences (dominated by dark counts of the anti-Stokes detectors randomly coincident with the detection of a Stokes photon), gives an estimated visibility of $63 \pm 3\%$ for N_+ and $60 \pm 3\%$ for N_-. We therefore estimate the concurrence to be $(5.6 \pm 2.6)\times 10^{-6}$ from N_+ and $(4.9 \pm 2.6)\times 10^{-6}$ from N_-, and the confidence intervals for positive concurrence to be $98.7 \pm 0.6\%$ and $98 \pm 1\%$ respectively, which implies entanglement to a high degree of certainty between the two diamond samples. Therefore, based on

[15] The motivation is that a flat prior can, in some cases, be 'informative'. Take the example of the estimating the variance σ^2 of a Gaussian distribution. A flat prior would assign a greater probability to $\sigma^2 > \sigma_0^2$ than $\sigma^2 < \sigma_0^2$ for any $\sigma_0^2 > 0$. In other words, the prior is not scale invariant [176].

the presence of entanglement between Stokes and anti-Stokes modes we can infer the presence of entanglement between the phonon modes of two macroscopic solids at room temperature.

The choice of what confidence level constitutes compelling evidence requires careful judgment as the potential for confounding systematic or spurious effects must be considered. In particle physics, 5σ significance level is considered 'proof' of a discovery, whereas 4σ is considered 'evidence'. Our results are less than 3σ and, by this metric, should we have reason to doubt our results? I would argue no in this instance, as there was no subtraction of background signal or of systematic effects. Systematic errors were unlikely to cause a false positive in our experiment as the photodetectors would have had to have detected fewer three-fold events than actually were registered. We tested the coincidence counting logic of the FPGA with a signal generator to verify that it was operating as expected. Given that there was no background subtraction and given the limited scope for systematic errors, we conclude that the measured confidence level offers compelling evidence that the diamonds are entangled. The confidence level could be further improved by increasing the amount of data or improving the read-out efficiency.

4.5.5 Quantum state tomography

Finally, I examined more closely the coherence of the entangled state of the diamonds by post-selecting on the terms in figure 4.8 with exactly one phonon distributed between the two ensembles. Here we can neglect the large vacuum component p_{00}, which was caused by inefficiencies in the read out of the anti-Stokes mode, as well as inefficiencies in the coupling and detection of the anti-Stokes photons. We also neglected the contribution from higher photon numbers, yielding an estimate of the ideal amount of entanglement between the phonons with no losses and unit efficiency.

We performed quantum state tomography [177] to measure the post-selected joint state of the Stokes and anti-Stokes modes. The Stokes and anti-Stokes photons from diamonds l and r were mapped onto the polarization states H and V and we then performed polarization quantum state tomography. The information on where the photon was generated was contained in the polarization. The observation of the maximally entangled

state,

$$|\Phi\rangle = \frac{1}{\sqrt{2}}\left[|H\rangle_{\rm S}|V\rangle_{\rm AS} + {\rm e}^{{\rm i}(\phi_{\rm s}+\phi_{\rm a})}|V\rangle_{\rm S}|H\rangle_{\rm AS}\right], \tag{4.56}$$

would demonstrate perfect coherence between the Raman-scattered optical fields from the two diamonds. We made 6 measurements of the polarization of each mode, given by H, V, D, A, R, L, where D, A denote diagonal/anti-diagonal polarization and R, L denote right and left circular polarization, giving a total of 36 measurements. We used detectors $D_{\rm s}$ and $D_{\rm a+}$, and reconstructed the state using maximum likelihood analysis [177, 172]. The basic principle is to minimize the likelihood function $\mathcal{L}$ subject to the constraint that the state be physical, i.e. the density matrix is Hermitian ($\rho = \rho^\dagger$), positive ($\langle\psi|\rho|\psi\rangle > 0$, $\forall|\psi\rangle$), and normalized (${\rm Tr}(\rho) = 1$). The likelihood function is [177, 172]

$$\mathcal{L}(\mathbf{t}) = \sum_m^{N_m} \frac{[\eta_m(\mathbf{t}) - n_m]^2}{n_m}, \tag{4.57}$$

where $\mathbf{t} = \{t_1, t_2 ... t_9\}$ are elements of the tri-diagonal matrix T such that $\rho(\mathbf{t}) = \Upsilon(\mathbf{t})/{\rm Tr}\left[\Upsilon(\mathbf{t})\right]$ for $\Upsilon(\mathbf{t}) = T^\dagger(\mathbf{t})T(\mathbf{t})$; n_m are the coincidence count data for a set of measurements along N_m bases, $m = 1, 2, ...N_m$; and the expected number of coincidence counts measured in the basis of state $|\psi_m\rangle$ is

$$\eta_m(\mathbf{t}) = \mathcal{N}\langle\psi_m|\rho(\mathbf{t})|\psi_m\rangle, \tag{4.58}$$

where $\mathcal{N}$ is the number of experimental runs and $|\psi_m\rangle = \{|H\rangle, |V\rangle, |D\rangle, |A\rangle, |R\rangle, |L\rangle\}$. The algorithm used to minimize equation 4.57 is based on the property that density matrices form a convex set. Convex sets have a simple geometric interpretation: any two points in a convex set can be joined by a line that rests entirely inside the set. The proof that density matrices form a convex set relies on the fact that any linear combination of density matrices $\rho = \lambda\rho_1 + (1-\lambda)\rho_2$ is also a valid, physical density matrix, i.e. Hermitian, non-negative and normalized. Therefore, the techniques of *convex optimization* can be applied to simplify the problem dramatically [178]; a local minimum is always a global minimum for a convex set.

When analysing the data, we subtracted accidental coincidences caused by uncorrelated coincidences between Stokes and anti-Stokes photons from two diamonds. The accidental coincidences were significant for two reasons. First, the Stokes singles rate

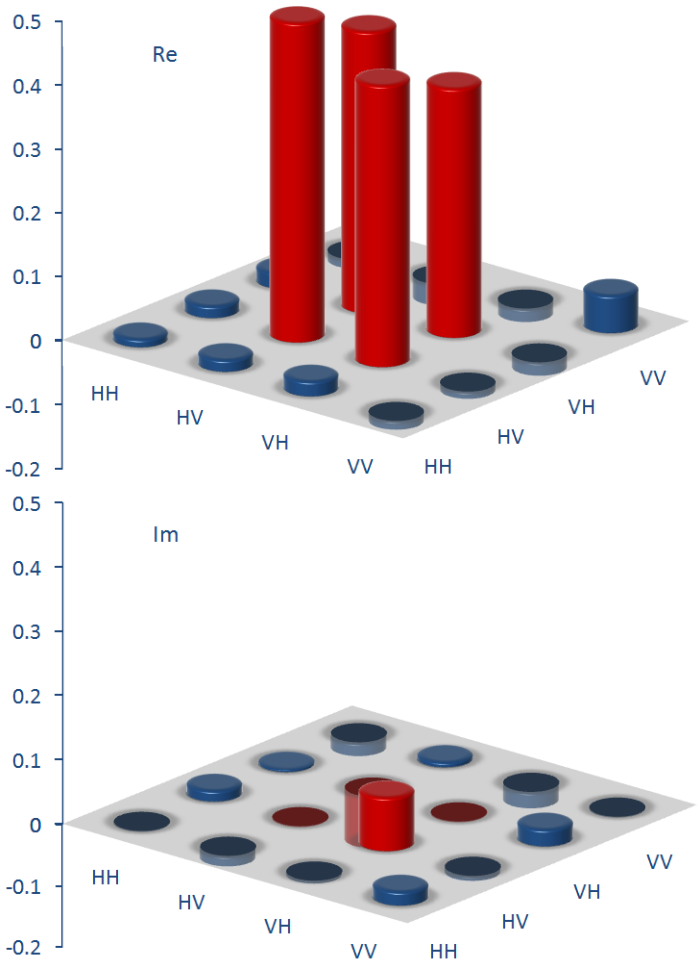

Figure 4.9: Quantum state tomography of the post-selected joint state of the Stokes/anti-Stokes fields, from reference [108]. The real and imaginary parts of the state are shown for a restricted sub-space of one phonon between the two modes. This process is a non-local operation and can increase the amount of entanglement.

was three orders of magnitude higher than the anti-Stokes singles, which was in turn two orders of magnitude larger than the coincidence counts. Second, the detection window for coincident photons (5 ns) was a significant fraction of the pulse spacing (12 ns). The accidental coincidences were calculated from the unheralded detection rates of the anti-Stokes and Stokes photons.

The reconstructed state is shown in figure 4.9, where we have subtracted accidental coincidences as discussed above. The concurrence of this subspace was 0.85, which provides an upper bound to the amount of entanglement between the diamonds, were the retrieval, collection and detection processes ideally efficient (i.e. $p_{00} \to 0$), and with the caveat that the existence of entanglement can only be rigorously inferred from figure 4.8

[162]. Even without the subtraction of accidental coincidence counts, the concurrence was 0.35, indicating a significant amount of entanglement. The fidelity of the reconstructed state to the nearest Bell state $[|HV\rangle + |VH\rangle]/\sqrt{2}$ was 0.91, which also provides a measure of how faithful the measured state was to a maximally entangled state. The high degree of coherence shows that the two processes – generation and read-out of a phonon in diamonds r and l – are, to a good approximation, indistinguishable and phase stable. These results provide a more complete account of the concurrence measured in figure 4.7; instead of projecting the Stokes photon onto one state and the anti-Stokes onto two states, each Stokes and anti-Stokes photon is projected onto six states.

4.6 Significance of the time ordering of the experiment

Unlike in similar experiments with cold atomic ensembles [164], in our experiment the phonon was converted to an anti-Stokes photon before the Stokes photon had reached D_s. The phonon was created at time t_{ph} and the detection of the Stokes photon that prepared the entangled phonon state occurred at time t_d, ∼10 ns after t_{ph}. The conversion of the phonon into an anti-Stokes photon needed to occur at time $t_{ph} + T$, where $T = 350$ fs, as the lifetime of the phonon was much less than $(t_d - t_{ph})$. As the state of the diamonds was conditioned on a measurement that happened after the phonon was converted into an optical field, it is instructive to consider the role of the time ordering of the Stokes measurement.

It is tempting to think that the detection of the Stokes photon *causes* the instantaneous collapse of the joint state of the two diamonds into an entangled state. Indeed, describing the DLCZ protocol, as summarized in section 3.1, naturally lends itself to this type of language. However, adopting this interpretation immediately leads to difficulty in understanding the causal effects of measurements. For example, given two space-like separated events, the chosen inertial frame can change the ordering of events such that the detection event occurs *after* the state is projected on to its measurement outcome [179, 180].

Instead, our experiment, and the DLCZ protocol in general, can be understood *retrodictively*; it is equally valid to consider a state evolving forward in time from state prepa-

ration to a measurement as a state propagating backwards in time from a final measurement to an initial preparation [181, 182]. Further, a measurement projection can always be back-propagated to any arbitrary time during the system evolution [183]. The events where the measurement was unsuccessful can then be ignored from the final statistics [184]. In our experiment, we evolve the Stokes measurement operator $E = \langle \mathrm{vac}_{\mathrm{opt}}|s$ backwards in time from the moment of detection, t_{d}, to the time t_{ph} at which the Stokes photon and phonon were created. The resulting projection leaves the diamonds in an entangled state at t_{s}, and it is this entanglement that is probed via anti-Stokes scattering at time $t_{\mathrm{a}} = t_{\mathrm{s}} + \tau$. To restore the conventional time-ordering of the DLCZ protocol would require the use of an integrated, chip-scale interferometer [185] and fast photodetectors [186]. It remains an outstanding goal of optomechanics to observe measurement-induced entanglement between the motion of two objects using the conventional time-ordering, without resort to retrodiction.

The complexity of temporal succession was in some sense presaged by Irish aeronautical engineer J. W. Dunne, who published the book *An Experiment with Time* in March 1927 [187]. In the book, he claims that dreams allowed the dreamer to become unanchored in time. Events from the present, past, and future intermingle and by keeping careful and conscientious records of the dreams the dreamer can achieve some level of clairvoyance. As Jorge Luis Borges writes in *Time and J. W. Dunne*, [188]

> "Dunne assures us that in death we shall learn how to handle eternity successfully. We shall recover all the moments of our lives and we shall combine them as we please. God and our friends and Shakespeare will collaborate with us.
>
> With such a splendid thesis as that, any fallacy committed by the author becomes insignificant."

4.7 Summary

We demonstrated entanglement between two room-temperature, sold-state objects for the first time. The optical phonon excitation was one quantum distributed over $\sim 10^{16}$

carbon atoms. Entanglement was generated by spontaneous Raman scattering and projective measurement via the DLCZ protocol. The entanglement was rigorously verified by measuring the concurrence of the heralded anti-Stokes fields in a restricted subspace of at most one photon originating from each diamond. From the entanglement between optical fields we could infer a lower bound on the entanglement of the optical phonon modes. Our approach can be applied to other optomechanical systems as a promising tool for the new field of quantum phononics [189] – the generation and manipulation of quantum states of motion.

Part II

Storage of Light in a Hollow-Core Photonic Crystal Fibre

5

Stimulated Raman Memory in a Warm Cesium Vapour

A three-level system with a Λ-structure – two dipole-decoupled ground states linked together by a single excited state, as shown in figure 5.1 – supports a number of non-linear effects including stimulated Raman scattering [190, 191], electromagnetically-induced transparency [192, 193], coherent population trapping [194], and stimulated Raman adiabatic passage [195, 196], among others. The wide range of behaviour is a result of two features of the Λ-system. One, multiple excitation channels can result in interference of the probability amplitudes. Two, population can be transferred entirely into either one of the two ground states, which is an important feature that is necessary for realizing a quantum memory. We now present a derivation of the relevant equations describing the interaction in a stimulated Raman memory.

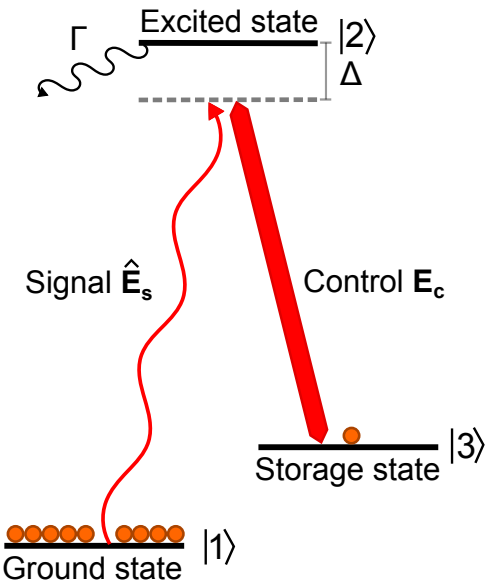

Figure 5.1: Diagram of a three-level Λ-system with signal $\hat{\mathbf{E}}_s$ and control $\mathbf{E}_c$ optical fields used to implement a Raman quantum memory. The optical fields are detuned by Δ from the excited state, which has a spontaneous decay rate Γ.

5.1 Light-matter interaction

The total Hamiltonian of the interaction between light and matter is given by

$$\hat{\mathcal{H}} = \hat{H}_A + \hat{H}_R + \hat{H}_{ED}, \tag{5.1}$$

where $\hat{H}_A$ is the bare atomic Hamiltonian, $\hat{H}_R$ is the radiative Hamiltonian arising from excitations of the electromagnetic field, and $\hat{H}_{ED}$ is the interaction between light and matter. The atomic Hamiltonian is

$$\hat{H}_A = \sum_i \hbar\omega_i |i\rangle\langle i| = \sum_i \hbar\omega_i \hat{\sigma}_{ii}, \tag{5.2}$$

where i denotes the energy eigenstate, $\hbar\omega_i$ the associated energy eigenvalue and $\hat{\sigma}_{ij} = |i\rangle\langle j|$ is the atomic transition-projection operator.

The radiative Hamiltonian can be expressed in terms of the continuous-mode field operators $\hat{a}(\omega)$

$$\hat{H}_R = \int_0^\infty \mathrm{d}\omega \hbar\omega \hat{a}^\dagger(\omega)\hat{a}(\omega), \tag{5.3}$$

where the divergent vacuum contribution is ignored [126]. The annihilation operators

obey the following commutator relation,

$$\left[\hat{a}(\omega),\, \hat{a}^{\dagger}(\omega')\right] = \delta\left(\omega - \omega'\right), \tag{5.4}$$

which is the continuous-mode analogue of the canonical commutation relation for the discrete bosonic operators. We ignore any transverse spatial dependence and develop the theory in one dimension (see [197] for an extension to three dimension).

Finally, the light-matter interaction Hamiltonian generated by the electric field operator $\hat{\mathbf{E}}$ is

$$\hat{H}_{\mathrm{ED}} = -e\hat{\mathbf{D}} \cdot \hat{\mathbf{E}}, \tag{5.5}$$

where the electric dipole operator $\hat{\mathbf{D}}$ is,

$$\hat{\mathbf{D}} = \sum_{ij} \langle i|\mathbf{D}|j\rangle |i\rangle\langle j| = \sum_{ij} \langle i|\mathbf{D}|j\rangle \sigma_{ij}. \tag{5.6}$$

The transverse electric field $\hat{\mathbf{E}}$ is expressed in the continuous-mode spectral representation in one dimension as

$$\hat{\mathbf{E}}(z,t) = \mathrm{i}\int \mathrm{d}\omega \left(\frac{\hbar\omega}{4\pi\varepsilon_0 cA}\right)^{1/2} \hat{a}(\omega)\mathrm{e}^{-\mathrm{i}\omega\left(t-\frac{z}{c}\right)}\boldsymbol{\epsilon} + \mathrm{H.c.}, \tag{5.7}$$

where A is the transverse area of the optical beam, $\boldsymbol{\epsilon}$ is the polarization unit vector, and H.c. refers to the Hermitian conjugate.[1] We will discuss some of the properties of the electric dipole interaction in the next section.

5.1.1 Dipole operator

The light-matter Hamiltonian in equation 5.5 is derived from the potential energy of an atom with valence electron at location $\mathbf{r}_{\mathrm{e}}$ with charge density $\sigma(\mathbf{r}) = -e\delta(\mathbf{r} - \mathbf{r}_{\mathrm{e}})$ in an electric field $\hat{\mathbf{E}}(\mathbf{r})$ [126]. The expression for the Hamiltonian is

$$\hat{H}_{\mathrm{ED}} = -\int \mathrm{d}\mathbf{r}\hat{\mathbf{P}}(\mathbf{r}) \cdot \hat{\mathbf{E}}(\mathbf{r}), \tag{5.8}$$

[1] The imaginary number i originates from the choice of the vector potential A, following the derivation by Loudon [126]. As a result, it will render our later equations slightly differently than Gorshkhov [35, 58].

where $\hat{\mathbf{P}}(\mathbf{r})$ is the polarization such that $\sigma(r) = -\nabla \cdot \hat{\mathbf{P}}(\mathbf{r})$. Equation 5.8 can be expanded in terms of the electric field

$$\hat{H}_{\mathrm{ED}} = e\left\{1 + \frac{1}{2!}\mathbf{r}_{\mathrm{e}} \cdot \nabla + \frac{1}{3!}\left(\mathbf{r}_{\mathrm{e}} \cdot \nabla\right)^2 + ...\right\}\mathbf{r}_{\mathrm{e}} \cdot \hat{\mathbf{E}}(0), \tag{5.9}$$

where the terms in the braces represent the multipole expansion of the electric field. Retaining the first term is called the *dipole approximation*. This is valid when the spatial variation of the electric field over the size of the atom is small, which is in general the case as the wavelength of light is much larger than the atomic radius. The next high-order moments, the magnetic dipole moment and the electric quadrupole moments, have a smaller energy by on the order of the fine structure constant $\alpha \ll 1$ and are ignored in the dipole approximation. The expression for the light-matter interaction reduces to equation 5.5.

Insight into the selection rules of the dipole operator can be gained by considering it in relation to the parity operator $\hat{\Pi}$. The parity operator flips the sign of the position operator r_{e} [198]

$$\hat{\Pi}\hat{r_{\mathrm{e}}}\hat{\Pi}^{\dagger} = -\hat{r_{\mathrm{e}}}. \tag{5.10}$$

The parity operator is an involutory matrix (i.e. $\hat{\Pi} = \hat{\Pi}^{-1}$ and therefore $\hat{\Pi}^2 = \hat{\mathrm{I}}$). The eigenvalues $\pi_{\pm}$ for the parity operator are ± 1. We can rewrite equation 5.10 as

$$\hat{\Pi}\hat{r_{\mathrm{e}}}\hat{\Pi}^{\dagger}\hat{\Pi} = -\hat{r_{\mathrm{e}}}\hat{\Pi} \tag{5.11}$$

$$\hat{\Pi}\hat{r_{\mathrm{e}}} = -\hat{r_{\mathrm{e}}}\hat{\Pi} \tag{5.12}$$

Equation 5.12 can be rewritten as $\{\hat{\Pi}, \hat{r_{\mathrm{e}}}\} = 0$, where $\{,\}$ is the anti-commutator of the operators. Applying this relation to the energy eigenstates $|\mu\rangle$ and $|\nu\rangle$ of the Λ-system gives [198]

$$\langle\mu|\{\hat{\Pi}, \hat{r_{\mathrm{e}}}\}|\nu\rangle = \langle\mu|\hat{\Pi}\hat{r_{\mathrm{e}}} + \hat{r_{\mathrm{e}}}\hat{\Pi}|\nu\rangle \tag{5.13}$$

$$= (\pi_{\mu} + \pi_{\nu})\langle\mu|\hat{r_{\mathrm{e}}}|\nu\rangle = 0, \tag{5.14}$$

where π_{μ}, π_{ν} are the eigenvalues of the parity operator. When $\mu = \nu$ the eigenvalues

are the same and, therefore $(\pi_\mu + \pi_\nu) \neq 0$, requiring that the diople matrix element $\langle\mu|\hat{r_e}|\nu\rangle = 0$ in order to satisfy equation 5.14. The selection rule for the dipole operator can be summarized as

$$\langle\mu|\hat{d}|\nu\rangle = 0, \qquad \text{for } \mu = \nu, \tag{5.15}$$

and non-zero only for states with opposite parity. Given the above selection rules, we can simplify the electric dipole operator to the following expression,

$$\hat{\mathbf{D}} = \sum_n \mathbf{D}_n \left(\hat{\sigma}_n^\dagger + \hat{\sigma}_n\right), \tag{5.16}$$

where the summation index $n = \{j, k\}$ runs over pairs $|j\rangle$, $|k\rangle$ of electric-dipole-coupled states.

The light-matter Hamiltonian can be further simplified be eliminating terms that are not significant when the optical field is tuned near an atomic resonance. Let's consider the light-matter Hamiltonian of a two-level system with eigenstates $|1\rangle$ and $|2\rangle$ separated by ω_0 where for the moment we ignore the spatial variable,

$$\hat{H}_{\text{ED}} = \mathrm{i}e \int \mathrm{d}\omega g(\omega) \left[\hat{a}(\omega)\mathrm{e}^{-\mathrm{i}\omega t} + \hat{a}^\dagger(\omega)\mathrm{e}^{\mathrm{i}\omega t}\right] \boldsymbol{\epsilon} \cdot \mathbf{D}_{12} \left(\hat{\sigma}_{12}^\dagger \mathrm{e}^{\mathrm{i}\omega_0 t} + \hat{\sigma}_{12}\mathrm{e}^{-\mathrm{i}\omega_0 t}\right), \tag{5.17}$$

where $g(\omega)$ is the mode function capturing the spectrum of the electric field. The highly oscillatory terms, rotating at $\pm(\omega + \omega_0)$, are ignored as they average out over the time scales considered here. This approximation is known as the *rotating-wave approximation* in reference to its original context in nuclear magnetic resonance spectroscopy.[2] With the rotating-wave approximation, the Hamiltonian in equation 5.17 simplifies to

$$\hat{H}_{\text{ED}} = \mathrm{i}e \int \mathrm{d}\omega g(\omega) \left[\hat{a}(\omega)\hat{\sigma}_{12}^\dagger \mathrm{e}^{-\mathrm{i}(\omega-\omega_0)t} + \hat{a}^\dagger(\omega)\hat{\sigma}_{12}\mathrm{e}^{\mathrm{i}(\omega-\omega_0)t}\right] \boldsymbol{\epsilon} \cdot \mathbf{D}_{12}. \tag{5.18}$$

Physically, the terms we have discarded correspond to emission of a photon and creation of an atomic excitation or absorption of a photon and the annihilation of an atomic excitation. These terms are seemingly not energy conserving, but can be part of a more

[2] It is worth mentioning, as pointed out by Steck [198], that the rotating-wave approximation is equally valid as the approximation that we limit the atomic states under consideration to two or three; when one breaks down the other is likely to be violated as well.

complicated interaction that does conserve energy (e.g. Stokes scattering involves the creation of a Stokes photon and phonon, which conserves energy when considering the pump photon).

We have now assembled before us the basic tools for describing the Raman memory. Before we make use of this machinery, we will make a short, scenic detour to single-mode quantum optics in order to describe the time-dependent behaviour of the atomic populations and coherences. These equations will be useful for understanding the results in chapter 6.

5.1.2 Three-level-system equations

The Hamiltonian in equation 5.1 can be expressed in terms of single-mode atomic states for a Λ-level system with two classical electric fields[3] – the signal and control field with frequencies ω_s and ω_c, respectively and amplitude E_0. The expression for the Hamiltonian is

$$\hat{\mathcal{H}} = \hbar\omega_2\hat{\sigma}_{22} + \hbar\omega_3\hat{\sigma}_{33} + \frac{\hbar\Omega_{12}}{2}\left(\hat{\sigma}_{12}\mathrm{e}^{\mathrm{i}\omega_\mathrm{s}t} + \hat{\sigma}_{12}^\dagger\mathrm{e}^{-\mathrm{i}\omega_\mathrm{s}t}\right) + \frac{\hbar\Omega_{23}}{2}\left(\hat{\sigma}_{23}\mathrm{e}^{\mathrm{i}\omega_\mathrm{c}t} + \hat{\sigma}_{23}^\dagger\mathrm{e}^{-\mathrm{i}\omega_\mathrm{c}t}\right), \quad (5.19)$$

where $\Omega_{ij} = \langle i|\boldsymbol{\epsilon}\cdot\mathbf{D}|j\rangle E_0/\hbar$ is the coupling rate between states i and j (the *Rabi frequency*), and the energy level of the energy eigenstate 1 is taken to be zero. This can be neatly expressed in matrix form,

$$\hat{\mathcal{H}} = \begin{pmatrix} 0 & \frac{\hbar\Omega_{12}}{2}\mathrm{e}^{\mathrm{i}\omega_\mathrm{s}t} & 0 \\ \frac{\hbar\Omega_{12}}{2}\mathrm{e}^{-\mathrm{i}\omega_\mathrm{s}t} & \hbar\omega_2 & \frac{\hbar\Omega_{23}}{2}\mathrm{e}^{-\mathrm{i}\omega_\mathrm{c}t} \\ 0 & \frac{\hbar\Omega_{23}}{2}\mathrm{e}^{\mathrm{i}\omega_\mathrm{c}t} & \hbar\omega_3 \end{pmatrix}. \quad (5.20)$$

The equation of motion of the atomic state ρ can be derived using the master equation,

$$\frac{\partial\hat{\rho}}{\partial t} = -\frac{\mathrm{i}}{\hbar}\left[\hat{\mathcal{H}},\hat{\rho}\right] + \Gamma_{12}\hat{\mathcal{D}}[\hat{\sigma_{12}}]\hat{\rho} + \Gamma_{23}\hat{\mathcal{D}}[\hat{\sigma_{23}}]\hat{\rho}, \quad (5.21)$$

[3] Even in the case the light field is quantized it can be neglected when considering the evolution of the atomic population and coherences as the optical mode operators commute with the atomic and electric dipole operators.

where Γ_{ij} is the spontaneous decay rate from the excited state $|2\rangle$ to ground states $|1\rangle$ and $|3\rangle$, and $\hat{\mathcal{D}}$ is the Lindblad (super)operator [198] (I can think of no greater honour than *becoming* a super-operator),

$$\hat{\mathcal{D}}[\hat{c}]\hat{\rho} = \hat{c}\hat{\rho}\hat{c}^{\dagger} - \frac{1}{2}\left\{\hat{c}^{\dagger}\hat{c}, \hat{\rho}\right\}. \tag{5.22}$$

The anti-commutator term in equation 5.22 can be absorbed into an effective Hamiltonian, except for the term on the left, which represents the transfer of population from the excited state to the ground states, which is needed to preserve the trace of the density matrix. The above equations can be derived by considering the Markovian, non-unitary evolution of a system in contact with an external environment [199]. We have neglected any additional dephasing of the coherence in excess of that caused by the spontaneous decay (i.e. $\gamma_c = \Gamma/2$, where γ_c is the decoherence rate).

The solution is simplified if we adopt the rotating frame with respect to the atomic coherences as follows

$$\rho_{12} = \tilde{\rho}_{12}\mathrm{e}^{\mathrm{i}\omega_{\mathrm{s}}t}, \tag{5.23}$$

$$\rho_{32} = \tilde{\rho}_{32}\mathrm{e}^{\mathrm{i}\omega_{\mathrm{c}}t}, \tag{5.24}$$

$$\rho_{13} = \tilde{\rho}_{13}\mathrm{e}^{\mathrm{i}(\omega_{\mathrm{s}}-\omega_{\mathrm{c}})t}. \tag{5.25}$$

By substituting equations 5.23, 5.24, and 5.25 into equation 5.21, we can solve for the atomic populations,

$$\partial_t\rho_{11} = \frac{\mathrm{i}\Omega_{12}}{2}\left(\tilde{\rho}_{12} - \tilde{\rho}_{21}\right) + \Gamma_{12}\rho_{22}, \tag{5.26}$$

$$\partial_t\rho_{22} = \frac{\mathrm{i}\Omega_{12}}{2}\left(\tilde{\rho}_{21} - \tilde{\rho}_{12}\right) + \frac{\mathrm{i}\Omega_{23}}{2}\left(\tilde{\rho}_{23} - \tilde{\rho}_{32}\right) - \Gamma\rho_{22}, \tag{5.27}$$

$$\partial_t\rho_{33} = \frac{\mathrm{i}\Omega_{23}}{2}\left(\tilde{\rho}_{32} - \tilde{\rho}_{23}\right) + \Gamma_{23}\rho_{22}, \tag{5.28}$$

where Γ_{12}/Γ and Γ_{23}/Γ are the branching ratios into the two ground-states, and $\Gamma = \Gamma_{12} + \Gamma_{23}$ is the total spontaneous decay rate. Note that we have not included any decay between the storage state and the ground state (as they are dipole-decoupled).

The rates of change of the atomic coherences are given by

$$\partial_t \tilde{\rho}_{21} = -\left(\frac{\Gamma}{2} - \mathrm{i}\Delta_\mathrm{s}\right)\tilde{\rho}_{21} + \frac{\mathrm{i}\Omega_{12}}{2}\left(\rho_{22} - \rho_{11}\right) - \frac{\mathrm{i}\Omega_{23}}{2}\tilde{\rho}_{31}, \tag{5.29}$$

$$\partial_t \tilde{\rho}_{23} = -\left(\frac{\Gamma}{2} - \mathrm{i}\Delta_\mathrm{c}\right)\tilde{\rho}_{23} + \frac{\mathrm{i}\Omega_{23}}{2}\left(\rho_{22} - \rho_{33}\right) - \frac{\mathrm{i}\Omega_{12}}{2}\tilde{\rho}_{12}, \tag{5.30}$$

$$\partial_t \tilde{\rho}_{31} = -\left(\mathrm{i}\left[\Delta_\mathrm{s} - \Delta_\mathrm{c}\right]\right)\tilde{\rho}_{31} - \frac{\mathrm{i}\Omega_{12}}{2}\tilde{\rho}_{32} + \frac{\mathrm{i}\Omega_{23}}{2}\tilde{\rho}_{21}, \tag{5.31}$$

where Δ_s and Δ_c are the detuning of the signal and control from the atomic transitions $1 \rightarrow 2$ and $3 \rightarrow 2$ respectively. Equations 5.26 to 5.31 are the three-level analogue to the optical Bloch equations. Strictly only five equations are needed as the normalization condition $\rho_{11} + \rho_{22} + \rho_{33} = 1$ acts as an additional constraint on the populations.

5.2 Raman memory interaction

5.2.1 Optical fields

The relevant optical fields for the Raman interaction are the control field and the signal field, as shown in figure 5.1. The anti-Stokes field arising from spontaneous four-wave mixing, which is a noise source for the memory, will be neglected for now, but we will return to this in chapter 7. The control field is comprised of many photons and will be described as the classical field

$$\mathbf{E}_\mathrm{c}(z,t) = \boldsymbol{\epsilon}_\mathrm{c} E_\mathrm{c}\left(t - z/c\right)\cos\left[\omega_\mathrm{c}(t - z/c)\right], \tag{5.32}$$

where $E_\mathrm{c}\left(t - z/c\right)$ is the amplitude of the electric field at retarded time $\tau = t - z/c$, ω_c is the optical frequency, and $\boldsymbol{\epsilon}_\mathrm{c}$ is the (linear) polarization vector.

The signal field is generally weak (ideally a single photon) and takes the form of equation 5.7 from section 5.1. The annihilation and creation operators obey the commutator relation from equation 5.4.

5.2.2 Hamiltonian for multi-mode light-matter interaction

We can now write down the Hamiltonian from equation 5.1 with the optical modes from section 5.2.1 using the dipole and rotating-wave approximation derived in section 5.1 [58],

$$\hat{\mathcal{H}} = \hat{H}_{\mathrm{R}} + \sum_{i=1}^{N_{\mathrm{A}}} \left(\hbar\omega_1 \hat{\sigma}_{11}^i + \hbar\omega_3 \hat{\sigma}_{33}^i - \Omega(\tau_i)\hbar\hat{\sigma}_{32}^i \mathrm{e}^{-\omega_{\mathrm{c}}\tau_i} + \mathrm{i}\hbar g\hat{\mathcal{E}}\mathrm{e}^{-\omega_{\mathrm{s}}\tau_i} + \mathrm{H.c.} \right), \tag{5.33}$$

where $\tau_i = (t - z_i/c)$, $g = \langle 2|\hat{\mathbf{D}}\cdot\hat{\boldsymbol{\epsilon}}_{\mathrm{s}}|1\rangle\sqrt{\omega_{\mathrm{s}}/4\pi\hbar\varepsilon_0 cA}$ is the coupling of the ground state to the excited state via the signal field, and $\Omega(t - z/c) = \langle 2|\hat{\mathbf{D}}\cdot\hat{\boldsymbol{\epsilon}}_{\mathrm{c}}|1\rangle E_{\mathrm{c}}(t - z/c)/2\hbar$ is the coupling of the storage and excited state driven by the control field.

5.2.3 Continuous atomic operators

Instead of summing the atoms over the index i, it is helpful to define continuous atomic operators that varying slowly over the ensemble compared to the density of atoms in the ensemble and the optical wavelength. We define these as [58]

$$\hat{\sigma}_{ii}(z,t) = \frac{1}{N_{\mathrm{A}}}\sum_{j=1}^{N_{\mathrm{A}}^z}\hat{\sigma}_{ii}^j(t), \tag{5.34}$$

$$\hat{\sigma}_{12}(z,t) = \frac{1}{N_{\mathrm{A}}}\sum_{j=1}^{N_{\mathrm{A}}^z}\hat{\sigma}_{12}^j(t)\mathrm{e}^{-\mathrm{i}\omega_{\mathrm{s}}(t-z/c)}, \tag{5.35}$$

$$\hat{\sigma}_{32}(z,t) = \frac{1}{N_{\mathrm{A}}}\sum_{j=1}^{N_{\mathrm{A}}^z}\hat{\sigma}_{32}^j(t)\mathrm{e}^{-\mathrm{i}\omega_{\mathrm{s}}(t-z/c)}, \tag{5.36}$$

$$\hat{\sigma}_{13}(z,t) = \frac{1}{N_{\mathrm{A}}}\sum_{j=1}^{N_{\mathrm{A}}^z}\hat{\sigma}_{13}^j(t)\mathrm{e}^{-\mathrm{i}[\omega_{\mathrm{s}}-\omega_{\mathrm{c}}(t-z/c)]}, \tag{5.37}$$

where $N_{\mathrm{A}}^z \gg 1$ is the number of atoms at position z. Using the continuous atomic operators we can re-express the total Hamiltonian in equation 5.33 as

$$\hat{\mathcal{H}} = \hat{H}_{\mathrm{R}} + \hbar\Delta\hat{\sigma}_{\mathrm{ee}} - \left[\hbar\Omega(t - z/c)\hat{\sigma}_{32}(z,t) + \hbar g\hat{\mathcal{E}}(z,t)\hat{\sigma}_{12}(z,t) + \mathrm{H.c.}\right], \tag{5.38}$$

where Δ is the detuning of the control field from the excited state.

We can now determine the equation of motion from the Heisenberg equation describing the time evolution of the operator with the Hamiltonian. Before we do so, we first consider

how to describe the propagation of the signal field through the atomic ensemble.

5.2.4 Propagation of the signal field

The propagation of the optical signal field is dictated by the wave equation

$$\left[\nabla^2 - \frac{1}{c^2}\partial_{\mathrm{t}}^2\right]\hat{\mathbf{E}}_{\mathrm{s}} = \mu_0\partial_{\mathrm{t}}^2\hat{\mathbf{P}}_{\mathrm{s}}, \tag{5.39}$$

where $\hat{\mathbf{P}}_{\mathrm{s}}$ is the atomic polarization. The expression for the signal field can be simplified by adopting the *slowly varying envelope approximation* where the frequency spectrum of the pulse envelope is small compared to the optical frequency ω_{s}, which gives

$$\hat{\mathbf{E}}_{\mathrm{s}} = \mathrm{i}\boldsymbol{\epsilon}_{\mathrm{s}}\nu\hat{\mathcal{E}}\mathrm{e}^{\mathrm{i}\omega_{\mathrm{s}}(t-z/c)}, \tag{5.40}$$

where $\nu = \sqrt{2}\hbar\omega_{\mathrm{s}}/4\sqrt{\pi}\varepsilon_0 cA$ and $\hat{\mathcal{E}}$ is the slowly varying annihilation operator. The atomic polarization can be written as $\hat{\mathbf{P}}_{\mathrm{s}} = \hat{\mathbf{P}}'_{\mathrm{s}}\exp\left[\mathrm{i}\omega_{\mathrm{s}}(t-z/c)\right]$. Substituting equation 5.40 into the wave equation, equation 5.39, gives

$$\left[\nabla_{\mathrm{T}}^2 + \partial_z^2 - \frac{1}{c^2}\partial_t^2\right]\hat{\mathcal{E}}\mathrm{e}^{[\mathrm{i}\omega_{\mathrm{s}}(t-z/c)]} = -\frac{\mathrm{i}\mu_0}{\nu_{\mathrm{s}}}\boldsymbol{\epsilon}^*\cdot\hat{\mathbf{P}}'_{\mathrm{s}}\mathrm{e}^{[\mathrm{i}\omega_{\mathrm{s}}(t-z/c)]}, \tag{5.41}$$

where $\nabla_{\mathrm{T}}^2 = (\partial_x^2 + \partial_y^2)$ is the transverse Laplacian, which we later ignore as we are considering only one-dimensional propagation.

In order to simplify the above equation, we adopt the *paraxial approximation* to the wave equation, which is the limit where

$$\partial_t^2 \ll \omega_{\mathrm{s}}\partial_t, \tag{5.42}$$

$$\partial_z^2 \ll k_{\mathrm{s}}\partial_z. \tag{5.43}$$

Physically this corresponds to waves that are weakly divergent and approximately planar. Applying equations 5.42 and 5.43 to equation 5.41 yields

$$\left[\partial_z + \frac{1}{c}\partial_t\right]\hat{\mathcal{E}} = -\frac{\mu_0\omega_{\mathrm{s}}^2}{2\nu_{\mathrm{s}}k_{\mathrm{s}}}\boldsymbol{\epsilon}_{\mathrm{s}}^*\cdot\hat{\mathbf{P}}'_{\mathrm{s}}. \tag{5.44}$$

5.2.5 Equations of motion for the Raman memory

The collective polarization operator $\hat{P}(z,t) = \sqrt{N_\mathrm{A}}\hat{\sigma}_{12}(z,t)$ is defined as proportional to the coherence between the ground state and the excited state. We assume that all the population is initially in the ground state $\langle\hat{\sigma}_{11}\rangle = 1$, $\langle\hat{\sigma}_{22}\rangle = \langle\hat{\sigma}_{33}\rangle = 0$, and the atomic coherences are initially zero. The spin-wave operator $\hat{S}$ is likewise defined as the coherence of the collective atomic operator such that $\hat{S}(z,t) = \sqrt{N_\mathrm{A}}\hat{\sigma}_{13}(z,t)$

The equations of motion can be determined from the paraxial wave equation (equation 5.41) and the Heisenberg equations of motion of the collective polarization operator and the spin-wave operator with the Hamiltonian in equation 5.38 [58]

$$\left[\partial_z + \frac{1}{c}\partial_t\right]\mathcal{E} = g\sqrt{N_\mathrm{A}}P, \tag{5.45}$$

$$\partial_t P = -(\gamma + \mathrm{i}\Delta)P + g\sqrt{N_\mathrm{A}}\mathcal{E} + \mathrm{i}\Omega S, \tag{5.46}$$

$$\partial_t S = \mathrm{i}\Omega^* P. \tag{5.47}$$

We have neglected the Langevin noise operators on the polarization and spin-wave as they are initially in a vacuum state and the normally ordered expectation values evaluate to zero. By ignoring these terms, we can treat the operators as complex numbers and have dropped the circumflex from the symbols [58]. We have also ignored the decoherence of the spin-wave here; it can be added in later 'by hand'.

In the adiabatic limit, where the detuning from the excited state is much greater than the coupling rate or bandwidth of the pulses, the excited state is not populated. In this case, the excited state can be adiabatically eliminated as $\partial_t\hat{P} = 0$. Therefore, equations 5.45, 5.46, and 5.47 can be rewritten as [51]

$$\left[\partial_z + \frac{d}{\Gamma_\mathrm{t}}\right]\mathcal{E} = \mathrm{i}\sqrt{d}\frac{\Omega(\tau)}{\Gamma_\mathrm{t}}S, \tag{5.48}$$

$$\left[\partial_\tau + \frac{|\Omega|^2}{\Gamma_\mathrm{t}}\right]S = -\mathrm{i}\sqrt{d}\frac{\Omega^*(\tau)}{\Gamma_\mathrm{t}}\mathcal{E}, \tag{5.49}$$

where $\tau = t - z/c$, $\Gamma_\mathrm{t} = \gamma + \mathrm{i}\Delta$ is the complex detuning, and $d = g^2 N_\mathrm{A}/(\gamma c)$ is the optical depth, which in experimental terms is the absorption of the signal field on resonance, parameterizing the strength of the coupling between the signal field and the atomic en-

semble. The second term in the brackets of equation 5.49 is the Stark shift caused by the control field, which causes some mode reshaping of the retrieved signal compared to the input signal [51].

5.2.6 Raman storage and retrieval

The equations describing the memory interaction are linear and can be uniquely solved by their impulse response functions, which are known as the Green's functions [51]. The memory efficiency is given by the Green's function $K(z,\tau)$ describing the light-matter interaction in the linear limit where the pump field is not depleted. In the adiabatic, one-dimensional limit the Raman kernel is $K(z,\omega) = CJ_0(2C\sqrt{\omega z})$ [71]. The z coordinate denotes the propagation direction (normalized so that z runs from 0 to 1) and $\omega(\tau) = \frac{1}{h}\int_{-\infty}^{\tau} |\Omega(\tau')|^2 \,\mathrm{d}\tau'$ is time under coordinate transformation, where $h = \int_{-\infty}^{\infty} |\Omega(\tau)|^2 \,\mathrm{d}\tau$. The Raman coupling constant C defines the strength of the interaction and is given by $C = \sqrt{d\Gamma h}/\Delta$, where Γ is the homogeneous linewidth of the excited-state transition. The stored spin coherence $S(z)$ for an input signal field $\mathcal{E}_{\mathrm{in}}(\tau)$ is given by [73]

$$S(z) = \int_{-\infty}^{\infty} K[z, 1-\omega(\tau)]\mathcal{E}_{\mathrm{in}}(\tau)\zeta(\tau)\mathrm{d}\tau. \tag{5.50}$$

The memory efficiency η for the stored spin coherence mode $S(z)$ is then given by [73]

$$\eta = \int_{-\infty}^{\infty} \left| \int_0^1 K(1-z, \omega(\tau))\zeta^*(\tau)S(z)\mathrm{d}z \right|^2 \mathrm{d}\tau, \tag{5.51}$$

where $\zeta(\tau) = C \cdot \Omega(\tau) \exp\left(\mathrm{i}RC\omega\right)/\sqrt{h}$, and $R = \sqrt{h/d\Gamma}$.

5.2.7 Raman coupling

As derived above, the Raman interaction is parametrized by the Raman coupling constant C, which can be re-written as [51]

$$C^2 \approx d \cdot \left(\frac{\Gamma}{\delta_{\mathrm{s}}}\right) \cdot \left(\frac{\Omega}{\Delta}\right)^2, \tag{5.52}$$

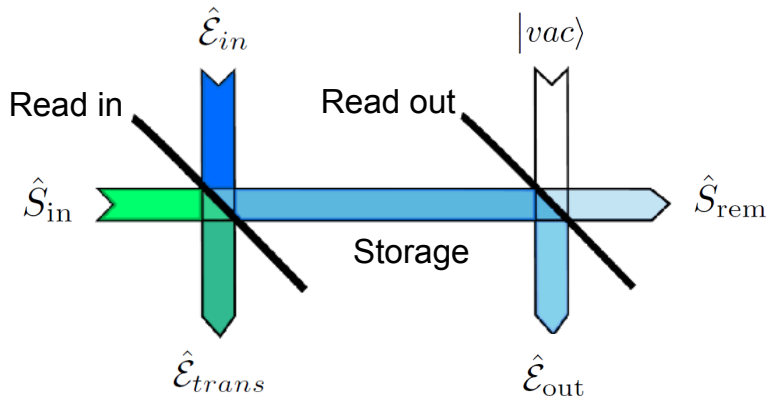

Figure 5.2: The Raman interaction as a beams splitter between optical and atomic modes. The reflectivity of the beam splitter is determined by the Raman coupling. Ideally the initial spin-wave $\hat{S}_{\rm in}$ is vacuum, as is the remaining spin-wave $\hat{S}_{\rm rem}$ when the interaction has concluded.

where Γ is the homogeneous linewidth of the excited state (not the Raman linewidth) and $\delta_{\rm s}$ is the bandwidth of the signal pulse. In the limit of small coupling, the memory efficiency scales as C^4. For efficient light-matter interaction, the Raman coupling constant should be on the order of unity. For values much larger than one, the memory can store multiple temporal modes of the signal; the multimode capacity of the memory scales with the square root of the optical depth [200]. The reason the scaling is so poor is that the spin wave is distributed near the front of the ensemble, so adding more atoms has only a marginal benefit towards increasing the mode capacity; it is more efficient to store light in multiple spatial modes.

We now motivate the magnitude of the optical depth required for efficient memory operation by considering the dimensionless Raman coupling term where $h \approx (\Omega^2/\delta_{\rm s})$. Adiabaticity requires that $\Delta \gg \Omega$ and, in our experiments, $\Gamma/\delta = (1/300)$, which implies that the optical depth must be several thousand for $C^2 > 1$, as required for efficient memory operation. The optical depth is the key parameter that determines the memory efficiency: the control power cannot be increased indefinitely as it is constrained to have a Rabi frequency less than the detuning in the adiabatic regime. Also, the signal bandwidth is generally fixed and so is the excited-state linewidth by the choice of the atomic transition.

5.2.8 Raman interaction as a beam splitter

An attractive feature of the Raman interaction is that, because it is far off resonance, any remaining signal field not absorbed into the memory is transmitted through the ensemble. In principle, this could be used to herald the failure of the memory storage process (provided the loss between the memory and detector were low). And at its most basic level, the action of the memory can be thought of as a beam splitter that combines optical and atomic modes, as illustrated in figure 5.2. A beam splitter is a key component for linear-optics quantum computing and we will now motivate the equivalence.

We can express equations 5.48 and 5.49 using the transformed variables for the electric field amplitude $\mathfrak{E}(z,\omega)$ and spin-wave $\mathcal{S}(z,\omega)$ [51],

$$\mathcal{E}(z,\tau) = \frac{\Omega(\tau)}{\sqrt{h}}\mathfrak{E}(z,\omega)\mathrm{e}^{-(h\omega+dz)/\Gamma}, \tag{5.53}$$

$$S(z,\tau) = \mathcal{S}(z,\omega)\mathrm{e}^{-(h\omega+dz)/\Gamma}, \tag{5.54}$$

which results in the following set of coupled equations,

$$\partial_z\mathfrak{E}(z,\omega) = \mathrm{i}C\mathcal{S}(z,\omega), \tag{5.55}$$

$$\partial_\omega\mathcal{S}(z,\omega) = -\mathrm{i}C\mathfrak{E}(z,\omega). \tag{5.56}$$

These equations have a similar form to the Heisenberg equations of motion for a beam splitter, the slight difference being the partial derivatives are for different coordinates. This, however, reflects the fact that one of the modes is stationary and the other propagating. These equation are unitary when the exponents in equations 5.53 and 5.54 are imaginary, which is the case in the adiabatic regime where $\Gamma_\mathrm{t} \approx \mathrm{i}\Delta$. A more detailed derivation is given in reference [51], where it is shown that the Green's functions of the transmitted and stored modes can be expressed by a single set of eigenfunctions where the square for the respective eigenvalues equals one. This is enforced by the unitarity of equations 5.55 and 5.56, which is known as the Bloch-Messiah reduction [201]. We stress again these results are only valid in the adiabatic regime in which the Raman memory operates.

5.2.9 Summary of theoretical derivation

We pause now in order to summarize the development of the Raman theory as presented in the preceding sections.

1. The Hamiltonian $\hat{\mathcal{H}}$ that determines the system evolution consists of a free radiation component $\hat{H}_{\mathrm{R}}$, a bare atomic component $\hat{H}_{\mathrm{A}}$ and an electric dipole component $\hat{H}_{\mathrm{ED}}$ that couples radiation to atomic states.

2. The electric dipole operator couples states with opposite parity, and consists of terms $\hat{a}^{\dagger}\hat{\sigma} + \hat{a}\hat{\sigma}^{\dagger}$ near resonance (the rotating-wave approximation).

3. The three-level-system equations derived from the master equation in the rotating frame describe the time-dependent behaviour of the atomic population and coherences, which can be simplified depending on the initial conditions.

4. The equations of motion of the memory interaction can be derived in a simple form from the Hamiltonian by defining continuous atomic operators that vary slowly over the length of the ensemble. The propagation of the electric field is described by the wave equation in the paraxial limit, linking the optical fields to the atomic polarization of the excited state. The equations of motion can be further simplified by taking the adiabatic limit where the excited state is not populated.

5. The solution to the equations of motion can be represented by a Green's function, which allows for the spin-wave and memory efficiency to be easily evaluated. The strength of the memory interaction is determined by the dimensionless Raman coupling constant $C^2 \approx d \cdot (\Gamma/\delta_{\mathrm{s}}) \cdot (\Omega/\Delta)^2$, which should be of order unity for efficient operation of the memory.

6. In the adiabatic limit, the interaction between the signal field and the spin-wave can be described via a set of beam splitter relations between light and matter.

5.3 Summary of past memory results

Previously our group demonstrated the first Raman memory using a warm vapour of cesium atoms. The storage and ground states were the hyperfine ground-state levels

$6^2S_{1/2}(F = 3)$ and $6^2S_{1/2}(F = 4)$, respectively. The excited state was the D_2 manifold ($6^2S_{3/2}(F')$) and the Raman resonance was detuned from the excited-state resonance by $\Delta = 15$ to 18 GHz. The signal and control were generated from a mode-locked titanium-sapphire laser specially modified to produce pulses with a bandwidth of 1 to 1.5 GHz (see section 5.4 for more details on the oscillator). The high bandwidth of our memory compared to other approaches (as discussed in chapter 2) along with the reasonably long storage time is the main novelty of this memory.

The main results of the research programme to date include the storage of bright, high-photon-number classical pulses using a Raman memory (section 5.3.1), followed by storage of single-photon-level pulses (section 5.3.2), and the storage of polarization states again using bright coherent states (section 5.3.3). The experimental work was carried out by PhD student Klaus Reim with theory developed by Josh Nunn. The polarization tomography was demonstrated by PhD students Duncan England, Patrick Michelberger, and Tessa Champion. My particular contributions to this research programme – aside from the hollow-core fibre memory presented in chapters 6 and 7 – are summarized in sections 5.4 and 5.5.

We will now review the salient results of their work, but leave a deeper exposition of the experimental techniques to chapters 6 and 7, where they will presented in relation to my work storing light in a hollow-core fibre.

5.3.1 Storage of bright coherent pulse

The Raman memory was shown to be able to store bright coherent light pulses consisting of 10^5 photons with an efficiency of 30% [72]. The total efficiency was limited by the available energy of the control pulse (10 nJ) and reabsorption of the signal field. The residual spin-wave coherence could be retrieved with additional control pulses in later time bins [202]. The lifetime of the memory was 1.5 μs, a limitation that was ascribed to a residual magnetic field that caused dephasing of the Zeeman sub-levels [72]. However, diffusion of the atoms out of the optical beam (in the presence of a buffer gas) was also significant at this time scale and a careful study of the relative influence of these two effects has yet to be performed.

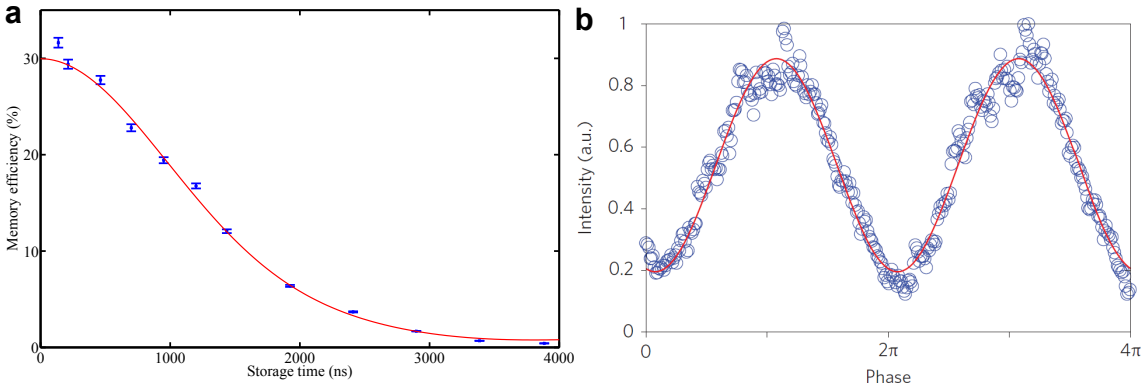

Figure 5.3: **a** Raman memory efficiency as function of the storage time [72]. The signal pulse consisted of 10^5 photons. **b** Interference of a retrieved pulse with an input pulse [73]. The interference visibility was 83%.

The coherence of the Raman memory was verified by measuring the interference of the stored pulse with the input pulse using a Mach-Zehnder interferometer [73]. The interference visibility was $82.7\% \pm 0.9\%$ (corrected for imperfect alignment and interferometer instability, see [73]). This is in excellent agreement with the prediction of the maximum visibility from the Raman theory (83%), which predicts a reshaping of the pulse from the dynamic Stark shift induced by the control field.

5.3.2 Storage of single-photon-level coherent pulse

A weak signal pulse with on average 1.6 photons/pulse was then stored and the unconditional noise floor was measured, as shown in figure 5.4. The noise floor was 0.25 photons/pulse and the signal-to-noise ratio was approximately 1:1 (and 0.625:1 if normalized to an input pulse of exactly 1 photons/pulse rather than 1.6 photons/pulse). The source of the noise is believed to be spontaneous four-wave mixing, which will be discussed in more detail in chapter 7. Part of the noise was caused by anti-Stokes photons from spontaneous Raman scattering, which could be filtered out with a sensibly designed etalon (see section 5.5). These measurements show that the system has the potential for storing heralded single photons provided that the signal-to-noise ratio can be increased substantially.

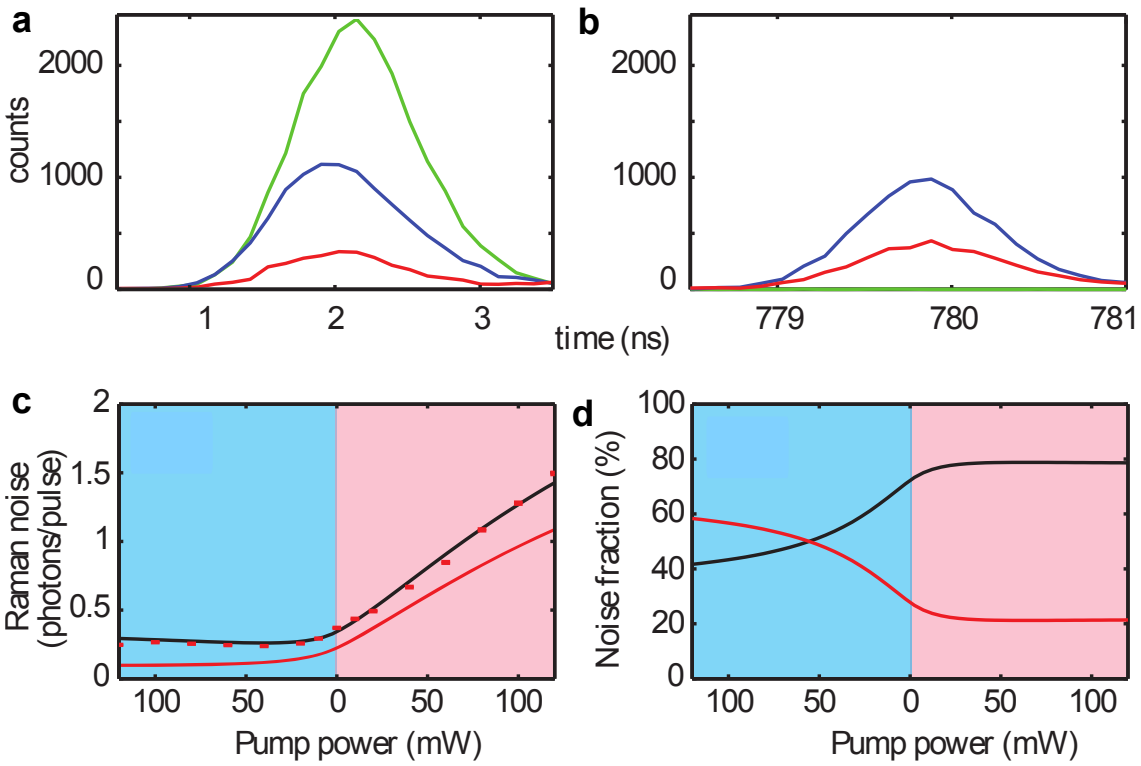

Figure 5.4: From reference [72] **a** Memory storage: The green line shows the input signal field with no control field, the blue line shows the signal field absorbed when the control field was present and the red line shows the noise when no signal was present, but the control pulses were present. **b** Memory retrieval: the blue line shows the retrieved signal when the control field was applied, and the red line show the noise output when no signal was stored in the memory. **c**, **d** The noise level and noise fraction as a function of the optical pumping power on the $|3\rangle \leftrightarrow |2\rangle$ transition (blue) and $|1\rangle \leftrightarrow |2\rangle$ (pink).

5.3.3 Storage of a polarization state

Storing information in the polarization degrees of freedom is particularly useful as it can be sent in a single spatial and temporal mode, and can be easily manipulated with wave plates. The Raman memory requires that the signal and control have orthogonal polarizations as a practical matter (and also related to the selection rules for the Raman interaction [51]). Therefore, storing an arbitrary polarization required storing two orthogonal polarization modes in two spatial modes of the ensemble within a phase-stable interferometer.

A polarization state was stored and the fidelity was compared to the transmitted light with no storage, as is shown in figure 5.5 [203]. The fidelity of the two states was $85 \pm 4\%$, indicating that the polarization information was faithfully retained by the memory. The transmitted modes were also found to be unaffected by the storage process. I should

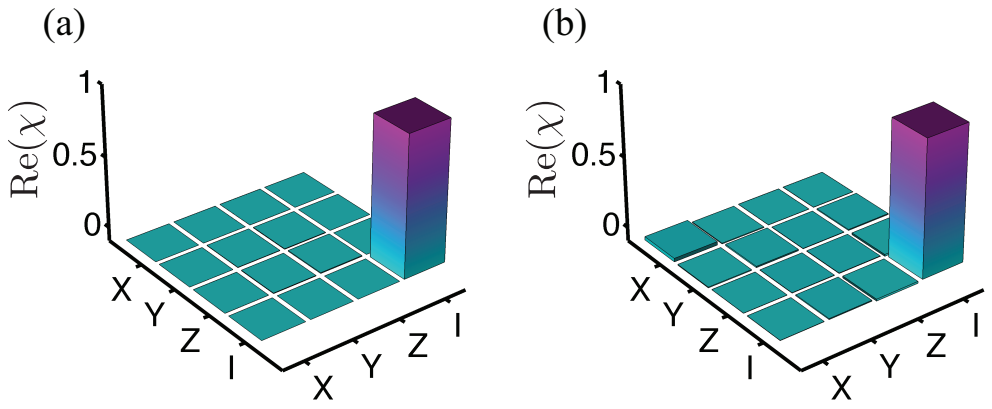

Figure 5.5: The process matrix characterizing the polarization state storage, from reference [203]. (a) The process matrix for the signal field transmitted through the interferometer (no storage). (b) Process matrix for the Raman memory storage. The fidelity of the process matrices was 85 ± 4%.

stress that the signal pulses were bright coherent states consisting of 10^3 to 10^4 photons.

5.3.4 Current research goals

The current research programme for the Raman memory proceeds along two tracks. One goal is the storage of a heralded single-photon Fock state. Heralded single photons are generated via spontaneous parametric down-conversion in a periodically-poled potassium titanyl phosphate waveguide. Spectral filtering of the heralded photon is used to set the bandwidth of the signal photon. This work is being led by Patrick Michelberger and Tessa Champion.

The second goal is to demonstrate a Raman memory in an integrated waveguide structure, specifically a kagome-structured hollow-core photonic-crystal fibre loaded with cesium atoms at room temperature. I present in chapters 6 and 7 the work I have undertaken to achieve this goal. Before doing so, I first review my work building a frequency-offset lock for the pulsed oscillator and a new set of solid-state etalons, which has broad applicability for both projects.

5.4 Frequency-offset lock for oscillator

5.4.1 Motivation

The Raman memory is far-detuned from the excited-state resonance. In the results summarized above, the excited-state detuning was 15 to 18 GHz. The laser frequency was measured with a scanning Fabry-Pérot interferometer (SFPI, Thorlabs SA210-8B). The laser was initially tuned into resonance with the $6^2S_{1/2}(F = 3)$ to $6^2P_{3/2}$ transition by monitoring the fluorescence of a cesium vapour cell. The laser frequency was then set to the desired detuning manually. The frequency was then manually adjusted to maintain the desired detuning by tuning the intra-cavity Gires-Tournois interferometer. An additional complication was that the scanning Fabry-Pérot interferometer cavity drifted due to fluctuations in the ambient conditions, requiring periodic referencing of the laser frequency to the cesium atomic transition. Taken together, these manual adjustments were tedious, introduced some degree of variability into the results, and limited long-duration measurements. This was especially an issue for the planned measurements with heralded single photons, where long data runs are required to obtain sufficient statistics on high-order cross-correlations. To address this problem, I designed and built a frequency-offset lock for the pulsed laser oscillator in the last two weeks of November 2011.

5.4.2 Operating principle

The drift of the laser frequency was typically slow, on the order of minutes to hours, which greatly simplified the technical requirements for the control system. I designed a control system that established a two-stage link between the frequency of an atomic transition – fixed and ever unchanging – to the centre frequency of the oscillator. First, the frequency of a diode laser, which was used for optical pumping, was locked to the bottom of the Doppler transition (see section 6.4.2). Second, the frequency of the pulsed oscillator was set relative to the frequency of the diode laser using the scanning Fabry-Pérot interferometer. The frequency difference between the diode laser and oscillator on the scanning Fabry-Pérot interferometer was the frequency offset modulo the free-spectral range of the SFPI.

I now consider how length fluctuations of the SFPI will affect the offset lock. Consider the diode laser locked at $f_{\text{fsr}} = c/4L$, where $L = 7.5$ mm is the length of the cavity. If the diode laser were locked at frequency f_0 then the frequency of the oscillator offset by Δf is $f_1 = f_0 + \Delta f$, where we will assume for the moment $\Delta f < f_{\text{fsr}}$. The offset frequency Δf is defined as a fraction h of the f_{fsr}, which gives

$$f_1(L) = f_0 + h\frac{c}{4L}. \tag{5.57}$$

The generalized uncertainty of the frequency of the offset lock is

$$\sigma_{f_1}^2 = \mathbf{J}\Sigma^{f_1}\mathbf{J}^{\intercal}, \tag{5.58}$$

where $\mathbf{J}$ is the Jacobian matrix and Σ^{f_1} is the variance-covariance matrix of f_1. When only considering fluctuations in length, equation 5.58 simplifies to

$$\sigma_{f_1} = \frac{\partial f_1}{\partial L}\sigma_L = -\frac{c}{4L^2}\sigma_L. \tag{5.59}$$

We can estimate the magnitude of the length fluctuations if we assume they arise from thermal fluctuations. The SFPI was made from Invar, with a low thermal expansion coefficient of $\alpha_T = 10^{-6}$ /K [204]. If we assume a very pessimistic fluctuation $\sigma_T = 5$ K, the length fluctuation becomes $\sigma_L = \alpha\sigma_T L$. Equation 5.59 can be evaluated and the fractional uncertainty of the frequency is on the order of $10^{-5} \times f_{\text{fsr}}$, which is much less than the bandwidth of the laser oscillator and can be safely ignored. Note that the general principle of using a high-stability reference cavity to lock a laser oscillator is used to stabilize ultra-narrow linewidth lasers. Reference cavities can be made compactly out of low-thermal-expansion materials without the confounding effects of a gain medium or other optical elements.

5.4.3 Experimental implementation

The centre frequency of the pulse oscillator was adjusted via the Gires-Tournois interferometer (GTI) inside the laser cavity. The GTI is an asymmetric Fabry-Pérot etalon

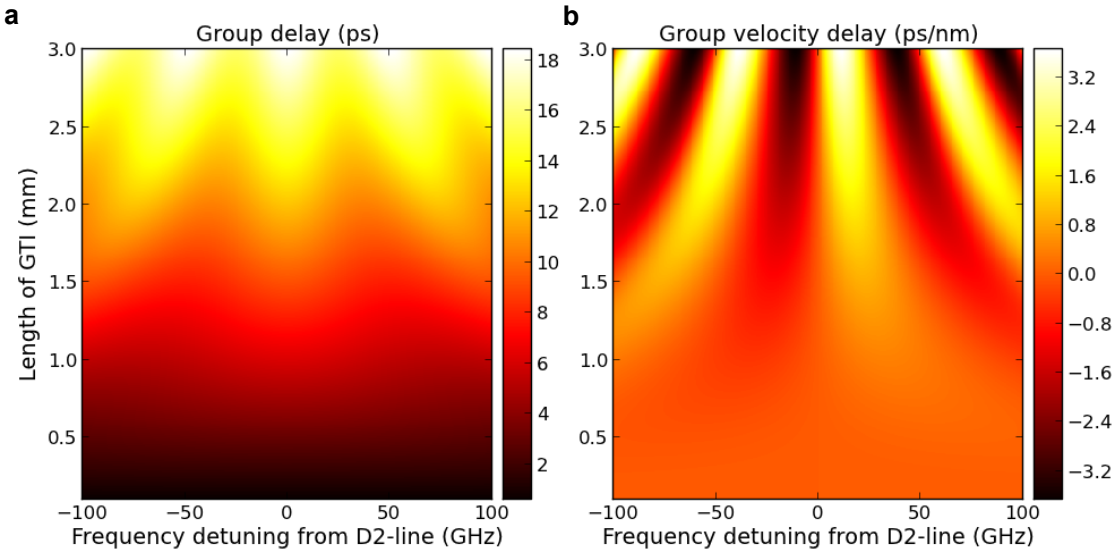

Figure 5.6: Group delay (**a**) and group velocity dispersion (**b**) of the GTI as a function of optical frequency and the length of the interferometer for reflectivity $R_1 = 0.04$.

where one mirror has very high reflectivity compared to the other. The group delay can be frequency dependent while the reflectivity is uniformly close to one. For a GTI with mirror reflectivity R_1 and length l (assuming $R_2 = 1$) the group delay τ is

$$\tau(f) = \frac{(1+R_1)}{(1-R_1)} \frac{t_\mathrm{r}}{\left\{1 + \left(\frac{4R_1}{(1-R_1)} \sin^2\left[\pi f t_\mathrm{r}\right)\right]\right\}}, \tag{5.60}$$

where $t_\mathrm{r} = 2l/c$ is the round trip time. The group velocity dispersion (GVD) is the change in the group delay with wavelength (or frequency). For mode-locked lasers, the overall GVD should be zero to keep the frequency components of the pulse in phase, avoiding temporal broadening (chirping) of the pulse. The optical components in the laser oscillator result in positive dispersion. In addition, the induced non-linear index of refraction causes a temporal chirp via self-phase modulation [205]. These effects needs to be compensated with negative GVD using a GTI. From the group delay in equation 5.60, the GVD $\Gamma_\mathrm{GVD}(l)$ can be expressed as

$$\Gamma_\mathrm{GVD}(l) = -\frac{\mathrm{d}\tau}{\mathrm{d}\lambda} = -\frac{\mathrm{d}\tau}{\mathrm{d}f}\frac{\mathrm{d}f}{\mathrm{d}\lambda} \tag{5.61}$$

$$= -\frac{(1+R_1)}{(1-R_1)^3} \frac{32\pi l^2 \cos(2\pi f l/c)\sin(2\pi f l/c)}{c^2\left[1 + \left(\frac{4R_1}{(1-R_1)}\right)\sin^2\left(2\pi f l/c\right)\right]^2}. \tag{5.62}$$

The GVD is proportional to the square of the length of the GTI (l^2), and is also modulated periodically with a spectral range inversely proportional to the length of the GTI. The depth of the modulation of the GVD depends on R_1, the reflectivity of the front mirror of the GTI. The dependence of the group delay and GVD on the frequency and length of the GTI is plotted in figure 5.6 for a fixed reflectivity $R_1 = 0.04$. The laser can mode lock in the region where the GVD is linear, which decreases according to l. By changing the GVD, the frequency of the laser can be adjusted. Changing the GVD can also change the pulse duration, although we did not find that this was significant over the mode-hop-free tuning range of our laser.

The GVD was changed by adjusting the input voltage to a piezoelectric driver that controlled the GTI mirror spacing. Normally this was altered manually via an external knob, but I bypassed the variable-resistance knob to directly control the input voltage. The range of the input voltage was zero to five volts, which was generated using a data acquisition card with I/O (National Instruments PCI-6602 with BNC-2110). The output of the SFPI (Thorlabs SA210-8B) was digitized using the same acquisition card. The input and output channels were controlled via a Labview interface shown in Appendix C. The logic for generating the error signal and implementing the feedback controller was written in a MATLAB module interfaced with the Labview program.

The error signal was generated from the SFPI by measuring the centre frequency of the pulsed oscillator relative to the diode laser. The linewidth of the laser diode was much less than the spectral resolution of the SFPI (<1 MHz vs 67 MHz) and appears like a narrow delta-function in the output of the SFPI, as shown in figure 5.7**a**. The oscillator pulse had a bandwidth of 1 GHz and the comb structure of the pulse can be resolved, showing the longitudinal cavity modes separated by 80 MHz. Finding the central peak of the pulse was complicated by the presence of these comb features, which fluctuated in intensity. I found that averaging the frequency of the four highest-intensity combs was a good compromise between simplicity and robustness. The frequency difference was multiplied by a proportional gain K_p and integrated in time proportional to an integral gain K_i for proportional-integral feedback, as described previously in a different context in section 4.4.5. The error signal was converted to a driving voltage for the pizeoelectric

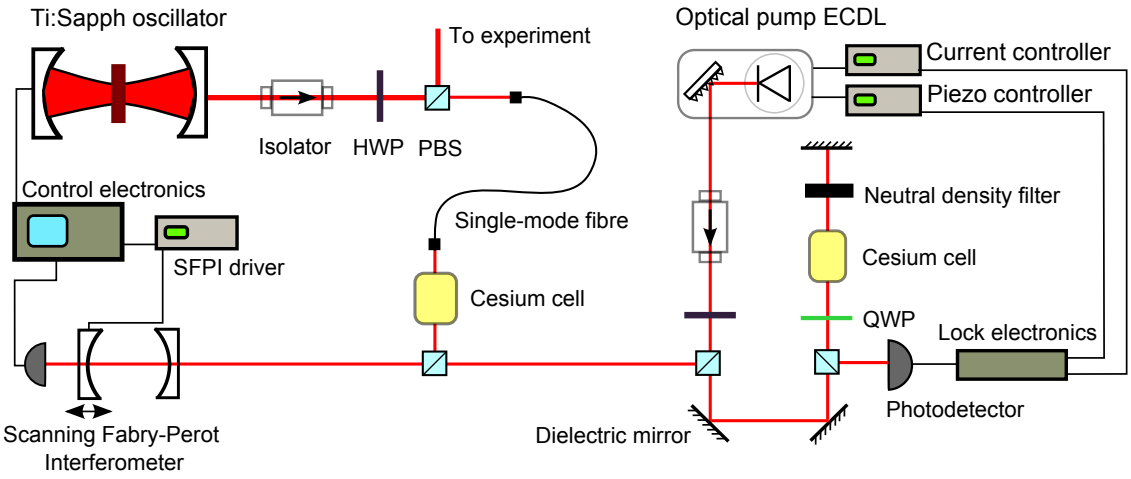

Figure 5.7: Frequency stability setup showing the mode-locked oscillator, the laser diode locked to the atomic transition, the SFPI, and the associated electronics.

actuator controlling the GTI spacing, closing the feedback loop.

The experimental setup, including the optical paths, is illustrated in figure 5.7. A small amount of light from the laser oscillator (<1 mW) was picked off with a PBS and coupled into a single-mode fibre.[4] Light from the oscillator and laser diode (locked to an atomic transition) was coupled into the SFPI.

The operating procedure is now briefly described. First, the GTI voltage was varied until fluorescence was detected from the cesium cell after the single-mode fibre. The correct atomic transition was selected by checking that the pulse oscillator was at the same frequency as the diode laser, which had been previously locked to the $6^2S_{1/2}(F = 3)$ to $6^2P_{3/2}$ transition.[5] The lock was then engaged with zero detuning. Setting the desired detuning changed the laser frequency. The control program kept track each time the pulsed laser exceeded the free spectral range of the SFPI. As a result, the pulsed laser could be locked over the mode-hop-free tuning range of the oscillator, which was approximately 50 GHz.

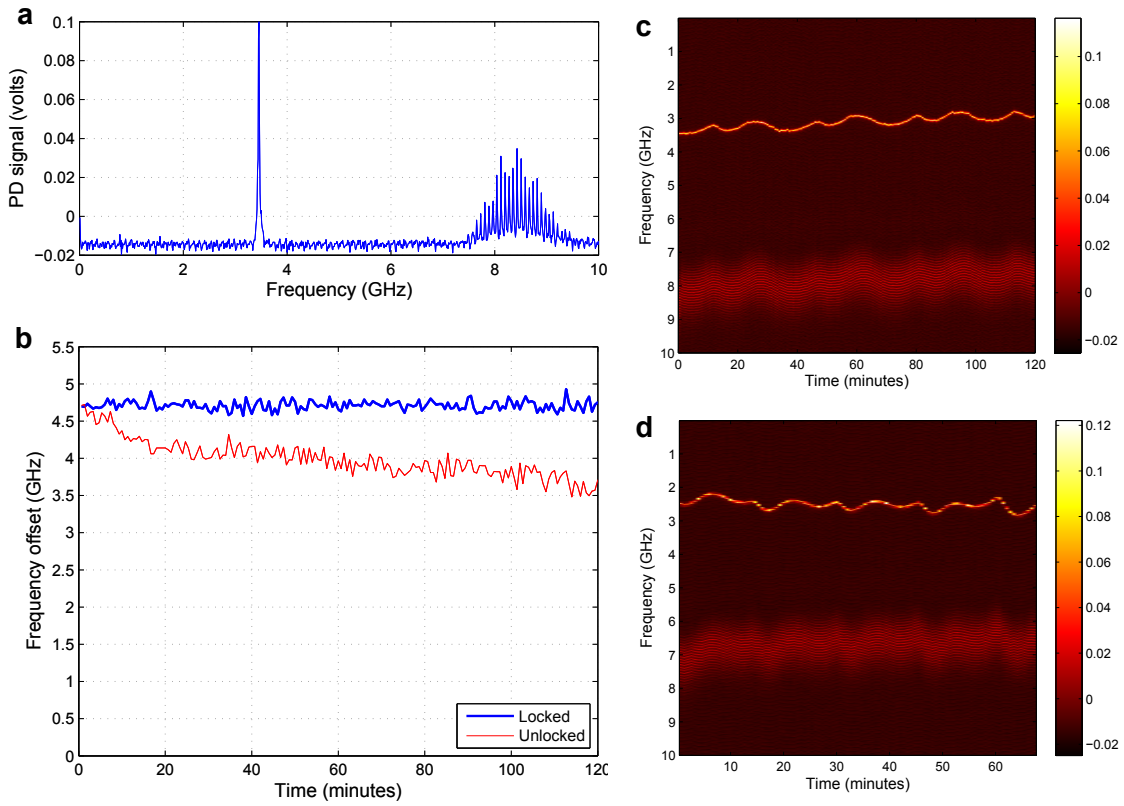

Figure 5.8: Frequency stability of the oscillator relative to the laser diode. a Output of the SFPI showing the pulse oscillator with its comb structure and the diode laser. **b**Frequency offset of the centre frequency of the pulsed oscillator relative to the diode laser when locked (blue line) and unlocked (red line). **c** SFPI output versus time when locked. **d** SFPI output versus time when unlocked. The oscillator behaviour is likely due to the air conditioner in the lab.

5.4.4 Results

The frequency stability of the laser is plotted in figure 5.8**b**. The thin red line shows the centre frequency of the pulsed laser free running without feedback; the frequency drifted by 1 GHz over a period of two hours. The thick blue line shows the centre frequency when the detuning was locked to 4.71 GHz. The mean frequency and standard deviation of the locked signal was 4.712 ± 0.07 GHz, showing excellent agreement with the desired detuning. The fluctuations were much less than the pulse bandwidth and could be safely ignored. Figures 5.8**c**, 5.8**d** show the SFPI traces versus time when the laser oscillator

[4]Even with angled fibre tips, the isolator was necessary to guard against back-scattered light interferring with the mode locking of the laser.

[5]This requires some care as the frequency difference between the two ground state transitions was 9 GHz and the FSR of the SFPI was 10 GHz, causing some overlap on the SFPI when the pulse was centred on the 'wrong' transition.

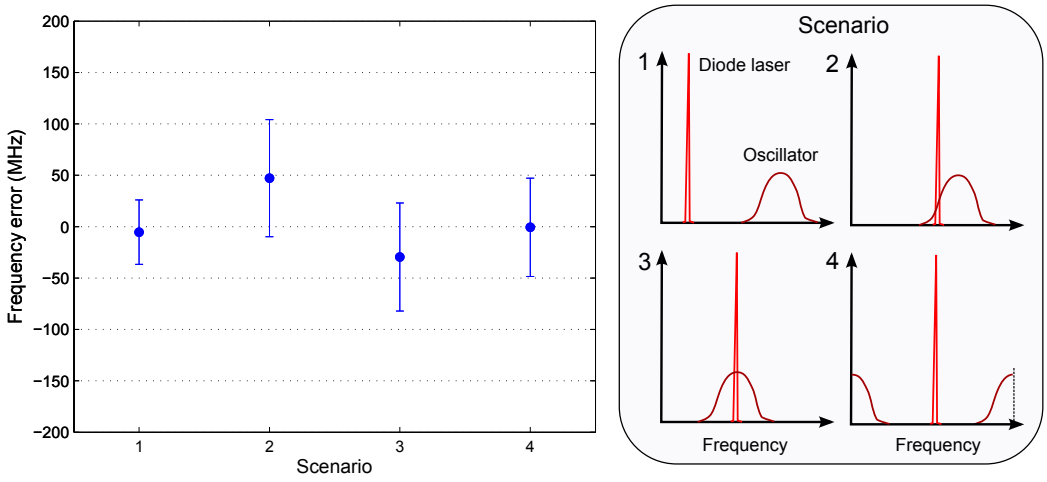

Figure 5.9: Frequency error relative to the lock position for four different scenarios of the diode laser relative to the pulsed oscillator, as detected by the SFPI.

frequency was locked and unlocked, respectively, when the laser diode was unlocked, showing that the pulsed oscillator frequency closely tracked the diode laser in the first instance, but not in the second.

The performance of the frequency offset was carefully validated in a few different regimes, as show in figure 5.9. The simplest case, captured by scenario 1, was when the diode laser and pulsed oscillator were locked at frequencies clearly resolved by the SFPI. In scenarios 2 and 3 there was some overlap between the two spectra, and in scenario 4 the pulse was at the edge of the free spectral range of the SFPI. Figure 5.9 show that in all cases the offset from the desired detuning and standard deviation of the fluctuations were less than 100 MHz and, therefore, acceptable for our requirements.

5.5 Solid-state etalons for control-field filtering

5.5.1 Motivation

After the memory interaction, the strong control field must be separated from the weak, single-photon-level signal. In the experiments summarized in section 5.3 the control field pulse had approximately 10^{12} photons, thereby requiring greater than 120 dB of filtering. The control and signal were orthogonally polarized and filtered according to their polarization state, which provide an extinction ratio of approximately 30 dB. The remaining

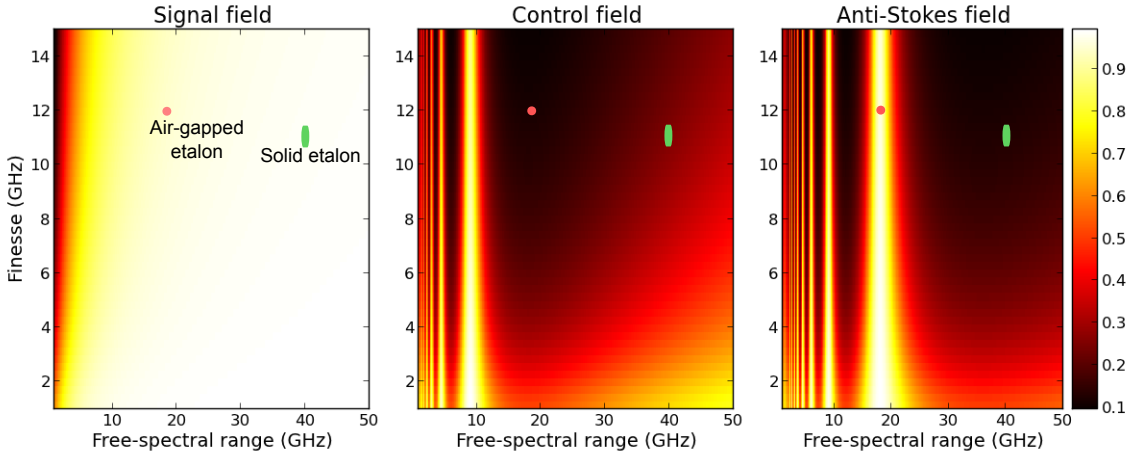

Figure 5.10: Transmission of the signal field, control field and anti-Stokes field through the etalon as a function of the free spectral range and finesse. The pink dot shows the planar, air-gapped etalon, with undesirable transmission at the anti-Stokes frequency, and the green square shows the plano-convex solid etalon as measured in figure 5.12

90 dB of extinction was achieved with spectral filtering.

The current spectral filters are air-gapped planar Fabry-Pérot etalons with a finesse of 10, free-spectral range of 18.4 GHz, and extinction ratio for the control field of 20 dB. These etalons have two very undesirable features. First, the transmission frequencies of the etalon slowly drift due to temperature fluctuations, requiring periodic readjustment of the angle of the etalon to maximize the transmission through the etalon. This is both a significant impediment for long-duration measurements and a hassle for day-to-day operation. Second, the free spectral range is exactly equal to the spectral spacing of the signal (Stokes) and noise (anti-Stokes) arising from four-wave mixing, which will be discussed in more detail in chapter 7. In the single-photon experiments summarized in section 5.3, a second etalon with FSR incommensurate with the first etalon (103 GHz) was double-passed in order to filter the anti-Stokes photons. Therefore, to circumvent the need for this additional filtering step, I designed and built a new temperature-stabilized monolithic etalon with a FSR incommensurate with the control field and anti-Stokes field.

5.5.2 Design considerations

The transmission T_i of a symmetric Fabry-Pérot etalon is

$$T_\mathrm{i}(f) = \frac{(1-R)^2}{(1-R)^2 + 4R\sin^2(\delta/2)}, \tag{5.63}$$

where R is the mirror reflectivity and $\delta = 4\pi f n l \cos\theta/c$ is the phase accumulated during the round trip of a cavity with length l at angle θ and an index of refraction n. The coefficient of finesse F of the etalon is defined as $F = 4R/(1-R)^2$ and the finesse $\mathcal{F}$ is $\mathcal{F} = \pi/[2\arcsin(F^{-1/2})]$. Equation 5.63 expressed in terms of the free spectral range f_fsr is

$$T_\mathrm{i}(f) = \left(1 + \frac{\sin^2(\pi f/f_\mathrm{fsr})}{\sin^2(\pi/2\mathcal{F})}\right)^{-1}. \tag{5.64}$$

The transmission of the signal field was maximized subject to the constraint that the transmission of the control field, which was detuned by 9 GHz, and the anti-Stokes field, which was detuned by 18 GHz, be minimized. The fraction of power transmitted (P_f) is

$$P_\mathrm{f} = \int_{-\infty}^{\infty} T_\mathrm{i}(f)\cdot S(f)\mathrm{d}f, \tag{5.65}$$

where $S(f)$ is the normalized power spectrum of the signal, control, or anti-Stokes field. The transmitted power is plotted in figure 5.10 for the signal, control and anti-Stokes fields. Based on these results, I chose the following etalon parameters: FSR = 39.2 GHz, finesse = 14 ± 2,[6] and FWHM = 2.8 GHz.

The etalon had a plano-convex geometry. This geometry was chosen because the requirements on the surface quality of the optics were more relaxed compared to planar etalons. In addition, plano-convex etalons, unlike planar etalons, afford some degree of spatial filtering as the transverse modes are not frequency-degenerate. The resonance condition for Hermite-Gaussian mode TEM_{mn} for a plano-convex lens is [206, 207]

$$f_{qmn} = f_\mathrm{fsr}\left[q + \frac{1+m+n}{\pi}\arccos\sqrt{\left(1-\frac{l}{r}\right)}\right], \tag{5.66}$$

[6] The uncertainty of the finesse is a result of the uncertainty in matching the specified reflectivity of the optical coating as indicated by the manufacturer.

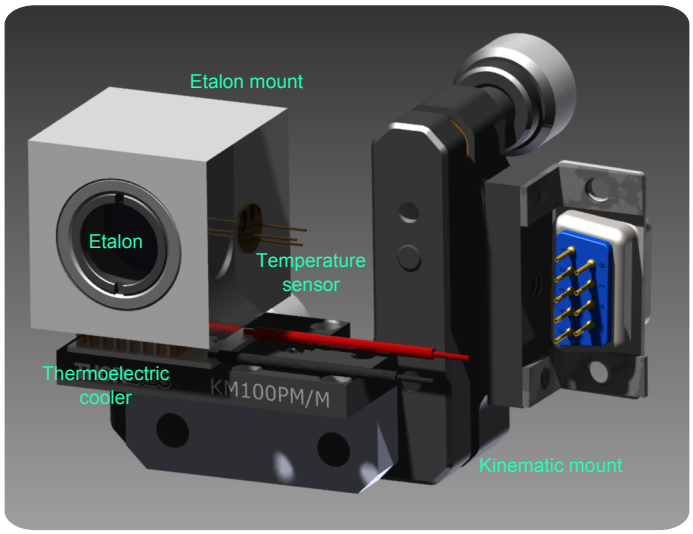

Figure 5.11: CAD drawing of the etalon with mount, temperature sensor, and thermoelectric cooler.

where q is the longitudinal mode number and r is the radius of curvature of the convex surface. Additionally, the stability condition of a plano-convex etalon is

$$0 < \left(1 - \frac{l}{r}\right) < 1. \tag{5.67}$$

The etalon length was 2.5 mm and radius of curvature $r = 50.1$ mm, rendering the modes inside the cavity stable.

5.5.3 Experimental implementation

The etalons were manufactured from plano-convex lenses made from BK7 glass applied with a reflective dielectric coating (by Castech). The surface quality was $\lambda/6$ ($\lambda/10$ before coating), which was the roughness over the entire surface of the lens; the roughness was lower for localized areas. The etalon was one-half inch (12.7 mm) in diameter and mounted in a lens tube (Thorlabs SM05M10). The lens mount was slotted into a custom, one-inch (25.5 mm) aluminum cube. The cube was mounted on a thermoelectric cooler (Thorlabs TEC3-2.5) affixed to a kinematic prism mount (Thorlabs KM100PM/M) with thermal epoxy (RS TBS20S), as shown in figure 5.11. A temperature sensor (AD-590) monitored the temperature of the aluminum cube, which was connected to a controller for the thermoelectric cooler (Thorlabs TTC001). The temperature could be set by the

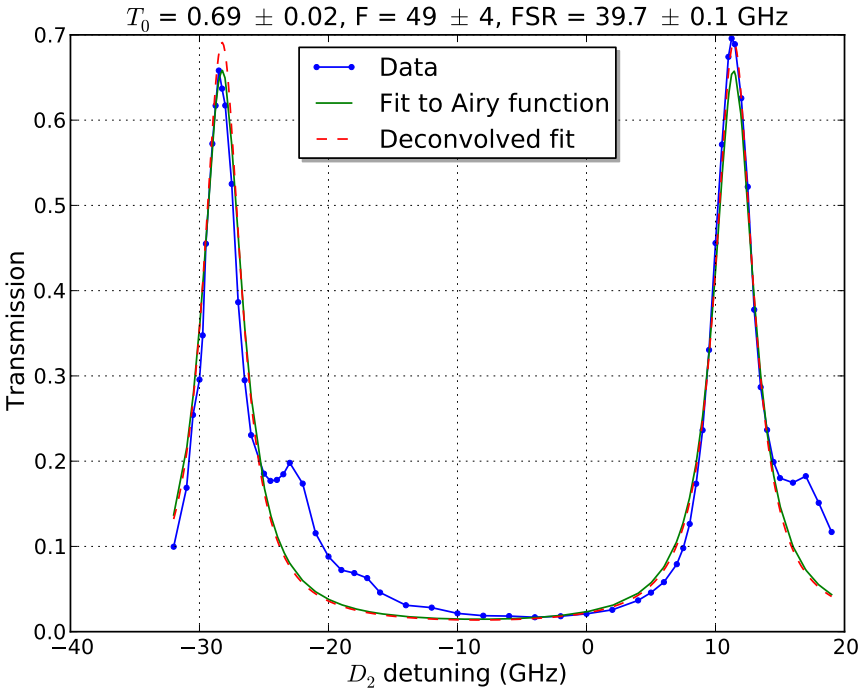

Figure 5.12: Transmission spectrum of etalon. The blue dots and line show the measured data, the solid green line shows the data fit to equation 5.63, and the dashed red line shows the same fit with data deconvolved by the bandwidth of the pulsed oscillator.

controller or remotely by an external interface. The kinematic prism mount was connected to a three-axis positioning stage (Thorlabs NanoMax) via a one-inch diameter aluminum pedestal, which acted as a heat sink.

5.5.4 Results

The etalon was placed in the centre of two plano-convex lenses (100 mm focal length) to focus and then collimate the light. The transmission spectrum of the etalon is plotted in figure 5.12, measured using the pulsed oscillator with a bandwidth of 1 GHz. The blue dots and line show the measured data, the solid green line shows the data fit to equation 5.63, and the dashed red line shows the same fit with data deconvolved by the spectrum of the pulsed oscillator. The maximum transmission given by the deconvolved fit was 0.69 ± 0.02, the free-spectral range was 39.7 ± 0.1 GHz, and the finesse was 11.0 ± 0.5 (the coefficient of finesse was 49 ± 4), which is in close agreement with the design parameters listed in section 5.5.2. Carefully matching the radius of curvature of the diffracting beam with the surface of the etalon would improve the maximum transmission on resonance.

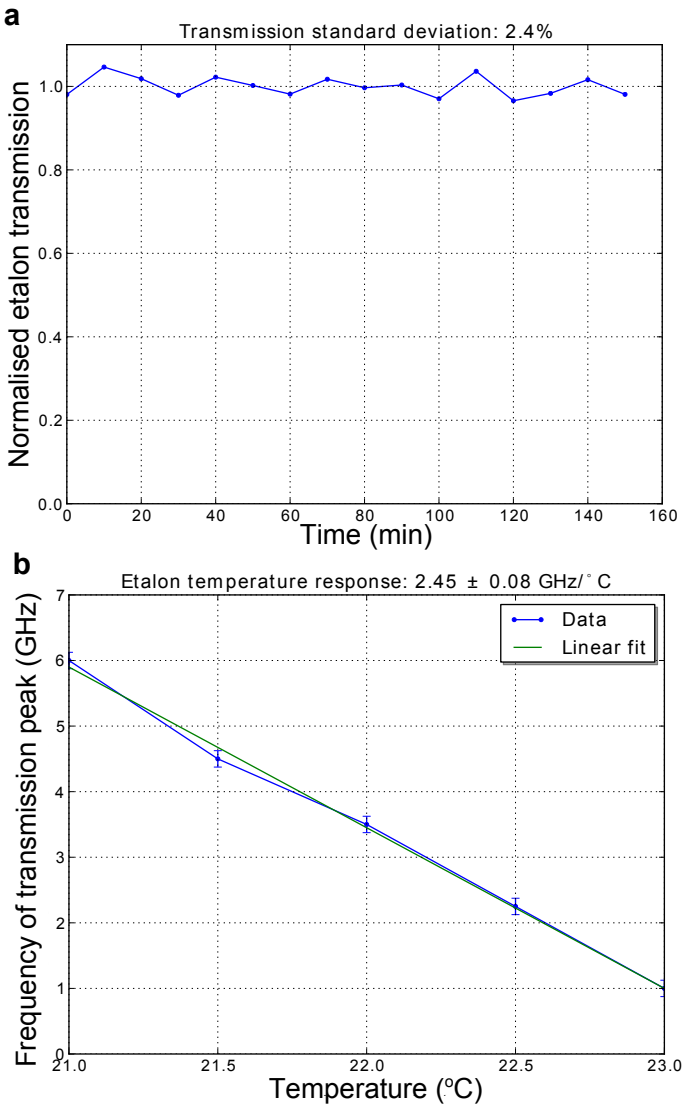

Figure 5.13: Stability (**a**) and temperature sensitivity (**b**) of the etalon.

Figure 5.12 shows additional transmission peaks displaced from the main resonance peak by 4 ± 0.5 GHz. These correspond to higher-order transverse spatial modes, where the modal spacing is given by equation 5.66. For our etalon design parameters, the calculated mode spacing was 4.2 GHz, indicating that we have excited the first high-order transverse spatial mode. These spatial modes can be reduced by more careful mode matching or filtered out with a single-mode fibre after the etalon.

The stability of the temperature-stabilized etalon was assessed by measuring the on-resonance transmission over time. The laser frequency was locked as described in section 5.4, so any change in transmission could be attributed to a change in the state of the cavity. The normalized transmission over time is shown in figure 5.13**a**. The standard

deviation of the fluctuations was 2.4%, showing excellent temperature stability over a period greater than two hours. Longer measurements (data not shown) demonstrated that the cavity was stable over several days, which is a significant improvement over the previous air-gapped etalons.

Lastly, to change the resonance frequency of the etalon the temperature of the etalon was altered. This is in contrast to the air-gapped etalons, where a small angle could alter the resonance frequency of the etalon. I investigated the temperature-tuning sensitivity by measuring the frequency of maximum transmission as a function of the temperature of the etalon as indicated by the AD 590 temperature sensor. The data are plotted in figure 5.13**b**, which were fit to a linear function. The temperature response of the etalon was 2.45 ± 0.08 GHz/°C; the entire free spectral range of the etalon can be spanned by a temperature change of 16 °C.

5.6 Summary

I have described the previous memory results to provide context for the following chapters on storing light in a hollow-core photonic crystal fibre. I have reviewed my work creating a frequency-offset lock using a stable scanning Fabry-Pérot etalon. The fluctuations of the lock were much less than the bandwidth of the pulse, and the scanning range was limited only by the mode-hop-free tuning range of the oscillator (50 GHz). I also designed and tested a new temperature-stabilized, solid-state etalon. I measured power functuations of 2.4% and a temperature sensitivity of 2.45 ± 0.08 GHz/°C. The maximum transmission was 0.69 ± 0.02, the free spectral range was 39.7 ± 0.1 GHz, and the finesse was 11.0 ± 0.5, in close agreement with our predictions.

6

Hollow-Core Photonic Crystal Fibre

6.1 Motivation

The efficiency of non-linear optical processes depends on the product of the interaction length and intensity (raised to some power), which is limited for diffractive, free-space optical beams. Consider a Gaussian optical beam with depth of focus determined by the Rayleigh length (or range),

$$z_{\mathrm{R}} = \frac{\pi w_0^2}{\lambda}, \tag{6.1}$$

where w_0 is the minimum beam waist at the focal point and λ is the wavelength of light. The Rayleigh length is defined as the distance from the focus where the beam waist is a factor $\sqrt{2}$ larger than at the focus. For a Gaussian beam, the product of the intensity I

and the depth of focus is constant,

$$z_{\mathrm{R}} \times I = \frac{\pi w_0^2}{\lambda} \times \frac{P}{\pi w_0^2} \propto \frac{1}{\lambda}. \tag{6.2}$$

where P is the optical power. The product of the intensity and Rayleigh length is proportional to the wavelength of the light, and independent of the focusing parameters. This is related to the conservation of the *etendue*, namely the product of the area and the solid angle in an optical system is a conserved quantity. There exists an inherent trade-off between the intensity of the beam and the depth of focus that cannot be altered by tighter or looser focusing.

This limit can be overcome by confining the transverse extent of the optical beams with a waveguide. Waveguide structures afford tight transverse confinement of optical modes over a long length, limited only by the attenuation in the waveguide, offering dramatic enhancement for non-linear light-matter interactions. This enhancement is evinced by supercontinuum generation in photonic crystal fibres [208] and parametric down-conversion in non-linear-crystal waveguides [209], among other examples [210].

A quantum memory in an integrated architecture is attractive for several reasons. First, owing to the tight transverse confinement of the optical beam, the optical power needed to achieve strong light-matter coupling can be reduced. This is especially important for a Raman memory, where a large Rabi frequency, on the order of several GHz, is needed to achieve efficient coupling, as discussed in section 5.2.7. These high Rabi frequencies require orders of magnitude larger optical intensities than on-resonant EIT [211] or photon-echo [95] memories. The memory efficiency of the present Raman memory experiments are limited by the available optical pulse energy from the oscillator (10 nJ) [73, 72]. A waveguide would allow for higher Raman coupling without the need for optical amplifiers.

There are several additional advantages to being able to use lower pulse energies to achieve the same Raman coupling. The lower power reduces the amount of filtering needed to isolate the weak signal from the strong control field. It also enables larger scale operation; multiple memories can be operated with the same power required for a single bulk memory. Finally, the control signal could be derived from the output of

a relatively inexpensive amplified continuous-wave diode laser carved into pulses with an integrated electro-optic modulator, which would obviate the need for the bulky and expensive titanium-sapphire mode-locked oscillator.

Finally, separate from the advantages of lower control powers, an integrated platform is attractive as it can be easily interfaced with existing photonic architectures, including fibres and photonic chips [212, 213]. Integrated optical components can be readily scaled up to build multiple units. Also, an integrated system would simplify the spatial overlap of the signal field, control field, and optical pumping field for the memory protocol.

Nonlinear optical effects have been investigated in a variety of integrated structures including on-chip waveguides coupled to cryogenic rare-earth doped solids [99], anti-resonant reflection optical waveguides [214], evanescent ridge waveguides [215], evanescently coupled optical fibres [216, 217], and hollow-core photonic-bandgap fibres [218] loaded with alkali atoms. Hollow-core photonic-bandgap fibres (HC-PBGFs), in particular, are attractive because of their low transmission loss and relatively large optical modes. Cross-phase modulation [219], electromagnetically induced transparency [220, 221] and four-wave mixing [222] have been realized in a HC-PBGF with a 6-μm diameter core.

The storage of light in a hollow-core photonic-bandgap fibre has not been realized, however, because of two main obstacles. First, the small optical mode causes significant transit-time broadening at room temperature; both the state initialization and the memory interaction must occur within the time that the atoms take to traverse the guided mode. Second, it is challenging to load a sufficient number of atoms into the core to achieve the high optical depth required for efficient light storage. In this chapter, and the next, I describe how these obstacles can be surmounted by using a large-core kagome-structured hollow-core photonic crystal (HC-PCF) to increase the transit time and the rate at which atoms are loaded into the fibre core [223, 224], and using a far-off-resonant, broadband Raman interaction [71, 72] to perform the memory protocol within the transit time. I show that the necessary conditions for light storage in a hollow-core photonic-crystal fibre can be achieved. I demonstrate that both high optical depth and efficient optical pumping can be achieved in a hollow-core fibre. First, I describe the fibre and vacuum system used in my experiment.

6.2 Microstructured photonic crystal fibres

6.2.1 Photonic crystal fibres

Conventional solid-core glass fibres guide light via total internal reflection; the core has a higher index of refraction than the surrounding cladding.[1] An alternative approach is to guide light via diffraction from a micro-structured cladding whereby light propagation is forbidden in the cladding (similar to how an electronic band-gap can be formed in semiconductors). This was first proposed by our collaborator Philip Russell, who had the important insight that a photonic band-gap is only required for a narrow range of transverse wavevectors about zero [226, 227]. In this case, he showed that the index of refraction contrast between air and glass was sufficient [228] (compared to silicon, with an index of refraction of ∼3.5, used for three-dimensional photonic band-gap structures [229]).

Photonic crystal fibres, which guide by a combination of total internal reflection and diffraction, have a host of applications that results from the ability to tune their guidance properties [230, 231]. By varying the core diameter and the air-filling fraction of the cladding, the waveguide dispersion can be modified in order to shift the location of zero dispersion (normally at 1.5 μm) to a desired wavelength. This has enabled supercontinuum generation with an un-amplified output of a titanium-sapphire mode-locked oscillator [208], paving the way for the development of frequency combs for optical metrology [232] and sources for optical coherence tomography [233].

6.2.2 Hollow-core photonic crystal fibres

A unique property of photonic crystal fibres is the ability to guide light in a core with a lower index of refraction than the cladding. When the core is air, these structures are known as hollow-core photonic crystal fibres (HC-PCFs), and were first demonstrated in 1999 [218]. It was initially hoped that guidance in hollow-core fibres could offer lower attenuation than solid core fibres as only a small fraction of the light overlaps with the glass material. The predominant loss mechanism in conventional fibres is Rayleigh scattering

[1] Geometric optics breaks down when considering the propagation of light in single-mode fibres, where the mode propagation needs to be solved with Maxwell's equations, but the basic insight holds that an index contrast is required to support propagating modes in the core [225].

at high frequencies (from microscopic variations in the index of refraction) and absorption at lower frequencies (where the light couples to atomic transitions or vibrational states in molecules) [101]. However, it was discovered that frozen capillary waves – thermodynamic in nature – on the surface of the core induces scattering that limits the attenuation to 0.1 dB/km at 1620 nm [234] (I should note that in practice the lowest reported loss is 1.7 dB/km at 1530 nm [235]). Nevertheless, hollow-core photonic crystal fibres have two countervailing applications: reducing non-linearities for high-power applications [236, 237, 238], and increasing and tailoring the non-linear response by loading fibres with atomic or molecular species [239]. Here I focus on the latter application.

HC-PCFs are divided into two main types: photonic bandgap fibres and kagome-structured photonic crystal fibres. Photonic bandgap fibres (PBGFs) possess a true bandgap as their guidance mechanism, which prevents light from propagating in the fibre cladding, confining the light within the core [218]. The spectral bandwidth of the bandgap is typically tens of nanometers, and the pitch size – the size of the repeated unit in the micro-structured cladding – is typically several micrometers at visible wavelengths (with tolerances a small fraction of this), which is very challenging to manufacture [240]. Manufacturing core diameters much larger than the pitch dimensions is also very challenging; most fibres have core diameters of several micrometers. Electromagnetically induced transparency [220, 221], four-wave mixing [222], two-photon absorption [241], and few-photon cross-phase modulation [219] have been previously demonstrated with alkali atoms in PBGFs with a 6-μm diameter core. However, the small core diameter of the fibres has limited the optical depth as it has proven difficult to load the core with a sufficient number of atoms. Additionally, the interaction time has been limited by the short time that the atoms take to traverse the core, which introduces significant transit-time broadening. These limitations can be overcome by using kagome-structured photonic crystal fibres.

6.2.3 Kagome-structured hollow-core photonic crystal fibres

The kagome structure is formed by a trigonal lattice with a set of defects that also forms a trigonal lattice, but with double the period, giving the structure a ‘Star of David’ pattern. The word kagome comes from a Japanese basket weaving pattern [242], and is pronounced

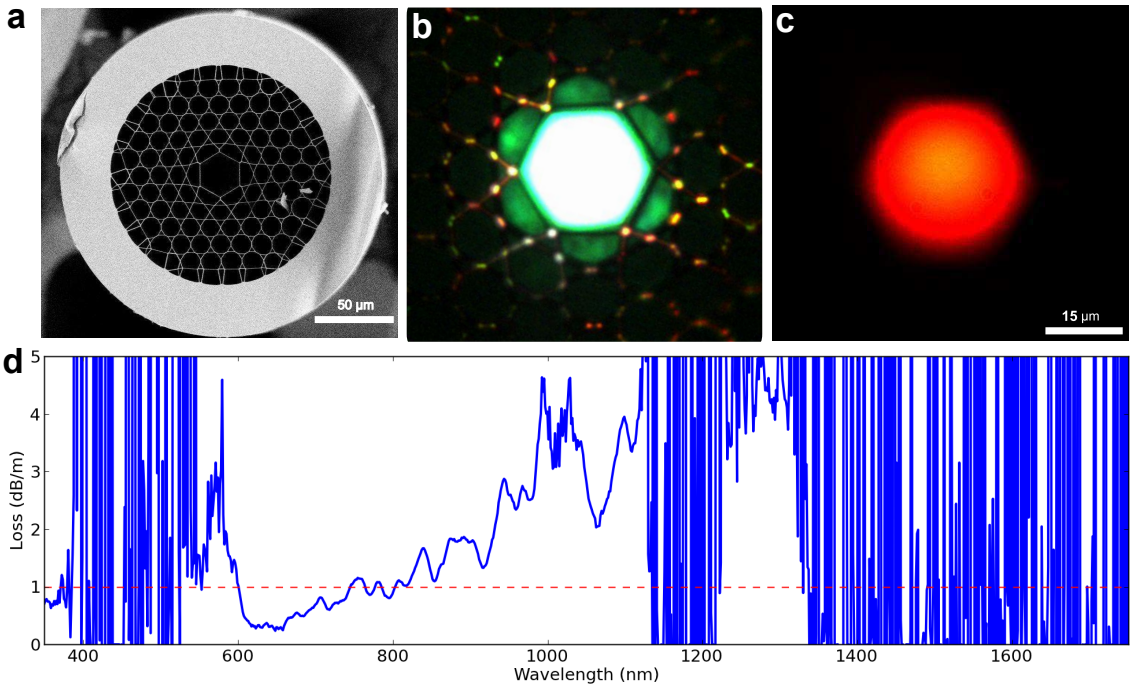

Figure 6.1: All images courtesy of Amir Abdolvand. **a** Scanning electron microscopy image of the cross-section of the kagome-structured hollow-core fibre with core diameter of 26 μm and pitch 13 μm. **b** Optical image of the fibre face with super-continuum light launched into the fibre. **c** Optical image of the fundamental mode (10 nm bandwidth) at the face of the fibre. **d** Transmission loss of the HC-PCF as a function of the wavelength; the transmission loss is 1.5 dB/m at 850 nm.

kah-goh-meh as an anapest, stress on the last syllable. The cross-section of a seven-cell defect kagome fibre is shown in figure 6.1**a**, where the core diameter is 26 μm and pitch 13 μm. Kagome fibres do not possess a band gap, but guide by a mechanism that, while still being elucidated [239, 240, 243], appears to be related to anti-resonant reflections [244]. Kagome fibres can easily be made with large core diameters (25 to 30 μm) because of their large pitch size as compared to standard PBGFs. Kagome fibres provide guidance over a spectral window several hundred nanometers wide at the cost of slightly higher transmission losses ($\sim$1 dB/m) than PBGFs [243, 245]. However, the recent development of hypocycloidal cores for kagome structures [246] have reduced the transmission losses by an order of magnitude to 70 dB/km [247, 248]; the losses may soon be comparable to PBGFs. The predominant loss mechanism of the kagome fibre is coupling to localized resonances in the struts of the microstructured cladding; this is beautifully demonstrated in figure 6.1**b**, where supercontinuum white light is launched into the fibre. The central core is white as it supports a broad spectrum whereas the localised resonances in the

struts are coloured, indicating they guide only a narrow bandwidth of light.

As a large core is critical to facilitate the loading of atoms and to allow for sufficient time to store and retrieve a pulse of light, I decided to use a kagome-structured HC-PCF for our demonstration of an optical memory. Our collaborators Amir Abdolvand and Philip Russell from the Max Planck Institute for the Science of Light in Erlangen, Germany designed and manufactured the fibre shown in figure 6.1. The fibre transmission loss was 1.5 dB/m at a wavelength of 852 nm. The coupling efficiency into the fibre was $65 \pm 1\,\%$. The fibre core did not only support a single spatial mode; higher-order transverse spatial modes could be excited, depending on the launch geometry. However, with careful alignment, the output mode can preserve the lowest-order transverse spatial mode, as is shown in figure 6.1**c**. The coupling efficiency of the mode emerging from the HC-PCF into a standard single-mode fibre was $67 \pm 1\,\%$.

A critical aspect of the Raman memory is that the signal and control fields must be orthogonally polarized; parallel polarizations are difficult to filter and also have zero Raman coupling [51]. We require that the HC-PCF preserve the orthogonality of the two fields. Not only that, we desire that the fields remain linearly polarized during propagation in the fibre; the Raman coupling for orthogonal, circularly polarized fields vanishes [249]. The kagome-structured fibre was not specifically designed to be polarization maintaining, as has been previously the case for PBGFs [250, 251, 252]. However, owing to a small amount of asymmetry introduced unintentionally during the drawing process, the fibre was found to be polarization maintaining. The polarization extinction ratio after transmission through the HC-PCF and coupling to a single-mode fibre, using cross-polarizers, was greater than 4000:1. The polarization extinction ratio was much lower, on the order of 35:1, when measured without coupling to a single-mode fibre first, indicating the majority of the unpolarized light did not overlap with the fundamental core mode.

A short note here on how to cleave HC-PCFs; first, remove the polymer coating with a razor blade, holding it between your index and middle finger at a slight oblique angle to the fibre, which will be compressed against your thumb. Now move the blade relative to the fibre in a smooth motion, like you would when whittling the smooth, waxen bark off the branch of a willow tree while casting an eye on the carp swimming below. Next,

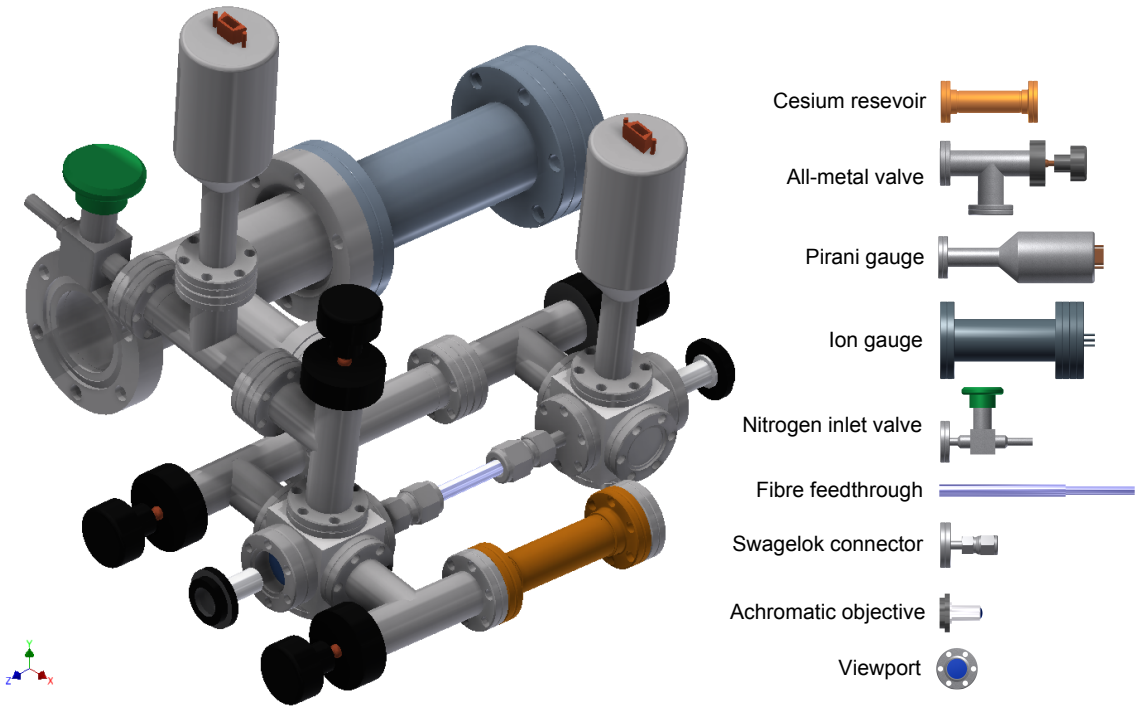

Figure 6.2: Ultra-high vacuum system for the hollow-core fibre experiments, along with the constituent parts. Not shown are the turbomolecular pump and the roughing pump connected to the vacuum system via a flexible bellows.

gently score the bare fibre with a ceramic plate at the location you would like to cleave. The depth should be a very small fraction of the core diameter (see the outer edge of figure 6.1**a** at approximately 4 o'clock); you should be able to hear the very faint sound of the ceramic scoring the glass. Finally, hold the fibre close to the location of the score, and gently push (think adiabatic) the other side of the fibre in the direction of the score until it breaks cleanly at this point.[2]

A 20-cm length of kagome-structured HC-PCF was mounted in an ultra-high-vacuum system prior to the introduction of cesium atoms [223], which will now be described in the next section.

6.3 Vacuum System

Cesium is pyrophoric; it reacts explosively with oxygen in the air and water, forming oxide compounds (which share the same colour palette as the front surfaces of the wings

[2]Thanks to Peter Mosley at the University of Bath for his helpful instructions on how to cleave HC-PCFs.

of *Anthocharis cardamines*). To prevent these reactions from occurring, the fibre was loaded with cesium under vacuum. I designed and built an ultra-high vacuum system to mount and load a kagome-structured HC-PCF with cesium atoms for an optical memory.

6.3.1 General design principles

The vacuum system was built with conflat (CF) flanges – knife-edge flanges with soft metal gaskets – as they offer the best vacuum performance; the elastomeric o-rings used in KF/QF fittings can be degraded through a chemical reaction with cesium atoms [253]. The desired fibre length was between 10 and 30 cm; the low end set by sufficient filtering of the high-order transverse spatial modes [254], and the high end set by the fibre attenuation – 30 cm corresponds to a transmission loss of 10% at 852 nm. The fibre was stably mounted in the vacuum chamber with optical access for in- and out-coupling optical fields. A mirrored surface was also mounted in the chamber in order to monitor the cesium density in the bulk chamber (to allow for comparisons with the cesium density in the fibre core). The vacuum system was also designed with the option of creating a differential pressure gradient between the two ends of the fibre in order to entrain the cesium atoms in a flow of a buffer gas; it was hoped this would increase the number of ceisum atoms loaded in the core of the fibre (I should note this has yet to be implemented in our system). A source of cesium atoms was opened under vacuum in order to passively and contiunously load the HC-PCF. Finally, I used mainly components that were available and in stock from commercial suppliers (e.g. LewVac and KJ Lesker) to reduce the cost and lead time. The vacuum apparatus is shown in figure 6.2; the constituent parts will now be discussed.

6.3.2 Fibre mount and viewports

I mounted a 20-cm length of kagome fibre in the vacuum system with two viewports to provide optical access for the coupling lenses positioned outside the vacuum system, as shown in figures 6.2 and 6.3. The viewports were made from uncoated Kodial glass brazed to Kovar metal (LewVac VP-16CF), which were mounted to the vacuum cube with annealed copper gaskets. Unfortunately, approximately six months into the experiment, two leaks developed in two of the viewports at the glass-metal seal, causing cesium oxide

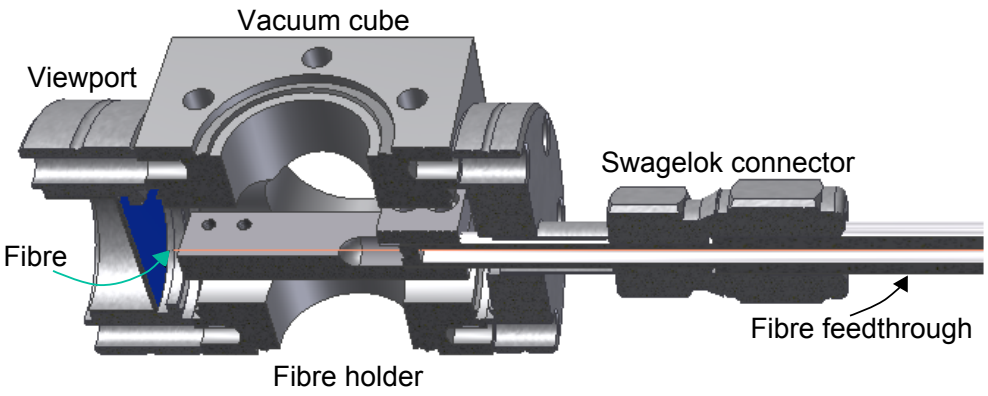

Figure 6.3: Half-section close-up of the interior of the vacuum cube showing the fibre, fibre holder and fibre feedthrough mounted in the Swagelok connector.

to form; this was also observed independently by another research group [255]. The exact materials used for the metal-glass brazing is proprietary, making it difficult to verify its reactivity with cesium; however, I have procured sapphire viewports for the next iteration of the experiment with the hope that they prove more resilient.

The fibre was mounted onto an aluminum holder impressed with a v-groove, as shown in figure 6.3. The clearance between the tip of the fibre and the inside surface of the viewport was 3 mm. The fibre was affixed in the v-groove with a dab of Vacseal®, a vacuum-compatible epoxy, a process which I would not repeat as it contained a significant amount of dissolved gas that took several days to outgas. The bottom surface of the fibre holder was polished to a mirror finish and another viewport was mounted on the bottom face of the vacuum cube. A laser beam reflected off the bottom of the fibre holder was used to monitor the cesium density in the bulk vacuum chamber, as discussed in section 6.5.

The fibre holder was attached to an aluminum tube that was connected to the two vacuum cubes via Swagelock fittings, forming a sheath around the fibre. When tightened, the stainless-steel Swagelock ferrules compressed the outer surface of the aluminum tube, forming a tight vacuum seal; tests with a helium leak detector put an upper limit on the conductance of $< 10^{-9}$ Torr·L/s. One end of the aluminum tube was capped with a 220-μm diameter hole drilled one millimeter deep.[3] The fibre (stripped of its polymer coating) was fed through this hole, which was then sealed with Vacseal® in order to

[3] A special thanks to Mike Tacon and his team at the Denys Wilkinson machine shop for their expert work in machining this piece

create a differential pressure gradient between the two vacuum cubes (see section 6.3.5).

My initial design had two short Swagelok connectors that did not join; the fibre emerged into the air through two small 220-μm diameter holes sealed with vacuum epoxy [256]. The design had two flaws: first, the vacuum seal formed by the sealant was very weak; any dissolved air in the epoxy that outgassed could rupture the seal during the vacuum bake. Second, the exposed fibre was heartbreakingly fragile, any errant screw could sever the fibre and ruin the experiment. The present design was superior as the air-vacuum seal was provided by the robust all-metal Swagelok seal and the weaker expoxy seal was only required for differential pumping of the fibre, where small leaks could be tolerated.

6.3.3 Vacuum pumps and gauges

The vacuum was generated with a set of two pumps. The first pump, known as a roughing pump (Edwards), reduced the pressure from atmosphere to several hundred mTorr. An oil filter was fitted to prevent any contaminants from entering the vacuum apparatus, and a vacuum gauge was fitted on the line connecting the roughing pump to the vacuum system to monitor the pressure. The second pump was a turbomolecular pump (Pfeiffer TMU 071 P), which was switched on after rough vacuum had been established. The turbomolecular pump reduced the pressure to $< 10^{-9}$ Torr (see section 6.3.5). A pneumatic gate valve (5G0150 PCCF) connected to a solenoid (Humphreys 410) and a pneumatic valve relay (made by the Oxford Central Electronics Workshop) was installed immediately after the turbomolecular pump. In the event the power was cut, the valve closed and remained so until manually reset, maintaining the vacuum in the experiment.

The vacuum pressure was measured with an ion gauge (KJ Lesker KJLC 354), as shown in figure 6.2.[4] The ion gauge worked only up to 10^{-3} Torr, requiring a second set of gauges – Pirani gauges[5] (KJ Lesker K9452205M and K34513) – to measure higher pressures. This was needed in case a buffer gas was introduced in the vacuum chamber.

[4] The electronics for the ion gauge were integrated on the vacuum system, which meant during the bake they had to be removed or kept cool at great inconvenience.

[5] Pirani gauges operate by measuring the heat loss of a heated conductor; the cooling rate is determined by the number of atoms colliding with the conductor.

6.3.4 Cesium reservoir

A prescored glass ampoule with one gram of cesium (ESPI Metals), broken under vacuum using a flexible bellows (KJ Lesker MEW1030551C3), provided a source of cesium atoms for loading the fibre, as shown in figure 6.2. The right-angle valve connecting the flexible bellow was closed when the glass ampoule was broken. Breaking the ampoule was difficult given the dimensions of the ampoule and the bend radius of the bellows; future iterations would be well served by adding a set of metal 'jaws' inside the bellows to facilitate this process. An optical viewport was mounted at the end of the flexible bellows so as to verify that the cesium ampoule had indeed broken open, however the risk of a vacuum leak at the air-glass interface would make me eliminate this window in future iterations. The vacuum chamber was heated to 80 °C for the duration of the experiment and the cesium reservoir was kept slightly cooler to form a cold spot where the cesium could accumulate.

The cesium atoms passively and continuously loaded the fibre. The mean free path length was much greater than the dimensions of the vacuum chamber (Knudsen number $\gg 1$), so the motion of the atoms was described by free molecular flow rather than diffusion.[6] I decided to use a cesium oven over cesium metal dispensers (from, e.g., SAES) because of the larger (essentially infinite) supply of cesium atoms from a cesium ampoule, which allowed for continuous loading of the fibre core. Also, anecdotally, previous attempts to load HC-PCFs with cesium dispensers had failed [257].

6.3.5 Buffer gas

The vacuum system was designed with the option of introducing a buffer gas; a gas inlet valve was connected to a right-angle valve on the top of the left vacuum cube in figure 6.2. Adding a buffer gas could be desirable for three reasons:

1. A buffer gas could increase the transit time of the cesium atoms in the core of the fibre, ultimately increasing the memory lifetime and the time available to perform optical pumping, as demonstrated with a vapour-cell Raman memory [72].

[6] In this regime, the flow through a hole does not depend on the pressure differential between the two reservoirs, so there is no advantage in creating a differential pressure gradient for the purpose of loading purely cesium into the core of the fibre.

2. A buffer gas could potentially reduce the loading time of cesium atoms in the core by entraining the cesium atoms within the buffer gas. As I noted in footnote 6, the flow rate of cesium into the fibre is independent of the pressure differential of cesium atoms. With a buffer gas in the low Knudsen regime, a pressure differential could drive diffusion between the two vacuum cubes, forcing cesium through the fibre core.

3. Lastly, a buffer gas of nitrogen could reduce the excited state lifetime, decreasing the optical pumping time. This process is known a *collisional quenching* [258, 259]. The cesium in the excited state couples to a vibrational mode of the buffer gas (absent in monatomic gases), causing the cesium atom to relax to the ground state with similar branching ratios to spontaneous emission [260]. There are several relaxation/exchange mechanisms: relaxation within the excited state hyperfine manifold (not resolved in our experiment due to Doppler broadening), transfer between the fine-structure manifolds $P_{1/2} \leftrightarrow P_{3/2}$, relaxation between the excited state and ground state, and exchange between the ground state hyperfine levels, $(F = 3) \leftrightarrow (F = 4)$. The penultimate process is desirable, the first process is irrelevant, and the remaining two processes are deleterious. For nitrogen and the D_2 transition of cesium, the collisional quenching cross-section is 69 $Å^2$ and fine-structure relaxation cross-section is 25 $Å^2$, and the hyperfine exchange is negligible [260]. The collisional quenching exceeds the transit-time broadening at 3.5 Torr, which indicates this approach may be a viable approach to increase the optical pumping rate.

Adding a buffer gas, however, carries significant risk; another research group found significant degradation in the optical depth (8 OD (optical depth) at 0 Torr neon to 0.38 OD at 30 Torr of neon when using LIAD, see section 6.5.2) [261, 256]. Oxygen and water contaminants in the buffer gas can also react with the cesium atom, reducing the optical depth [260]. I ordered moisture and oxygen traps (Agilent OT2-4 and IOT-4-SS-HP, good to 20 ppb purity) to eliminate any contaminants; nonetheless, I remained trepidatious about using a buffer gas unless needed. Fortunately, I found that sufficient optical depth could be achieved using light-induced atomic desorption (LIAD, see section 6.5.2)

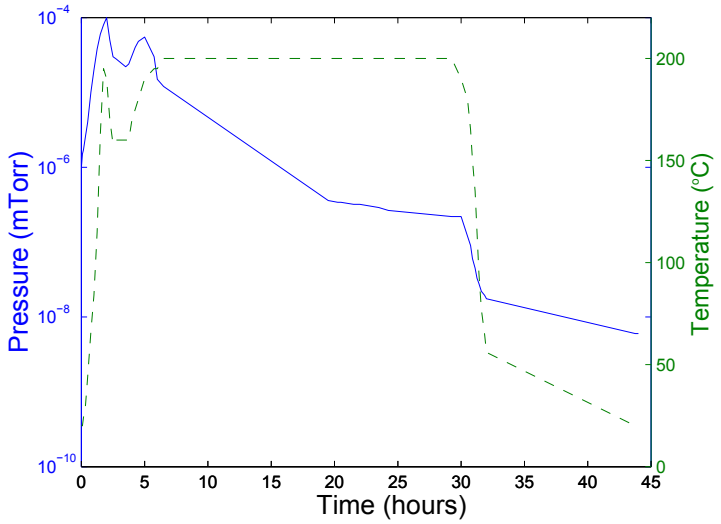

Figure 6.4: Pressure and (mean) temperature of the vacuum system during the bake as measured by the ion gauge.

and I could also perform efficient optical pumping (see section 6.7), which reduced the initial motivation for using a buffer gas.

6.3.6 Vacuum bake

After the fibre was mounted, but before the cesium ampoule was loaded, the entire vacuum system up to the turbomolecular pump was wrapped with electrical heaters powered by four variable transformers (Carroll & Meynell) in order to bake the system. Thermocouples were placed on the viewports to ensure that their maximum temperature gradients (25°C/min) were not exceeded. Figure 6.4 shows the mean temperature of the vacuum system and the pressure measured by the ion gauge during the bake. After the bake, the base pressure at the ion gauge eventually reached 5×10^{-10} Torr prior to the introduction of cesium. A conservative estimate of the pressure inside the fibre was 1×10^{-6} Torr based on the fibre conductance and outgassing rate [262].

After the bake, the flexible bellows was removed (with the associated right-angle all-metal valve closed) and the cesium ampoule inserted. The cesium reservoir was heated again for a 'mini-bake' to remove any residual contaminants from the surface of the glass. After the cesium ampoule was broken, a small amount of inert gas was released from the ampoule; the right-angle valve was slowly opened in order to reduce the load on the

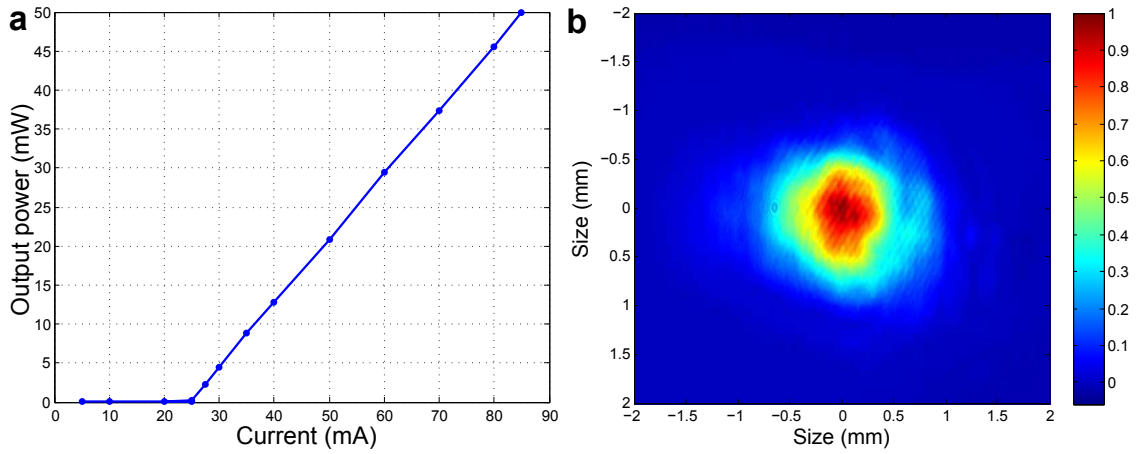

Figure 6.5: **a** Output power of the unlocked laser diode versus driving current. **b** Spatial mode of the external-cavity diode laser after the anamorphic prisms.

turbomolecular pump. During the experiment the turbomolecular pump and roughing pump were left on, although it may be possible to turn them off and close the metal gate valve up-stream from the pumps. Before I describe the measurements of the optical depth in the hollow-core fibre, I describe the laser system used to make these measurements.

6.4 Laser System

A narrowband diode laser was needed to measure the linear absorption caused by cesium in the fibre, as well as to perform the optical pumping needed to prepare the atoms in one of the ground-state hyperfine levels. I now describe the set up of an external-cavity diode laser locked to an atomic transition via saturation spectroscopy.

6.4.1 External-cavity diode laser

I rebuilt a 780-nm external-cavity diode laser (ECDL) for use at 852 nm by replacing the laser diode and the external grating. The laser diode and grating were arranged in a Littrow configuration with the grating mounted on one side of a retro-reflector; this translated a change in the angle of the grating to a lateral displacement of the beam downstream. The angle of the grating was controlled by a piezoelectric stack (Thorlabs AE0505D08F) driven by a high voltage supply (Piezomechanik LE 150). The output power of the laser diode (Thorlabs HL8342MG) as a function of the applied current (Thorlabs LDC201CU) is shown in figure 6.5**a**. The spatial mode of the laser diode

output was elliptical (2.4:1 ratio of major to minor axis) and corrected with a pair of anamorphic prisms (Thorlabs PS877-B). The output spatial mode of the ECDL after the anamorphic prism is shown in figure 6.5**b**.

I will now briefly digress in order to explain some features of the ECDL. The longitudinal mode, or lasing frequency, of the ECDL is determined by the combination of the gain curve of the semiconductor, the cavity formed inside the diode laser, and the external cavity formed by the diode laser and the grating. The frequency dependence and free spectral range of these components is shown in figure 6.6**a**. The narrowest feature is provided by the external cavity, which has a free spectral range of approximately 15 GHz. Naively, we might expect the bandwidth to be determined by the FWHM of the external cavity – several GHz. Instead, the actual linewidth of my laser is < 1 MHz, as measured with a self-heterodyne delay-line method [263]. Why is this? The external cavity does not enforce the narrow bandwidth, but rather forces the laser to operate with a single longitudinal mode. The highest value of the gain experiences exponential growth according to the formula [264]

$$I(l, f) = I_0 \exp\left[g(f) \cdot l \cdot p\right], \tag{6.3}$$

where l is the length of the gain medium, p is the number of round trips in the gain medium, $g(f)$ is the spectral gain profile, and I_0 is the intensity before amplification. The frequency class with the highest gain will saturate the atomic transition first, reducing the number of atoms available to amplify other frequencies, narrowing the spectral profile; this process is known as *gain narrowing* [264]. An illustration of how this operates is shown in figure 6.6**b**; for typical experimental values (p = 2, l = 0.25 mm, $g_{\max} = 10^5$/m) the argument of the exponential in equation 6.3 is ∼40, corresponding to a gain of 10^6. The actual laser linewidth is dominated by mechanical and thermal instabilities [265] and depends upon, of course, the integration time of the measurement. Competition between adjacent modes determines the mode-hop-free tuning range, which is a fraction of the free spectral range of the external cavity; the laser I rebuilt had a mode-hop-free tuning range of 2.3 GHz compared to a FSR of 15 GHz.

The external cavity was aligned by looking at the laser output below threshold while

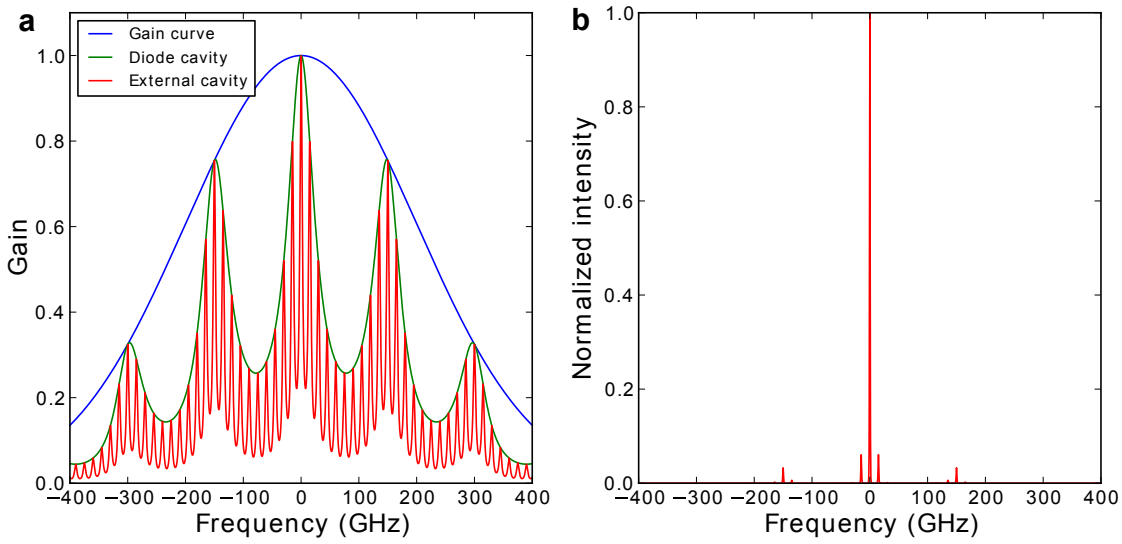

Figure 6.6: **a** Illustration of the gain curves for the lasing medium (blue line, FWHM = 470 GHz), internal diode cavity (green line, FSR = 150 GHz), and the external grating cavity (red line, FSR = 15 GHz) as a function of the frequency about maximum gain. Note the finesses were chosen for illustrative purposes. **b**. The exponential gain of the lasing medium causes one (narrowed) longitudinal cavity mode to dominate, ensuring the laser is single mode far above the lasing threshold.

adjusting the grating so the diffracted light was aligned with the outgoing mode (this is straightforward if you can see the faint reflection from the front facet of the laser diode). When the external cavity was properly aligned, the diode would lase because the threshold current was lower, producing a noticeable increase in brightness.[7] Once injection locked, the wavelength of the diode laser was tuned by changing the temperature of the laser using a thermoelectric cooler, temperature sensor (AD 590), and controller (Newport 325B) until it was within 0.1 to 0.2 nm of the atomic transition, as measured by a spectrometer (Ocean Optics HR2000). The diode current and piezoelectric voltage were then swept while looking at a vapour cell with an infrared camera to find the atomic resonance.

6.4.2 Locking laser via sub-Doppler spectroscopy

A schematic of the diode laser locked to an atomic transition is shown in figure 6.7**a**. I used sub-Doppler saturated-absorption spectroscopy to lock the laser to an atomic transition

[7] The reason injection locking decreased the threshold current for the laser was that the reflected light acted as a seed that initiated the stimulated emission. The external cavity corresponds to a narrower spectral mode than the cavity in the diode laser, so the initiation of stimulated emission could occur at a lower current.

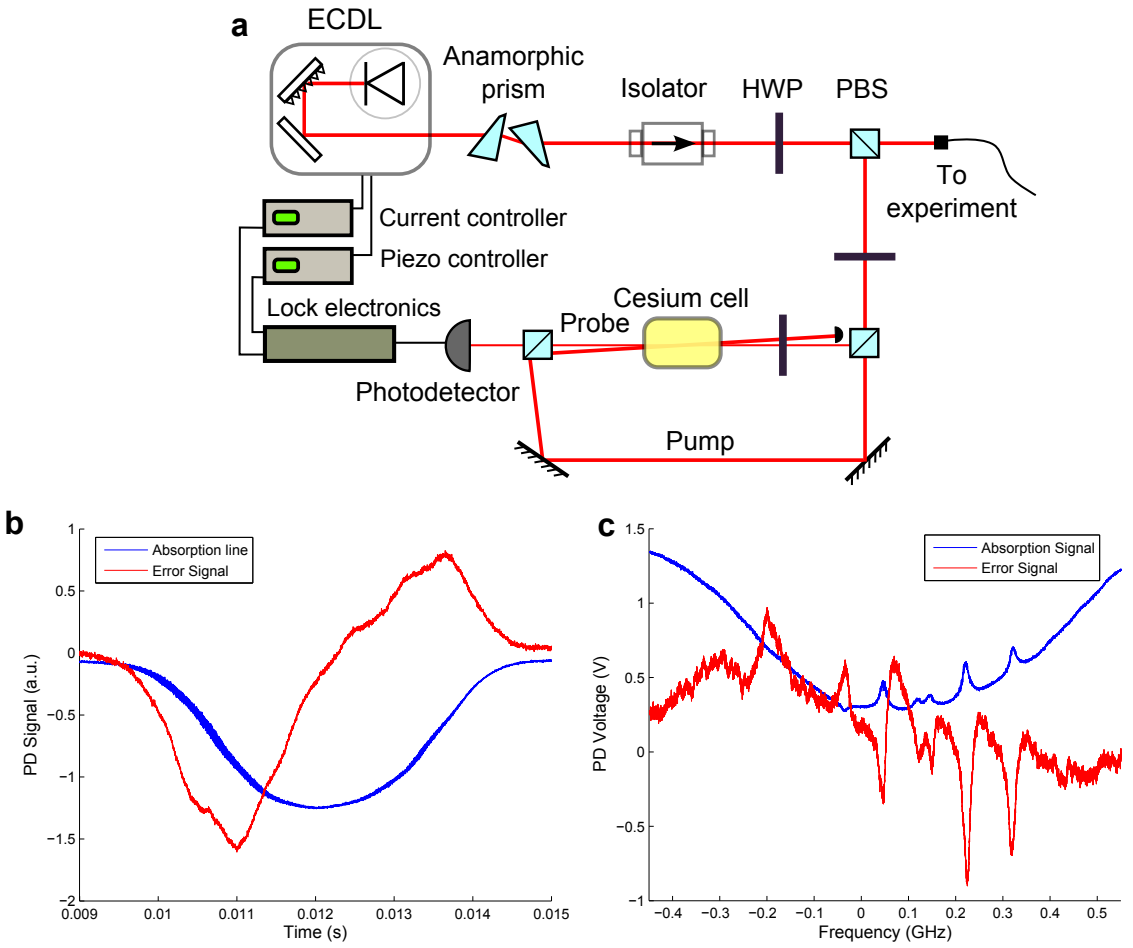

Figure 6.7: **a** Schematic of saturated-absorption spectroscopy showing ECDL, cesium cell, and the pump and probe beams. **b** Photodiode signal of the Doppler-broadened absorption line and the error signal generated via frequency modulation of the diode current. The x-axis is proportional to the laser frequency. **c** Sub-Doppler absorption and the error signal derived from frequency modulation. Note the features are much narrower, implying a superior laser linewidth when locked.

for our experiments. I will defer a detailed treatment of saturated-absorption spectroscopy until section 6.6; now it suffices to say that the method generated sub-Doppler peaks on the order of the natural linewidth (5.2 MHz for the D_2-line in cesium [266]), which I used to lock the laser. The sub-Doppler features were detected with an amplified photodiode (Thorlabs PDA36A) with a weak probe beam below the saturation intensity, as shown in figure 6.8. The sub-Doppler features for the $6^2S_{1/2}(F = 3) \rightarrow 6^2P_{3/2}$ and $6^2S_{1/2}(F = 4) \rightarrow 6^2P_{3/2}$ are shown in figure 6.8**a** and 6.8**b**, respectively. Close-ups of two sub-Doppler features are shown in the insets. The width of the features were greater than the natural linewidth of the transition (5.2 MHz), which indicates that the transitions were power-broadened.

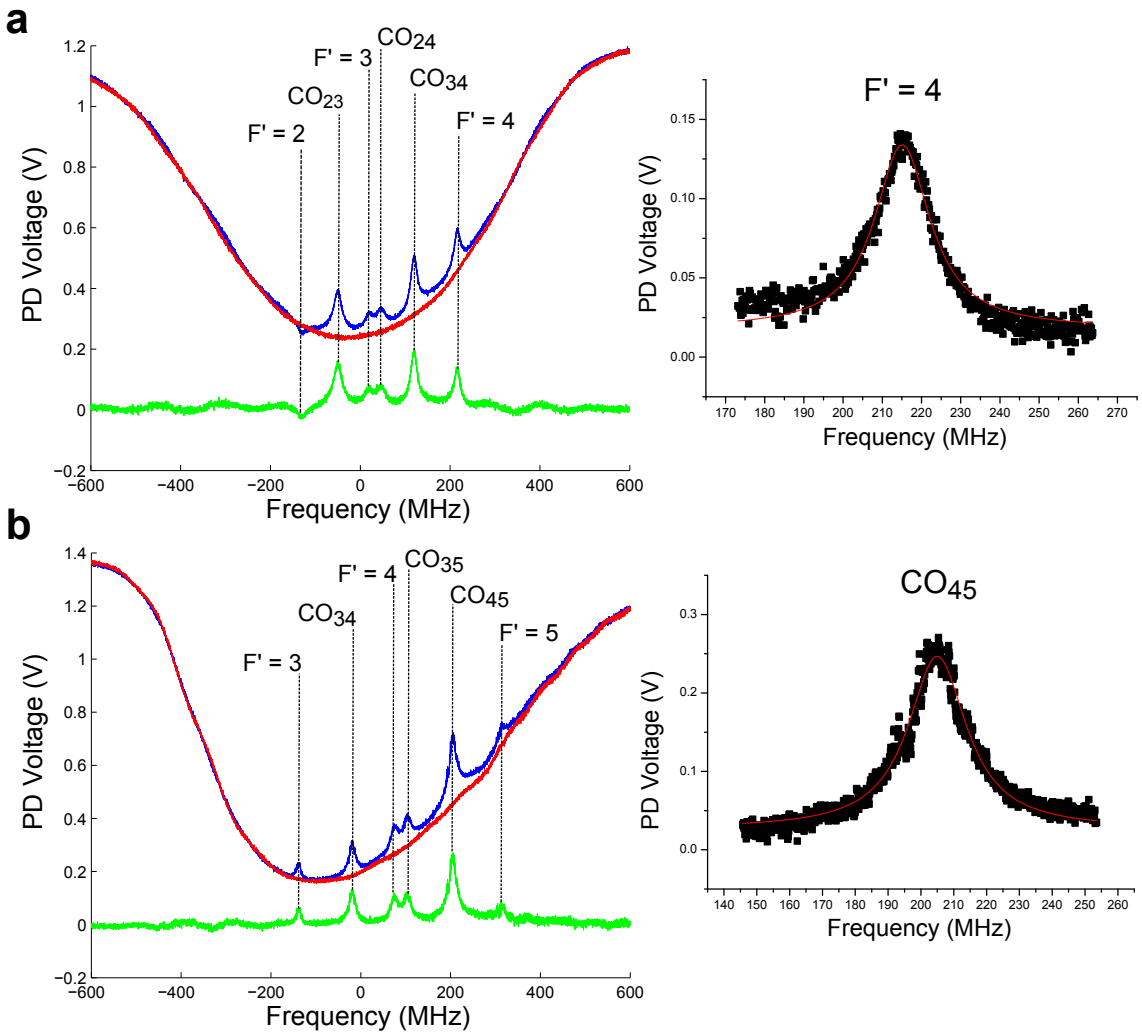

Figure 6.8: **a** Saturated-absorption spectroscopy of the $6^2S_{1/2}(F = 3) \rightarrow 6^2P_{3/2}$ transition in cesium. The red line shows the absorption spectrum with the probe blocked, showing the Doppler linewidth. The inset shows a close-up of the $F' = 4$ transition with Lorentzian FWHM = 17.3 ± 0.4 MHz. The blue line shows the sub-Doppler features arising from saturation spectroscopy and the green line shows the Doppler-free spectrum. **b** Saturated-absorption spectroscopy of the $6^2S_{1/2}(F = 4) \rightarrow 6^2P_{3/2}$ transition. The linewidth of the inset was 21.6 ± 0.3 MHz. The piezoelectric driver voltage calibration was 248 MHz/v.

From the sub-Doppler peaks, an error signal was generated by modulating the current, which changes the frequency of the laser.[8] Consider the phase modulated signal ϕ_{m},

$$\phi_{\mathrm{m}} = \omega_{\mathrm{c}} t + M \sin(\Omega_{\mathrm{m}} t), \tag{6.4}$$

where M is known as the modulation index, Ω_{m} is the modulation frequency, and ω_{c} is the carrier frequency. When locking to a sub-Doppler peak, the base-band signal will have a Lorentzian lineshape but here, to gain some insight, let's consider a simple sinusoidal signal A_{in} with amplitude A_0,

$$A_{\mathrm{in}} = A_0 \sin\left[\omega_{\mathrm{c}} t + M \sin(\Omega_{\mathrm{m}} t)\right]. \tag{6.5}$$

Equation 6.5 can be expressed as an infinite sum of Bessel functions; in the spectral domain the modulation generates sidebands whose relative weights are determined by high-order Bessel functions with the modulation depth as the argument. Here I show that frequency modulation followed by demodulation and integration yields the derivative of the envelope (or carrier) signal. Equation 6.5 can be rewritten by using a trigonometric identity

$$A_{\mathrm{in}} = A_0 \left\{\sin\left(\omega_{\mathrm{c}} t\right) \cos\left[M \sin(\Omega_{\mathrm{m}} t)\right] + \cos\left(\omega_{\mathrm{c}} t\right) \sin\left[M \sin(\Omega_{\mathrm{m}} t)\right]\right\}. \tag{6.6}$$

The nested trigonometric function can be expressed in terms of Bessel functions [267],

$$\cos\left[M \sin(\Omega_{\mathrm{m}} t)\right] = J_0(M) + 2\sum_{k=1} J_{2k} \cos\left(2k\Omega_{\mathrm{m}} t\right) \approx J_0(M) + 2J_2(M) \cos\left(2\Omega_{\mathrm{m}} t\right) + ... \tag{6.7}$$

$$\sin\left[M \sin(\Omega_{\mathrm{m}} t)\right] = 2\sum_{k=0} J_{2k+1} \sin\left((2k+1)\Omega_{\mathrm{m}} t\right) \approx 2J_1(M) \sin\left(\Omega_{\mathrm{m}} t\right) + 2J_3(M) \sin\left(3\Omega_{\mathrm{m}} t\right) + ... \tag{6.8}$$

In the limit $M \ll 1$ the spectral energy is concentrated in the first term of the summations

[8] The preferable approach would be to use an acousto-optic modulator or electro-optic modulator to modulate the frequency and to leave the current unchanged so as to avoid unnecessarily broadening the laser linewdith. In these experiments we are not overly concerned about the laser linewidth and modulate the current directly.

in equations 6.7 and 6.8, resulting in the approximate expression for A_{in} from equation 6.5,

$$A_{\text{in}} \approx A_0 \left[J_0(M) \sin(\omega_c t) + 2J_1(M) \sin(\Omega_m t) \cos(\omega_c t) \right]. \tag{6.9}$$

To generate an error signal, the signal from equation 6.9 is sent to a lock-in amplifier, which demodulates and then integrates the input to produce the output A_{out},

$$A_{\text{out}}(t, \phi) = \int_{t-T}^{t} \sin(\Omega_m \tau + \phi) A_{\text{in}}(\tau) \mathrm{d}\tau, \tag{6.10}$$

where the output is maximum when $\phi = 0$.[9] In the limit $\Omega_m \gg \omega_c$ the lock-in amplifier acts as a phase-sensitive filter, picking out the spectral component in phase with $\sin(\Omega_m t + \phi)$ from equation 6.10. The output signal is, therefore, proportional to the derivative of the input

$$A_{\text{out}} \approx 2J_1(M) \cos(\omega_c t) \propto \frac{\mathrm{d}A_{\text{in}}}{\mathrm{d}t}. \tag{6.11}$$

This can be generalized for an arbitrary signal as the Fourier basis forms a complete basis. In our case, the frequency modulation of a spectral peak results in an amplitude modulated signal that, when filtered, is the derivative of the spectral peak with a zero crossing at the resonance frequency, as shown in figures 6.7**b** and 6.7**c**.[10]

The error signal is then split into two paths. In one path, the high-frequency components of the signal are removed with a low-pass filter (cut-off ∼1 kHz)[11] and the signal modulates the piezoelectric voltage. This changes the cavity length to correct for slow drifts and mechanical vibrations. The second path is sent directly to the current controller to modulate the diode current, providing fast feedback on the order of 1 MHz.[12]

[9] Generally ϕ is adjustable to account for any phase delay introduced by the circuit used to modulate the laser frequency.

[10] Why lock to a peak in the first place, instead of the side of an atomic transition? If the atomic density changes then a change in the optical depth would be erroneously interpreted as a change in frequency, introducing unwanted instability to the frequency of the laser.

[11] Chosen to avoid any mechanical resonances in the piezoelectric stack, which typically occur at frequencies of several kHz.

[12] The feedback frequency is limited to 1 MHz as the frequency response of the diode has a phase shift at several MHz [268].

6.5 Linear absorption in hollow-core fibre

I have now assembled all the tools I need to start studying the light-matter interactions in a kagome-structured HC-PCF. Before I store light in a HC-PCF (proceed immediately to chapter 7 if you cannot wait!), I wanted to verify that I could load a sufficient number of atoms in the fibre core, and efficiently prepare the atoms in the ground state.

6.5.1 Optical depth

The number of atoms in the fibre can be parametrized by the optical depth d, as described in section 5.2.7. The optical depth quantifies the strength of the light-matter coupling in an ensemble-based memory. It is the parameter that defines the efficiency of the memory interaction for an equivalence-class of memory protocols [269, 35, 58, 68, 69]. The optical depth d is defined as the on-resonance absorption of the atomic transition

$$\alpha_{\mathrm{N}} = \frac{d\,(\Gamma_{\mathrm{N}}/2)^2}{(f-f_0)^2 + (\Gamma_{\mathrm{N}}/2)^2}, \tag{6.12}$$

where Γ_{N} is the natural linewidth of the transition (FWHM) and f_0 is the resonance frequency. The on-resonance absorption is

$$d = -\ln\left(I/I_0\right), \tag{6.13}$$

where I_0 is the input intensity and I is the transmitted intensity.

At room temperature, the excited state transition is broadened by the motion of the atoms. The motion of the atoms relative to the beam axis causes a shift in the emission frequency known as Doppler broadening. While the motion is small compared to the speed of light, the fractional change is greater than the fractional change caused by the hyperfine interaction, resulting in the Doppler-broadened spectrum. The Doppler-broadened absorption is

$$\alpha_{\mathrm{D}} = d^* \exp\left[-\frac{1}{2}\left(\frac{f-f_0}{\sigma_{\mathrm{D}}}\right)^2\right], \tag{6.14}$$

where $\sigma_{\mathrm{N}} = f_0\sqrt{k_{\mathrm{B}}T/m_{\mathrm{Cs}}c^2}$ is the standard deviation of the Doppler profile, T is the temperature, m_{Cs} is the mass of a cesium atom, and d^* is the effective optical depth ac-

counting for inhomogeneous broadening. Equating the integrated power spectral densities of equations 6.14 and 6.12 results in the following relationship between d and d^*

$$\frac{d^*}{d} = \sqrt{\pi \ln 2}\left(\frac{\Gamma_N}{\Gamma_D}\right), \tag{6.15}$$

where $\Gamma_D = 2\sqrt{2\ln 2}\sigma_D$ is the FWHM of the Doppler spectrum. For cesium atoms at room temperature $\Gamma_D/\Gamma_N \approx 100$. The effective optical depth is the experimentally accessible parameter whereas the optical depth d is the fictitious on-resonance absorption if there were no inhomogeneous broadening and all the atoms emitted at the same frequency, modulo their natural linewidth. However it is the fictitious number d that is important in determining the strength of the Raman coupling (see section 5.2.7).

The optical depth in the fibre was measured with a low-power, continuous-wave probe beam (10 nW) swept over the Doppler-broadened resonance. An APD (Thorlabs APD110A) detected the transmitted light. The normalized transmission spectrum for the ground-state hyperfine manifold F was fit to the function

$$T(f) = \exp\left[-d^* \cdot \sum S_{FF'} \exp\left(-\frac{1}{2}\left(\frac{f-f_0}{\sigma_D}\right)^2\right)\right], \tag{6.16}$$

where the summation is over the excited-state hyperfine manifolds F'. The Doppler width σ and the optical depth were free parameters and the relative transition strengths of the hyperfine manifolds $S_{FF'}$ and the frequency spacing of the excited-state hyperfine manifolds were fixed parameters. The fit was calculated with a weighted nonlinear least squares algorithm. Simultaneously, I performed saturated-absorption spectroscopy in a bulk vapour cell in order to calibrate the frequency span of the sweep. The overall optical depth, including the atoms inside the fibre and in the vacuum system, was $d^* = 5.7 \pm 0.1$ for the $6^2S_{1/2}(F=3)$ to $6^2P_{3/2}$ transition, as shown in figure 6.9**a**, and $d^* = 5.7 \pm 0.3$ for the $6^2S_{1/2}(F=4)$ to $6^2P_{3/2}$ transition, as shown in figure 6.9**b**. This optical depth corresponds to approximately 10^7 atoms involved in the interaction.

The effective optical depth in the fibre was three approximately one week after breaking the cesium ampoule, rose to six – as shown in figure 6.9 – three months later and continued to rise slowly thereafter. Eventually the vapour pressure inside the fibre will

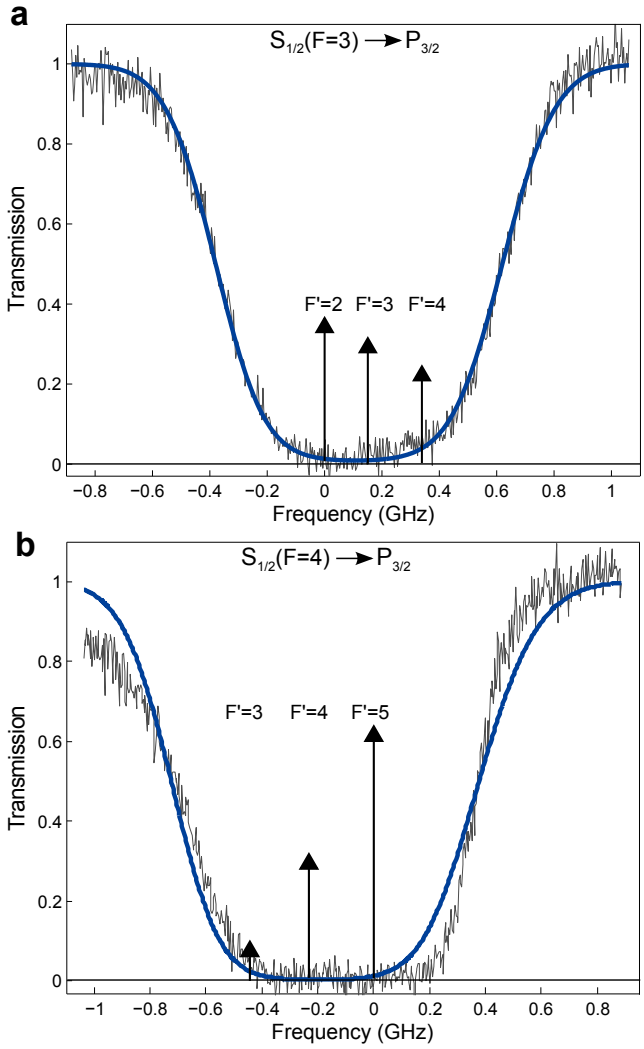

Figure 6.9: **a** Linear absorption in the HC-PCF at the $6^2S_{1/2}(F = 3) \rightarrow 6^2P_{3/2}(F')$ transition. The optical depth $d^* = 5.7 \pm 0.1$ MHz **b** Linear absorption in the HC-PCF at the $6^2S_{1/2}(F = 4) \rightarrow 6^2P_{3/2}(F')$ transition. The optical depth $d^* = 5.5 \pm 0.3$ MHz. The arrows indicate the relative strength of the transitions in the hyperfine manifold.

reach equilibrium with the bulk vapour cell, although this requires the inner surface of the core to be 'ripened' first with a coating of cesium atoms [255]. The length of time for the ripening to occur is unknown, but, based on our observation, is in excess of several months. The fibre temperature was typically 80 °C and increasing the temperature to 100 °C increased the optical depth to 10. Operating at high temperatures, however, increased the reactivity of cesium with the glass viewports, making a vacuum leak more likely.

I estimated that 84±2% of the absorption occurred in the fibre core as opposed to between the viewport and fibre face, which has a separation of 3 mm. To arrive at this

estimate, the probe beam was coupled into a mode confined to the solid silica cladding, avoiding any interaction with atoms confined in the fibre core. The optical depth measured by this probe beam was then compared to the optical depth measured with a mode confined to the fibre core in order to determine the fraction of atoms in the fibre as seen by the probe beam. The silica-cladding mode had a maximum optical depth of 0.90 ± 0.02 compared to 5.7 ± 0.1 for the mode confined to the core. Care was taken to ensure that the optical power in both instances was sufficiently low such that it did not saturate the atomic transition.

The measured optical depth was an order of magnitude larger than that obtained previously in a PBGF [220, 245], which is likely a consequence of the larger core diameter (and possibly lower vacuum pressure). For a Raman memory, the coupling C^2 is given by equation 5.52 as $C^2 \approx d\left(\frac{\Gamma_N}{\delta}\right)\left(\frac{\Omega}{\Delta}\right)^2$, where δ is the bandwidth of the pulse to be stored, Ω is the Rabi frequency of the control field and Δ is the excited-state detuning [51]. Efficient memory operation requires $C^2 \geq 1$. In the adiabatic regime, the Rabi frequency is much less than the detuning and, therefore, the condition for efficient memory becomes $d \gg (\delta\ /\Gamma_N)$. In the presence of inhomogeneous broadening, the effective optical depth d^* is reduced by the ratio of the inhomogeneous broadening Γ_D to the homogeneous broadening (equation 6.15), giving the condition $d^* \gg (\delta/\Gamma_D)$. As an example, storing 1.5 GHz pulses in cesium at room temperature (cf. [73, 72]) requires an effective optical depth $d^* \gg 5$. Therefore, the measured optical depth is slightly lower than that required for a Raman memory. I next investigated ways to transiently increase the optical depth.

6.5.2 Light-induced atomic desorption

The optical depth could be further increased through light-induced atomic desorption (LIAD), a transient process where alkali atoms are ejected from a surface by interaction with light far-detuned from resonance [270]. This effect in most marked in vapour cells coated with paraffin or other spin-preserving compounds [271, 272], and is most efficient when using blue-detuned light [273]. The mechanism is not believed to be thermal and can increase the vapour pressure beyond the thermal equilibrium point [274]. This effect was previously observed with rubidium in uncoated PBGFs [220, 255, 261], where the

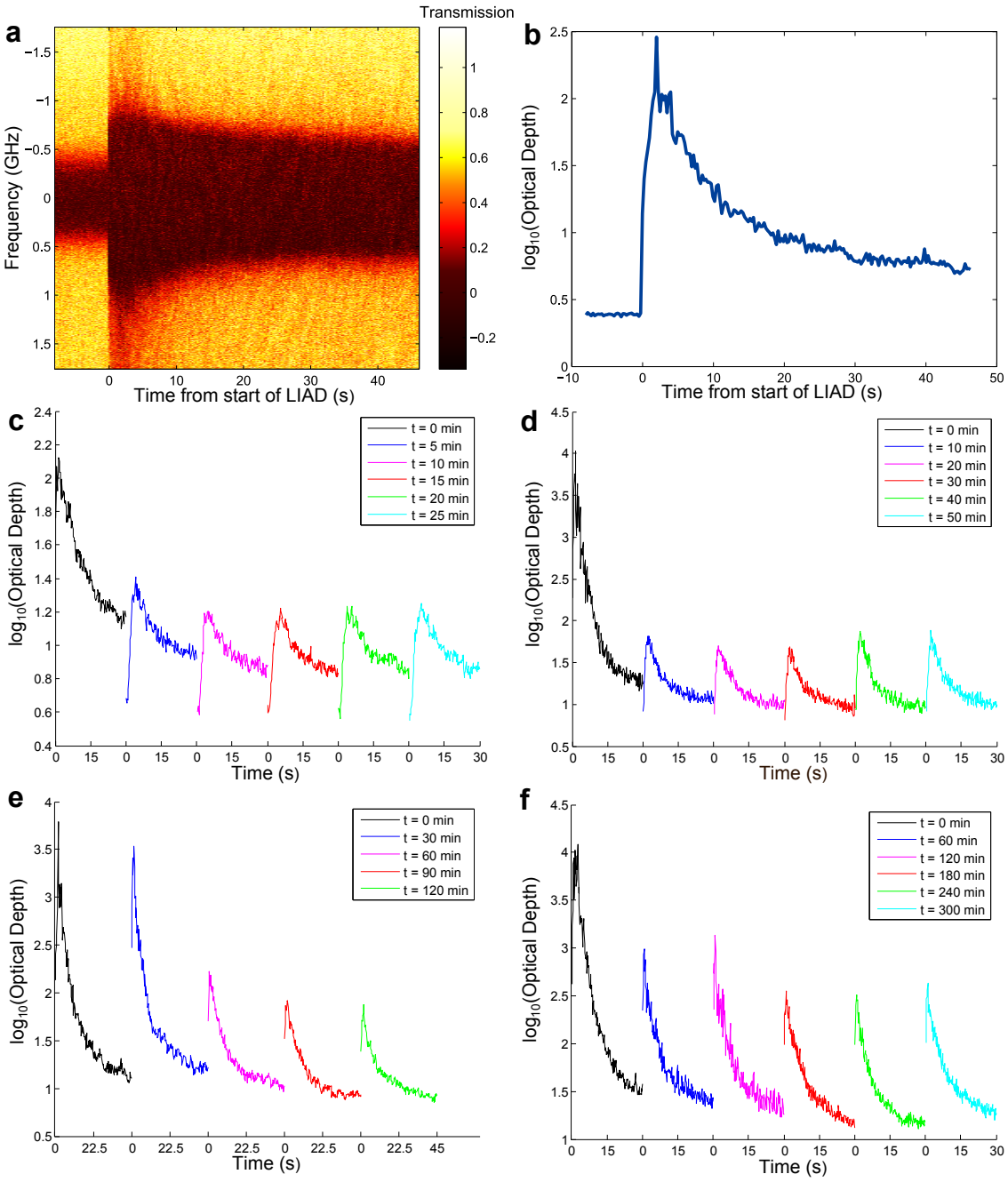

Figure 6.10: **a** Transmission spectra during the application of LIAD (80 mW beam at 780 nm wavelength). **b** Extracted effective optical depth d^* from figure 6.9, plotted as the logarithm base ten. The dashed line indicates the onset of LIAD. Time-dependent optical depth induced by LIAD as a function of a pulse repetition of **c** 5 minutes, **d** 10 minutes, **e** 30 minutes, and **f** 60 minutes. Adapted from reference [223]

optical depth was found to increase by several orders of magnitude.

Here I examined the feasibility of LIAD in kagome-structured HC-PCF using cesium atoms. I studied the evolution of the optical depth during repeated exposure to LIAD. The LIAD beam was derived from a 780-nm, continuous-wave diode laser (Toptica

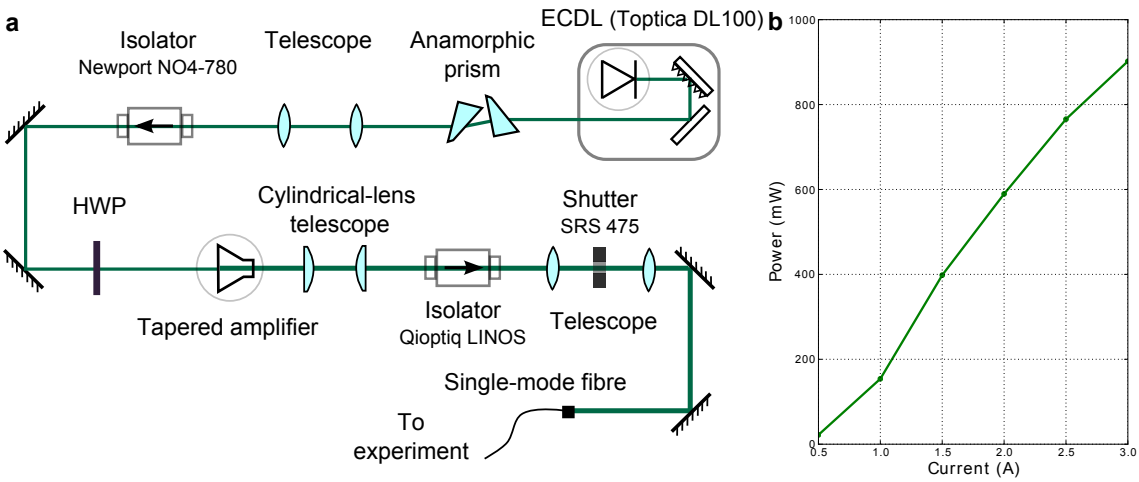

Figure 6.11: **a** Schematic of the LIAD beam setup showing the ECDL, tapered amplifier and the associated optics. The fibre-coupled light was then sent, via a single-mode fibre, to the HC-PCF setup (see chapter 7) **b** Output power from the tapered amplifier before fibre coupling as a function of the current supplied to the tapered amplifier. The maximum fibre-coupled output power was 250 mW.

DL100) amplified using a tapered amplifier, as shown in figure 6.11**a**. One advantage of kagome-structured HC-PCFs is that far-blue-detuned light is guided in the core (down to 600 nm, see figure 6.1). The output power versus current for the tapered amplifier is plotted in figure 6.11**b**; the maximum fibre-coupled output power of the tapered amplifier was 250 mW. The electronic shutter (SRS 475) switched on and off the LIAD beam at controllable intervals.

The LIAD beam was coupled, counter-propagating, into the fibre with the aid of a low-pass optical filter (Semrock BLP01-785R-25). Accounting for the coupling efficiency, the power in the core of the uncoated kagome fibre was 80 mW. After application of the LIAD beam, the optical depth rapidly increased, within 100 ms, by two orders of magnitude, and then slowly decreased over one minute, even though the LIAD beam remained on. Figure 6.10**a** shows an example of how the transmission spectrum changed as LIAD was applied. The effective optical depth is plotted in figure 6.10**a**, and reached an estimated maximum $d^* = 300 \pm 50$. The Doppler width σ during LIAD corresponded to a temperature of 480 K (compared to the cell temperature of 363 K), although in this transient regime atoms may not have reached thermal equilibrium with the fibre [255]. I develop a more robust method for measuring the optical depth during LIAD in section 7.2.

I repeated the application of LIAD at 5-minute, 15 minute, 30-minute, and 60-minute

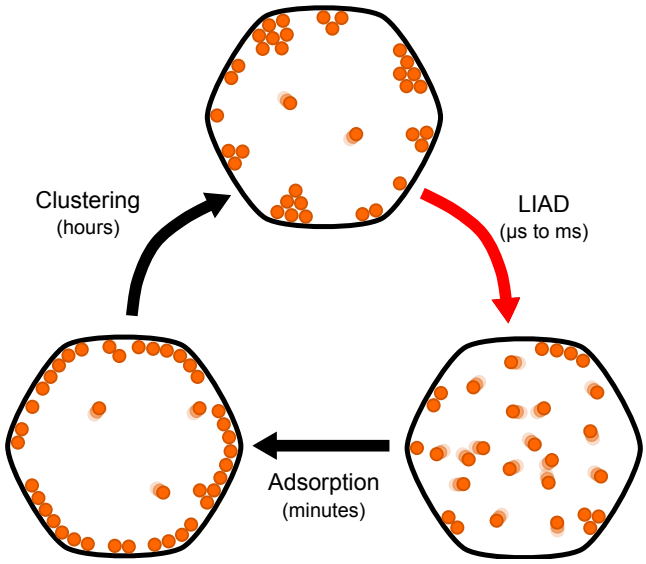

Figure 6.12: Illustration of the proposed mechanism by which LIAD operates as proposed in references [255, 261]. The LIAD desorbs nano-clusters on the surface of the fibre core, causing a transient increase in the optical depth. After several minutes the atoms adsorb back on the wall in a quasi-uniform, unclustered arrangement. After several hours, the atoms form energetically favourable clusters that can be desorbed once again.

intervals, as shown in figures 6.10**c-f**. I observed a third timescale; the peak optical depth decreased with each application of LIAD; the recovery was more pronounced during longer time intervals. Further measurements showed that a full recovery of the maximum optical depth required several hours of quiescence. This is qualitatively consistent with previous observations in a PBGF, where a phenomenological model was proposed involving the formation and plasmon-excitation of nano-clusters [255, 261]. The authors proposed that the cesium atoms form nano-clusters resonant with the LIAD beam, causing the atoms to be excited and ejected from the surface. The atoms readsorb on the surface initially in a random, unclustered configuration and later, after some time – the recovery time – they migrate to form nano-sized clusters once again. This process is illustrated in figure 6.12 with the relevant time-scales.

While this time-scale limits the use of LIAD at these powers, more modest increases in optical depth, sufficient for a quantum memory, can be achieved reproducibly at lower powers with a much shorter time-scale, on the order of hundreds of microseconds [261]. For instance, figure 6.13 shows the repeated application of LIAD for one-second intervals. After 20 to 30 seconds the optical depth induced by LIAD reaches a steady-state value three times higher than its initial value. To summarize this section, I have shown that

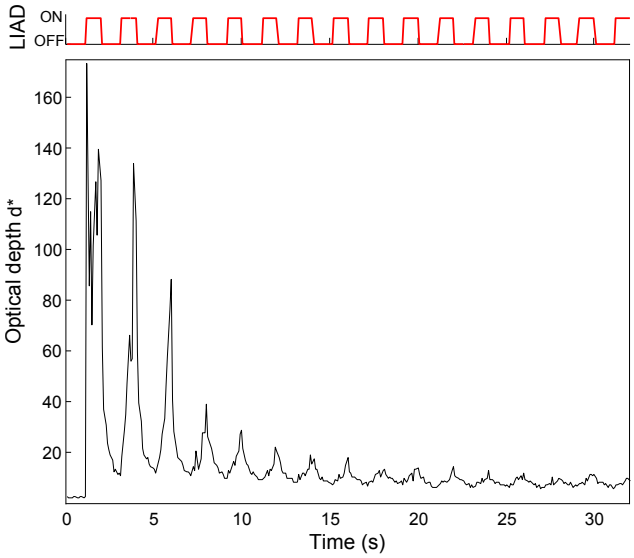

Figure 6.13: Time-dependent optical depth induced by LIAD for a pulse repetition rate of one second. The power of the LIAD beam before the fibre was 255 mW.

extremely high optical depths, $d^* = 300$ and $d = 4.5 \times 10^4$ can be reached with LIAD in kagome fibres, sufficient for a Raman memory.

6.6 Spectroscopy in hollow-core fibre

Next, I examined the linewidth of the atoms confined within the core of the fibre. If the transit time were comparable to the excited-state lifetime, the width of the homogeneous linewidth would be greater than the natural linewidth of the transition. The transit time is important for optical pumping, as will be discussed in section 6.7. It also determines the lifetime of the memory, which will be discussed in section 7.5. I directly measured, with saturated-absorption spectroscopy, the homogeneous linewidth of atoms confined within the core of the fibre. To resolve the excited-state hyperfine manifold, a weak probe beam (10 nW), coupled into the fibre, was scanned over the Doppler-broadened transition and a higher power, counter-propagating pump beam, derived from the same laser, was launched into the fibre.

I now briefly explain the principle of saturated-absorption spectroscopy. Consider counter-propagating, frequency-degenerate pump and probe fields impinging on an ensemble of atoms with a thermal velocity distribution. Atoms with velocity $\mathbf{v}$ will see the optical field with wave vector $\mathbf{k}$ Doppler shifted by $-\mathbf{k} \cdot \mathbf{v}$. Atoms with a non-zero

Doppler shift will see the pump and probe as different frequencies; only one field can be resonant at any instant. However, atoms where $\mathbf{k}\cdot\mathbf{v}=0$ will see no Doppler shift; they can be resonant with the pump and probe fields simultaneously. On resonance, the pump field drives atoms to the excited state, reducing the absorption of the probe, which creates sub-Doppler peaks in the absorption spectrum. In cesium atoms, the splittings of the excited states in the hyperfine manifold are less than the Doppler width, adding an additional set of features known as cross-over resonances. Mid-way between two atomic resonances spaced by Δf, atoms with the Doppler shift $\mathbf{k}\cdot\mathbf{v}=\pm\Delta f/2$ see the probe resonant with one transition and the pump resonant with the other. The pump depletes the ground state, reducing the absorption of the probe beam as both fields address the same ground state. The resultant absorption dip is spaced evenly between the excited states, as shown in figures 6.8 and 6.14**a**.

I now derive how the width of the absorption feature scales with the power – or Rabi frequency – of the pump field (the probe power is fixed at a low power level[13]). Consider the three-level-system equations derived in section 5.1.2 for the case of a two-level atom (known as the Optical Bloch equations). The expressions for the time evolution of the atomic coherences and populations are

$$\partial_t\rho_{\mathrm{ee}} = \mathrm{i}\frac{\Omega}{2}\left(\tilde{\rho}_{\mathrm{eg}}-\tilde{\rho}_{\mathrm{ge}}\right)-\Gamma\rho_{\mathrm{ee}}, \tag{6.17}$$

$$\partial_t\rho_{\mathrm{gg}} = -\mathrm{i}\frac{\Omega}{2}\left(\tilde{\rho}_{\mathrm{eg}}-\tilde{\rho}_{\mathrm{ge}}\right)+\Gamma\rho_{\mathrm{ee}}, \tag{6.18}$$

$$\partial_t\tilde{\rho}_{\mathrm{ge}} = -\left(\frac{\Gamma}{2}+\mathrm{i}\Delta\right)\tilde{\rho}_{\mathrm{ge}}-\mathrm{i}\frac{\Omega}{2}\left(\rho_{\mathrm{ee}}-\rho_{\mathrm{gg}}\right), \tag{6.19}$$

$$\partial_t\tilde{\rho}_{\mathrm{eg}} = -\left(\frac{\Gamma}{2}+\mathrm{i}\Delta\right)\tilde{\rho}_{\mathrm{eg}}+\mathrm{i}\frac{\Omega}{2}\left(\rho_{\mathrm{ee}}-\rho_{\mathrm{gg}}\right), \tag{6.20}$$

where the tilde denotes the slowly varying coherences, and the coherence rate is lifetime-limited (i.e. $\gamma_{\mathrm{e}}=\Gamma/2$). The steady state solution to these equations can be found by

[13] It is not sufficient to state that the intensity of the probe remains much less than the saturation intensity; the product of the Rabi frequency of the probe field and the transit time must be less than one.

setting $\partial_t \rho_{ij} = 0$;

$$\tilde{\rho}_{\mathrm{ge}}^{t\to\infty} = \frac{\mathrm{i}\Omega}{\Gamma/2 + \mathrm{i}\Delta}\left(\rho_{\mathrm{ee}} - 1\right), \tag{6.21}$$

$$\rho_{\mathrm{ee}}^{t\to\infty} = \mathrm{i}\frac{\Omega}{2\Gamma}\left(\tilde{\rho}_{\mathrm{eg}} - \tilde{\rho}_{\mathrm{ge}}\right). \tag{6.22}$$

Combining the two previous equations yields

$$\rho_{\mathrm{ee}}^{t\to\infty} = \frac{\left(\Omega/\Gamma\right)^2}{1 + \left(\frac{2\Delta}{\Gamma}\right)^2 + \frac{2\Omega^2}{\Gamma^2}}. \tag{6.23}$$

Equation 6.23 describes the excited state population as a function of detuning Δ, pump Rabi frequency Ω and natural linewdith Γ. In the weak pump limit $\Omega \gg \Gamma$, the excited-state population $\rho_{\mathrm{ee}}^{t\to\infty} = (\Omega/\Gamma)^2$, scaling linearly with intensity. The spectral linewidth is simply the natural linewidth Γ. In the strong pump limit $\Omega \gg \Gamma$, the excited-state population asymptotes to $1/2$ and the spectral FWHM of the absorption is $\sqrt{2}\Omega$. The non-linear response to the probe field is caused by the saturation of the transition, which underlies saturated-absorption spectroscopy discussed above. The general expression for the spectral linewidth Γ_{p} of the transition at steady-state is

$$\Gamma_{\mathrm{p}} = \Gamma\sqrt{1 + \frac{2\Omega^2}{\Gamma^2}} = \Gamma\sqrt{1 + \frac{I}{I_{\mathrm{sat}}}}, \tag{6.24}$$

where I_{sat} is termed the saturation intensity and I is the intensity of the pump field. The spectral broadening caused by the pump power is known as *power broadening*.

The experimentally measured saturated-absorption spectrum in the HC-PCF is shown in figure 6.14**a**. The width of the $6^2S_{1/2}(F = 3)$ to $6^2P_{3/2}(F' = 4)$ transition was measured as a function of the pump intensity I scaled to the experimentally determined saturation intensity I_{sat}. Outside the vacuum chamber, saturated-absorption spectroscopy was performed in a bulk vapour cell to estimate the homogeneous linewidth in a parameter range where transit-time broadening is known to be negligible; this served as a verification for my analysis. The Doppler-free linewidths are plotted in figure 6.14**b**, along with a weighted nonlinear least-squares fit according to the equation 6.24. The pressure broadening due to cesium-cesium collisions is negligible at these atomic densities in both the

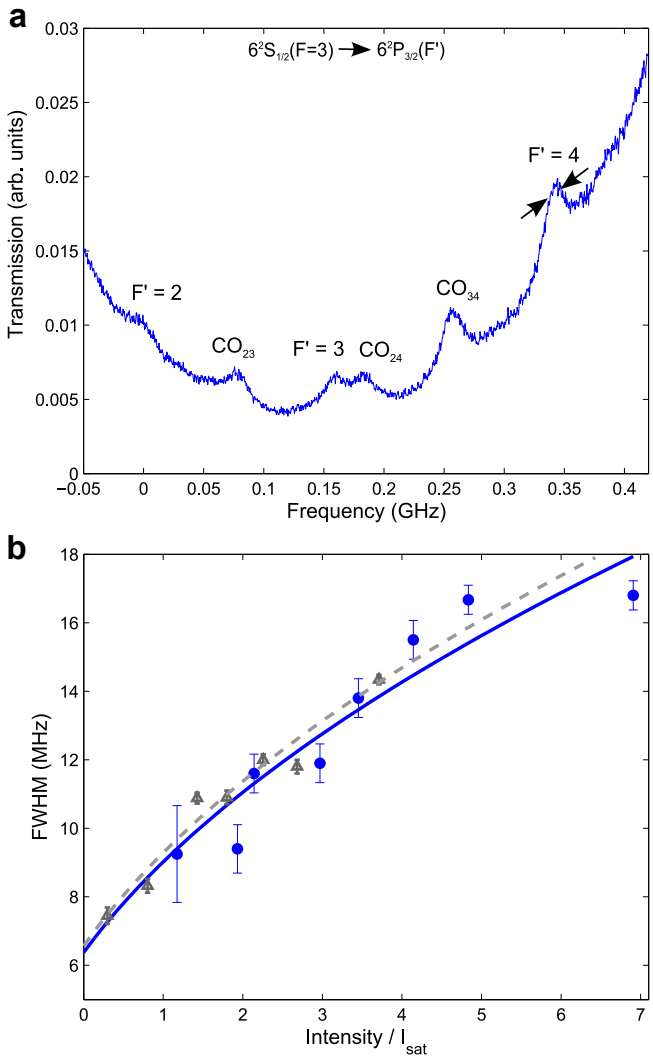

Figure 6.14: **a** Saturated-absorption spectroscopy of atoms inside the kagome fibre, adapted from reference [223]. The probe power was 10 nW ($0.2 \cdot I_{\mathrm{sat}}$). CO_{23} refers to the cross-over resonance of the $F' = 2$ and $F' = 3$ excited-state hyperfine manifold. **b** The width of the $(F = 3)$ to $(F' = 4)$ transition as a function of intensity (power). Blue circles refer to measurements in the kagome fibre, and the blue solid line is the fit (see text). Grey triangles refer to measurements made in the bulk vapour cell, and the grey dashed line is the fit.

fibre and the reference cell [275].

The linewidth of the sub-Doppler features were measured as a function of pump power to determine the unbroadened homogeneous linewidth. The measured linewidth was compared to the natural linewidth of the cesium transition in order to quantify the presence of any additional transit-time broadening. The homogeneous linewidth in the fibre was 6 ± 2 MHz and the saturation power was 50 ± 20 nW, which agrees with the homogeneous linewidth in the vapour cell of 6.5 ± 0.6 MHz; both are consistent with the natural

linewidth of 5.2 MHz [266]. There was no apparent transit-time broadening within the resolution of our measurement. In contrast, previous measurements done with commercially available hollow-core photonic crystal fibre, with a 6 μm core, measured a homogeneous linewidth of 27 $\pm$ 3 MHz [276], indicating significant transit-time broadening. Furthermore, the saturated-absorption spectroscopy shows that the transit time exceeds the excited-state lifetime in the large-core kagome fibre, a critical condition for initializing pure quantum states.

6.7 Optical pumping

In a Λ-system quantum memory, the atoms must be efficiently prepared into the ground state by means of optical pumping. At room temperature, however, the two hyperfine ground-state manifolds of cesium are essentially equally populated; thermal excitations in the storage state can be read out during retrieval of the stored excitation via spontaneous Raman scattering, contributing noise to the memory process and reducing the fidelity of the memory. The number of signal photons to noise photons is determined by the optical pumping efficiency η_{p}; the signal-to-noise ratio is then approximately [73]

$$\mathrm{SNR} = 1/(1-\eta_{\mathrm{p}}). \tag{6.25}$$

In addition, in the limit of equal populations, the competing processes of absorption and emission reduce the memory efficiency; therefore, efficient optical pumping is critical for the realization of a quantum memory. In a confined geometry such as in a hollow-core fibre, the atoms should ideally be optically pumped during the time that the atoms traverse the optical mode in the fibre. Collisions with the fibre wall can, with some probability, thermalize the hyperfine polarisation of the atoms [277]. For cesium, the thermalization probability per collision is approximately one half, although this number is not well constrained [278]. The limiting time-scale for optical pumping is the excited-state lifetime, since multiple spontaneous decay events are required to prepare all the atoms in the ground state. The transit time should ideally exceed the excited-state lifetime. In a 26-μm fibre, the mean transit time across the optical mode (with a 12 μm Gaussian

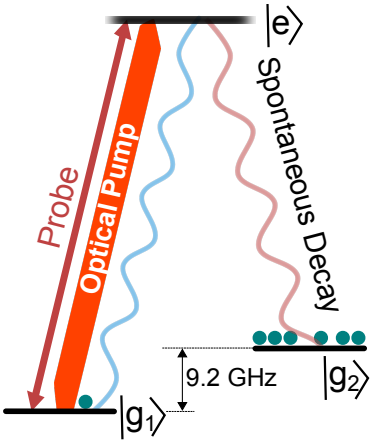

Figure 6.15: Schematic of the energy levels and the optical beams for optical pumping, where $|e\rangle$ is the excited-state $6^2P_{3/2}(F = 2, 3, 4, 5)$ D_2 line, $|g_1\rangle$ is the $6^2S_{1/2}(F = 3)$ manifold and $|g_2\rangle$ is the $6^2S_{1/2}(F = 4)$ manifold.

beam width) is ∼100 ns and the excited-state lifetime of the D_2 line is 30 ns [266]. This motivated an experimental study of the maximum achievable optical pumping efficiency in the fibre.

I measured the optical pumping efficiency as a function of the optical pumping power, parametrized by the Rabi frequency $\Omega = \mathbf{d} \cdot \mathbf{E}_\mathrm{p}/\hbar$, where $\mathbf{d}$ is the dipole moment and $\mathbf{E}_\mathrm{p}$ is the electric field of the pump beam. A weak probe beam (10 nW) was scanned in frequency over the $6^2S_{1/2}(F = 3)$ to $6^2P_{3/2}$ hyperfine manifold in order to measure the change in optical depth due to the counter-propagating optical pumping beam. The pump beam was derived from a separate diode laser and remained on for the duration of the measurement. The pump and probe beams had orthogonal linear polarizations. The frequency of the optical-pump laser was locked to the $6^2S_{1/2}(F = 3)$ to $6^2P_{3/2}(F' = 3)$ sub-Doppler peak and the linewidth was 1 MHz. A schematic of the energy levels with the optical fields is shown in figure 6.15.

Figure 6.16**a** shows the change in the transmission over the entire Doppler-broadened profile due to optical pumping, where the Rabi frequency of the pump was 650 MHz. From the change in optical depth, I extracted the optical pumping efficiency, that is the percentage of atoms in the ground state, which is plotted as a function of the Rabi frequency in figure 6.16**b**. The optical depth, in the linear regime, is proportional to the imaginary component of the linear susceptibility, which is in turn proportional to the

coherence between the ground and excited state,

$$d \propto \mathrm{Im}\left\{\chi^{(1)}\right\} \propto \rho_{12}. \tag{6.26}$$

According to the optical Bloch equations and, specifically, equations 6.19 and 6.20, the coherence is proportional to the population difference between the two states,

$$\rho_{12} \propto (\rho_{22} - \rho_{11})\,. \tag{6.27}$$

Initially, the population was evenly distributed between the two hyperfine levels ($\rho_{11} = \rho_{33} = 1/2$, $\rho_{22} = 0$) and, therefore, the change in optical depth can be expressed as

$$\frac{\Delta d}{d_\mathrm{i}} = \frac{1}{2}\left(\rho_{11} - \frac{1}{2}\right) = \eta_\mathrm{p}, \tag{6.28}$$

where d_i is the initial optical depth.

The maximum pumping efficiency that I measured was $\eta_\mathrm{p} = 90 \pm 1\,\%$ for $\Omega_p = 700$ MHz, which exceeded the Doppler-broadened linewidth of the transition (FWHM = 420 MHz). I measured the same optical pumping efficiency with the LIAD beam switched on. Figure 6.16**a** represents the first observation of efficient pumping in a hollow-core fibre with a warm alkali vapour; previous experiments with small-core PBGFs were limited to an optical pumping efficiency of 55% [222]. From equation 6.25, the signal-to-noise ratio for $\eta_\mathrm{p} = 0.9$ is equal to 10, which is favorable for single-photon-level storage for a quantum memory.

My results imply that a narrow-linewidth pump beam was sufficiently power-broadened in order to optically pump all velocity classes in the Doppler-broadened transition. This represents a significant advantage of the hollow-core geometry as compared to free-space systems: high Rabi frequencies can be achieved with relatively low, and easily accessible, optical power (<1 mW). This is in contrast to previous experiments with bulk vapour cells [73, 72], where, instead of power broadening, optical pumping required collisions with a buffer gas in order to sweep all the atoms through the velocity class resonant with the frequency of the laser diode.

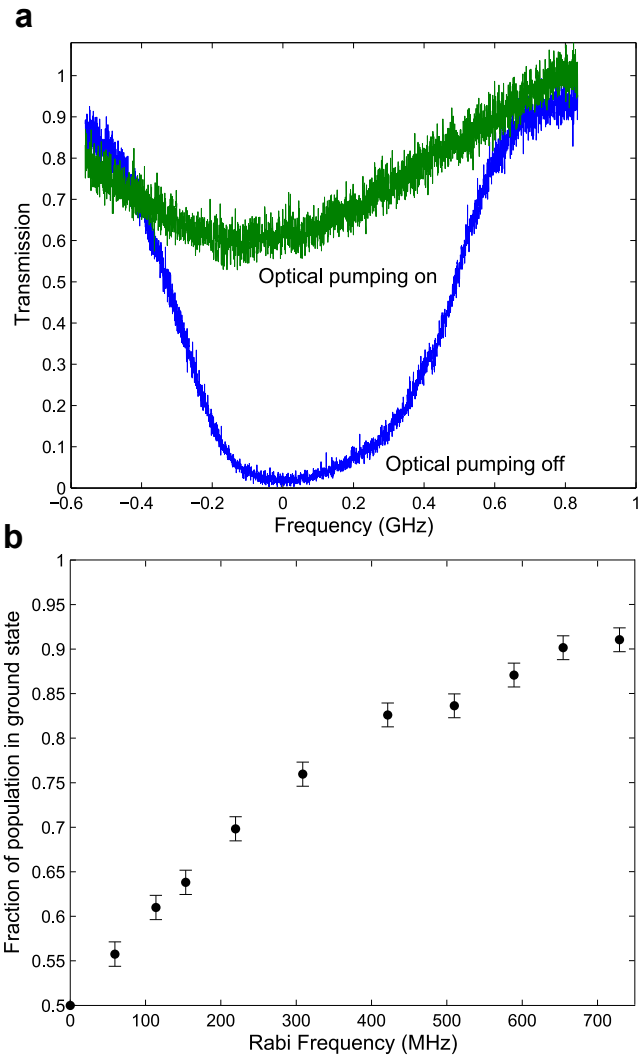

Figure 6.16: **a** Optical pumping of the Doppler-broadened transition with a fixed-frequency pump at a Rabi frequency of 650 MHz. **a** The fraction of the population pumped into the ground hyperfine state ($F = 4$) as a function of the Rabi frequency of the optical pumping beam, adapted from reference [223]

6.8 Summary

This chapter has laid the groundwork for the demonstration of light storage in a kagome-structured hollow-core photonic crystal fibre. I built an ultra-high vacuum system to mount the HC-PCF and load it with cesium atoms. I set up a stabilized external-cavity diode laser in order to measure the linear and non-linear absorption of cesium confined to the fibre core. I assessed whether the optical depth and optical pumping efficiency were compatible with a storing light at the quantum level. I carefully quantified the optical depth in the hollow-core fibre across the two hypefine levels in the ground state

manifold, where the effective optical depth $d^* = 5.7 \pm 0.1$ for the $6^2S_{1/2}(F = 3)$ to $6^2P_{3/2}$ transition, and $d^* = 5.7 \pm 0.3$ for the $6^2S_{1/2}(F = 4)$ to $6^2P_{3/2}$ transition. I showed that the optical depth could be increased by two orders of magnitude using light-induced atomic desorption, reaching an optical depth for a far-detuned Raman memory.

I then investigated the transit-time broadening as a result of the small optical mode. I measured the homogeneous linewidth in the HC-PCF using sub-Doppler saturated-absorption spectroscopy; the homogeneous linewidth was 6 ± 2 MHz, the narrowest linewidth measured in such a system. I then observed, for the first time, efficient optical pumping in a hollow-core photonic crystal fibre; the maximum efficiency was $90 \pm 1\,\%$.

7

Light Storage in a HC-PCF

Storing information encoded in light is desirable for optical signal processing [279, 76]; it has remained a long-standing goal to develop a robust optical buffer that could supplant bulky fibre delay lines for optical communication [280, 281]. Additionally, the ability to store the full quantum state of light in a quantum memory is critical for the realization of non-trivial quantum information processing tasks [16, 14], as discussed in chapter 2. Optical memories require efficient light-matter interaction mediated by a well-defined optical mode, which can be accomplished with an integrated waveguide architecture, as discussed in section 6.1. Photonic crystal fibres, in particular, can enhance light-matter interactions, and have engendered a broad range of nonlinear effects outlined in section 6.2. The storage of light, however, has proven elusive. In this chapter I present the first observation of light storage in a HC-PCF. I show that GHz-bandwidth laser pulses can be stored in a warm vapour of cesium atoms confined to a HC-PCF with an

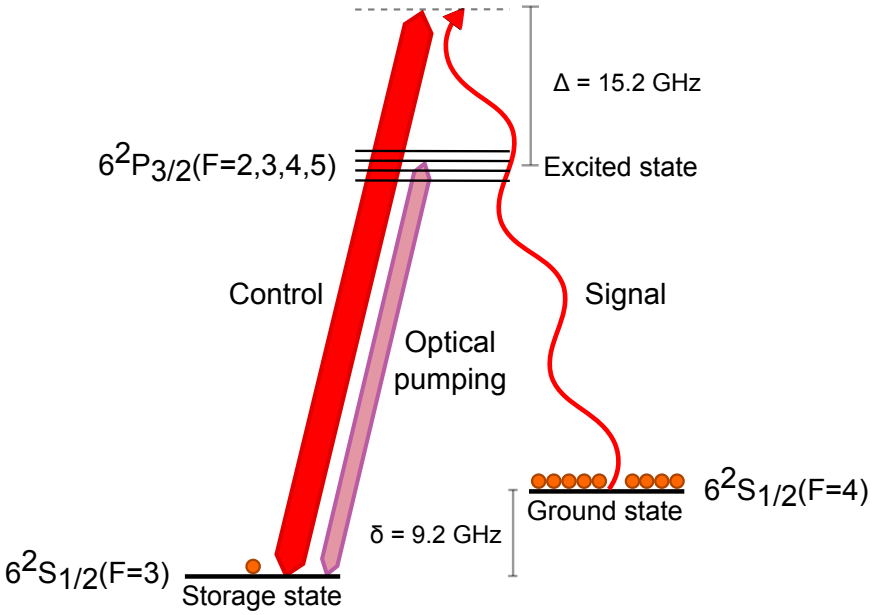

Figure 7.1: Three-level Λ-system showing the signal and control field in two-photon resonance detuned from the D_2 excited-state manifold by 15.2 GHz. The control and signal pulses had a bandwidth of 1.0 GHz at a centre wavelength of 852 nm. The optical pumping beam was switched off with a Pockels cell 5 ns prior to the memory interaction. The orange circles represent the population of the cesium atoms in the hyperfine levels. The LIAD field, which was far blue-detuned from the atomic transition, is not shown.

efficiency of $27 \pm 1\%$. The control pulse energy was two hundred times less than previous implementations of a Raman memory [73, 72]. I also show that single-photon-level pulses can be stored with a signal-to-noise ratio larger than one (SNR = 2.6:1). Finally, I measure the memory lifetime to be 27 ± 9 ns.

Before I present these results, I will first summarize the experimental techniques used to demonstrate the storage of light in a HC-PCF. I will describe the oscillator and optical components used to generate the signal and control field (section 7.1.1), the optical pumping setup (section 7.1.2), the coupling of the optical fields into the HC-PCF (section 7.1.4), the filtering and detection of the retrieved signal (section 7.1.5), the data acquisition and control system (section 7.1.6), and, finally, the method I developed to measure the optical depth (section 7.2).

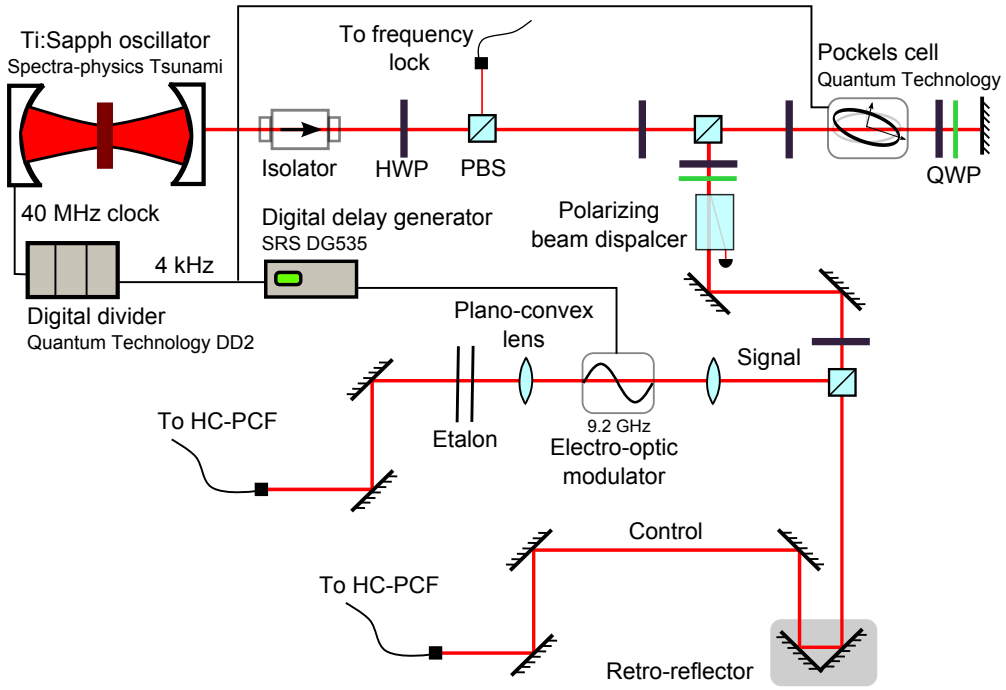

Figure 7.2: Schematic showing the generation of the signal and control field from the laser oscillator. The Pockels cell was synchronized to the laser oscillator pulse repetition frequency – divided by two – and reduced the repetition rate of the experiment from 80 MHz to several kHz. An electro-optic modulator created sidebands at 9.192 GHz and the red-detuned sideband was selectively filtered with a Fabry-Pérot etalon. The retro-reflector was used to adjust the temporal delay between the signal and control pulse. Both signal and control fields were fibre-coupled and sent to the HC-PCF setup (see figure 7.4).

7.1 Setup for memory experiment

7.1.1 Oscillator and pulse preparation

The Raman resonance condition is met when the two optical fields – the strong control field and the weak signal field (section 5.2.1) – are separated in frequency by the splitting of the ground and storage states (here 9.192 GHz); the energy levels and optical modes for the memory interaction are shown in figure 7.1. The signal and control pulses were derived from a mode-locked titanium-sapphire laser with an intracavity Gires-Tournois interferometer, as described in section 5.4. The laser produced an 80-MHz pulse train of 1.0-GHz-bandwidth pulses with a centre wavelength of 852 nm. The frequency of the laser was locked, using a cavity, to the frequency of a diode laser (section 6.4.1) that was locked to the $6^2S_{1/2}(F = 3) \rightarrow 6^2P_{3/2}(F')$ transition (section 5.4.3).

The repetition rate of the experiment was reduced from 80 MHz to between 1 and

8 kHz using a Pockels cell (Quantum Technology QC) triggered by a signal synchronized to the repetition rate of the laser oscillator. The Pockels cell was double-passed (as it was designed for use in a cavity) with a measured extinction ratio of 3000:1. The Pockels cell had a rise time of < 1 ns and a minimum pulse spacing of 100 ns. For each iteration of the experiment, the Pockels cell selected two pulses, which I refer to as the read-in and read-out time bins. The reduced pulse train was then split into two spatial modes using a polarizing beam splitter to form the control and signal fields, as shown in figure 7.2. The signal pulse was then generated with an electro-optic modulator (EOM) driven at 9.192 GHz, which created two sidebands.[1] The baseband and blue-detuned sideband were filtered with an air-spaced etalon (FSR = 38.9 GHz) in order to isolate the red-detuned sideband for the signal field. The EOM was only switched on for the duration of the read-in time bin; the response time of the EOM and microwave switch was 3-4 ns. The finite response time of the EOM caused a residual amount of signal power to be present in the read-out time bin, which was subtracted from all the calculations of the memory efficiency presented later in the chapter. The signal and control fields were then launched into separate polarization-maintaining single-mode fibres and sent to the HC-PCF.

7.1.2 Optical pumping

The atoms must be prepared in the ground state before the signal field is stored. Efficient optical pumping in the HC-PCF was previously shown in section 6.7. The optical pumping beam was generated by an an external-cavity diode laser stabilized to the $6^2S_{1/2}(F = 3) \rightarrow 6^2P_{3/2}$ transition, as discussed in section 6.4.1 and illustrated in figure 7.1. The beam was launched counter-propagating into the HC-PCF. The in-coupled power of the optical pumping beam was 770 μW and the out-coupled power was 330 μW; the total coupling efficiency of the optical pumping beam was 43%.

In the initial memory experiments, the optical pumping beam remained on during the memory interaction. The optical pumping beam excited atoms from the storage state into the excited state, at which point they spontaneously decayed with a time constant of 30 ns. The storage time was 12.5 ns and I initially assumed that the decay would be

[1] The modulation strength imposed on the light was small, and the higher-order sidebands had a negligible amount of power.

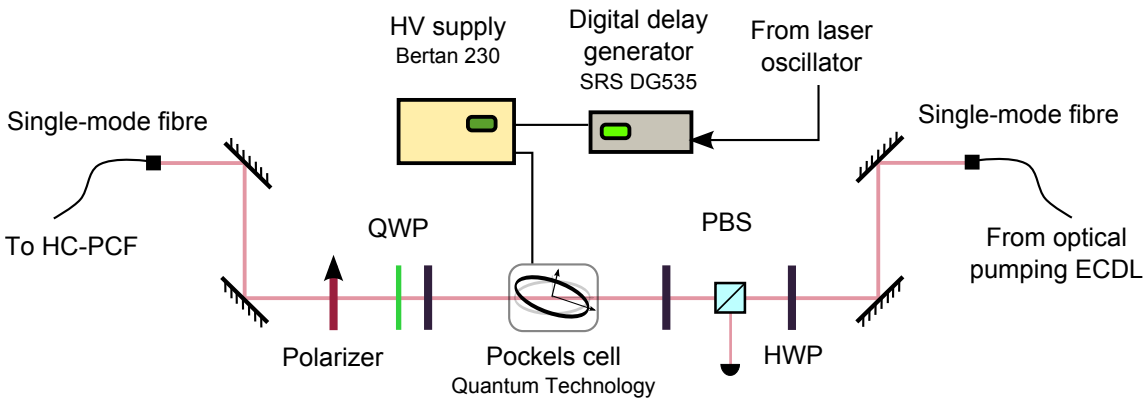

Figure 7.3: Schematic showing the optical pumping gated by the Pockels cell. The laser oscillator triggered the operation of the Pockels cell through the high-voltage power supply delayed by the digital delay generator.

minor over this period. However, the first measurements of the memory efficiency showed a high storage efficiency ($> 50\%$) and a very low retrieval efficiency, on the order of a few percent, which implied that the memory lifetime was much shorter than expected. I realized that the optical pumping beam was inducing a spatially varying Stark shift across the fibre core. The Rabi frequency of the optical pump was extremely high – on the order of several hundred MHz in order to optically pump the entire Doppler-broadened spectrum – making the dephasing rate extremely short (on the order of the inverse of the Rabi frequency).

In order to test this hypothesis, I installed a switch in the path of the optical pumping beam in order to quickly turn off the optical pumping during the light storage. The response time of the switch had to be much shorter than the transit time (100 ns), which was realized with a second Pockels cell (Quantum Technology QC), as shown in figure 7.3. The optical pump beam was turned on 300 ns prior to the light storage, and turned off approximately 5 ns prior to the memory interaction. The timing of the Pockels cell was controlled by a digital delay unit (SRS DG535) synchronized to the laser oscillator and connected to a high-voltage power supply (Bertan 230). The first data after the Pockels cell was installed – the culmination of three months of investigation – showed an order of magnitude increase in the memory efficiency, to on the order of 20%, confirming that the optical pump had been limiting the memory efficiency. The switching was performed with a Pockels cell with extinction ratio of 40, which was limited by transient oscillations

in the driving voltage when the Pockels cell was switched off (the extinction ratio when switching on from off was greater than 3000). We will return to a discussion of the memory decoherence in section 7.5.

7.1.3 LIAD

The optical depth was not high enough to observe light storage at (quasi-)steady state in the HC-PCF, as discussed in section 6.5. As a result, I used light-induced atomic desorption (LIAD) to transiently increase the optical depth (see section 6.5.2). The laser used for LIAD had an operating wavelength of 780 nm and was amplified with a tapered amplifier. The optical field was coupled, counter-propagating, into the HC-PCF using a dichroic mirror (Semrock BLP01-785R-25). The power coupled into the HC-PCF was 75 mW and the LIAD beam remained on during the measurement run.[2] The LIAD beam could be switched on and off with an electronic shutter connected to the data acquisition and control program discussed in section 7.1.6.

The LIAD increased the optical depth by two orders of magnitude, which decayed over the period of a minute; the full effect could only be repeated every few hours and a more modest effect more frequently [223]. This remained a significant impediment to acquiring data with the experiment. The short term solution was to acquire as much data as possible during each acquisition. I set up computer-controlled fast shutters linked to a time-tagged data acquisition system in order to make measurements with all the relevant permutations of the optical fields switched on and off. Longer term solutions to this problem will be discussed in the chapter 8.

7.1.4 HC-PCF optical setup

The signal and control pulses, separated in frequency by 9.2 GHz, were combined on a PBS so that they were co-propagating and orthogonally polarized, as depicted in figure 7.4. The signal and control pulses were temporally overlapped with a retro-reflector. The overlap was initially set by measuring the arrival times on a fast photodiode and then more

[2] I experimented with turning the LIAD beam off for short periods during the measurements and did not see any positive effect on the memory efficiency. As switching it on and off introduced another time-scale, I decided to leave the LIAD on during the measurements.

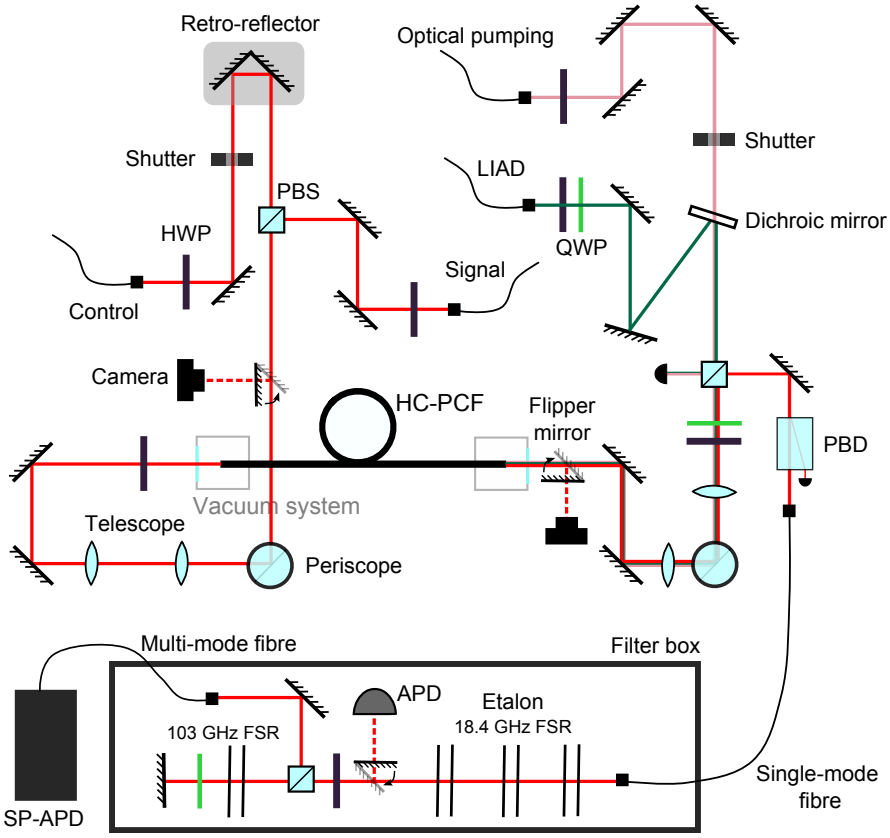

Figure 7.4: Schematic showing HC-PCF with signal, control, optical pumping and LIAD optical fields. The cameras were used to image the forward- and counter-propagating spatial modes from the HC-PCF. The signal field was filtered from the control field using a PBS, polarizing beam displacer (PBD) and a series of etalons. An APD and set of three etalons were used for the classical memory results. For the single-photon-level measurements, an additional etalon (double-passed) and the single-photon APD (PerkinElmer SPCM-AQRH-R-FC) were used.

carefully by measuring the interference visibility between identical pulses sent through the signal and control spatial modes. The signal and control were then launched into the HC-PCF using an aspheric lens (Thorlabs C260TME-B, focal length = 15.3 mm). The coupling efficiency of the signal and control was $65 \pm 1\,\%$, factoring out losses from the uncoated glass viewport. Interestingly, the coupling efficiency seemed to increase slightly as the fibre was loaded with cesium atoms. A detailed description of the HC-PCF and the vacuum apparatus was presented in sections 6.2 and 6.3, respectively. The optical pumping and LIAD optical fields were coupled, counter-propagating, into the HC-PCF with a coupling efficiency of 50% and 25%, respectively.

7.1.5 Filtering and detection

The signal retrieved from the memory needed to be separated from the other optical fields, especially the control field. The retrieved signal was filtered from the control field according to the polarization and frequency of the optical modes. The orthogonal control and signal fields were separated according to their polarization with a polarizing beam splitter and a polarizing beam displacer (PBD), as shown in figure 7.4. The total extinction ratio of the polarization filtering was $> 10^{-3}$, limited by the extinction ratio of the PBS used to initially combine the two fields. In the future, it may be desirable to replace this with a PBD.

The filtering of the control frequency relative to the signal frequency was implemented with a series of three planar air-spaced etalons with a free spectral range of 18.4 GHz and finesse of 10. The relative attenuation of the control field compared to the signal field was 10^{-2} for each etalon, for a total extinction ratio of 10^{-6}. The retrieved signal was coupled into a single-mode fibre and then sent through the etalons, which were angle-tuned in order to maximize the transmission; the total transmission of the signal through each etalon was approximately 65%. As discussed in section 5.5, the FSR of the etalons exactly coincided with the frequency shift of the anti-Stokes noise photons (see section 7.4), which was detrimental for the storage of single-photon-level pulses. An additional filter – a double-passed 103-GHz-FSR planar air-spaced etalon – was added on order to eliminate photons at the anti-Stokes sideband.

For the bright coherent-state memory measurements (section 7.3), the signal was detected with a high-sensitivity APD (Menlo Systems APD210) connected to a GHz-bandwidth oscilloscope (LeCroy WavePro 7100). For the single-photon-level measurements, a single-photon APD (PerkinElmer SPCM-AQRH-R-FC) operated in Geiger mode detected the signal photons. The photons in the read-in and read-out time bins were recorded with a field-programmable gate array (Xilinx) and, simultaneously, with a time-to-amplitude converter and multi-channel analyser.

The estimation of the number of signal photons sent into the memory N_{true} was backed out from the number of detected photons per pulse N_{det} by dividing by $p_{\text{det}} \cdot p_{\text{mmf}} \cdot p_{\text{etl}} \cdot p_{\text{pbf}} \cdot p_{\text{flt}} \cdot p_{\text{smf}} = (2.0 \pm 0.1) \times 10^{-2}$, where $p_{\text{det}} = 0.45 \pm 0.05$ was the APD detection efficiency;

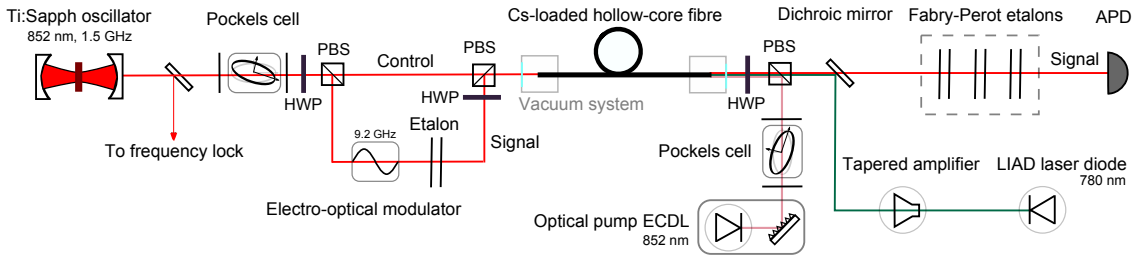

Figure 7.5: Simplified schematic of the experimental setup from figure 7.6 showing the four optical modes, adapted from reference [282].

$p_{\mathrm{mmf}} = 0.90 \pm 0.02$ was the coupling efficiency into the multi-mode fibre leading to the APD, $p_{\mathrm{etl}} = 0.15 \pm 0.01$ was the combined transmission through three 18-GHz etalons and one 103-GHz etalon double-passed; $p_{\mathrm{flt}} = 0.70 \pm 0.01$ was the transmission through an 852-nm bandpass filter; and $p_{\mathrm{smf}} = 0.7^2 = 0.49 \pm 0.02$ was the coupling efficiency of two single-mode fibres that connected the hollow-core fibre output to the filtering stage.

7.1.6 Data acquisition and control system

The data acquisition and control system recorded the signal pulses – interfaced through the high-speed oscilloscope – and synchronized the operation of the shutters on the control, optical pumping, and LIAD paths; the details of the program are presented in Appendix D. I will now describe its operation during a typical experimental run, which is depicted in figure 7.1.1**a**. When the program was gracefully started, the oscilloscope settings were loaded and the oscilloscope was primed to record a sequence of 10 000 traces of duration 100 ns separated by 1 ms (a time set by the inverse of the pulse repetition rate of the Pockels cell after the laser oscillator, see section 7.1.1). Initially, the shutters in the path of the control, optical pumping, and LIAD beams were closed; only the signal field was transmitted through the HC-PCF. The oscilloscope then recorded the transmitted signal for 0.5 s, or approximately 500 traces, which formed the baseline signal for further analysis. Note that the data acquisition clock (derived from the computer) and the Pockels cell clock (derived from the laser oscillator) were not synchronized; we will return to this issue shortly.

After 0.5 s, the LIAD shutter was opened and the optical depth in the HC-PCF increased (see section 6.5.2). At the same time, the optical pumping and control shutters

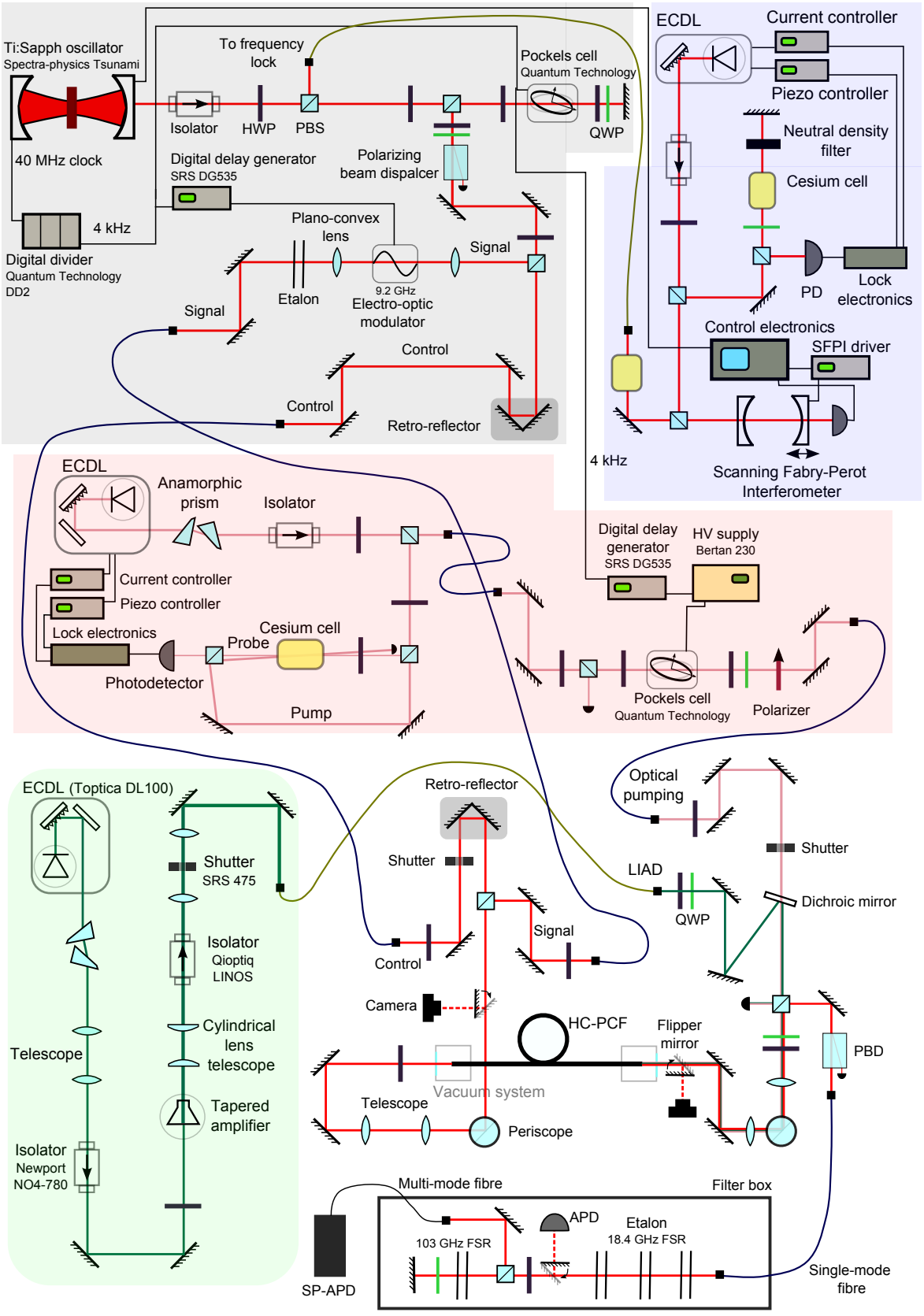

Figure 7.6: Schematic of the complete HC-PCF experiment. The grey shading shows the control and signal preparation stage (section 7.1.1); the light blue shading, the frequency-offset lock for the laser oscillator (section 5.4); the light pink shading, the optical pumping setup (section 7.1.2); the light green shading shows the LIAD setup (section 6.5.2); and the unshaded white area, the HC-PCF setup. The blue fibres are polarization-maintaining and the gold fibres non-polarization-maintaining.

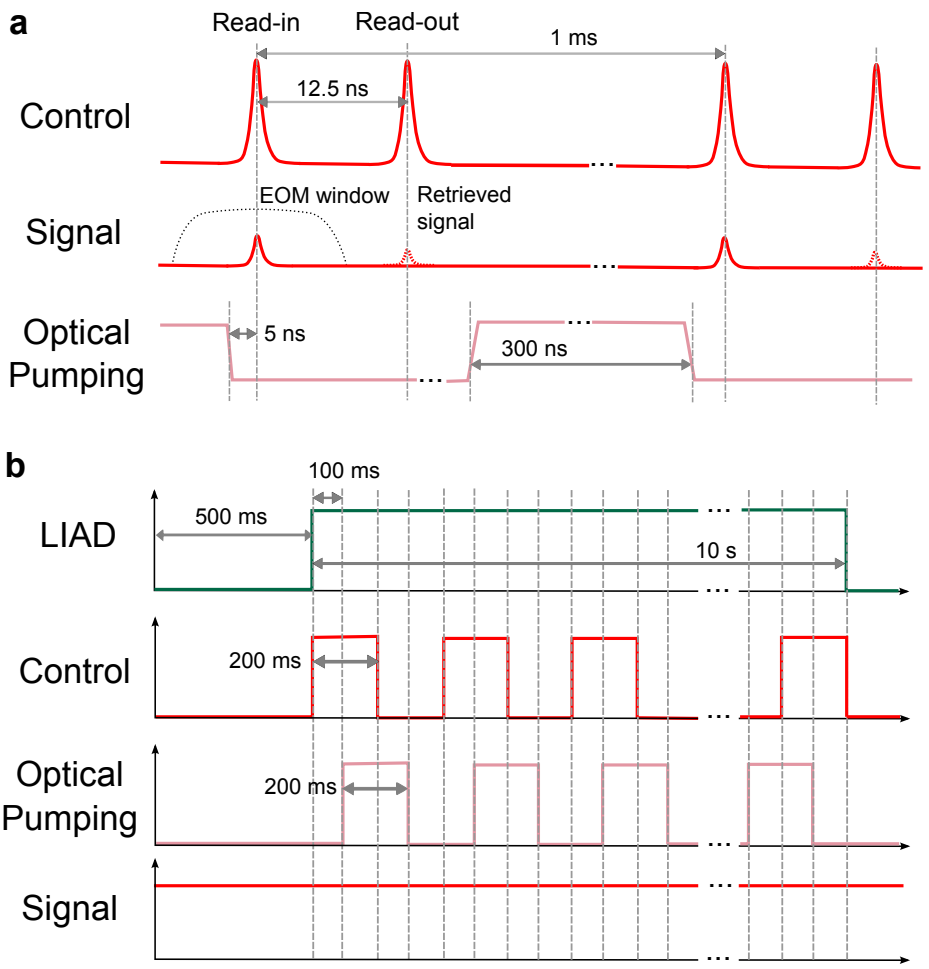

Figure 7.7: **a** Pulse sequence for one run of the memory experiment, showing the timing of the signal, control, and optical pumping beams (the LIAD beam remained on). **b** Ten-second acquisition sequence with fast shutters on the LIAD, control, and optical pumping beams. Each constant acquisition window of 100 ms consisted of approximately 100 runs of the experimental pulse sequence shown in 7.7**a**.

opened for 200 ms with a relative delay of 100 ms, as plotted in figure 7.7**b**. Approximately 100 traces were recorded with the following combinations of optical beams sent through the HC-PCF: signal only; signal and control only; signal and optical pumping only; and signal, control, and optical pumping (the LIAD beam always remained on). There was some variation in the number of traces acquired for each combination of optical modes because the acquisition program clock was not synchronized to the repetition rate of the Pockels cell. The state of the shutters during each acquisition was encoded in a voltage signal (using National Instruments PCI-6602) that was recorded with the oscilloscope in parallel with the signal from the APD. In this way, each measurement of the signal

pulse was 'tagged' so as to indicate exactly which optical fields were present during the measurement. After 10 s from the start of the program, the acquisition was complete and the data from the oscilloscope (the signal pulse traces and shutter-state voltage tags) were transferred to the acquisition program. The data was segmented and analysed off-line using Python with the NumPy and matplotlib packages; an example of the acquisition sequence data is given in figure 7.8.

Acquiring as much data as possible during the experiment was critical because the repetition rate of LIAD was so low. From the analysed data, the behaviour of the signal field in the read-in and read-out time bin was reconstructed as a function of the acquisition time in the presence or absence of the control field and optical pumping field. This was important for a number of reasons. First, by examining how the signal field changed when the auxiliary fields were present, I could gain some insight into what physical processes were occurring in the fibre. For instance, absorption of the signal field in the absence of the control field could indicate linear absorption of the signal field. As another example, the memory interaction requires that the atoms were initially optically pumped into the ground state. My first experiments revealed a small increase in the signal at the read-out time bin. The retrieved signal was small, and it was initially unclear if it was the result of some spurious or confounding effect. When I implemented the shutter control system, I immediately saw that the retrieved signal disappeared when either the control or optical pumping was absent, confirming my suspicion that the signal was a genuine signature of the memory process. Second, by measuring the time delay of the signal pulse during LIAD when the control and optical pumping field were blocked, the optical depth in the HC-PCF could be calculated.

7.2 Optical depth measurements

The Raman coupling and, hence, memory efficiency depended on the optical depth in the HC-PCF, as defined in section 6.5.1. The optical depth was measured by scanning the laser frequency over the Doppler-broadened transition. The absorption linewidth was fitted to an equation that modeled the broadening (see equation 6.14), enabling the optical depth to be extracted. The problems with this approach are several. First, it requires another

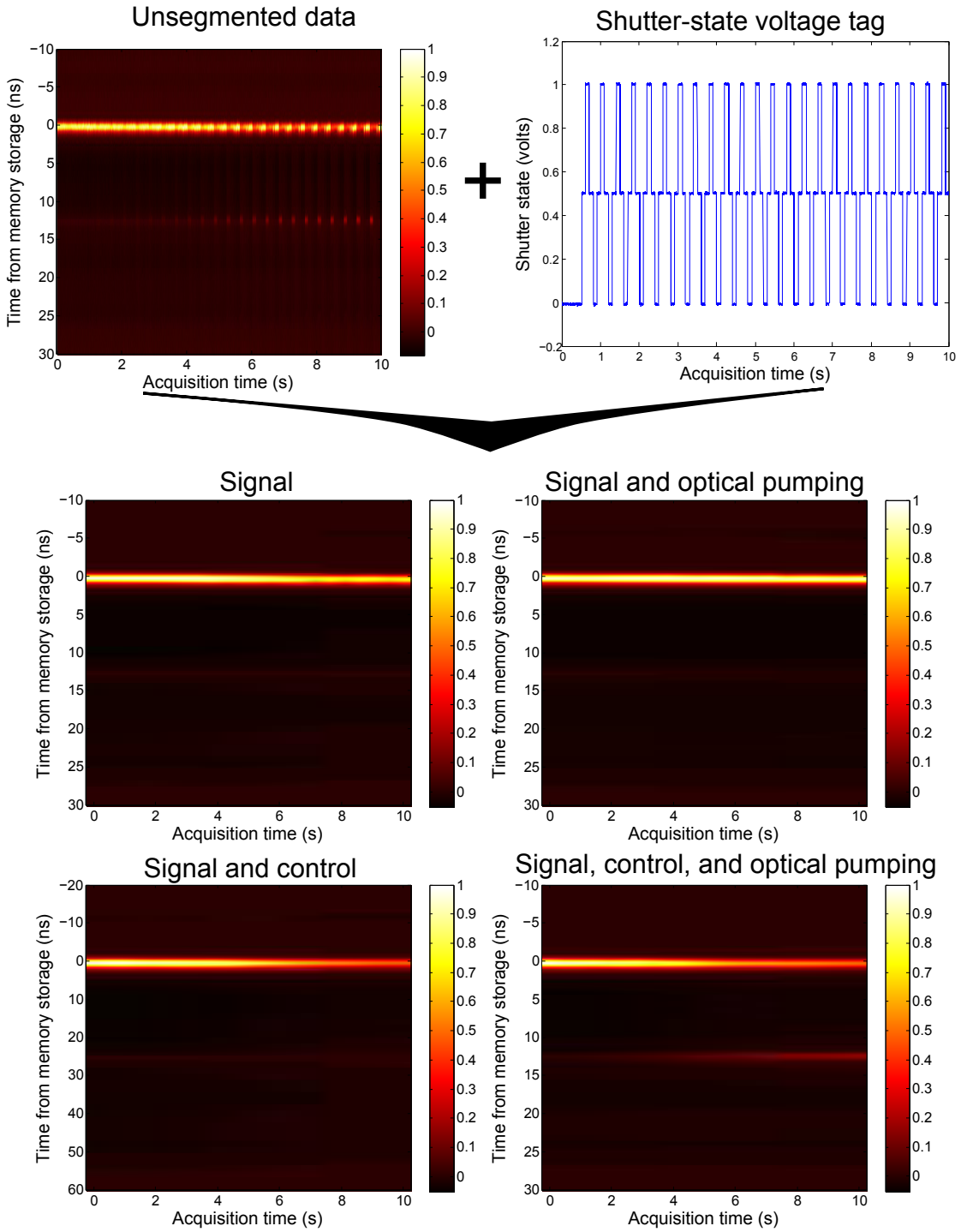

Figure 7.8: Example of the segmentation of 10 000 data traces according to state of the shutter on the control field and optical pumping field. The LIAD beam was switched on after 0.5 s, as illustrated in figure 7.7. The oscilloscope traces for each configuration are averaged (over each 100 ms segment) and plotted in the figures labeled according to which optical fields were present. The retrieved signal from the memory can be seen in the signal at 12.5 ns in the lower right plot.

laser on another transition (for instance, the D_1 line) to measure the absorption profile. The scan rate must be fast in order to achieve high temporal resolution and the data must be recorded by the acquisition system. Second, the estimate of the optical depth was very sensitive to the estimate of the width and shape of the assumed absorption profile. The width of the profile was determined by the temperature inside the fibre, which is different from the temperature of the vacuum system as the LIAD beam (with intensity 2×10^8 W/m^2) heats up the fibre core. Further, during LIAD the atoms will not be at thermal equilibrium, as assumed in equation 6.14, complicating the definition of a temperature.

I developed a simpler and more robust approach to measure the optical depth. I measured the pulse delay experienced by the signal field when LIAD was applied and the control and optical pumping fields were blocked. The signal pulse was delayed by the increased dispersion from the far-detuned excited state. The dispersion could then be related to the absorption and, hence, optical depth, through the Kramers-Kronig relations [283]. Because the signal detuning was much greater than the width of the absorption profile, the exact details and shape of the broadening were not important; the light 'sees' only an effective atomic transition located at the detuned frequency (we will return to this issue shortly). The signal pulse delay could be measured during the acquisition sequence described in section 7.1.6, allowing the time-varying optical depth to be reconstructed for each moment during the acquisition time. I will now derive the exact relationship between the time delay of the signal pulse and the optical depth.

The linear susceptibility $\chi(\omega, z)$ of the atomic transitions $g \to n$ with bare resonance frequency ω_{ng} is given by

$$\chi(\omega, z) \simeq \sum_n \frac{f_{\mathrm{ng}}}{2\omega_{\mathrm{ng}}} \left[\frac{\mathcal{N}(z) e^2/m_{\mathrm{e}}}{(\omega_{\mathrm{ng}} - \omega) - \mathrm{i}\Gamma_{\mathrm{ng}}} \right], \tag{7.1}$$

$$\simeq \sum_n \frac{f_{\mathrm{ng}} \mathcal{N}(z) e^2}{2 m_{\mathrm{e}} \omega_{\mathrm{ng}}} \left[\frac{(\omega_{\mathrm{ng}} - \omega) + \mathrm{i}\Gamma_{\mathrm{ng}}}{(\omega_{\mathrm{ng}} - \omega)^2 + \Gamma_{\mathrm{ng}}^2} \right], \tag{7.2}$$

where $f_{ng} = 2m\omega_{\mathrm{ng}} |\mu_{\mathrm{ng}}|^2 / (3\hbar e^2)$ is the oscillator strength of the $g \to n$ transition, Γ_{ng} is the homogeneous linewidth, $\mathcal{N}(z)$ is the number density of atoms (atoms per unit distance), m_{e} is the electron mass, the electron charge is e, and μ_{ng} is the dipole moment.

The linear susceptibility is related to the complex index of refraction $\tilde{n}(\omega, z)$ of the system by

$$\tilde{n}(\omega, z) = \sqrt{1 + 4\pi\chi(\omega, z)} \simeq 1 + 2\pi\chi(\omega, z) \tag{7.3}$$

in the limit that $4\pi\chi \ll 1$. The real part of the index of refraction determines the dispersion and the imaginary part the absorption, linked together by the Kramers-Kronig relations. The absorption coefficient of the atomic system in the linear regime is [283]

$$\alpha(\omega, z) = 4\pi \mathrm{Im}\left\{\chi^{(1)}\right\}\left(\frac{\omega}{c}\right), \tag{7.4}$$

$$= \sum_n \frac{2\pi f_{\mathrm{ng}} \mathcal{N}(z) e^2}{m_{\mathrm{e}} c \Gamma_{\mathrm{ng}}} \left[\frac{\Gamma_{\mathrm{ng}}^2}{(\omega_{\mathrm{ng}} - \omega)^2 + \Gamma_{\mathrm{ng}}^2}\right]. \tag{7.5}$$

The optical depth is simply the integral of the absorption coefficient over the length L of the HC-PCF on resonance (here we consider only one atomic transition a),

$$d = \int_0^L \alpha(\omega = \omega_{\mathrm{ng}}, z)\mathrm{d}z = \frac{2\pi f_{\mathrm{a}} N e^2}{m_{\mathrm{e}} c \Gamma_{\mathrm{a}}}, \tag{7.6}$$

where $N = \int_0^L \mathcal{N}(z)\mathrm{d}z$ in the total number of atoms in the HC-PCF core.

Now we can express the real part of the index of refraction in terms of the optical depth as expressed in equation 7.6,

$$\mathrm{Re}\left\{\tilde{n}\right\} = n(\omega, z) = 1 + 2\pi \mathrm{Re}\left\{\chi^{(1)}(\omega)\right\}, \tag{7.7}$$

$$= 1 + \frac{\pi \mathcal{N}(z) f_{\mathrm{a}} e^2}{m_{\mathrm{e}} \omega_{\mathrm{a}}} \left[\frac{\omega_{\mathrm{a}} - \omega}{(\omega_{\mathrm{a}} - \omega)^2 + \Gamma_{\mathrm{a}}^2}\right], \tag{7.8}$$

$$= 1 + \frac{d}{2}\frac{\mathcal{N}(z)}{N}\frac{c}{\omega_{\mathrm{a}}}\left[\frac{\Delta_{\mathrm{a}}}{\Delta_{\mathrm{a}}^2 + \Gamma_{\mathrm{a}}^2}\right], \tag{7.9}$$

where $\Delta_{\mathrm{a}} = (\omega_{\mathrm{a}} - \omega)$ is the detuning of the signal field from the excited-state manifold. The group delay τ_{g} is related to the group index n_{g} by [36]

$$\tau_{\mathrm{g}}(\Delta) = \frac{1}{c}\int_0^L n_{\mathrm{g}}(\Delta, z)\mathrm{d}z, \tag{7.10}$$

where

$$n_{\mathrm{g}} = n(\Delta, z) + \omega_{\mathrm{a}} \left.\frac{dn}{d\omega}\right|_{\omega=\omega_{\mathrm{a}}}. \tag{7.11}$$

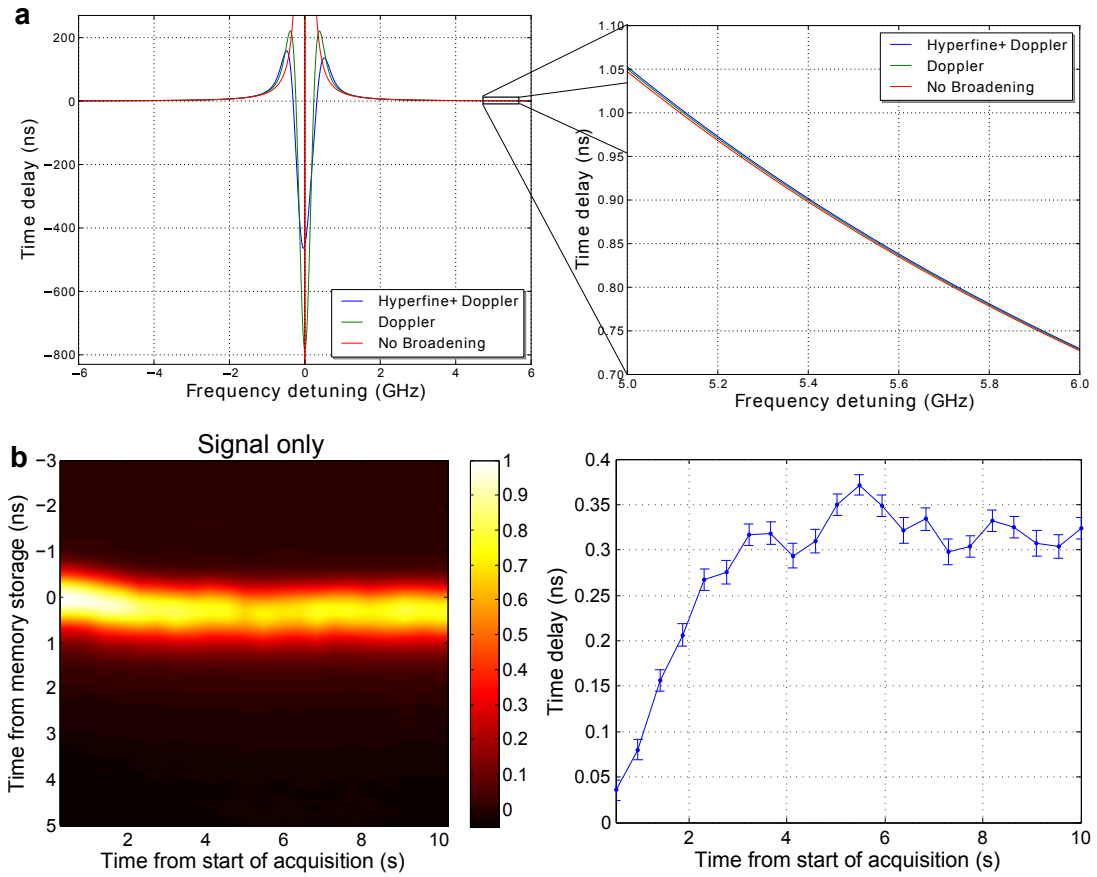

Figure 7.9: **a** Pulse delay as a function of detuning when the excited state is treated as a single transition (red line), with Doppler broadening (green line), and with the excited hyperfine manifold splitting (blue line). The time delay for all three cases is nearly identical when the detuning exceeds 2 GHz. The inset shows the region between 5 and 6 GHz. **b** Example of the pulse delay extracted from an experimental trace. The signal pulse shown in the experimental trace (along y-axis) arrives later as the optical depth increases from LIAD. The time delay was defined as the shift in the centre of the signal pulse, whose profile was fit to a Gaussian function.

By combining equations 7.9 and 7.10, the group delay of the signal pulse can be expressed as a function of detuning,

$$\tau_{\mathrm{g}}(\Delta) = \frac{L}{c} + \frac{d\,\Gamma}{2}\frac{\Delta^2 - \Gamma^2}{(\Delta^2 + \Gamma^2)^2}, \tag{7.12}$$

where I have dropped the atomic subscript a. The left part of the right-hand side in equation 7.12 is the propagation time in the absence of any material dispersion. As desired, the pulse delay $t_{\mathrm{p}} = \tau_{\mathrm{g}} - L/c$ depends only on the optical depth, frequency, and homogeneous linewidth of the transition; the latter two are known beforehand and fixed during an experiment. In the limit that $\Delta \gg \Gamma$, the pulse delay scales with the inverse

square of the detuning,

$$t_{\mathrm{p}} = \frac{d\,\Gamma}{2\Delta^2}. \tag{7.13}$$

In the opposite limit, where $\Delta \ll \Gamma$ the pulse delay is seemingly negative, however it is precisely here that absorption is strongest and, as a result, the pulse would be significantly distorted. In our experiments, $\Delta/2\pi = 6$ GHz and $\Gamma/2\pi = 6$ MHz is the homogeneous linewidth. The delay only depends on the total optical depth and is independent of the actual distribution of atoms along the fibre. Because no optical pumping was applied during these measurements, the signal field acted on the nearer $6^2S_{1/2}(F = 3) \rightarrow 6^2\mathrm{P}_{3/2}$ transition in addition to the further-detuned $6^2\mathrm{S}_{1/2}(F = 4)$ ground state.

The presence of inhomogeneous broadening and multiple excited-state hyperfine manifolds can be safely ignored in the limit that the detuning is much greater than the Doppler broadening (450 MHz) and the excited-state splitting (between 150 to 250 MHz); the deviation from equation 7.12 when taking account this factors, was 0.3%, as shown in figure 7.9**a**. This points to the robustness of the method as it is insensitive to the exact nature of the broadening so long as the broadening is much less than the detuning. The change in pulse delay was in this way related directly to a change in optical depth, which was then added to the estimate of the optical depth before LIAD was applied [223][3]. Typical pulse delays ranged from several hundred picoseconds to one nanosecond. An example of the extraction of the pulse delay is shown in figure 7.9**b**, where the maximum pulse delay was 0.35 ns.

In summary, up to this point I have built an apparatus where I can couple the signal, control, optical pump and LIAD beam into a HC-PCF loaded with cesium atoms in a vacuum system. A data acquisition and control program acquired the signal field in the presence or absence of the optical pumping and control field when LIAD was applied. The optical depth was measured during the acquisition period in order to quantify the Raman coupling constant during the measurements. I now present the storage of bright coherent pulses in section 7.3, followed by the storage of single-photon-level pulses in section 7.4 and the measurement of the lifetime of the memory in section 7.5.

[3] I factored in the fact that $> 85\%$ of the atoms were confined within the fibre core, as opposed to between the vacuum window and fibre face.

7.3 Classical memory results

The weak signal field was stored in the hyperfine spin coherence between the dipole-decoupled storage and ground states, the $6^2S_{1/2}(F = 3, 4)$ hyperfine levels. The Raman interaction was mediated by a two-photon transition with the strong control field, as illustrated in figure 7.1. The excited-state detuning was 15.2 GHz and the signal and control were in two-photon resonance. The stationary hyperfine coherence was then converted into a propagating retrieved signal pulse through the time-reversed scattering process; the application of a second control pulse after a programmable delay. In these experiments the storage time was 12.5 ns, set by the period of the pulse train from the laser oscillator; the precise pulse sequence is shown in figure 7.7**a**.

Figure 7.10 shows the storage and retrieval of a bright signal pulse comprising $\sim 10^6$ photons. The control field energy per pulse coupled into the fibre was 40 pJ (2×10^8 photons per pulse). When the control field was blocked, the signal field was transmitted through the fibre as it was far-detuned from the excited state. This is in contrast to on-resonant memory protocols (such as EIT), where the residual signal not stored in the memory is absorbed and then spontaneously emitted. As discussed in section 5.2.8, the Raman memory can be thought of a beam splitter where the two output modes are storage and transmission; this may be useful for certain quantum information proposals [82, 202].

When the control pulse was applied in the read-in time bin ($t = 0$), the signal pulse was partially absorbed into the memory. After a delay ($t = 12.5$ ns), a second control pulse retrieved the signal in the read-out time bin. Note that there was a small amount of spurious signal in the read-out time bin when the control was blocked. This was caused by the finite response time of the electro-optic modulator and switch (4 to 5 ns) used to generate the signal in the read-in time, which created a small amount of residual signal in the read-out time bin; this signal was subtracted from all the estimates of the memory efficiency. The total memory efficiency was $27 \pm 1\%$ for a control pulse energy of 40 pJ, which is a two-hundred-fold reduction in energy as compared to a free-space memory [72]. For a typical experimental run with LIAD, the memory efficiency was between 20% to 30%. In the case where the control field energy and optical depth were higher, the total signal (transmitted plus retrieved) could exceed the input signal, a clear sign of gain

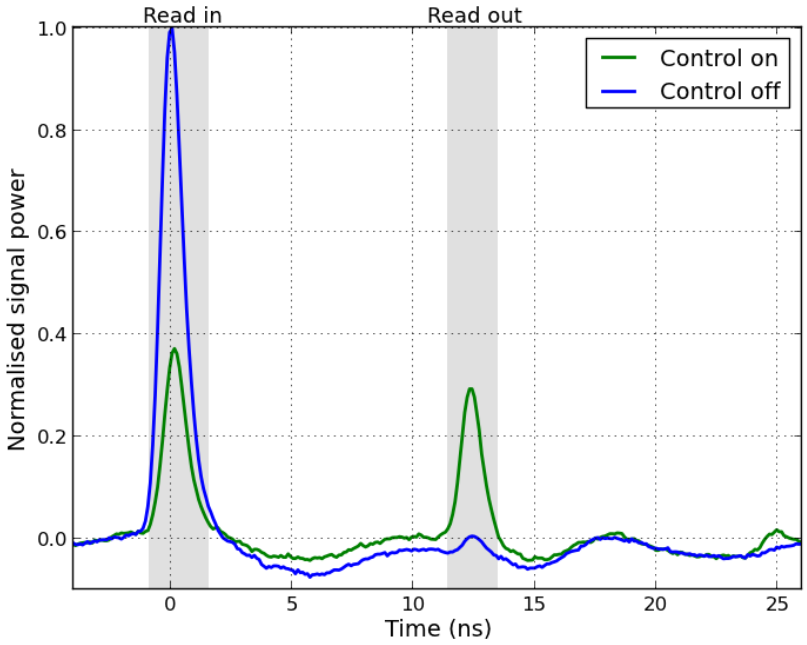

Figure 7.10: Storage of classical, coherent-state light in a kagome hollow-core fibre, adapted from reference [282]. Time-domain trace showing the signal consisting of 10^6 photons with (green line) and without (blue line) the control pulse applied in the read-in and read-out time bins (grey shading). The small amount of signal at 25 ns is the retrieved signal from a third control pulse.

caused by stimulated Raman scattering [284]. Investigating this regime in more detail is ongoing work that will be discussed in chapter 8.

The memory efficiency was calculated from the ratio of the integrated intensity of the retrieved and transmitted signal with a 5-ns integration window. The total memory efficiency was defined as

$$\eta_{\text{tot}} = \frac{\int_{-\infty}^{\infty} \Xi(t)\,|\mathcal{E}_{\text{out}}(t)|^2\,\mathrm{d}t}{\int_{-\infty}^{\infty} |\mathcal{E}_{\text{in}}(t)|^2\,\mathrm{d}t}, \tag{7.14}$$

where $\mathcal{E}_{\text{in}}$ and $\mathcal{E}_{\text{out}}$ are in input and output (retrieved) electric field envelopes of the signal field, and $\Xi(t)$ defines the time bin, which is equal to one for a 5-ns-wide window centred at the storage time.[4] I now study in detail how these measurements compare to the theory of the Raman interaction summarized in sections 5.1 to 5.2.9.

[4]Ideally, with a fast enough detector, the mode overlap with the input signal field can be used to define the memory efficiency. Or the retrieved signal could be overlapped temporally with the input signal via homodyne detection [285] if the input and output modes are identical.

7.3.1 Comparison to Raman theory

I now examine how the memory efficiency depended on the optical depth and, hence, Raman coupling. As discussed in section 5.2.7, the Raman coupling constant C^2 defines the relative 'mixing angle' between the optical and atomic modes and is given by $C^2 \approx d\,(\Gamma/\delta)\,(\Omega/\Delta)^2$, where Γ is the homogeneous linewidth of the excited state, δ is the bandwidth of the pulse to be stored, Ω is the Rabi frequency of the control field, Δ is the excited-state detuning and d is the resonant optical depth (see section 6.5.1) [71]. Here, the Rabi frequency was kept constant and the optical depth in the fibre was dynamically varied using LIAD (see section 6.5.2). This was preferable to varying the control power as the Rabi frequency of the control field was always constrained to be much less than the detuning (the adiabatic limit) and, as well, any Stark shift was kept constant. The optical depth was measured from the delay experienced by signal pulses in the absence of a control pulse (see section 7.2). These measurements were interleaved with the memory interaction to record, simultaneously, the optical depth and memory efficiency, which is plotted in figure 7.11 along with the Raman coupling constant. The uncertainty in the optical depth was dominated by the uncertainty in the estimation of the initial optical depth. The uncertainty in the efficiency was dominated by fluctuations in the retrieved signal power.

The estimated Raman coupling is plotted on the upper horizontal axis in figure 7.11. The bandwidth of the signal pulse was 1.0 GHz. The Rabi frequency of the control field varies according to the spatial profile of the guided mode. The average intensity inside with core of the fibre with diameter D is

$$I_{\mathrm{avg}} = \frac{2P_{\mathrm{c}}}{\pi w_0^2}\frac{2}{D}\int_0^{D/2}\exp\left(-\frac{2r^2}{w_0^2}\right)\mathrm{d}r, \tag{7.15}$$

where $w_0 = 10\,\mu$m is the Gaussian beam radius, $P_{\mathrm{c}} = \rho/\tau_{\mathrm{p}}$ is the pulse energy, τ_{p} is the pulse duration, ρ is the pulse energy, and r is the radial coordinate. The average intensity is then related to the average Rabi frequency by

$$\Omega_{\mathrm{avg}} = \frac{\mathbf{d}\cdot\boldsymbol{\epsilon}_{\mathrm{c}}}{\hbar}\sqrt{\frac{2I_{\mathrm{avg}}}{cn\varepsilon_0}}, \tag{7.16}$$

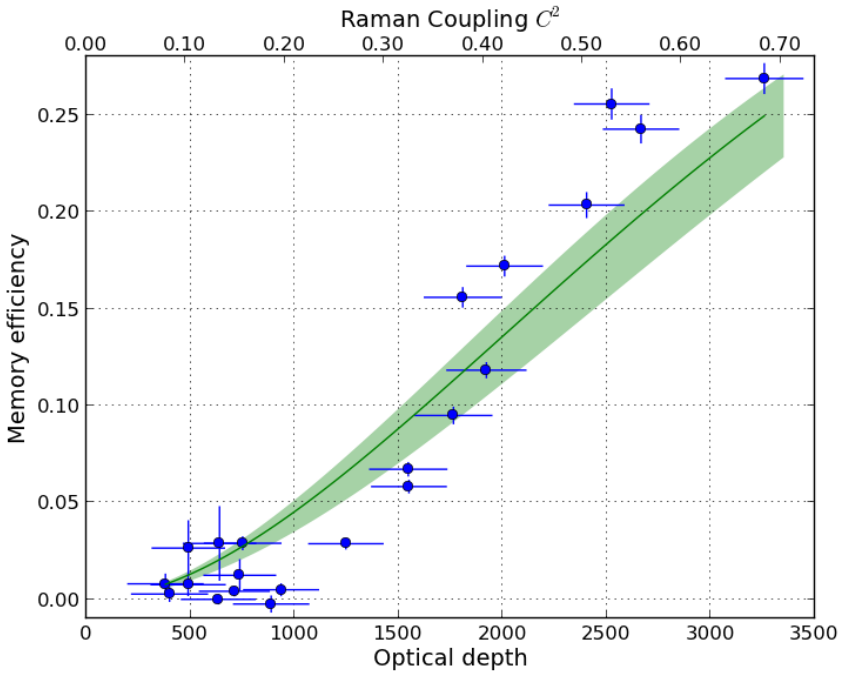

Figure 7.11: The dependence of the memory efficiency on the optical depth fitted to a theoretical model of the Raman interaction [71] with one standard deviation confidence interval, adapted from reference [282]. The corresponding Raman coupling constant C^2 is shown on the upper x-axis. Errors bars represent the uncertainty in pulse delay (horizontal bars) and the signal pulse energy (vertical bars).

where $\mathbf{d}$ is the far-detuned dipole moment for the D_2 line and $\boldsymbol{\epsilon}_c$ is the polarization unit vector of the control field. In the experiment, the calculated Rabi frequency was $\Omega_{avg}/2\pi = 3.4 \pm 0.5$ GHz. The magnitude of the optical depth required for efficient memory operation can checked by considering the dimensionless Raman coupling term. Adiabaticity requires that $\Delta \gg \Omega$ and noting that $\Gamma_N/\delta = 1/300$ implies that the optical depth must be several thousand for $C^2 \gtrsim 1$, which is required for efficient memory operation. This is in agreement with the results in figure 7.11. As expected, the efficiency of the Raman memory is negligible when the Raman coupling constant $C^2 \ll 1$ and the retrieved signal begins to be detectable as the C^2 increases above 0.1.

The results in figure 7.11 were compared to an adiabatic, linear, one-dimensional model of the Raman interaction [71] from chapter 5, section 5.2.6. The memory efficiency η for the stored spin coherence mode $S(z)$ is then given by

$$\eta = \int_{-\infty}^{\infty} \left| \int_0^1 K(1-z, \omega(\tau)) \zeta^*(\tau) S(z) \mathrm{d}z \right|^2 \mathrm{d}\tau, \tag{7.17}$$

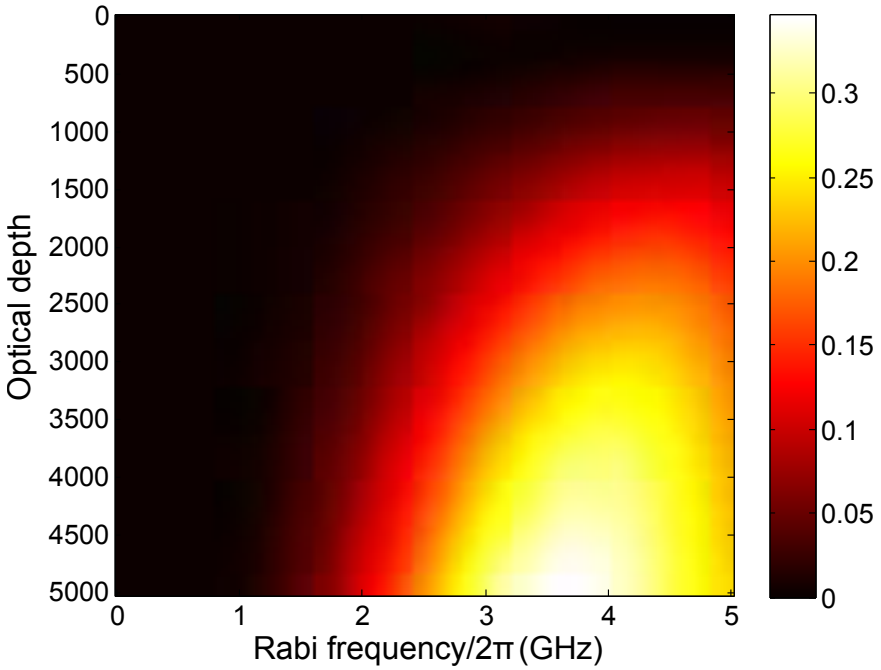

Figure 7.12: Theoretical prediction of the Raman memory efficiency as a function of the optical depth and the Rabi frequency of control field.

where $\zeta(\tau) = C \cdot \Omega(\tau) \exp(\mathrm{i}RC\omega)/\sqrt{h}$, $R = \sqrt{h/(d\Gamma_{\mathrm{N}})}$, $\tau = t - z/c$ is the retarded time, $\omega(\tau) = \frac{1}{h}\int_{-\infty}^{\tau} |\Omega(\tau')|^2 \,\mathrm{d}\tau'$ is time under coordinate transformation, $h = \int_{-\infty}^{\infty} |\Omega(\tau)|^2 \,\mathrm{d}\tau$ is the integrated Rabi frequency, and $K(z,\omega) = CJ_0(2C\sqrt{\omega z})$ is the Green's function of the Raman interaction. The length of the spatial coordinate z is normalized to run from 0 to 1. The stored spin coherence $S(z)$ is given by

$$S(z) = \int_{-\infty}^{\infty} K(z, 1-\omega(\tau))\mathcal{E}_{\mathrm{in}}(\tau)\zeta(\tau)\mathrm{d}\tau, \tag{7.18}$$

where $\mathcal{E}_{in}(\tau)$ is the input signal field. The signal field duration was 30% larger than the control field in order to account for the temporal broadening introduced by the etalon after the electro-optic modulator. The relative time delay between the signal and control field was zero. The total memory efficiency as a function of the optical depth and the Rabi frequency of the control field is plotted in figure 7.12.

The theoretical model was fit to the data using a weighted non-linear least squares optimization algorithm. The only free parameter in the model was the Rabi frequency Ω. The best fit was achieved for a Rabi frequency $\Omega_{\mathrm{fit}}/2\pi = 2.8 \pm 0.1$ GHz. This compares well

with the experimentally estimated mean Rabi frequency of $\Omega_{\text{exp}}/2\pi = 3.4 \pm 0.5$ GHz; the reasonable accordance shows that this model faithfully describes the memory interaction in the HC-PCF.

The memory efficiency is currently limited by the Raman coupling and, ultimately, limited to $\sim 50\%$ by the spatial mode mismatch between the stored spin-wave and the read-out control pulse [71]. This can be understood intuitively: at high optical depths the spin-wave is more concentrated near the front of the ensemble than the back [58]. To retrieve the spin-wave, the retrieved control field amplitude should increase with time to match the mode of the spin-wave. Otherwise incomplete constructive interference will cause signal retrieved at the front of the ensemble to be reabsorbed in the memory. Higher efficiency could be reached by either increasing the integrated intensity of the read-out control pulse or reading out the memory in the backward direction. Ideally, the integrated intensity should be increased by lengthening the duration of the control pulse. Increasing the peak intensity is not desirable as the control field could potentially violate the adiabatic limit, generating noise through spontaneous scattering.

7.4 Single-photon-level measurements

The ability to store single photons is necessary for quantum information processing tasks. The main challenge is to ensure that the noise level is less than the signal from a single photon. The principal noise sources for the Raman memory are spontaneous four-wave mixing, residual 'leak-through' of the control field, or spontaneous Raman scattering from imperfect optical pumping. While the initial optical pumping results were promising (see section 6.7), it remained an open question as to whether the storage of single photons is feasible in a confined waveguide structure.

To assess the suitability of the Raman memory in a HC-PCF for single-photon storage, I stored weak coherent-state signal pulses with a mean photon number per pulse on the order of one. These measurements required several changes to the filtering and detection setup, which are illustrated in figure 7.4. An additional double-passed etalon was added to provide further suppression of the control field and eliminate any spontaneously scattered anti-Stokes photons. An 850-nm band-pass optical filter (Thorlabs FL850-10) was also

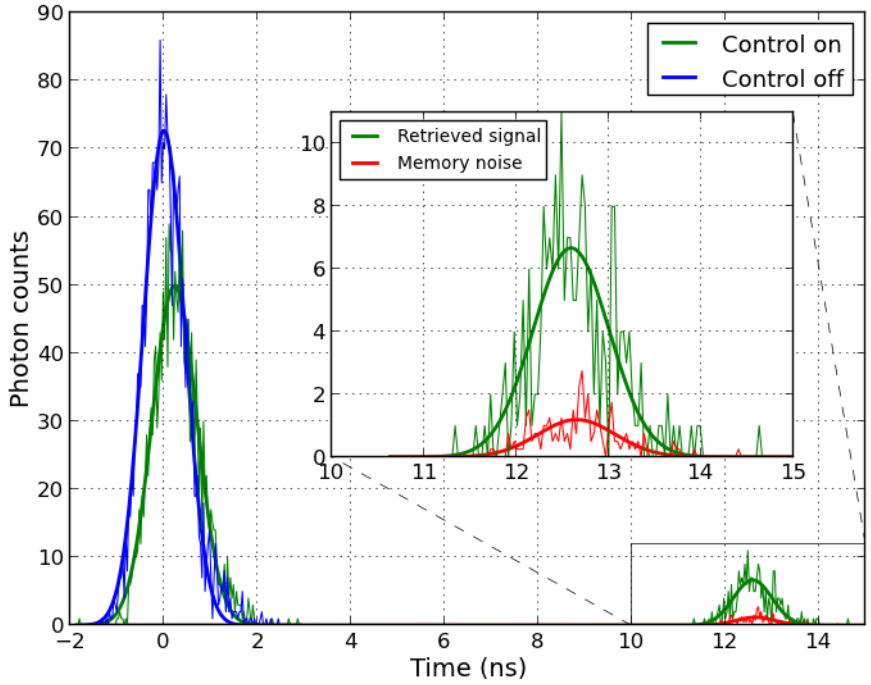

Figure 7.13: Storage of single-photon-level pulses, adapted from reference [282]. Time-domain histogram reconstructed from the single-photon APD and time-to-amplitude converter, fit to a Gaussian function (thick line). The signal is shown with (green line) and without (blue line) the control field applied. The inset shows the unconditional noise (red line) in the read-out time bin.

added to remove the residual back-scattered light from the LIAD beam. The filtered signal was then coupled into a shielded multi-mode fibre connected to a single-photon counting module (PerkinElmer SPCM-AQRH-R-FC). The signal pulse was derived, as before, from the frequency-modulated control field, attenuated down such that the mean photon number per pulse in the HC-PCF was approximately one.

Storage at the single-photon level is shown in figure 7.13. I coupled a weak coherent-state signal pulse with an average of $\bar{n} = 1.8 \pm 0.1$ photons per pulse inside the fibre for storage. The read-in time bin showed Raman absorption and the read-out time bin retrieval when the memory interaction was turned on via LIAD. The inset in figure 7.13 shows the signal retrieved when no signal was sent into the memory; this is the unconditional noise level of the memory. These traces were reconstructed from a series of measurements with a single-photon detector connected to a time-to-amplitude converter and multi-channel analyser. While the dead-time of the detector (50 ns) was longer than

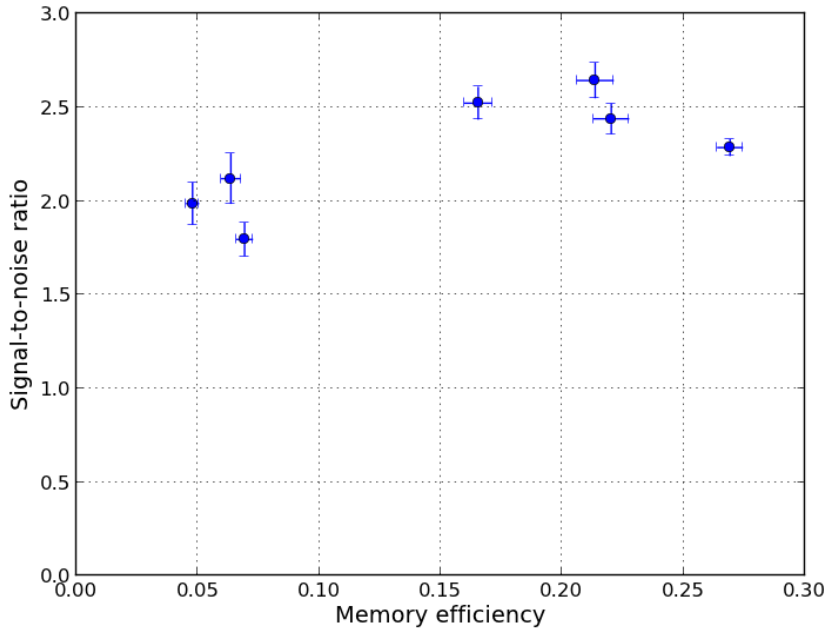

Figure 7.14: SNR at the single-photon level as a function of memory efficiency (normalized to 1 input photon per pulse); error bars are estimated from the standard deviation of the count statistics, adapted from reference [282].

the storage time, the probability of a detection event per pulse was much less than one $(2.0 \pm 0.1) \times 10^{-2}$ and, therefore, the probability that a photon was present in both the read-in and read-out time bins was negligible.

The signal-to-noise ratio (SNR) at the single-photon level as a function of memory efficiency is plotted in figure 7.14, normalized for an input of strictly one photon per pulse, giving a maximum value of 2.6. This data was collected with a single-photon detector connected to a field-programmable gate array (FPGA). The FPGA also recorded a signal from the Pockels cell; only photodetection events within the 5-ns detection window that were coincident with the Pockels cell (suitably delayed) were recorded. The noise level was calculated from the noise generated by an additional control pulse separated by 50 ns from the memory interaction (with no signal field). Any residual spin-wave coherence remaining in the memory after 50 ns could seed the noise process, so the estimate of the SNR represents a lower bound. However, as discussed in section 7.5, the memory lifetime was less than 50 ns.

The noise was in the same spatial, temporal, and spectral mode as the retrieved signal.

The noise was caused by spontaneous four-wave mixing (SFWM) [72]; the control pulse can act on the ground state, in addition to the storage state, scattering an anti-Stokes photon and creating a spurious spin excitation. This spin coherence can then be read out from the storage state by a second interaction with the control pulse, creating a Stokes photon with the same frequency as the retrieved signal mode. The noise source for this memory is the same process we used to implement a spontaneous Raman memory in diamond in chapters 3 and 4. While each type of interaction alone can be used to implement a useful memory protocol, the combination of both processes is undesirable; the presence of uncorrelated noise reduces the fidelity of the signal to the desired single-photon state [284].

As shown in figure 7.14, the SNR was approximately independent of the memory efficiency, indicating that the memory retrieval and noise generation had the same scaling with C^2. This is consistent with SFWM as opposed to imperfect control field filtering because the control field power was kept constant throughout the measurements and only the optical depth was varied. Reducing the optical depth would reduce the memory efficiency, but not the leak-through, so in this case one would expect a reduction in the SNR, which we did not observe. The single-photon-level SNR measured in figure 7.14 is, to our knowledge, the highest yet demonstrated for a room-temperature memory with an atomic vapour [72]. For interfacing the memory with a heralded single-photon source, the heralding efficiency should exceed the inverse of the SNR to enable non-classical operation. This requires a minimum 40% heralding efficiency, which is potentially feasible, albeit still very challenging, given current heralded single-photon sources [286]. To be useful for demanding single-photon applications, the noise floor needs to be lowered.

I will now briefly discuss ways to improve the SNR at the single-photon level in the Raman memory. One possibility is to decrease the excited-state detuning. The ratio of the strength of the four-wave mixing interaction to the memory interaction scales as $[\Delta/(\Delta+\omega_{sg})]^2$, where $\omega_{sg}/2\pi = 9.192$ GHz is the splitting between the storage and ground states. As the the detuning increases the relative strengths of the noise and signal process converge; likewise, reducing the detuning increases the differential weighting. This was tried in the bulk-vapour-cell Raman memory [287], where it was found that the buffer

gas broadened the transition to several GHz, causing linear absorption of the signal field when the detuning was reduced to 10-12 GHz. It may be possible to reduce detuning in the fibre memory as there is no buffer gas present that could broaden the transition.[5]

Another possibility is to filter the anti-Stokes mode in order to disrupt the four-wave mixing. We are developing a birefringent cavity for the bulk vapour-cell Raman memory that is transmissive for the signal and control field, but reflective for the anti-Stokes field. There are several possibilities to create a frequency-selective filter in an optical fibre: an etched Bragg grating in a hollow-core fibre (not attempted yet), an optical Bragg grating created by the Stark shift induced by a standing optical wave [288], or a hollow-core fibre-optic ring resonator [289]. Accommodating the narrow spacing between the signal, control, and anti-Stokes field (9.192 GHz) combined with the broad bandwidth of the signal and control is the main experimental challenge.

As a final note, the memory process is inherently phase matched owing to the fact that the signal and control have identical wave-vectors during read in and read out. This is in contrast to the SFWM processes, where the different dispersion between the Stokes and anti-Stokes fields results in a phase mismatch on axis (and only increases off axis when blue detuned, as is the case here). The change in the index of refraction at 15.2 GHz depends on the optical depth, and is approximately 10^{-6} for our experimental parameters, resulting in minimal on-axis suppression, and no possibility of off-axis phase matching; the sum of the Stokes and anti-Stokes wave-vectors is less than twice the wave-vector of the control field as the optical fields are blue-detuned from the optical transition.

7.5 Memory lifetime

As the memory was realized with thermal atoms in a compact, confined geometry, the lifetime of the memory is of particular interest. The lifetime of the memory was measured by changing the delay between the read-in and read-out control pulses. The spacing of the pulse train from the laser oscillator was fixed, so a single pulse was selected using the first Pockels cell in figure 7.2. The control pulse was split into two using a PBS, and one

[5] Another constraint is the adiabatic condition where the detuning must be greater than the Rabi frequency. If the detuning were decreased the signal bandwidth would also need to be decreased in order to maintain the same Raman coupling at the same optical depth.

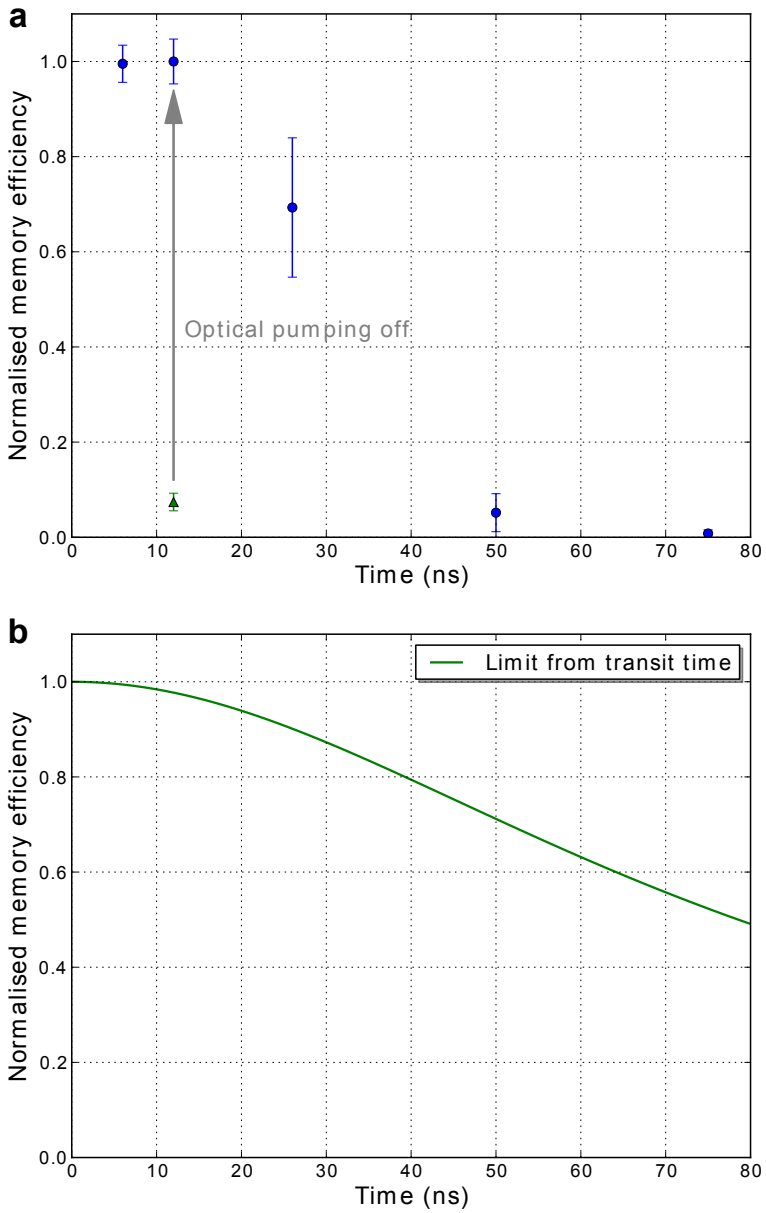

Figure 7.15: Lifetime of the memory in the hollow-core fibre. **a** Normalized memory efficiency as the delay between read-in and read-out control pulses was increased. The triangular point shows the memory efficiency at 12.5 ns when the optical pumping was left on. Error bars are the standard deviations from repeated measurements. **b** Prediction of the memory lifetime solely based on the estimated transit time of the atoms across the optical mode.

path was delayed using an unbalanced, fibre-based Mach-Zehnder interferometer. The read-in and read-out control pulses were then combined in the same spatial mode using a PBS and polarizer (with the concomitant partial loss of power).

The lifetime of the memory is shown in figure 7.15**a**, which was measured at an

optical depth of 2500. As in section 7.3, both the memory efficiency and optical depth were recorded together, and the memory efficiency was averaged from data with the same optical depth (±200), and the error bars are the standard deviation of the measurements. The memory efficiency was normalized to the memory efficiency of the shortest time delay (6 ns), and the control field energy per pulse for these measurements was approximately 10 pJ.

The measured lifetime ($1/e$) was 27 ± 9 ns, although I note the shape indicates the decoherence mechanism is non-Markovian (i.e. not a simple decaying exponential function). The measurements in section 7.3 and 7.4 were made with the optical pumping beam switched off with a fast Pockels cell. Figure 7.15**a** shows that when the optical pumping beam was left on, the total memory efficiency decreased by an order of magnitude (see section 7.1.2), while the storage efficiency (i.e. the amount of absorption) remained the same. This was clear evidence that the optical pumping beam was responsible for the decoherence of the memory. The optical pumping beam spoiled the spin coherence by coupling the storage and excited state, leading to spontaneous decay from the excited state and, also, a spatially dependent Stark shift that disrupted the transverse phase of the spin-wave.

Figure 7.15**b** shows the expected decoherence induced by the transit time of the atoms across the fibre mode, which predicts a lifetime ($1/e$) of 100 ns. This is much longer than the measured lifetime. A possible explanation for the discrepancy is due to residual transmission of the optical pumping beam, which is a technical limitation of the current Pockels cell. The extinction ratio of the Pockels cell for rapidly turning off the optical pumping beam was quite poor (approximately 40:1 versus 3000:1 for rapidly switching *on*)[6], and the leak-through from the optical pumping beam was still significant (10 mW).

The prediction of the memory lifetime in figure 7.15**b** was calculated from the time taken for the atoms to traverse the optical mode. The velocity v of the atoms was assumed to obey a Maxwell-Boltzmann distribution. The initial spin-coherence spatial distribution

[6] I tried several configurations, including where the optical pumping beam was switched off for a short window during the memory interaction, and the optical pumping beam was switched on for a short period before the memory interaction. In both cases the extinction ratio was poor; 15:1 in the first instance and 40:1 in the second.

was

$$\beta(r) = (2/w)\exp(-r^2/w^2), \tag{7.19}$$

where w is the Gaussian beam waist and r is the cylindrical radial coordinate. The spin-wave in equation 7.19 was defined such that its integral $\int_0^\infty \beta(r) r \mathrm{d}r = 1$. During storage, the atoms move ballistically, which reduces the mode overlap with the original spin-wave. This can be calculated by the overlap integral weighted by the probability distribution for the *speed* of the atoms in two dimensions (as motion parallel to the fibre axis can be ignored here),

$$S(t) = \int_0^\infty \beta(r) \left[\int_0^\infty p(v)\beta(r+vt)\mathrm{d}v \right] r\mathrm{d}r, \tag{7.20}$$

where $p(v) = 2v\lambda\exp(-\lambda v^2)$, $\lambda = m_{\mathrm{Cs}}/(2k_{\mathrm{B}}T)$, m_{Cs} is the mass of a cesium atom, k_{B} is the Boltzmann constant, and T is the temperature of the cesium atoms. Integration over the angular coordinate was ignored given the symmetry of the distribution. This can be expressed in analytic form as

$$S(t) = \left[1 + \left(\frac{t}{\tau} \right)^2 \right]^{-1}, \tag{7.21}$$

which gives a lifetime of 100 ns, where $\tau = w\sqrt{2\lambda}$. This agrees with a rough estimate of the transit time based on the speed of the atoms (250 nm/ns) and the size of the core (26 μm). In addition, previous measurements in section 6.6 placed a bound that the transit-time broadening was much less than the natural linewidth of the optical transition. Cesium-cesium collisions occur at a rate of $\sim 5 \times 10^5$ s^{-1} at the highest optical depth and could be neglected.

While in absolute terms the memory lifetime is short, the time-bandwidth product T of the memory is one hundred. This could result in a base factor enhancement $\Gamma = \eta T = 30$ in the generation rate of two synchronized single photons [14] provided low-noise single-photon storage. The memory lifetime could be further extended by using a buffer gas or larger diameter core to increase the transit time across the fibre core. Further, it may be possible to apply a spin-preserving coating to reduce the decoherence rate due to wall collisions. This is a promising approach for large-diameter hollow-core fibres such

as kagome fibres, although initial experiments by other groups have so far have achieved mixed results [220, 245, 248].

7.6 Summary

In conclusion, I have demonstrated, for the first time, the storage of light in a hollow-core photonic crystal fibre. I stored GHz-bandwidth light in the hyperfine coherence of cesium atoms at room temperature using a far-detuned Raman interaction. I developed a conveneint method for measuring the optical depth dynamically during LIAD. The atoms were pumped efficiently to the ground state using an intense optical pumping field combined with a fast-switching Pockels cell. The memory efficiency $\eta = 27\%$ agreed with a theoretical model for the Raman interaction and confirmed that the system was behaving as expected. The fibre memory required two hundred times less pulse energy than a free-space Raman memory, which could enable the operation of multiple memory units using a single control laser. As a result, it may be possible to derive the control field from an inexpensive amplified diode laser with an integrated, $LiNbO_3$ electro-optical amplitude modulator (e.g. from EOSPACE Inc) instead of a bulky and expensive mode-locked, titanium-sapphire oscillator.

The noise at the single-photon level – 0.1 noise photons per pulse for $\eta = 27\%$ – and high time-bandwidth product underpins the memory's potential for synchronizing heralded single-photon sources. The memory efficiency was measured to be 27 ± 9 ns, limited by residual coupling of the optical pumping beam, and the transit time of cesium atoms in the core was 100 ns. Finally, splicing the kagome fibre to a single-mode fibre [290] would realize a compact, integrated 'plug-and-play' optical memory at room temperature.

The inventor continued to talk. Dreyer threw down the pencil, reclined limply in his armchair and surrendered to the fascination.

"What was that?" he interrupted. "The noble slowness of a sleep-walker's progress?"

"Yes, if desired," said the inventor. "Or at the other extreme, the restrained agility of a convalescent."

"Go on, go on," Dreyer said, closing his eyes. "This is pure witchcraft."

Vladimir Nabokov; King, Queen, Knave

8 Conclusion

8.1 Summary of thesis

The work outlined in the thesis represents a small contribution to the overarching goal of creating new correlated states of light and, above all, seeing what is now unseen. The thesis has proceeded along two seams joined at a common point: the use of a far-off-resonant, broad-bandwidth Raman memory to store light in systems with short coherence times. The Raman memory has a lifetime determined by the Raman linewidth, which can be very narrow, and a bandwidth determined by the pulse bandwidth, which can be large; the pulse bandwidth is only limited by the frequency splitting of the storage and ground states. The large ratio between the storage time and the pulse duration – known as the time-bandwidth product – makes the Raman memory suitable for quantum information processing tasks described in chapter 2. In this thesis, I explored two material excitations: optical phonons in diamond and hyperfine spin states in a warm vapour of cesium, which

I will now summarize.

In the first part, I showed how far-detuned Raman scattering in diamond can create correlated, non-classical states of light. The non-classical nature of these optical fields was verified by their violation of the Cauchy-Schwarz inequality. It is interesting to note that detection of a Stokes photon heralds the creation of an optical phonon – we have created a heralded single-*phonon* source. Two diamonds were entangled using a primitive of the DLCZ protocol for long-distance quantum communication. The Raman-scattered optical modes from the two diamonds were combined and a single photon detected in order to project the optical phonon modes into an entangled state. The entangled state was verified by converting the optical phonon into an anti-Stokes photon. The density matrix of the joint state of the heralded anti-Stokes fields was reconstructed in the number basis by measuring the visibility of the quantum interference combined with measurements of high-order number statistics. The concurrence – an entanglement monotone – of the state was shown to be positive with a high confidence level, with no correction for any system inefficiencies or accidental photodetection events. These results represent the first instance of entanglement between two room-temperature solid-state objects. The coherence time of the optical phonon was extremely short (less than 10 ps), however, which prompted me to consider another system in which to implement a Raman memory, with a view toward an integrated structure.

In the second part, I implemented a stimulated Raman memory in cesium atoms confined in a kagome-structured hollow-core photonic crystal fibre. First, I reviewed the theory underpinning the Raman interaction and described the necessary system parameters required for high Raman coupling. I orientated my proposed experiment in terms of the previous work on Raman memories done by our group, and described my contribution: the development of a new frequency-offset lock stabilized, through an external-cavity diode laser, to an atomic reference, and the development and characterization of a set of temperature-stabilized, solid-state plano-convex etalons.

A large-core, kagome-structured HC-PCF was chosen as the most promising integrated structure for a Raman memory with alkali atoms; the large core diameter provided a long interaction time and efficient loading of the atoms. I designed and built an ultra-high

vacuum system that loaded the HC-PCF with cesium atoms at room temperature. I characterized the HC-PCF in terms of the optical depth (steady-state and with LIAD), the sub-Doppler linewidth, and the optical pumping efficiency, which all were found to be favourable for realizing a Raman memory. Light storage of classical optical pulses was demonstrated with an efficiency of 27±1%. The memory efficiency was studied as a function of the Raman coupling, as parameterized by the optical depth. The optical depth was measured via the dispersion of the signal pulse, which was collected alongside the memory results using my data acquisition and control system. The memory efficiency was found to be in agreement with the predicted efficiency based on the theory of the Raman interaction. Single-photon-level pulses were stored with similar memory efficiency and a SNR of 2.6:1, highlighting the system's potential as a quantum memory. Finally, the memory lifetime was 27±9 ns, which represents a time-bandwidth product of 100, indicating the memory could be suitable for implementing local nodes of quantum information networks.

8.2 Future work

8.2.1 Optimize memory in HC-PCF

A practical limitation of the HC-PCF memory is that currently LIAD is needed in order to generate a sufficiently high optical depth, which limits the pulse repetition rate of the memory. Increasing the pulse repetition rate could proceed along two directions:

1. Systematically study LIAD in more detail in order to optimize it for lower, more frequent increases in optical depth. Specifically, examine the dependence of LIAD on the wavelength, pulse duration, and focusing parameters of the LIAD beam.

2. Eliminate the need for LIAD with even larger core diameters. The larger core diameter should make it easier to load with alkali atoms and obtain a higher optical depth for the memory interaction. Our collaborators from the Max Planck Institute in Erlangen have drawn a new 45-μm-diameter kagome-structured HC-PCF, which we intend to install in our vacuum system.

Apart from the issue of LIAD, it would be of interest to examine the non-adiabatic regime – where the control field Rabi frequency is comparable to the detuning – in order to examine the cross-over between storage and stimulated emission. The limit that the noise places on the memory fidelity, and the resultant optimal optical depth, has only begun to be considered [284, 287] and further theoretical and experimental work is needed. Additionally, it remains an open question as to how best characterize the noise, whether it be with second and third-order correlation functions [125] or more complete homodyne measurements.

Finally, and longer term, splicing the HC-PCF to a standard single-mode fibre is needed to make a truly integrated quantum memory. Splicing to standard HC-PBGF has been demonstrated with a loss of 1.0 dB per splice [290], of which the authors estimate 0.15 dB to be from refractive index mismatch and 0.4-0.6 dB from modal mismatch. This process has since been adapted to larger core kagome-structured HC-PCFs [291]. However, it has yet to be demonstrated under high vacuum, which remains an outstanding challenge.

8.2.2 Storage of heralded single photons

Optical phonons

A natural extension of the work in chapters 3 and 4 is the implementation of a stimulated Raman memory with optical phonons in diamond. An initial study has shown that the unconditional noise floor is low enough for the storage of single photons [75]. Storage of a heralded single photon would create a single-phonon Fock state in the diamond, without resort to 'retrodictive' inference (see section 4.6 in chapter 4). However, beyond this proof-of-principle demonstration, the optical phonon memory is of limited use for practical applications. While the TBP is high, any conditional measurement requires photodection, which has a response time (100s ps) much longer than the coherence time of the phonon. The memory lifetime cannot be significantly extended by cooling (the optical phonon mode is already 'cool' compared to the thermal environment). A proposal to use a super-lattice made from alternating layers of carbon-12 and carbon-13, creating a three-dimensional phononic band-gap structure that would eliminate decay through the

'Klemens' channel [129, 292], is extremely demanding and would not increase the phonon lifetime beyond 100 ps [293].

HC-PCF cesium memory

The HC-PCF memory is more promising for synchronizing single-photon sources as it has a high time-bandwidth product, a memory lifetime compatible with active optical elements, and requires a low control-field pulse energy (see chapter 7). Storage of heralded single photons requires a bright source of GHz-bandwidth heralded single photons, which has been developed by our group [287]. It would also likely require a lower noise floor (see section 7.4). Finally, the coupling efficiency into the HC-PCF and the attendant transmission through the optical viewports would also need to be improved by more careful mode-matching and the addition of anti-reflection coatings.

8.2.3 Heralded single-photon source in HC-PCF

Another natural extension is to consider implementing a HC-PCF memory based on spontaneous four-wave mixing [29]. Indeed, as the noise source of the stimulated Raman memory appears to be SFWM, it seems that we may have inadvertently done so already. This could be confirmed by observing non-classical correlations between the Stokes and anti-Stokes fields, as shown in chapter 3 with diamond, or by observing the heralded auto-correlation of the anti-Stokes (or Stokes, depending on which level is the ground state) field to be less than one. An advantage of this approach is that the memory synchronization and source can be incorporated into a single compact, fibre-based package [290]. The disadvantage is that the interaction is inherently not phase matched, and the two control pulses must be be collinear,[1] which will limit the retrieval efficiency.

8.2.4 Magnetic-field sensing in HC-PCF

An interesting application for a HC-PCF memory is the measurement of magnetic fields. Atomic magnetometers have demonstrated sensitivities on the order of 1 fT/$\sqrt{\text{Hz}}$ [294], equaling SQUID-based magnetometers, and have the potential to reach ∼aT/$\sqrt{\text{Hz}}$ [295].

[1] Keep in mind that the guided mode in a HC-PCFs has a finite acceptance angle.

Compact atomic magnetometers based on microfabricated vapour cells have reached sensitivities on the order 70 fT/$\sqrt{\text{Hz}}$ [296]. And an evanescent-wave, fibre-based magnetometer has reached a sensitivity of 10 pT/$\sqrt{\text{Hz}}$ [297]. The sensitivity of an atomic magnetometer is based on the minimum resolvable Zeeman splitting of the magnetic sublevels in the hyperfine ground states. The linewidth of these states is determined by the coherence time of the atomic spin states. The same considerations for choosing a platform for an integrated memory – long coherence time and high optical depth – are present in choosing an integrated fibre-based magnetometer. Therefore, a kagome-structured HC-PCF magnetometer would offer superior performance for a compact, fibre-integrable package capable of high-spatial-resolution magnetic field sensing. To be competitive with microfabricated vapour-cell-based magnetometers, however, would likely require spin-preserving coatings applied to the fibre core. Paraffin coatings are thick, on the order of several microns at minimum [271] and are liable to occlude the fibre core. Either thinner coatings (e.g. octadecyltrichlorosilane [298]) or larger cores could be used to overcome this limitation, although the results so far have been mixed [220, 245].

Another approach is to exploit the memory itself to measure magnetic fields. The memory efficiency is sensitive to magnetic fields; an applied magnetic field causes the magnetic sub-levels to dephase, reducing the memory efficiency [72]. Measuring the memory efficiency at a fixed delay, or alternatively, measuring the Raman linewidth could be used to probe the magnetic field inside the HC-PCF. Finally, it would also be interesting to investigate the Faraday effect during memory storage [299].

8.2.5 Rydberg atoms in HC-PCF

There is a delightful scene in *Dead Souls* by Nikolai Gogol where 'our hero' Pavel Ivanovich Chichikov visits the home of Manilov, a local landowner. For several minutes the characters stand at the threshold of the drawing room, each imploring the other to enter the door first. Eventually they attempt to pass through the door at the same time, which is too narrow to accommodate both of them [300]. A not dissimilar effect arises between Rydberg atoms where, instead of being blocked from entering the room due to a cloying sense of politeness, two Rydberg atoms are prevented from being excited with a certain

radius (the blockade radius) by a laser with a fixed frequency and narrow bandwidth. The doubly excited Rydberg-Rydberg interaction causes a frequency shift greater than the linewidth of the excitation laser, blocking the local creation of two Rydberg atoms [301, 302].

The Rydberg-Rydberg interaction is an optical non-linearity that can be used to implement two-photon computational gates [303, 304]. An ensemble of Rydberg atoms localised to within a Rydberg blockade radius forms the symmetric state from equation 3.1. Through inhomogeneous broadening, the excitation can be spread over all N atoms, which enables efficient single-photon absorption [305]. More recently, Rydberg interactions have generated attractive interactions between photons, creating bound two-photon states [306].

It would be interesting to generate Rydberg atoms confined in HC-PCFs. Here the dimensions of the HC-PCF can be comparable to the Rydberg blockade radius, creating an extended one-dimensional atomic system. With cold atoms, exotic phenomena such as the fermionization of photons – the converse of a Tomonaga-Luttinger liquid – can emerge [307]. In addition, coupling the spin-wave of a memory to an excited Rydberg state could create non-classical optical states [308]. Previous studies have shown that Rydberg atoms can be formed in micro-cells in close proximity to dielectric quartz flats [309]. It was found that particular Rydberg states (e.g. 32s) did not couple to surface polaritons in the quartz, which was attributed to a minimal overlap between the surface polaritons and the allowed dipole transitions. Further, the amount of dielectric material in HC-PCFs is greatly reduced compared to quartz flats, making HC-PCFs a promising platform for investigating nonlinear optical effects.

Appendix A

Here I review the statistical tools I deployed in chapter 4 in order to calculate the confidence interval of the concurrence of the joint optical state from the diamonds.

Rare events, where the probability of each event is much less than one for each realization of the experiment, have a Poissonian distribution, and are defined by a single parameter μ, which is both the mean and variance. The probability of an observation X (an integer), given a known μ is simply

$$P(X|\mu) = \frac{\mu^X \mathrm{e}^{-\mu}}{X!}. \tag{1}$$

Often, however, the inverse question is more relevant: given an observation X, what is the likelihood that this observation comes from a Poissonian distribution with parameter μ? We now try to answer this question.

Frequentist approach

The unbiased maximum likelihood estimate $\hat{\mu}$ of parameter μ given an observation X is $\hat{\mu} = X$. This can be seen from the likelihood function $L(\mu|X)$ for a Poissonian distribution,

$$L(X|\mu) = \frac{\mu^X \mathrm{e}^{-\mu}}{X!}. \tag{2}$$

To find the maximum likelihood, we differentiate equation 2 with respect to μ and equate it to zero,

$$\begin{aligned} \frac{\partial L(X|\mu}{\partial \mu}|_{\mu=\hat{\mu}} &= \frac{X\hat{\mu}^{X-1}\mathrm{e}^{-\hat{\mu}}}{X!} - \frac{\hat{\mu}^{X}\mathrm{e}^{-\hat{\mu}}}{X!} = 0, \\ \Rightarrow 0 &= \frac{X}{\hat{\mu}} - 1, \\ \Rightarrow \hat{\mu} &= X. \end{aligned} \tag{3}$$

The maximum likelihood estimate of the parameter $\hat{\mu}$ is simply given by the number of observations X.

Bayesian approach

Matters become considerably more interesting when we use the likelihood function and a prior distribution $P(\mu)$ to derive a probability distribution function. A given observation X most likely came from a Poissonian distribution with parameter $\hat{\mu} = X$ (the maximum likelihood), but there is a finite probability it came from some other μ. The specific probability is

$$P\left(\mu|X\right) = \frac{L(X|\mu)P(\mu)}{\int L(X|\mu)P(\mu)\mathrm{d}\mu}. \tag{4}$$

The likelihood function is well-defined. The choice of prior, however, is a delicate matter, which is to say there is much disagreement [310]. There are two main approaches: subjective and objective priors [175, 311, 312].

Objective priors

The goal at hand is to a choose a prior that reflects your ignorance toward the parameter μ. This is more difficult than it sounds. The simplest choice, perhaps, is a uniform, flat prior that is constant over the real line (or some part of it). This is what physicists refer to as an 'uninformative' prior. From equation 4, the posterior distribution is, therefore,

$$P\left(\mu|X\right) = \frac{\mu^{X}\mathrm{e}^{-\mu}}{\int_0^\infty \mu^{X}\mathrm{e}^{-\mu}\mathrm{d}\mu}. \tag{5}$$

There are three problems with this choice. One, it can cause the posterior to be improper, i.e. it diverges (this is not the case here). Two, a flat prior in some circumstances is not 'uninformative'. Take the example of the estimating the variance σ^2 of a Gaussian distribution. A flat prior would assign a greater probability to $\sigma^2 > \sigma_0^2$ than $\sigma^2 < \sigma_0^2$ for any $\sigma_0^2 > 0$ [310]. In other words, the prior is not scale invariant. In this case, it is desirable that the scale parameter is found in the interval 1 to 10 with the same probability as the interval 10 to 100. An appropriate prior, therefore, would be flat with respect to the logarithm of the variance. Finally, and related, the posterior distribution is not invariant under transformations of the parameter μ.

A putative solution is offered by Jeffreys' construction of a non-informative prior based on Fisher's information. For a simple parameter, the Jeffreys prior $P_J(\mu)$ is given by the square root of the Fisher information $I(\mu)$,

$$P_J(\mu) = \sqrt{I(\mu)}. \tag{6}$$

The Fisher information quantifies the amount of information an observation X contains about a distribution parametrized by μ, which in turn determines the probability of X. Specifically,

$$I(\mu) = \mathrm{E}\left(\left[\frac{\partial}{\partial \mu} \log P(X|\mu) \right]^2 \middle| \mu \right), \tag{7}$$

which can be written, if $\log P(X|\mu)$ is twice differentiable with respect to μ, as

$$I(\mu) = -\mathrm{E}\left(\frac{\partial^2}{\partial \mu^2} \log P(X|\mu) \middle| \mu \right), \tag{8}$$

where E(...) is the expectation value. The Fisher information of a Poissonian process is

then

$$\begin{aligned} I(\mu) &= -\mathrm{E}\left(\frac{\partial^2}{\partial\mu^2}\log\frac{\mu^X \mathrm{e}^{-\mu}}{X!}\middle|\mu\right) \\ &= -\mathrm{E}\left(\frac{\partial^2}{\partial\mu^2}\left(X\log\mu-\mu-\log X!\right)\middle|\mu\right) \\ &= -\mathrm{E}\left(\left(-\frac{X}{\mu^2}\right)\middle|\mu\right) \\ &= \frac{1}{\mu}, \end{aligned} \tag{9}$$

as the expectation value of X is μ (see equation 3). The Fisher information is inversely proportional to the parameter μ. The correct intuition here is that a larger μ (and hence larger variance) means that each observation will carry a smaller amount of information to bound the variance; many observations will be needed to accurately estimate the variance. If the distribution is sharply peaked (and μ is consequently small) fewer observations will be needed to estimate the variance, and the Fisher information from each observation will be higher.

The Jeffreys prior for a Poissonian distribution is, therefore,

$$P_J(\mu) = \frac{1}{\sqrt{\mu}}, \tag{10}$$

and the posterior probability distribution is, from equations 4 and 10

$$P\left(\mu|X\right) = \frac{\mu^{X-\frac{1}{2}}\mathrm{e}^{-\mu}}{\int_0^\infty \mu^{X-\frac{1}{2}}\mathrm{e}^{-\mu}d\mu}. \tag{11}$$

The most probable μ is shifted lower as the Jeffreys prior weighs lower values more heavily. Specifically,

$$\begin{aligned} \left.\frac{\partial L(X|\mu)}{\partial\mu}\right|_{\mu=\hat{\mu}} &= \frac{(X-\frac{1}{2})\hat{\mu}^{X-\frac{3}{2}}\mathrm{e}^{-\hat{\mu}}}{X!} - \frac{\hat{\mu}^{X-\frac{1}{2}}\mathrm{e}^{-\hat{\mu}}}{X!} = 0, \\ \Rightarrow 0 &= \frac{(X-\frac{1}{2})}{\hat{\mu}} - 1, \\ \Rightarrow \hat{\mu} &= X - \frac{1}{2}. \end{aligned} \tag{12}$$

It is important to note that the Jeffreys prior leaves the probability invariant under

transformations (e.g. $\mu \to \mu^2$).

There are other objective priors that are based on other principles, such as maximal missing information (called a reference prior), where a prior maximizes the 'distance' (the Kullback-Leibler distance) between the prior and posterior distribution [310]. In this case, a prior is chosen that is maximally transformed by the addition of new information, therefore the initial prior is least informative. This is related to Jeffreys prior, and is only distinct when considering multi-parameter estimation [176]. Specifically, a Jeffreys prior is a reference prior with all parameters given equal importance, whereas reference priors can incorporate varying degrees of prior knowledge distributed over many parameters. There are also approaches based on maximum entropy advocated by Edwin T. Jaynes (of Jaynes-Cummings model fame). These approaches (maximum entropy, maximum missing information), however, all lead to the Jeffreys prior for single parameter estimation. [176]

Subjective priors

If you have other information indicating a prior belief in the value of the parameter, then it may be sensible to construct a prior that reflects this knowledge [311]. For instance, when taking more data the posterior distribution of the previous measurement forms a subjective prior distribution of a new posterior distribution contingent on the likelihood function of the new data. The shape of the distribution will then reflect your *a priori* state of knowledge of the parameter. One possibility is to use a conjugate prior, such that the posterior and likelihood distribution are of the same form, and to parametrize it to reflect your *a priori* belief in the parameter of interest [313]. For instance, the conjugate prior of a Poissonian distribution is a Gamma function.

Confidence intervals

Maximum likelihood estimation

As discussed above, the maximum likelihood estimate $\hat{\mu}$ for X observations is $\hat{\mu} = X$. We can calculate the probability that the concurrence is zero $X > \lceil \mu_0 \rceil$, where $\lceil .. \rceil$ denotes

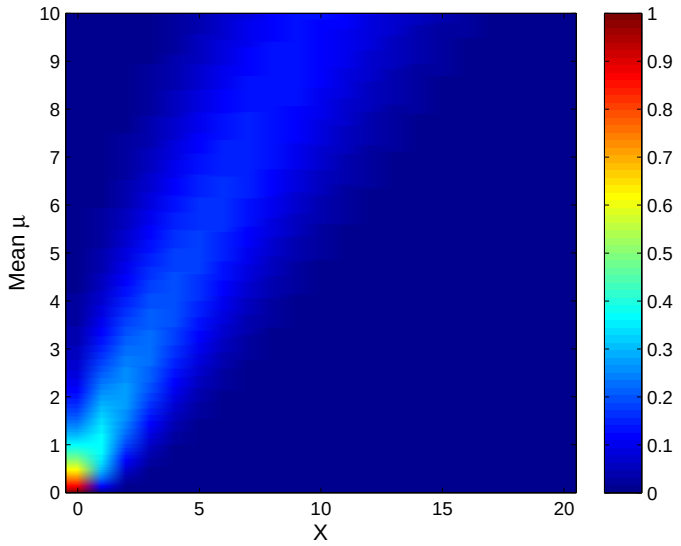

Figure 1: Poissonian probability as a function of the parameters μ and X over a limited range. The continuous variable μ was calculated in discrete increments of 0.005.

the ceiling function, for a Poissonian distribution with mean $\hat{\mu}$,

$$P(X \geq \lceil \mu_0 \rceil | \hat{\mu}) = \sum_{X=\lceil \mu_0 \rceil}^{\infty} \frac{\mu^X \mathrm{e}^{-\mu}}{X!}. \tag{13}$$

For $X = 3$ and $\mu_0 = 9.1$, the probability is 0.1%. This approach, however, is overly optimistic, we start out by assuming that which we wish to test (whether the state has positive concurrence).

Frequentist confidence interval

Here we calculate the confidence level α given X observations such that the confidence interval is $0 \leq \mu \leq \mu_0$, where μ_0 is the smallest value consistent with zero concurrence. A frequentist confidence interval encompasses a belief in a single, fixed, value for the parameter μ_t and, for a given confidence level, gives the fraction of experiments that the confidence interval will contain μ_t. This is in contrast to the Bayesian approach, where the credible level indicates the 'degree of belief' that μ_t is within the credible interval $0 \leq \mu \leq \mu_0$ [174]. The distinction may seem slight, but is valid.

Formally, the confidence interval is given by

$$P(\mu \in [0, \mu_0]) = \alpha. \tag{14}$$

This is found by calculating $P(X|\mu)$ [2] from equation 1 for each value of μ (a continuous variable) and each value of X (a non-negative integer), as is shown in figure 1. For a given observation X, one integrates with respect to μ at that value of X until the confidence level in equation 14 is met. In the case of an upper limit, the expression is

$$\int_0^{\mu_0} P(X = 3|\mu)\mathrm{d}\mu = \alpha. \tag{15}$$

For $X = 3$ and $\mu_0 = 9.1$ the confidence level is 98%.

In this case, we were interested in the one-sided confidence interval (from 0 to μ_0) and not the two-sided confidence interval (from μ_l to μ_u). However, a serious problem develops if the choice of whether to use one-sided or two-sided confidence is based on the data. This is done, for instance, to avoid non-physical results such as the confidence interval extending below zero. As more events are recorded it may be desirable to switch to a two-sided confidence interval. Doing so in an *ad hoc* way will lead the quoted confidence interval to undercover (underestimate) the true confidence level [174]. A method proposed by Feldman and Cousins [174] gives an objective way to construct the confidence interval that automatically transitions from one-sided confidence intervals for a low number of events to two-sided confidence intervals as the number of events increase.

The method constructs confidence intervals by ordering the probabilities as a function of X (for fixed μ) based on the ratio of likelihoods R. The ratio of likelihoods weights the probability $P(X|\mu)$ by an alternative hypothesis that maximises $P(X|\mu)$ (for fixed X). Specifically, [174]

$$R = \frac{P(X|\mu)}{P(X|\mu_\mathrm{max})}. \tag{16}$$

From the maximum likelihood analysis, we showed that $\mu_{max} = X$ maximises $P(X|\mu_{max})$. Figure 2 gives the likelihood ratio over the same parameter range as figure 1. It can be

[2] This notation should be interpreted with care in the context of the Frequentist approach to statistics. It is not a conditional probability in the Bayesian sense, and the distinction between $P(X|\mu)$ and $P(X;\mu)$ is illusory (cf. [174] footnote 5).

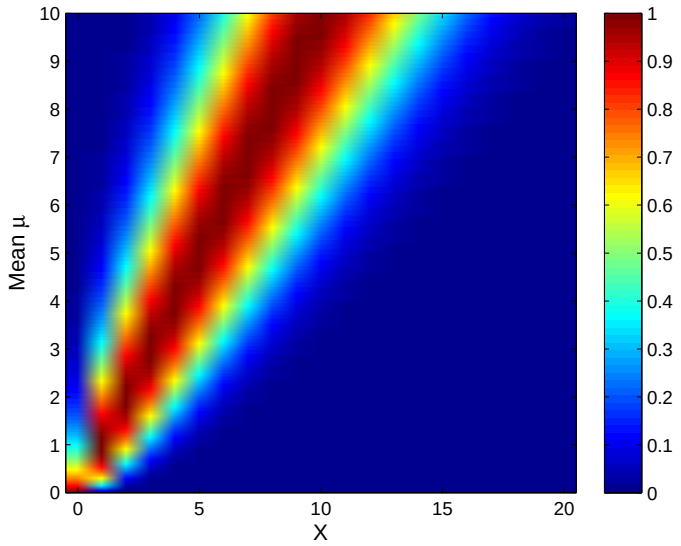

Figure 2: Ratio of the likelihoods used to rank the Poissonian probabilities when constructing the confidence intervals.

seen that the ratio effectively normalizes each likelihood for a fixed X.

The probabilities $P(X|\mu)$ are summed according to the ranking in figure 2 for a fixed μ until the confidence level in equation 14 is exceeded (the confidence interval will be inherently conservative because the summed probability will, in general, exceed the confidence level owing to the discrete nature of the Poissonian distribution) [174]. The 68.3% and 95% confidence intervals are calculated in figure 3. Therefore, for the observation $X = 3$, the confidence intervals are 1.1 to 5.3 at a 68.3% confidence level, and 0.82 to 8.25 at a 95% confidence interval, in complete agreement with the results of Feldman and Cousins [174]. For zero concurrence, $\mu = 9.1$, which corresponds to a confidence level of 97.5%. In some instances the confidence interval has the particular pathology that they are not simply connected. In this case, the maximum and minimum points are taken to be the confidence interval, again making the estimate slightly conservative [174].

Bayesian credible interval

Here we calculate the posterior distribution $P(\mu|X)$ (equation 4) from the likelihood function $L(\mu|X)$ (equation 2) and a prior distribution of $P(\mu)$,

$$P(\mu|X) = \frac{L(X|\mu)P(\mu)}{\int L(X|\mu')P(\mu')\mathrm{d}\mu'}. \tag{17}$$

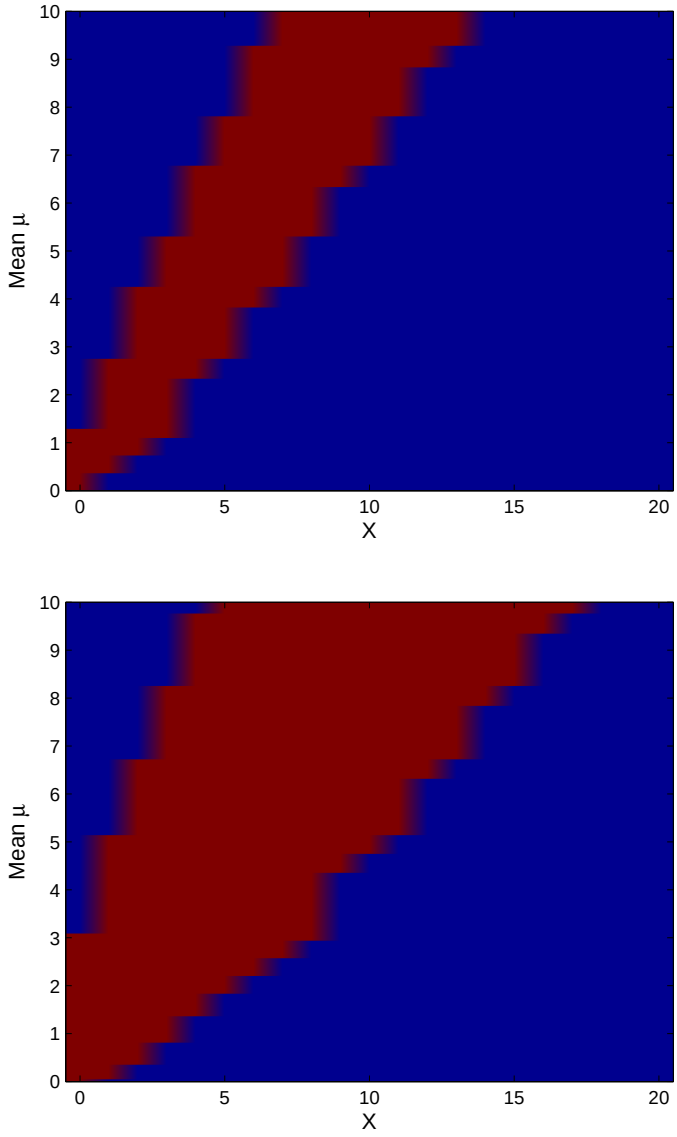

Figure 3: Likelihood ordered confidence intervals (in red). **Top** Confidence level = 68.3% (1σ) **Bottom** Confidence level = 95% (2σ).

We examine the two priors discussed above, the flat prior and the Jeffreys prior.

Flat prior

A flat prior is given by $P(\mu) = \text{const.}$ (an improper prior), which gives a posterior distribution (equation 5)

$$P(\mu|X=3) = \frac{\mu^3 \mathrm{e}^{-\mu}}{\int_0^\infty \mu'^3 \mathrm{e}^{-\mu'} \mathrm{d}\mu'}. \tag{18}$$

The Bayesian credible level is therefore given by integrating all $\mu \geq \mu_0$,

$$\begin{aligned} P(\mu \geq \mu_0|X) &= \int_{\mu_0}^{\infty} \frac{\mu'^X \mathrm{e}^{-\mu'}}{\int_0^{\infty} \mu'^X \mathrm{e}^{-\mu'} \mathrm{d}\mu'} \mathrm{d}\mu' \\ &= \int_{\mu_0}^{\infty} \frac{\mu'^X \mathrm{e}^{-\mu'}}{X!} \mathrm{d}\mu' \\ &= \frac{1}{X!} \left[-\Gamma(X+1, \mu')\right]_{\mu_0}^{\infty} \\ &= \frac{\Gamma(X+1, \mu_0)}{\Gamma(X+1, 0)}, \end{aligned} \tag{19}$$

where $\Gamma(4, \mu_0)$ is the incomplete Gamma function. For $X = 3$ and $\mu_0 = 9.1$ the credible level is 2.0%.

Jeffreys prior

The Jeffreys prior for a Poissonian distribution is given by $P(\mu) = 1/\sqrt{\mu}$, which gives a posterior distribution (equation 5)

$$P(\mu|X) = \frac{\mu^{X-1/2} \mathrm{e}^{-\mu}}{\int_0^{\infty} \mu'^{X-1/2} \mathrm{e}^{-\mu'} \mathrm{d}\mu'}. \tag{20}$$

The Bayesian credible level is therefore given by integrating all $\mu \geq \mu_0$,

$$\begin{aligned} P(\mu \geq \mu_0|X) &= \int_{\mu_0}^{\infty} \frac{\mu'^{X-1/2} \mathrm{e}^{-\mu'}}{\int_0^{\infty} \mu'^{X-1/2} \mathrm{e}^{-\mu'} \mathrm{d}\mu'} \mathrm{d}\mu' \\ &= \int_{\mu_0}^{\infty} \frac{\mu'^{X-1/2} \mathrm{e}^{-\mu'}}{\Gamma(X+\frac{1}{2}, 0)} \mathrm{d}\mu' \\ &= \frac{1}{\Gamma(X+\frac{1}{2}, 0)} \left[-\Gamma(X+\frac{1}{2}, \mu')\right]_{\mu_0}^{\infty} \\ &= \frac{\Gamma(X+\frac{1}{2}, \mu_0)}{\Gamma(X+\frac{1}{2}, 0)}. \end{aligned} \tag{21}$$

For $X = 3$ and $\mu_0 = 9.1$, the credible level is 1.1%. The Jeffreys prior results in a slightly more optimistic credible level as it weights the lower values of μ as compared to the flat prior. In conclusion, the most pessimistic estimate of the confidence level between the objective and Jeffreys prior is 98.0%.

Appendix B

The following program was used to lock the relative phase of the Stokes and anti-Stokes interferometers. The program was written in Matlab and uses the Data Acquisition Toolbox V2.13 and the NI DAQ driver V9.0 along with the NI PCI-6602 data acquisition card. It consists of two separate sub-programs. The first one scans the piezo voltage to produce a sinusoidal interference fringe from both interferometers. The data are automatically fit to a sine function to extract the range and midpoint, which is saved to a file. The second program reads the saved data and uses the midpoint as the setpoint for the feedback program. Proportional-integral feedback generates an error signal that is then output as a voltage (and sent to piezoelectric elements in the interferometers).

```
%-------------------------------------------------------------------------
%Program to initialize phase locking program (DAQ_IOContinuous2Channel.m)
%Software used: DAQ toolbox v2.13, NI DAQ driver v9.0
%Hardware used: NI PCI-6602
%Operation: Piezo voltage swept to acquire inteference fringe, mid-point,
%and range were determined and saved to file read by phase-lock program
%M.R. Sprague May 2011
%-------------------------------------------------------------------------

close all
clear all

%Channel 1 = AI/O(0)
%Channel 2 = AI/O(1)

%Set system Parameters for Channel1

PiezoSens1   =  150/9.1;  %(V/um) Thorlabs AE050D08F
Wavelength1  =  0.8;      %(um) Wavelength of locking light
NumCyc1      =  1.0;        %Number of cycles to scan over
PiezoAmp1    =  15;       %(V/V)Amplification of Piezo-controller (MDT694A)
OperatingV1  =  100;      %Ideal operating Voltage for Piezo (AE050D08F)
PointPerCyc1 =  15;       %Points per cycle

IncrementV1  = PiezoSens1*Wavelength1/(PointPerCyc1*PiezoAmp1);
```

```
Vrange1      = PiezoSens1*Wavelength1*NumCyc1/(PiezoAmp1);
Vmax1        = Vrange1;
Vmin1        = 0;         %Piezo controller does not allow negative voltage

V1 = Vmin1:IncrementV1:Vmax1;

%Set system Parameters for Channel2

PiezoSens2   =  150/9.1;  %(V/um) Thorlabs AE050D08F
Wavelength2  =  0.8;      %(um) Wavelength of locking light
NumCyc2      =  1.0;        %Number of cycles to scan over
PiezoAmp2    =  10;       %(V/V)Amplification of Piezo-controller (Posi-Con)
OperatingV2  =  100;      %Ideal operating Voltage for Piezo (AE050D08F)
PointPerCyc2 =  15;       %Points per cycle

IncrementV2  = PiezoSens2*Wavelength2/(PointPerCyc2*PiezoAmp2);
Vrange2      = PiezoSens2*Wavelength2*NumCyc2/(PiezoAmp2);
Vmax2        = Vrange2;
Vmin2        = 0;

V2 = Vmin2:IncrementV2:Vmax2;

% Define two analog input/output channels
AI = analoginput('nidaq','Dev3');
chan = addchannel(AI,0:1);
AO = analogoutput('nidaq','Dev3');
chan2 = addchannel(AO,0:1);

% Analog Input Settings
duration = .06;% 0.06;
set(AI,'SampleRate',100);
ActualRate = get(AI,'SampleRate');
% Number of samples acquired
length = floor(ActualRate*duration);
set(AI,'TriggerType','Manual','SamplesPerTrigger',length);

% Analog Output Settings
set(AO,'SampleRate',ActualRate,'TriggerType','Manual');

% Set length of program
looplength = max(size(V1,2),size(V2,2));

%Concatenate with zero if unequal voltage range
if size(V1,2)>size(V2,2)
    V2 = cat(2,V2,zeros(1,(size(V1,2)-size(V2,2))));
elseif size(V2,2)>size(V1,2)
    V1 = cat(2,V1,zeros(1,(size(V2,2)-size(V1,2))));
end

% Initialise data input arrays and integrated error
```

```
dm = zeros(length,2,looplength);
atm = zeros(length,looplength);

for i=1:1:looplength
    tic

    %Load voltage scan values
    control1(1:6) = V1(:,i);
    control2(1:6) = V2(:,i);

    % Load voltage scan into array for output
    putdata(AO,[control1' control2'])
    start(AO)
    trigger(AO)
    % Wait until A0 written before proceeding
    wait(AO,duration*20+1)

    %Read photodiode signal
    start(AI)
    trigger(AI)
    % Wait until AI read before proceeding
    wait(AI,duration*20+1)
    % wait(AI,duration+1)
    [data t abst] = getdata(AI);

    dm(:,:,i) = data;
    atm(:,i) = abst;

    toc
end

%Reformat photodiode output signal
pdt = mean(dm,1);
pd  = reshape(pdt,2,looplength);

%Initial guess for parameters of fit
set = mean(pd,2);
rangeg1=max(pd(1,:))-min(pd(1,:));
rangeg2=max(pd(2,:))-min(pd(2,:));

%Fit to sine curve, channel 1
v01 = [set(1); rangeg1/2; 2*pi/PointPerCyc1/IncrementV1; 0];
[fit1,resnorm1] = lsqcurvefit(@sinefunc,v01,V1,pd(1,:));

setpoint1 = fit1(1);
range1    = abs(2*fit1(2));

%Fit to sine curve, channel 1
v02 = [set(2); rangeg2/2; 2*pi/PointPerCyc2/IncrementV2*2; 0];
[fit2,resnorm2] = lsqcurvefit(@sinefunc,v02,V2,pd(2,:));
```

```
setpoint2 = fit2(1);
range2    = abs(2*fit2(2));

%Save setpoint, range to file for reading later
save('PhaseLockParameters.mat','setpoint1','range1','setpoint2','range2')

fitcurve1 = fit1(1)+fit1(2)*sin((fit1(3)*V1)+fit1(4));
fitcurve2 = fit2(1)+fit2(2)*sin((fit2(3)*V2)+fit2(4));

setstr1 = strcat('Setpoint = ', num2str(setpoint1));
rangestr1 = strcat('Range = ',num2str(range1));

setstr2 = strcat('Setpoint = ',num2str(setpoint2));
rangestr2 = strcat('Range = ',num2str(range2));

%Plot results of scan for Stokes/anti-Stokes interferometer
figure(1)
hold on
plot(V1,pd(1,:))
plot(V1,fitcurve1,'r')
title('Stokes Interferometer','FontSize',12,'FontWeight','bold');
xlabel('Applied Voltage (V)','FontSize',12);
ylabel('Photodiode Signal (V)','FontSize',12);
text(Vrange1*0.75,setpoint1+range1/2.5,setstr1)
text(Vrange1*0.75,setpoint1+range1/3,rangestr1)
hold off

figure(2)
hold on
plot(V2,pd(2,:))
plot(V2,fitcurve2,'r')
title('Anti-Stokes Interferometer','FontSize',12,'FontWeight','bold');
xlabel('Applied Voltage (V)','FontSize',12);
ylabel('Photodiode Signal (V)','FontSize',12);
text(Vrange2*0.75,setpoint2,setstr2)
text(Vrange2*0.75,setpoint2+0.3,rangestr2)
hold off

% Close Analog Input
delete(AI)
clear AI

% Close Analog Output
delete(AO)
clear AO
```

```
%-------------------------------------------------------------------------
%Phase locking program run after (DAQ_IO_Initialize.m)
%Software used: DAQ toolbox v2.13, NI DAQ driver v9.0
%Hardware used: NI PCI-6602
%Operation: PI loop implemented for two interferometers. Acquires voltage
%input from interference signal, generates error signal that is output to
%modulate the length of the piezo-element in interferometers.
%M.R. Sprague May 2011
%-------------------------------------------------------------------------

close all
clear all

%Channel 1 = AI/O(0)
%Channel 2 = AI/O(1)

% Load Phase lock Parameters from DAQ_IO_Initialize
vars = load('PhaseLockParameters.mat');

% Setpoint (volts) for Channel 1 and 2
setpoint1 = vars.setpoint1;  %4.2
setpoint2 = vars.setpoint2;  %8.5
range1    = vars.range1;
range2    = vars.range2;

% PI Gains for Channel 1
Kp1 = -0.001; %-0.01
Ki1 = -0.03; %-0.2

% PI Gains for Channel 2
Kp2 = -0.0005; %-0.0005
Ki2 = -0.05; %-0.1

% Define two analog input/output channels
AI = analoginput('nidaq','Dev3');
chan = addchannel(AI,0:1);
AO = analogoutput('nidaq','Dev3');
chan2 = addchannel(AO,0:1);

% Analog Input Settings
duration = .06;% 0.06;
set(AI,'SampleRate',100);
ActualRate = get(AI,'SampleRate');
% Number of samples acquired
length = floor(ActualRate*duration);
set(AI,'TriggerType','Manual','SamplesPerTrigger',length);

% Analog Output Settings
set(AO,'SampleRate',ActualRate,'TriggerType','Manual');
```

```
% Set length of program
looplength = 300000;

% Initialise data input arrays and integrated error
dm = zeros(length,2,looplength);
errtest=zeros(length,looplength);
atm = zeros(length,looplength);

%initialize integral error to zero
sumerr1 = 0;
sumerr2 = 0;

for i=1:1:looplength
    tic
    start(AI)
    trigger(AI)
    % Wait until AI read before proceeding
    wait(AI,duration*20+1)
    % wait(AI,duration+1)
    [data t abst] = getdata(AI);

    %Separate channel data
    data1 = data(:,1);
    data2 = data(:,2);

    if rem(i,20)==0
        hold on
        plot(i*0.25,mean(data1),'xk')
        plot(i*0.25,mean(data2),'or')
        xlabel('Time (s)');
        legend('Stokes', 'AStokes','Location','East');
        %[mean(data1) mean(data2)]
    end

    dm(:,:,i) = data;
    atm(:,i) = abst;

    % Calculate error signal
    err1(1,1:length) = (mean(data1)-setpoint1);
    err2(1,1:length) = (mean(data2)-setpoint2);
    % Calculate integrated error
    sumerr1 = sumerr1+err1;
    sumerr2 = sumerr2+err2;
    % Sum proportional and integral feedback to give control signal
    control1 = Kp1*err1+Ki1*sumerr1+range1/2*1.1;   %1.1 = safety factor
    control2 = Kp2*err2+Ki2*sumerr2+range2/2*1.1;

    % Load control signal into array for output
    putdata(AO,[control1' control2'])
    start(AO)
```

```
    trigger(AO)
    % Wait until A0 written before proceeding
    wait(AO,duration*20+1)
    %wait(AO,duration+1)
    toc
end

outa=mean(dm,1);
out=reshape(outa,2,looplength);

% Close Analog Input
delete(AI)
clear AI

% Close Analog Output
delete(AO)
clear AO
```

Appendix C

Here we present the Labview program used to implement the frequency-offset lock program described in section 5.4. The program acquired, from the scanning Fabry-Pérot etalon, the frequency of the locked diode laser and pulsed, mode-locked laser. An error signal was calculated from the frequency difference between the lasers and then was sent through a proportional-integral controller implemented in software via Matlab. The feedback signal was output as a voltage signal to the Gires-Tournois interferometer, which adjusted the centre frequency of the pulsed oscillator. Figure 4 shows the front panel of the program and figure 5 the back panel. The sub-VIs, labelled lepidopterically, containing the save file, I/O initialization, channel termination, and Matlab logic are shown in figures 6 through 9.

Frequency-offset lock program – front panel

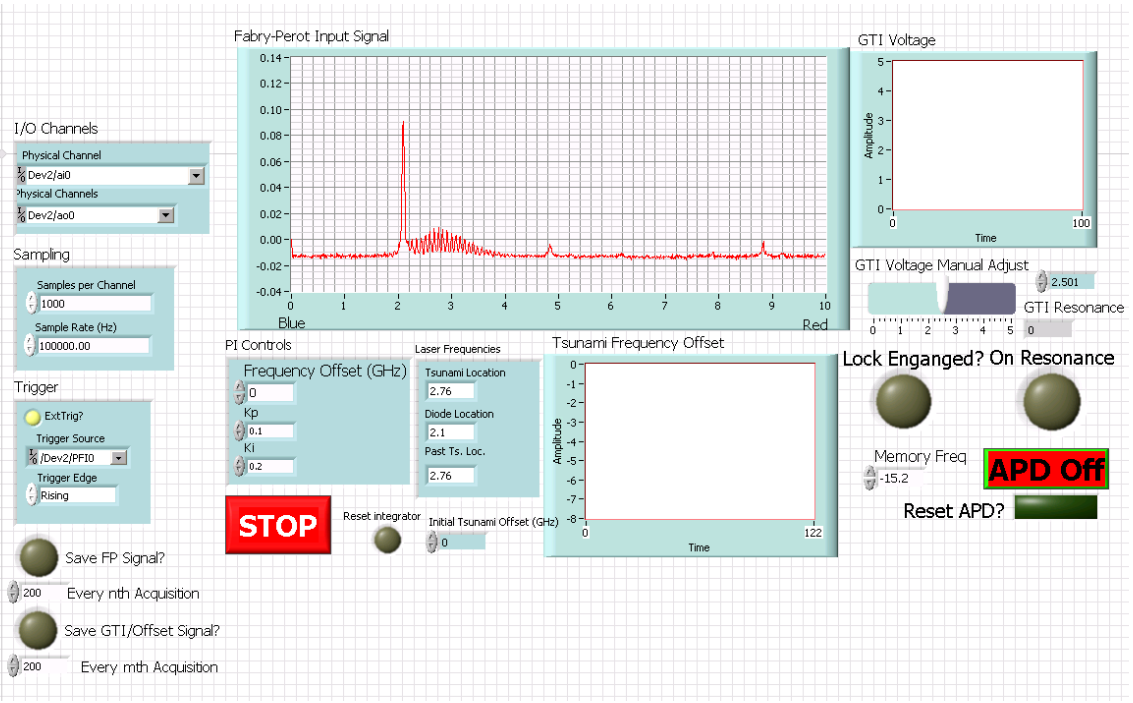

Figure 4: Front panel of the frequency-offset program showing the SFPI output, GTI voltage, frequency offset of the oscillator, PI feedback parameters, and the I/O settings.

Frequency-offset lock program – back panel

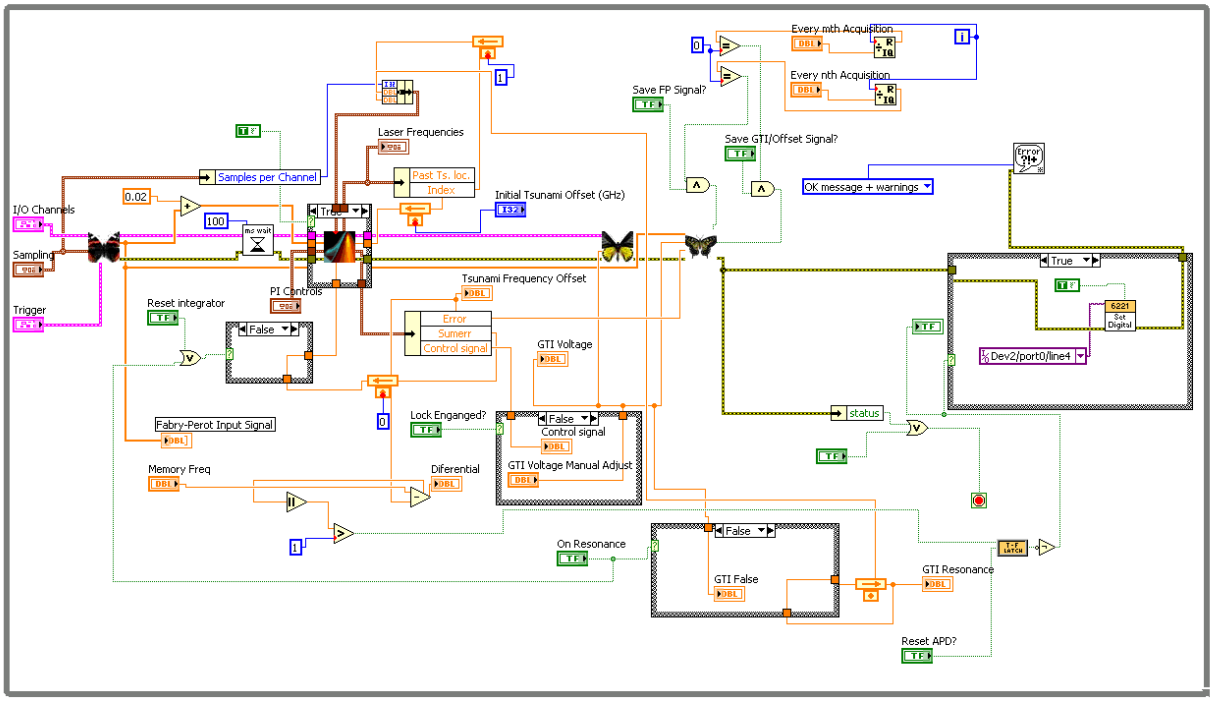

Figure 5: Block diagram of the frequency-offset lock program. *Vanessa atalanta* calls the I/O initialize sub-VI, *Troides helena* calls the data output and channel close sub-VI, *Papilio* calls the save file sub-VI, and the Matlab icon calls the Matlab logic sub-VI.

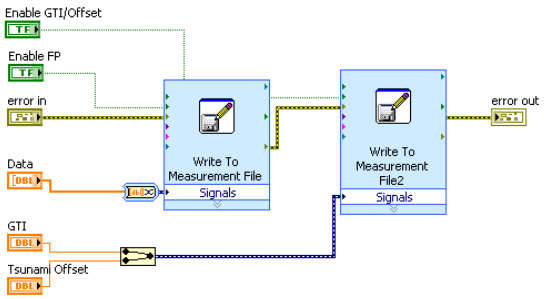

Figure 6: Block diagram of the save file sub-VI for the frequency-offset lock program.

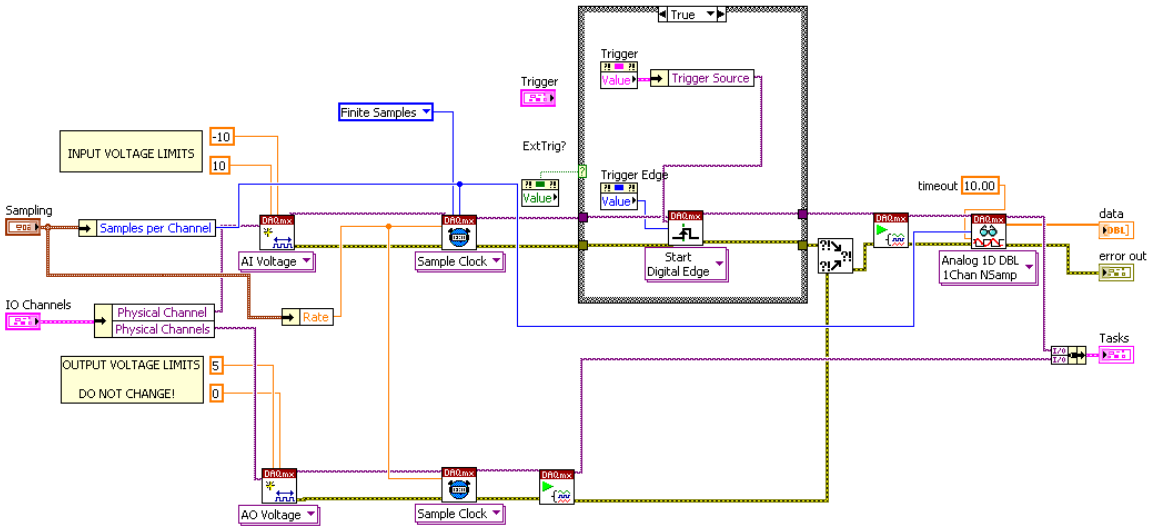

Figure 7: Block diagram of the I/O initialize sub-VI for the frequency-offset lock program.

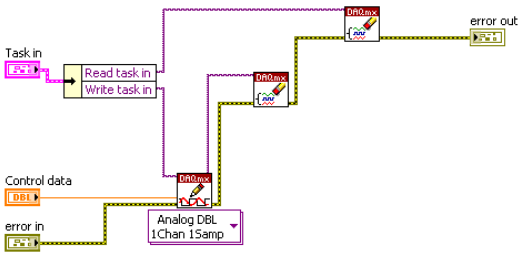

Figure 8: Block diagram of the data output and channel close sub-VI for the frequency-offset lock program.

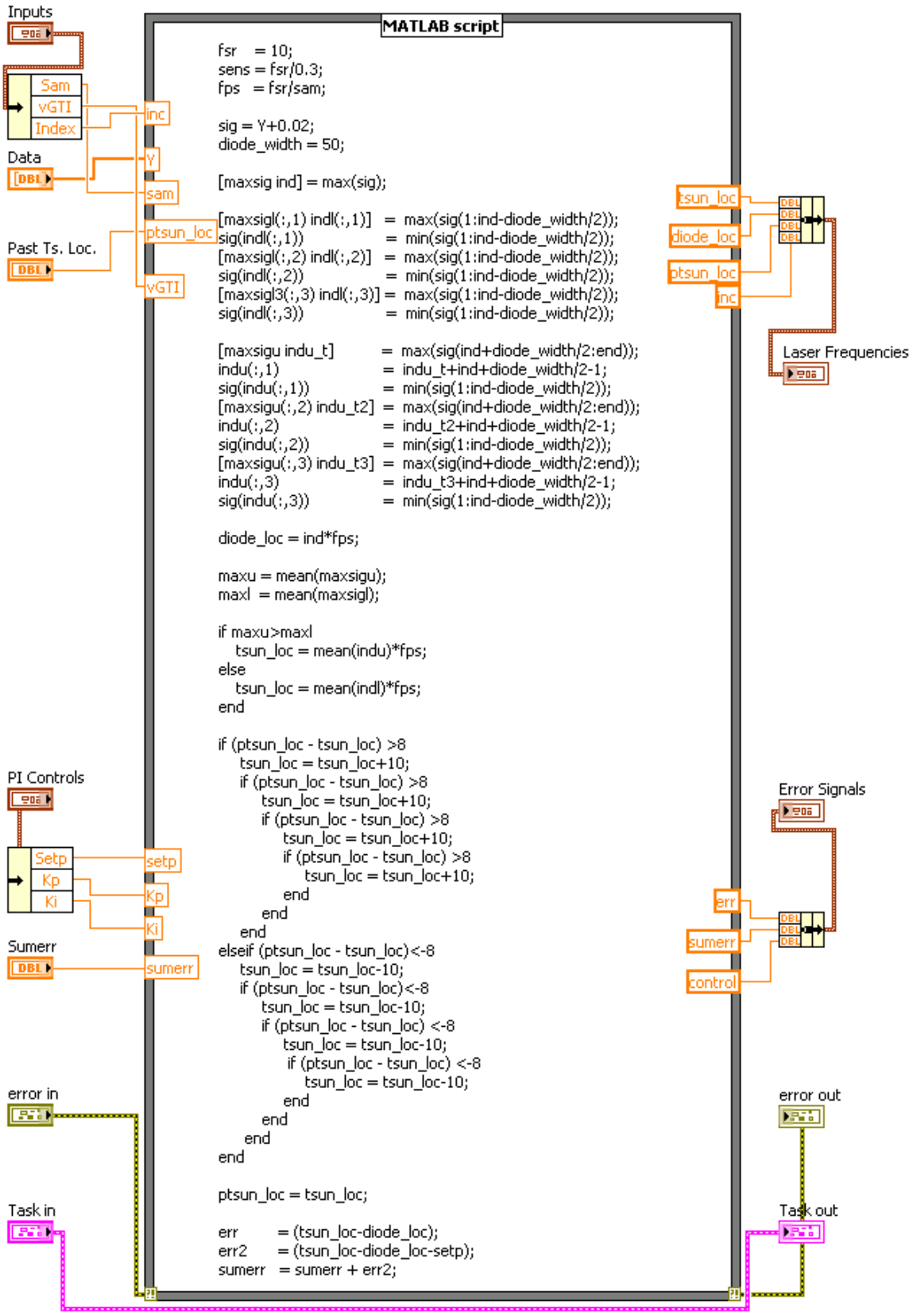

Figure 9: Block diagram showing the MATLAB implementation of the find-peak algorithm and the PI controller for the frequency-offset lock program.

Appendix D

Here we present the Labview program that controlled the HC-PCF memory experiment, and acquired the data. The front panel of the program is shown in figure 10 and the back panel in figure 11. The logic controlling the shutters in the optical paths of the control, optical pumping, and LIAD beams is shown in figure 12.

Memory data acquisition and control program – front panel

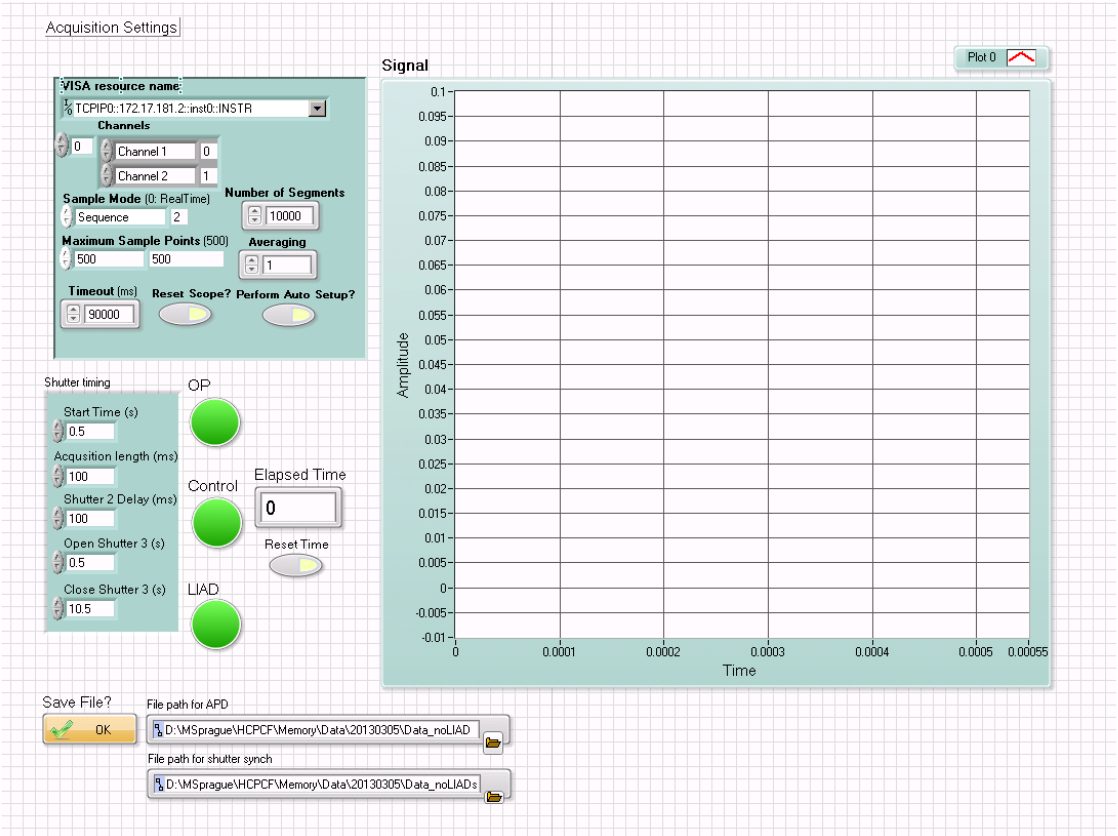

Figure 10: Front panel of the data acquisition and control program showing the oscilloscope trace from the APD, shutter status signal, and the I/O parameters.

Memory data acquisition and control program – back panel

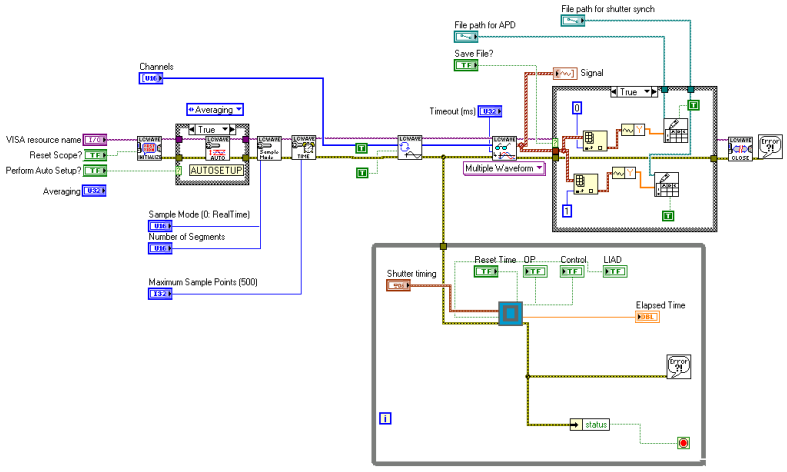

Figure 11: Block diagram of the data acquisition and control program. The blue and grey icon calls the shutter control sub-VI.

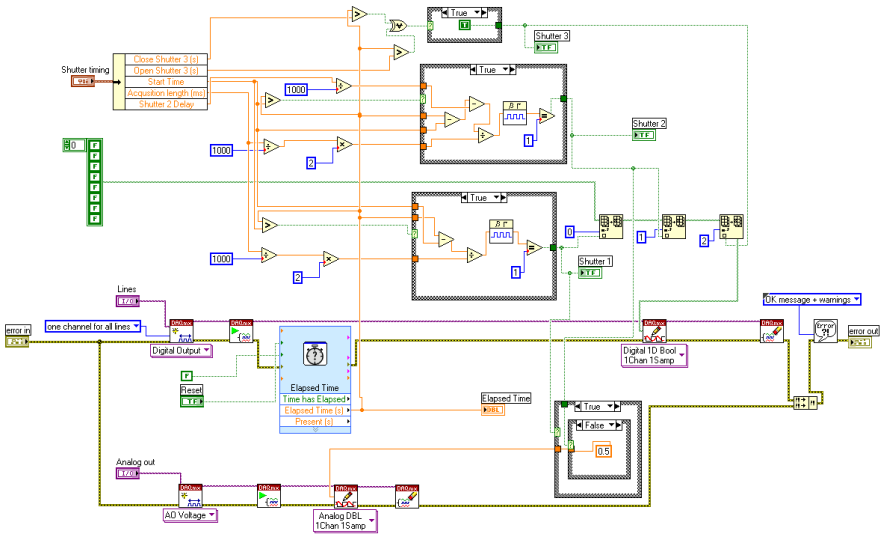

Figure 12: Block diagram of the shutter control sub-VI for the data acquisition and control program.

References

[1] Nabokov, V. V. *Speak, Memory: An Autobiography Revisted*. Pyramid, (1966). 1

[2] Kinoshita, S. and Yoshioka, S. *ChemPhysChem* **6**(8), 1442–1459 (2005). 1

[3] Fraser, A. B. *Appl. Opt.* **33**(21), 4539–4547 (1994). 1

[4] McPhedran, R. C., Nicorovici, N. A., McKenzie, D. R., Botten, L. C., Parker, A. R., and Rouse, G. W. *Australian Journal of Chemistry* **54**(4), 241–244 (2001/01/01). 1

[5] Lynch, D. K. *J. Opt. Soc. Am. A* **4**(3), 609–611 (1987). 1

[6] Kimble, H. J., Dagenais, M., and Mandel, L. *Physical Review Letters* **39**, 691–695 Sep (1977). 2

[7] Hong, C. K., Ou, Z. Y., and Mandel, L. *Physical Review Letters* **59(18)**, 2044–2046 (1987). 2

[8] Bell, J. S. *Physics 1* **3**, 195–200 (1964). 2, 59

[9] Bennett, C. H., Brassard, G., Crépeau, C., Jozsa, R., Peres, A., and Wootters, W. K. *Physical Review Letters* **70**, 1895–1899 Mar (1993). 2, 59

[10] Wootters, W. K. and Zurek, W. H. *Nature* **299**(5886), 802–803 October (1982). 2, 10, 12

[11] Dieks, D. *Physics Letters A* **92**(6), 271–272 November (1982). 2

[12] Coffman, V., Kundu, J., and Wootters, W. K. *Physical Review A* **61**, 052306 Apr (2000). 2

[13] Kwiat, P. G., Mattle, K., Weinfurter, H., Zeilinger, A., Sergienko, A. V., and Shih, Y. *Physical Review Letters* **75**, 4337–4341 Dec (1995). 2

[14] Nunn, J., Langford, N. K., Kolthammer, W. S., Champion, T. F. M., Sprague, M. R., Michelberger, P. S., Jin, X.-M., England, D. G., and Walmsley, I. A. *Physical Review Letters* **110**(13), 133601– March (2013). 3, 10, 11, 12, 167, 196

[15] Briegel, H.-J., Dür, W., Cirac, J. I., and Zoller, P. *Physical Review Letters* **81**(26), 5932–5935 Dec (1998). 3, 13

[16] Sangouard, N., Simon, C., de Riedmatten, H., and Gisin, N. *Review of Modern Physics* **83**(1), 33–80 Mar (2011). 3, 13, 14, 23, 54, 167

[17] Duan, L. M., Lukin, M. D., Cirac, J. I., and Zoller, P. *Nature* **414**(6862), 413–418 11 (2001). 3, 14, 19, 27, 28, 33, 56

[18] Knill, E., Laflamme, R., and Milburn, G. J. *Nature* **409**(6816), 46–52 (2001). 3, 56

[19] Tanji, H., Ghosh, S., Simon, J., Bloom, B., and Vuletić, V. *Physical Review Letters* **103**(4), 043601 Jul (2009). 9

[20] Julsgaard, B., Sherson, J., Cirac, J. I., Fiurasek, J., and Polzik, E. S. *Nature* **432**(7016), 482–486 (2004). 9, 15

[21] Zhao, R., Dudin, Y. O., Jenkins, S. D., Campbell, C. J., Matsukevich, D. N., Kennedy, T. A. B., and Kuzmich, A. *Nature Physics* **5**(2), 100–104 February (2009). 9

[22] Varnava, M., Browne, D. E., and Rudolph, T. *New Journal of Physics* **9**(6), 203 (2007). 10

[23] Grosshans, F. and Grangier, P. *Physical Review A* **64**(1), 010301 Jun (2001). 10

[24] Massar, S. and Popescu, S. *Physical Review Letters* **74**(8), 1259–1263 Feb (1995). 10

[25] Claudon, J., Bleuse, J., Malik, N. S., Bazin, M., Jaffrennou, P., Gregersen, N., Sauvan, C., Lalanne, P., and Gerard, J.-M. *Nature Photonics* **4**(3), 174–177 March (2010). 11

[26] Babinec, T. M., M., H. J., Khan, M., Zhang, Y., Maze, J. R., Hemmer, P. R., and Loncar, M. *Nature Nanotechnology* **5**(3), 195–199 March (2010). 11

[27] Diedrich, F. and Walther, H. *Physical Review Letters* **58**, 203–206 Jan (1987). 11

[28] McKeever, J., Boca, A., Boozer, A. D., Miller, R., Buck, J. R., Kuzmich, A., and Kimble, H. J. *Science* **303**(5666), 1992–1994 (2004). 11

[29] Yuan, Z.-S., Chen, Y.-A., Chen, S., Zhao, B., Koch, M., Strassel, T., Zhao, Y., Zhu, G.-J., Schmiedmayer, J., and Pan, J.-W. *Physical Review Letters* **98**(18), 180503– May (2007). 11, 203

[30] Nagayama, K., Kakui, M., Matsui, M., Saitoh, I., and Chigusa, Y. *Electronics Letters* **38**(20), 1168 – 1169 sep (2002). 12

[31] Bennett, C. and Brassard, G. *Proceedings of the IEEE International Conference on Computers, Systems, and Signal Processing, Bangalore* , 175 (1984). 12

[32] Ekert, A. K. *Physical Review Letters* **67**(6), 661–663 Aug (1991). 12

[33] Yang, T., Zhang, Q., Chen, T.-Y., Lu, S., Yin, J., Pan, J.-W., Wei, Z.-Y., Tian, J.-R., and Zhang, J. *Physical Review Letters* **96**, 110501 Mar (2006). 13

[34] Sangouard, N., Simon, C., Minar, J., Zbinden, H., de Riedmatten, H., and Gisin, N. *Physical Review A* **76**(5), 050301 (2007). 14

[35] Gorshkov, A. V., André, A., Lukin, M. D., and Sørensen, A. S. *Physical Review A* **76**, 033804 Sep (2007). 15, 17, 99, 150

[36] Gehring, G., Boyd, R. W., Gaeta, A. L., Gauthier, D. J., and Willner, A. E. *J. Lightwave Technol.* **26**(23), 3752–3762 December (2008). 15, 181

[37] Sherson, J. F., Krauter, H., Olsson, R. K., Julsgaard, B., Hammerer, K., Cirac, I., and Polzik, E. S. *Nature* **443**(7111), 557–560 October (2006). 15

[38] Krauter, H., Salart, D., Muschik, C. A., Petersen, J. M., Shen, H., Fernholz, T., and Polzik, E. S. *Nature Physics* **9**(7), 400–404 July (2013). 15

[39] Kielpinski, D., Meyer, V., Rowe, M. A., Sackett, C. A., Itano, W. M., Monroe, C., and Wineland, D. J. *Science* **291**(5506), 1013–1015 (2001). 15

[40] Blinov, B. B., Moehring, D. L., Duan, L.-M., and Monroe, C. *Nature* **428**(6979), 153–157 March (2004). 15

[41] Langer, C., Ozeri, R., Jost, J. D., Chiaverini, J., DeMarco, B., Ben-Kish, A., Blakestad, R. B., Britton, J., Hume, D. B., Itano, W. M., Leibfried, D., Reichle, R., Rosenband, T., Schaetz, T., Schmidt, P. O., and Wineland, D. J. *Physical Review Letters* **95**, 060502 Aug (2005). 15

[42] Maitre, X., Hagley, E., Nogues, G., Wunderlich, C., Goy, P., Brune, M., Raimond, J. M., and Haroche, S. *Physical Review Letters* **79**, 769–772 Jul (1997). 15

[43] Specht, H. P., Nolleke, C., Reiserer, A., Uphoff, M., Figueroa, E., Ritter, S., and Rempe, G. *Nature* **473**(7346), 190–193 May (2011). 15

[44] Balasubramanian, G., Neumann, P., Twitchen, D., Markham, M., Kolesov, R., Mizuochi, N., Isoya, J., Achard, J., Beck, J., Tissler, J., et al. *Nature Materials* **8**(5), 383–387 (2009). 15

[45] Dutt, M. V. G., Childress, L., Jiang, L., Togan, E., Maze, J., Jelezko, F., Zibrov, A. S., Hemmer, P. R., and Lukin, M. D. *Science* **316**(5829), 1312–1316 (2007). 15

[46] Fuchs, G. D., Burkard, G., Klimov, P. V., and Awschalom, D. D. *Nature Physics* **7**, 789–793 June (2011). 15

[47] Maurer, P. C., Kucsko, G., Latta, C., Jiang, L., Yao, N. Y., Bennett, S. D., Pastawski, F., Hunger, D., Chisholm, N., Markham, M., Twitchen, D. J., Cirac, J. I., and Lukin, M. D. *Science* **336**(6086), 1283–1286 (2012). 15

[48] Morton, J. J. L., Tyryshkin, A. M., Brown, R. M., Shankar, S., Lovett, B. W., Ardavan, A., Schenkel, T., Haller, E. E., Ager, J. W., and Lyon, S. A. *Nature* **455**(7216), 1085–1088 October (2008). 15

[49] Saeedi, K., Simmons, S., Salvail, J. Z., Dluhy, P., Riemann, H., Abrosimov, N. V., Becker, P., Pohl, H.-J., Morton, J. J. L., and Thewalt, M. L. W. *Science* **342**(6160), 830–833 (2013). 15

[50] Lvovsky, A., Sanders, B., and Tittel, W. *Nature Photonics* **3**(12), 706–714 (2009). 15, 17, 20

[51] Nunn, J. *Quantum Memory in Atomic Ensembles*. PhD thesis, University of Oxford, (2008). 15, 107, 108, 110, 114, 135, 153

[52] Lee, J. Y., Yin, L., Agrawal, G. P., and Fauchet, P. M. *Optics Express* **18**(11), 11514–11523 (2010). 15

[53] Mower, J. and Englund, D. *Physical Review A* **84**, 052326 Nov (2011). 15

[54] Hall, M. A., Altepeter, J. B., and Kumar, P. *Physical Review Letters* **106**, 053901 Feb (2011). 15

[55] Migdall, A. L., Branning, D., and Castelletto, S. *Phys. Rev. A* **66**, 053805 Nov (2002). 16

[56] Yoshikawa, J.-i., Makino, K., Kurata, S., van Loock, P., and Furusawa, A. *Physical Review X* **3**(4), 041028 (2013). 16

[57] Lukin, M. D. *Review of Modern Physics* **75**(2), 457–472 Apr (2003). 16

[58] Gorshkov, A. V., Andre, A., Lukin, M. D., and Sorensen, A. S. *Physical Review A* **76**, 033805 (2007). 16, 17, 18, 99, 105, 107, 150, 189

[59] Liu, C., Dutton, Z., Behroozi, C. H., and Hau, L. V. *Nature* **409**(6819), 490–493 (2001). 16

[60] Phillips, D. F., Fleischhauer, A., Mair, A., Walsworth, R. L., and Lukin, M. D. *Physical Review Letters.* **86**, 783–786 Jan (2001). 16

[61] Choi, K. S., Deng, H., Laurat, J., and Kimble, H. J. *Nature* **452**, 67–71 March (2008). 16

[62] Longdell, J. J., Fraval, E., Sellars, M. J., and Manson, N. B. *Physical Review Letters* **95**(6), 063601 (2005). 16

[63] Chen, Y.-H., Lee, M.-J., Wang, I.-C., Du, S., Chen, Y.-F., Chen, Y.-C., and Yu, I. A. *Physical Review Letters* **110**, 083601 Feb (2013). 17

[64] Dudin, Y. O., Li, L., and Kuzmich, A. *Physical Review A* **87**, 031801 Mar (2013). 17

[65] Heinze, G., Hubrich, C., and Halfmann, T. *Physical Review Letters* **111**(3), 033601 (2013). 17

[66] Höckel, D. and Benson, O. *Physical Review Letters* **105**, 153605 Oct (2010). 17

[67] Manz, S., Fernholz, T., Schmiedmayer, J., and Pan, J.-W. *Physical Review A* **75**, 040101 Apr (2007). 17

[68] Gorshkov, A. V., Andre, A., Lukin, M. D., and Sorensen, A. S. *Physical Review A* **76**, 033806 (2007). 17, 150

[69] Gorshkov, A. V., Calarco, T., Lukin, M. D., and Sorensen, A. S. *Physical Review A* **77**(4), 043806 (2008). 17, 150

[70] Kozhekin, A. E., Mølmer, K., and Polzik, E. *Physical Review A* **62**, 033809 (2000). 18

[71] Nunn, J., Walmsley, I. A., Raymer, M. G., Surmacz, K., Waldermann, F. C., Wang, Z., and Jaksch, D. *Physical Review A* **75**(1), 011401 (2007). 18, 108, 131, 186, 187, 189

[72] Reim, K. F., Michelberger, P., Lee, K. C., Nunn, J., Langford, N. K., and Walmsley, I. A. *Physical Review Letters* **107**(5), 053603 Jul (2011). 19, 112, 113, 114, 130, 131, 140, 153, 163, 168, 184, 192, 204

[73] Reim, K., Nunn, J., Lorenz, V., Sussman, B., Lee, K., Langford, N., Jaksch, D., and Walmsley, I. *Nature Photonics* (2010). 19, 108, 113, 130, 153, 161, 163, 168

[74] Bustard, P. J., Lausten, R., England, D. G., and Sussman, B. J. *Physical Review Letters* **111**, 083901 Aug (2013). 19

[75] England, D. G., Bustard, P. J., Nunn, J., Lausten, R., and Sussman, B. J. *Physical Review Letters* **111**, 243601 Dec (2013). 19, 202

[76] Zhu, Z., Gauthier, D. J., and Boyd, R. W. *Science* **318**(5857), 1748–1750 (2007). 19, 167

[77] Hahn, E. L. *Physical Review* **80**, 580–594 Nov (1950). 20

[78] Kurnit, N. A., Abella, I. D., and Hartmann, S. R. *Physical Review Letters* **13**, 567–568 Nov (1964). 20

[79] Tittel, W., Afzelius, M., Chanelire, T., Cone, R., Kroll, S.ll, S., Moiseev, S., and Sellars, M. *Laser & Photon. Rev.* **4**(2), 244–267 (2010). 20, 21

[80] Kraus, B., Tittel, W., Gisin, N., Nilsson, M., Kroll, S., and Cirac, J. I. *Physical Review A* **73**(2), 020302 (2006). 20

[81] Lauritzen, B., Minář, J. c. v., de Riedmatten, H., Afzelius, M., Sangouard, N., Simon, C., and Gisin, N. *Physical Review Letters* **104**(8), 080502 Feb (2010). 20, 23

[82] Hosseini, M., Sparkes, B. M., Hetet, G., Longdell, J. J., Lam, P. K., and Buchler, B. C. *Nature* **461**(7261), 241–245 09 (2009). 20, 184

[83] Hedges, M. P., Longdell, J. J., Li, Y., and Sellars, M. J. *Nature* **465**, 1052–1056 (2010). 20, 22

[84] Hosseini, M., Campbell, G., Sparkes, B. M., Lam, P. K., and Buchler, B. C. *Nature Physics* **7**, 794–798 (2011). 20, 21, 22

[85] de Riedmatten, H., Afzelius, M., Staudt, M. U., Simon, C., and Gisin, N. *Nature* **456**(7223), 773–777 12 (2008). 20, 23

[86] Afzelius, M., Usmani, I., Amari, A., Lauritzen, B., Walther, A., Simon, C., Sangouard, N., Minář, J. c. v., de Riedmatten, H., Gisin, N., and Kröll, S. *Physical Review Letters* **104**(4), 040503– January (2010). 20

[87] Clausen, C., Usmani, I., Bussieres, F., Sangouard, N., Afzelius, M., de Riedmatten, H., and Gisin, N. *Nature* **469**(7331), 508–511 January (2011). 20, 23

[88] Damon, V., Bonarota, M., Louchet-Chauvet, A., Chanelire, T., and Gout, J.-L. L. *New Journal of Physics* **13**(9), 093031 (2011). 20, 24

[89] McAuslan, D. L., Ledingham, P. M., Naylor, W. R., Beavan, S. E., Hedges, M. P., Sellars, M. J., and Longdell, J. J. *Physical Review A* **84**, 022309 Aug (2011). 20, 24

[90] Hétet, G., Longdell, J., Alexander, A., Lam, P., and Sellars, M. *Physical Review Letters* **100**(2), 23601 (2008). 20, 22

[91] Moiseev, S. A. and Kröll, S. *Physical Review Letters* **87**(17), 173601 Oct (2001). 20

[92] Alexander, A., Longdell, J., Sellars, M., and Manson, N. *Physical Review Letters* **96**(4), 43602 (2006). 21

[93] Afzelius, M., Simon, C., De Riedmatten, H., and Gisin, N. *Physical Review A* **79**(5), 52329 (2009). 21, 22, 23

[94] Hétet, G., Hosseini, M., Sparkes, B., Oblak, D., Lam, P. K., and Buchler, B. C. September (2008). 22

[95] Hosseini, M., Sparkes, B., Campbell, G., Lam, P., and Buchler, B. *Nature Communications* **2**, 174– February (2011). 22, 130

[96] Fekete, J., Rieländer, D., Cristiani, M., and de Riedmatten, H. *Physical Review Letters* **110**, 220502 May (2013). 22

[97] Sparkes, B. M., Bernu, J., Hosseini, M., Geng, J., Glorieux, Q., Altin, P. A., Lam, P. K., Robins, N. P., and Buchler, B. C. *Journal of Physics: Conference Series* **467**(1), 012009 (2013). 22

[98] Sabooni, M., Li, Q., Kröll, S., and Rippe, L. *Physical Review Letters* **110**, 133604 Mar (2013). 23

[99] Saglamyurek, E., Sinclair, N., Jin, J., Slater, J. A., Oblak, D., Bussieres, F., George, M., Ricken, R., Sohler, W., and Tittel, W. *Nature* **469**(7331), 512–515 January (2011). 23, 131

[100] Timoney, N., Usmani, I., Jobez, P., Afzelius, M., and Gisin, N. *Physical Review A* **88**, 022324 Aug (2013). 24

[101] Miya, T., Terunuma, Y., Hosaka, T., and Miyashita, T. *Electronics Letters* **15**, 106–108(2) February (1979). 27, 133

[102] Ye, J., Vernooy, D. W., and Kimble, H. J. *Physical Review Letters* **83**, 4987–4990 Dec (1999). 28

[103] Chou, C. W., de Riedmatten, H., Felinto, D., Polyakov, S. V., van Enk, S. J., and Kimble, H. J. *Nature* **438**(7069), 828–832 December (2005). 28

[104] Dicke, R. H. *Physical Review* **93**, 99–110 Jan (1954). 29

[105] Lee, K. C., Sussman, B. J., Nunn, J., Lorenz, V. O., Reim, K., Jaksch, D., Walmsley, I. A., Spizzirri, P., and Prawer, S. *Diamond and Related Materials* **19**(10), 1289–1295 10 (2010). 29, 35, 52, 54

[106] Afzelius, M., Staudt, M. U., de Riedmatten, H., Simon, C., Hastings-Simon, S. R., Ricken, R., Suche, H., Sohler, W., and Gisin, N. *New Journal of Physics* **9**(11), 413 (2007). 30

[107] Scully, M. O. and Zubairy, M. S. *Quantum Optics*. Cambridge University Press, (1997). 32, 46, 65

[108] Lee, K. C., Sprague, M. R., Sussman, B. J., Nunn, J., Langford, N. K., Jin, X.-M., Champion, T., Michelberger, P., Reim, K. F., England, D., Jaksch, D., and Walmsley, I. A. *Science* **334**(6060), 1253–1256 December (2011). 34, 68, 81, 84, 90

[109] Wootters, W. K. *Physical Review Letters* **80**(10), 2245–2248 Mar (1998). 35, 60

[110] Birman, J. L. *Physical Review* **127**, 1093–1106 Aug (1962). 35

[111] Bundy, F. P., Hall, H. T., Strong, H. M., and Wentrof, R. H. *Nature* **176**(4471), 51–55 07 (1955). 35

[112] Proust, M. *The Lemoine Affair*. Meville House, (2008). 35

[113] Kittel, C. *Introduction to Solid State Physics*. Wiley, New York, (1996). 36

[114] Hoesch, M., Fukuda, T., Mizuki, J., Takenouchi, T., Kawarada, H., Sutter, J. P., Tsutsui, S., Baron, A. Q. R., Nagao, M., and Takano, Y. *Physical Review B* **75**, 140508 Apr (2007). 37

[115] Kresse, G., Furthmuller, J., and Hafner, J. *EPL (Europhysics Letters)* **32**(9), 729– (1995). 38

[116] O'Connell, A., Hofheinz, M., Ansmann, M., Bialczak, R., Lenander, M., Lucero, E., Neeley, M., Sank, D., Wang, H., Weides, M., et al. *Nature* **464**(7289), 697–703 (2010). 38, 57

[117] Teufel, J. D., Donner, T., Li, D., Harlow, J. W., Allman, M. S., Cicak, K., Sirois, A. J., Whittaker, J. D., Lehnert, K. W., and Simmonds, R. W. *Nature* **475**(7356), 359–363 July (2011). 38, 57

[118] Chan, J., Alegre, T. P. M., Safavi-Naeini, A. H., Hill, J. T., Krause, A., Groblacher, S., Aspelmeyer, M., and Painter, O. *Nature* **478**(7367), 89–92 October (2011). 38, 57

[119] Hayes, W., Loudon, R., and Scott, J. *American Journal of Physics* **47**, 571 (1979). 39

[120] Loudon, R. *Proceedings of the Physical Society* **82**, 393–400 (1963). 39

[121] Loudon, R. *Proceedings of the Royal Society of London. Series A, Mathematical and Physical Sciences (1934-1990)* **275**(1361), 218–232 (1963). 39

[122] Hayes, W. and Loudon, R. *Scattering of Light by Crystals*. Dover Publications, New York, (2004). 39, 70

[123] Mosley, P. *Generation of Heralded Single Photons in Pure Quantum States*. PhD thesis, University of Oxford, (2007). 42, 44

[124] Peter, F. *Z. Phys.* **15**, 358 (1923). 43

[125] Goldschmidt, E. A., Piacentini, F., Berchera, I. R., Polyakov, S. V., Peters, S., Kück, S., Brida, G., Degiovanni, I. P., Migdall, A., and Genovese, M. *Physical Review A* **88**, 013822 Jul (2013). 45, 46, 82, 202

[126] Loudon, R. *The Quantum Theory of Light*. Oxford University Press, (2004). 46, 48, 98, 99

[127] Chou, C. W. *Towards a Quantum Network with Atomic Ensembles*. PhD thesis, California Institute of Technology, (2006). 47, 61, 62, 64, 66

[128] Chuu, C., Strassel, T., Zhao, B., Koch, M., Chen, Y., Chen, S., Yuan, Z., Schmiedmayer, J., and Pan, J. *Physical Review Letters* **101**(12), 120501 (2008). 48

[129] Lee, K. C., Sussman, B. J., Sprague, M. R., Michelberger, P., Reim, K. F., Nunn, J. and, L. N. K., Bustard, P. J., Jaksch, D., and Walmsley, I. A. *Nature Photoncs* **4**, 41–44 December (2011). 50, 51, 53, 54, 203

[130] Klemens, P. G. *Physical Review* **148**(2), 845–848 Aug (1966). 52, 53

[131] Waldermann, F. C., Sussman, B. J., Nunn, J., Lorenz, V. O., Lee, K. C., Surmacz, K., Lee, K. H., Jaksch, D., Walmsley, I. A., Spizziri, P., Olivero, P., and Prawer, S. *Physical Review B* **78**(15), 155201 (2008). 52

[132] Debernardi, A., Baroni, S., and Molinari, E. *Physical Review Letters* **75**(9), 1819–1822 (1995). 53

[133] Liu, M., Bursill, L., Prawer, S., and Beserman, R. *Physical Review B* **61**(5), 3391–3395 (2000). 53

[134] Schrödinger, E. and Born, M. *Mathematical Proceedings of the Cambridge Philosophicall Society* **4**, 555–563 (1935). 56

[135] Vidal, G., Latorre, J. I., Rico, E., and Kitaev, A. *Physical Review Letters* **90**, 227902 Jun (2003). 56

[136] Herrmann, L. G., Portier, F., Roche, P., Yeyati, A. L., Kontos, T., and Strunk, C. *Physical Review Letters* **104**, 026801 Jan (2010). 56

[137] Alba, V., Haque, M., and Läuchli, A. M. *Physical Review Letters* **110**, 260403 Jun (2013). 56

[138] Schuch, N. *ArXiv e-prints* June (2013). 56

[139] Vedral, V. *eprint arXiv:quant-ph/0703129* March (2007). 56

[140] Fidkowski, L. *Physical Review Letters* **104**, 130502 Apr (2010). 56

[141] Jozsa, R. and Linden, N. *Proceedings of the Royal Society of London. Series A: Mathematical, Physical and Engineering Sciences* **459**(2036), 2011–2032 August (2003). 56

[142] Vidal, G. *Physical Review Letters* **91**, 147902 Oct (2003). 56

[143] Datta, A. and Vidal, G. *Physical Review A* **75**, 042310 Apr (2007). 56

[144] Zurek, W. *Ann. Phys.* **9**(11-12), 855–864 (2000). 56

[145] Henderson, L. and Vedral, V. *Journal of Physics A: Mathematical and General* **34**(35), 6899– (2001). 56

[146] Datta, A., Shaji, A., and Caves, C. M. *Physical Review Letters* **100**, 050502 Feb (2008). 56

[147] Lanyon, B. P., Barbieri, M., Almeida, M. P., and White, A. G. *Physical Review Letters* **101**, 200501 Nov (2008). 56

[148] Penrose, R. *Mathematical physics* , 266–282 (2000). 56

[149] Schliesser, A., Del'Haye, P., Nooshi, N., Vahala, K. J., and Kippenberg, T. J. *Physical Review Letters* **97**, 243905 Dec (2006). 57

[150] Schliesser, A., Riviere, R., Anetsberger, G., Arcizet, O., and Kippenberg, T. J. *Nature Physics* **4**(5), 415–419 May (2008). 57

[151] Safavi-Naeini, A. H., Groblacher, S., Hill, J. T., Chan, J., Aspelmeyer, M., and Painter, O. *Nature* **500**(7461), 185–189 August (2013). 57

[152] Purdy, T. P., Yu, P.-L., Peterson, R. W., Kampel, N. S., and Regal, C. A. *Physical Review X* **3**, 031012 Sep (2013). 57

[153] Panitchayangkoon, G., Hayes, D., Fransted, K., Caram, J., Harel, E., Wen, J., Blankenship, R., and Engel, G. *Proceedings of the National Academy of Sciences* **107**(29), 12766 (2010). 57

[154] Collini, E., Wong, C. Y., Wilk, K. E., Curmi, P. M. G., Brumer, P., and Scholes, G. D. *Nature* **463**(7281), 644–647 February (2010). 57

[155] Gerlich, S., Eibenberger, S., Tomandl, M., Nimmrichter, S., Hornberger, K., Fagan, P. J., Taxen, J., Mayor, M., and Arndt, M. *Nature Communications* **2**, 263– April (2011). 57

[156] Wootters, W. *Physical Review Letters* **80**(10), 2245–2248 (1998). 58, 85

[157] Plenio, M. B. and Virmani, S. *Quant. Inf. Comput* **7**, 1–51 (2007). 58

[158] Horodecki, R., Horodecki, P., Horodecki, M., and Horodecki, K. *Rev. Mod. Phys.* **81**, 865–942 Jun (2009). 59

[159] Wu, Y.-C. and Guo, G.-C. *Physical Review A* **75**, 052333 May (2007). 59

[160] Gisin, N. *Physics Letters A* **154**(56), 201–202 April (1991). 59

[161] Żukowski, M., Brukner, i. c. v., Laskowski, W., and Wieśniak, M. *Physical Review Letters* **88**, 210402 May (2002). 59

[162] van Enk, S., Lütkenhaus, N., and Kimble, H. *Physical Review A* **75**(5), 052318 (2007). 59, 80, 83, 91

[163] Lombardi, E., Sciarrino, F., Popescu, S., and De Martini, F. *Physical Review Letters* **88**, 070402 Jan (2002). 60

[164] Chou, C., De Riedmatten, H., Felinto, D., Polyakov, S., Van Enk, S., and Kimble, H. *Nature* **438**(7069), 828–832 (2005). 60, 61, 81, 83, 85, 91

[165] Rungta, P. and Caves, C. M. *Physical Review A* **67**, 012307 (2003). 61

[166] Laurat, J., Choi, K. S., Deng, H., Chou, C. W., and Kimble, H. J. *Physical Review Letters* **99**(18), 180504 Nov (2007). 66

[167] von Kaenel, Y., Stiegler, J., Michler, J., and Blank, E. *Journal of Applied Physics* **81**(4), 1726–1736 (1997). 70

[168] Solin, S. A. and Ramdas, A. K. *Physical Review B* **1**, 1687–1698 (1970). 70

[169] Ziegler, J. G. and Nichols, N. B. *Journal of Dynamic Systems, Measurement, and Control* **115**(2B), 220–222 (1993). 76

[170] Pancharatnam, S. *Proceedings Mathematical Sciences* **41**, 137–144 (1955). 10.1007/BF03047098. 78

[171] Englert, B., Kurtsiefer, C., and Weinfurter, H. *Physical Review A* **63**(3), 032303 (2001). 78

[172] Langford, N. K. *Encoding, manipulating and measuring quantum information in optics*. PhD thesis, School of Physical Sciences, University of Queensland, (2007). 78, 79, 89

[173] Bennett, C. H., Bernstein, H. J., Popescu, S., and Schumacher, B. *Physical Review A* **53**(4), 2046–2052 Apr (1996). 83

[174] Feldman, G. J. and Cousins, R. D. *Physical Review D* **57**(7), 3873–3889 Apr (1998). 85, 86, 212, 213, 214

[175] Berger, J. *Bayesian Analysis* **1**, 385:402 (2006). 87, 208

[176] Ghosh, J., Chakrabarti, A., and Samanta, T. *International Workshop on Objective Bayes Methodology* , 1–10 (2009). 87, 211

[177] James, D. F. V., Kwiat, P. G., Munro, W. J., and White, A. G. *Physical Review A* **64**(5), 052312 Oct (2001). 88, 89

[178] Boyd, S. and Vandenberghe, L. *Convex Optimization*. Cambridge University Press, (2004). 89

[179] Cohen, O. and Hiley, B. *Foundations of Physics* **25**, 1669–1698– (1995). 91

[180] Walmsley, I., Lee, K., Sprague, M., Sussman, B., Nunn, J., Langford, N., Jin, X., Champion, T., Michelberger, P., Reim, K., and Jaksch, D. *Journal of Physics: Conference Series* **442**, 012004 (2013). 91

[181] Aharonov, Y. and Vaidman, L. *Physical Review A* **41**, 11–20 (1990). 92

[182] Pegg, D. T., Barnett, S. M., and Jeffers, J. *Physical Review A* **66**, 022106 (2002). 92

[183] Barnett, S. M., Pegg, D. T., Jeffers, J., and Jedrkiewicz, O. *Physical Review Letters.* **86**(11), 2455–2458 (2001). 92

[184] Pegg, D. T. and Pregnell, K. L. *AIP Conference Proceedings* **734**(1), 377–382 (2004). 92

[185] Greentree, A., Fairchild, B., Hossain, F., and Prawer, S. *Materials Today* **11**(9), 22–31 (2008). 92

[186] Prechtel, L., Song, L., Manus, S., Schuh, D., Wegscheider, W., and Holleitner, A. W. *Nano Letters* **11**(1), 269–272 (2011). 92

[187] Dunne, J. *An Experiment with Time*. Faber and Faber Limited, (1952). 92

[188] Borges, J. L. *Selected Non-Fictions*. Penguin Books, (1999). 92

[189] Aspelmeyer, M., Kippenberg, T. J., and Marquardt, F. *ArXiv e-prints* March (2013). 93

[190] Shen, Y. R. and Bloembergen, N. *Physical Review* **137**, A1787–A1805 Mar (1965). 97

[191] Raymer, M. G. and Mostowski, J. *Physical Review A* **24(4)**, 1980–1993 (1981). 97

[192] Boller, K.-J., Imamoglu, A., and Harris, S. E. *Physical Review Letters* **66**(20), 2593–2596 (1991). 97

[193] Fleischhauer, M., Imamoglu, A., and Marangos, J. P. *Reviews of Modern Physics* **77**(2), 633 (2005). 97

[194] Arimondo, E. volume 35, 257–354. Elsevier (1996). 97

[195] Parkins, A. S., Marte, P., Zoller, P., Carnal, O., and Kimble, H. J. *Physical Review A* **51**, 1578–1596 Feb (1995). 97

[196] Hennrich, M., Legero, T., Kuhn, A., and Rempe, G. *Physical Review Letters* **85**(23), 4872–4875 (2000). 97

[197] Zeuthen, E., Grodecka-Grad, A., and Sørensen, A. S. *Physical Review A* **84**, 043838 (2011). 99

[198] Steck, D. A. *Quantum and Atom Optics*. available online at http://steck.us/teaching (revision 0.9.8), (2007). 100, 101, 103

[199] Brasil, C. A., Fanchini, F. F., and de Jesus Napolitano, R. *arXiv:1110.2122* (2013). 103

[200] Nunn, J., Reim, K., Lee, K. C., Lorenz, V. O., Sussman, B. J., Walmsley, I. A., and Jaksch, D. *Physical Review Letters* **101**(26), 260502 (2008). 109

[201] Braunstein, S. L. *Physical Review A* **71**(5), 055801 (2005). 110

[202] Reim, K. F., Nunn, J., Jin, X.-M., Michelberger, P. S., Champion, T. F. M., England, D. G., Lee, K. C., Kolthammer, W. S., Langford, N. K., and Walmsley, I. A. *Physical Review Letters* **108**(26), 263602– June (2012). 112, 184

[203] England, D. G., Michelberger, P. S., Champion, T. F. M., Reim, K. F., Lee, K. C., Sprague, M. R., Jin, X.-M., Langford, N. K., Kolthammer, W. S., Nunn, J., and Walmsley, I. A. *Journal of Physics B: Atomic, Molecular and Optical Physics* **45**(12), 124008– (2012). 114, 115

[204] Roy, R., Agrawal, D. K., and McKinstry, H. A. *Annu. Rev. Mater. Sci.* **19**(1), 59–81 August (1989). 117

[205] Stolen, R. H. and Lin, C. *Physical Review A* **17**, 1448–1453 Apr (1978). 118

[206] Hercher, M. *Appl. Opt.* **7**(5), 951–966 (1968). 124

[207] Palittapongarnpim, P., MacRae, A., and Lvovsky, A. I. *Review of Scientific Instruments* **83**(6), – (2012). 124

[208] Ranka, J. K., Windeler, R. S., and Stentz, A. J. *Optics Letters* **25**(1), 25–27 (2000). 130, 132

[209] Fiorentino, M., Spillane, S. M., Beausoleil, R. G., Roberts, T. D., Battle, P., and Munro, M. W. *Optics Express* **15**(12), 7479–7488 (2007). 130

[210] Russell, P. S. *J. Lightwave Technol.* **24**(12), 4729–4749 December (2006). 130

[211] Novikova, I., Gorshkov, A. V., Phillips, D. F., Sorensen, A. S., Lukin, M. D., and Walsworth, R. L. *Physical Review Letters* **98**(24), 243602 (2007). 130

[212] Schreiber, A., Gábris, A., Rohde, P. P., Laiho, K., Štefaňák, M., Potoček, V., Hamilton, C., Jex, I., and Silberhorn, C. *Science* **336**(6077), 55–58 (2012). 131

[213] Shadbolt, P. J., Verde, M. R., Peruzzo, A., Politi, A., Laing, A., Lobino, M., Matthews, J. C. F., Thompson, M. G., and O'Brien, J. L. *Nature Photonics* **6**(1), 45–49 January (2012). 131

[214] Wu, B., Hulbert, J. F., Lunt, E. J., Hurd, K., Hawkins, A. R., and Schmidt, H. *Nature Photonics* **4**(11), 776–779 November (2010). 131

[215] Stern, L., Desiatov, B., Goykhman, I., and Levy, U. *Nature Communications* **4**, 1548– March (2013). 131

[216] Spillane, S. M., Pati, G. S., Salit, K., Hall, M., Kumar, P., Beausoleil, R. G., and Shahriar, M. S. *Physical Review Letters* **100**, 233602 Jun (2008). 131

[217] Vetsch, E., Reitz, D., Sagué, G., Schmidt, R., Dawkins, S. T., and Rauschenbeutel, A. *Physical Review Letters* **104**, 203603 May (2010). 131

[218] Cregan, R. F., Mangan, B. J., Knight, J. C., Birks, T. A., Russell, P. S. J., Roberts, P. J., and Allan, D. C. *Science* **285**(5433), 1537–1539 September (1999). 131, 132, 133

[219] Venkataraman, V., Saha, K., and Gaeta, A. L. *Nature Photonics* **7**, 138–141 December (2012). 131, 133

[220] Ghosh, S., Bhagwat, A. R., Renshaw, C. K., Goh, S., Gaeta, A. L., and Kirby, B. J. *Physical Review Letters* **97**, 023603 Jul (2006). 131, 133, 153, 197, 204

[221] Bajcsy, M., Hofferberth, S., Balic, V., Peyronel, T., Hafezi, M., Zibrov, A. S., Vuletic, V., and Lukin, M. D. *Physical Review Letters* **102**(20), 203902 May (2009). 131, 133

[222] Londero, P., Venkataraman, V., Bhagwat, A. R., Slepkov, A. D., and Gaeta, A. L. *Physical Review Letters* **103**(4), 043602– July (2009). 131, 133, 163

[223] Sprague, M. R., England, D. G., Abdolvand, A., Nunn, J., Jin, X.-M., Kolthammer, W. S., Barbieri, M., Rigal, B., Michelberger, P. S., Champion, T. F. M., Russell, P. S. J., and Walmsley, I. A. *New Journal of Physics* **15**(5), 055013 (2013). 131, 136, 154, 160, 164, 172, 183

[224] Perrella, C., Light, P. S., Stace, T. M., Benabid, F., and Luiten, A. N. *Physical Review A* **85**, 012518 Jan (2012). 131

[225] Saleh, B. E. A. and Teich, M. C. *Fundamentals of Photonics*. John Wiley & Sons, Inc, (1991). 132

[226] Russell, P. *Science* **299**(5605), 358–362 (2003). 132

[227] Knight, J. C. *Nature* **424**(6950), 847–851 August (2003). 132

[228] Russell, P. S. J. In *NATO Advanced Study Institute on Confined Electrons and Holes*, (1993). 132

[229] Bowden, C. M., Dowling, J. P., and Everitt, H. O. *J. Opt. Soc. Am. B* **10**(2), 280–280 Feb (1993). 132

[230] Birks, T. A., Knight, J. C., and Russell, P. S. *Optics Letters* **22**(13), 961–963 (1997). 132

[231] Knight, J. C., Birks, T. A., Russell, P. S. J., and Atkin, D. M. *Optics Letters* **21**(19), 1547–1549 (1996). 132

[232] Udem, T., Holzwarth, R., and Hansch, T. W. *Nature* **416**(6877), 233–237 March (2002). 132

[233] Hartl, I., Li, X. D., Chudoba, C., Ghanta, R. K., Ko, T. H., Fujimoto, J. G., Ranka, J. K., and Windeler, R. S. *Optics Letters* **26**(9), 608–610 (2001). 132

[234] Roberts, P. J., Couny, F., Sabert, H., Mangan, B. J., Williams, D. P., Farr, L., Mason, M. W., Tomlinson, A., Birks, T. A., Knight, J. C., and Russell, P. S. *Optics Express* **13**(1), 236–244 (2005). 133

[235] Mangan, B., Farr, L., Langford, A., Roberts, P., Williams, D. P., Couny, F., Lawman, M., Mason, M., Coupland, S., Flea, R., Sabert, H., Birks, T., Knight, J., and Russell, P. In *Optical Fiber Communication Conference, 2004. OFC 2004*, volume 2, 3 pp. vol.2–, (2004). 133

[236] Ouzounov, D. G., Ahmad, F. R., Mller, D., Venkataraman, N., Gallagher, M. T., Thomas, M. G., Silcox, J., Koch, K. W., and Gaeta, A. L. *Science* **301**(5640), 1702–1704 (2003). 133

[237] Humbert, G., Knight, J., Bouwmans, G., Russell, P., Williams, D., Roberts, P., and Mangan, B. *Optics Express* **12**(8), 1477–1484 (2004). 133

[238] Gbel, W., Nimmerjahn, A., and Helmchen, F. *Optics Letters* **29**(11), 1285–1287 (2004). 133

[239] Benabid, F., Knight, J. C., Antonopoulos, G., and Russell, P. S. J. *Science* **298**(5592), 399–402 (2002). 133, 134

[240] Couny, F., Benabid, F., and Light, P. S. *Optics Letters* **31**(24), 3574–3576 December (2006). 133, 134

[241] Saha, K., Venkataraman, V., Londero, P., and Gaeta, A. L. *Physical Review A* **83**(3), 033833 Mar (2011). 133

[242] Mekata, M. *Physics Today* **February**, 13 (2003). 133

[243] Pearce, G. J., Wiederhecker, G. S., Poulton, C. G., Burger, S., and St. J. Russell, P. *Optics Express* **15**(20), 12680–12685 October (2007). 134

[244] Benabid, F. and Roberts, P. *Journal of Modern Optics* **58**(2), 87–124 January (2011). 134

[245] Light, P. S., Benabid, F., Couny, F., Maric, M., and Luiten, A. N. *Optics Letters* **32**(10), 1323–1325 May (2007). 134, 153, 197, 204

[246] Benabid, F. In *OSA Technical Digest (CD)*, OTuL6– (Optical Society of America, Los Angeles, California, 2011). 134

[247] Bradley, T. D., Alharbi, M., Wang, Y., Dutin, C. F., and Benabid, F. In *OSA Technical Digest (online)*, CM3N.1– (Optical Society of America, San Jose, California, 2012). 134

[248] Bradley, T., McFerran, J. J., Jouin, J., Thomas, P., and Benabid, F. In *OSA Technical Digest (online)*, CM3I.2–. Optical Society of America, June (2013). 134, 197

[249] Vurgaftman, I. and Bashkansky, M. *Physical Review A* **87**, 063836 Jun (2013). 135

[250] Chen, X., Li, M.-J., Venkataraman, N., Gallagher, M. T., Wood, W. A., Crowley, A. M., Carberry, J. P., Zenteno, L. A., and Koch, K. W. In *Technical Digest (CD)*, OTuI1– (Optical Society of America, Anaheim, California, 2005). 135

[251] Roberts, P. J., Williams, D. P., Sabert, H., Mangan, B. J., Bird, D. M., Birks, T. A., Knight, J. C., and Russell, P. S. J. *Optics Express* **14**(16), 7329–7341 (2006). 135

[252] Kim, G., Cho, T., Hwang, K., Lee, K., Lee, K. S., Han, Y.-G., and Lee, S. B. *Optics Express* **17**(4), 2481–2486 (2009). 135

[253] Birnbaum, K. M. *Norman Bridge Laboratory, Caltech Institute of Technology* , 1–16 (2005). 137

[254] Jin, X.-M., Dai, H.-N., Rui, J., Yang, S.-J., Jiang, X., Deng, Y.-J., Chen, S., and Pan., J.-W. In *International Conference on Quantum Foundation and Technology : Frontier and Future (ICQFT'09) Shanghai, China,*, (2009). 137

[255] Slepkov, A. D., Bhagwat, A. R., Venkataraman, V., Londero, P., and Gaeta, A. L. *Optics Express* **16**(23), 18976–18983 Nov (2008). 138, 152, 153, 155, 156

[256] Bhagwat, A. R. *Low-light-level nonlinear optics with rubidium atoms in hollow-core photonic band-gap fibers*. PhD thesis, Cornell University, (2010). 139, 141

[257] Marquardt, C. Private Communication, 2012. 140

[258] Franz, F. A. *Physics Letters A* **27**, 457–458 August (1968). 141

[259] Franz, F. A., Boggy, R., and Sooriamoorthi, C. E. *Physical Review A* **11**, 1–9 Jan (1975). 141

[260] Andalkar, A. *Spontaneous spin polarization and hysteresis in cesium vapor pumped by linearly polarized light: an experimental, theoretical, and computational study*. PhD thesis, University of Washington, (2001). 141

[261] Bhagwat, A. R., Slepkov, A. D., Venkataraman, V., Londero, P., and Gaeta, A. L. *Physical Review A* **79**(6), 063809 Jun (2009). 141, 153, 156

[262] Chambers, A. *Basic Vacuum Technology, 2nd edition*. CRC Press, (2010). 142

[263] Horak, P. and Loh, W. H. *Optics Express* **14**(9), 3923–3928 (2006). 144

[264] Azmoun, B. and Metz, S. Technical report, Stony Brook University, (2002). 144

[265] Arnold, A. S., Wilson, J. S., and Boshier, M. G. *Review of Scientific Instruments* **69**(3), 1236–1239 (1998). 144

[266] Steck, D. A. (Available online at http://steck.us/alkalidata (revision 2.1.4, 23 December 2010).). 146, 161, 162

[267] Abramowitz, M. and Stegun, I. *New York* (1965). 148

[268] Fox, R. W., Oates, C. W., and Hollberg, L. W. *Elsevier Science* **40**, 1–45 (2003). 149

[269] Gorshkov, A. V., Andre, A., Fleischhauer, M., Sorensen, A. S., and Lukin, M. D. *Physical Review Letters* **98**(12), 123601 (2007). 150

[270] Meucci, M., Mariotti, E., Bicchi, P., Marinelli, C., and Moi, L. *EPL (Europhysics Letters)* **25**(9), 639 (1994). 153

[271] Alexandrov, E. B., Balabas, M. V., Budker, D., English, D., Kimball, D. F., Li, C.-H., and Yashchuk, V. V. *Physical Review A* **66**, 042903 Oct (2002). 153, 204

[272] Atutov, S. N., Calabrese, R., Guidi, V., Mai, B., Rudavets, A. G., Scansani, E., Tomassetti, L., Biancalana, V., Burchianti, A., Marinelli, C., Mariotti, E., Moi, L., and Veronesi, S. *Physical Review A* **67**, 053401 May (2003). 153

[273] Karaulanov, T., Graf, M. T., English, D., Rochester, S. M., Rosen, Y. J., Tsigutkin, K., Budker, D., Alexandrov, E. B., Balabas, M. V., Kimball, D. F. J., Narducci, F. A., Pustelny, S., and Yashchuk, V. V. *Physical Review A* **79**, 012902 Jan (2009). 153

[274] Burchianti, A., Marinelli, C., Bogi, A., Brewer, J., Rubahn, K., Rubahn, H.-G., Valle, F. D., Mariotti, E., Biancalana, V., Veronesi, S., and Moi, L. *EPL (Europhysics Letters)* **67**(6), 983 (2004). 153

[275] Jabbour, Z., Sagle, J., Namiotka, R., and Huennekens, J. *Journal of Quantitative Spectroscopy and Radiative Transfer* **54**(5), 767 – 778 (1995). 160

[276] Slepkov, A. D., Bhagwat, A. R., Venkataraman, V., Londero, P., and Gaeta, A. L. *Physical Review A* **81**(5), 053825 May (2010). 161

[277] Haverkort, J., Hoogeveen, R., and Woerdman, J. *Optics Communications* **61**(2), 109 – 115 (1987). 161

[278] de Freitas, H., Oria, M., and Chevrollier, M. *Applied Physics B* **75**, 703–709 (2002). 161

[279] Ramaswami, R., Sivarajan, K., and Sasaki, G. *Optical Networks: a Practical Perspective*. Morgan Kaufmann, (2009). 167

[280] Hunter, D. K., Chia, M. C., and Andonovic, I. *J. Lightwave Technol.* **16**(12), 2081– (1998). 167

[281] Tucker, R., Ku, P.-C., and Chang-Hasnain, C. *Lightwave Technology, Journal of* **23**(12), 4046–4066 (2005). 167

[282] Sprague, M. R., Michelberger, P. S., Champion, T. F. M., England, D. G., Nunn, J., Jin, X.-M., Kolthammer, W. S., Abdolvand, A., Russell, P. S. J., and Walmsley, I. A. *Nature Photoncs* (2014). 175, 185, 187, 190, 191

[283] Boyd, R. *Nonlinear Optics*. Academic Press, Boston, (2003). 180, 181

[284] Lauk, N., O'Brien, C., and Fleischhauer, M. *Physical Review A* **88**, 013823 Jul (2013). 185, 192, 202

[285] Bimbard, E., Boddeda, R., Vitrant, N., Grankin, A., Parigi, V., Stanojevic, J., Ourjoumtsev, A., and Grangier, P. *ArXiv e-prints* October (2013). 185

[286] Krapick, S., Herrmann, H., Quiring, V., Brecht, B., Suche, H., and Silberhorn, C. *New Journal of Physics* **15**(3), 033010– (2013). 192

[287] P. M. Michelberger, Champion, T. F. M., Nunn, J. and, S. M. R., Jin, X.-M., England, D. G., and Walmsley, I. A. *In preparation* (2013). 192, 202, 203

[288] Little, B., Starling, D. J., Howell, J. C., Cohen, R. D., Shwa, D., and Katz, N. *Physical Review A* **87**, 043815 Apr (2013). 193

[289] Feng, L., Ren, X., Deng, X., and Liu, H. *Optics Express* **20**(16), 18202–18208 (2012). 193

[290] Benabid, F., Couny, F., Knight, J. C., Birks, T. A., and Russell, P. S. J. *Nature* **434**(7032), 488–491 March (2005). 197, 202, 203

[291] Wang, C., Bradley, T., Wang, Y., Corwin, K. L., Grme, F., and Benabid, F. In *OSA Technical Digest (online)*, CM3I.1– (Optical Society of America, San Jose, California, 2013). 202

[292] Lee, K. C. *Generation of room-temperature entanglement in diamond with broadband pulses*. PhD thesis, University of Oxford, (2012). 203

[293] Klemens, P. *Physical Review* **148**(2), 845–848 (1966). 203

[294] Budker, D. and Romalis, M. *Nature Physics* **3**(4), 227–234 April (2007). 203

[295] Kominis, I. K., Kornack, T. W., Allred, J. C., and Romalis, M. V. *Nature* **422**(6932), 596–599 April (2003). 203

[296] Schwindt, P. D. D., Knappe, S., Shah, V., Hollberg, L., Kitching, J., Liew, L.-A., and Moreland, J. *Applied Physics Letters* **85**(26), 6409–6411 (2004). 204

[297] Zhao, K. F. and Wu, Z. *Applied Physics Letters* **89**(26), – (2006). 204

[298] Seltzer, S. J., Meares, P. J., and Romalis, M. V. *Physical Review A* **75**, 051407 May (2007). 204

[299] Siddons, P., Bell, N. C., Cai, Y., Adams, C. S., and Hughes, I. G. *Nature Photonics* **3**(4), 225–229 April (2009). 204

[300] Gogol, N. *Dead Souls*. Penguin Classics, (1961). 204

[301] Jaksch, D., Cirac, J. I., Zoller, P., Rolston, S. L., Côté, R., and Lukin, M. D. *Physical Review Letters* **85**(10), 2208–2211 Sep (2000). 205

[302] Lukin, M. D., Fleischhauer, M., Cote, R., Duan, L. M., Jaksch, D., Cirac, J. I., and Zoller, P. *Physical Review Letters* **87**(3), 037901 Jun (2001). 205

[303] Urban, E., Johnson, T. A., Henage, T., Isenhower, L., Yavuz, D. D., Walker, T. G., and Saffman, M. *Nature Physics* **5**(2), 110–114 February (2009). 205

[304] Gaetan, A., Miroshnychenko, Y., Wilk, T., Chotia, A., Viteau, M., Comparat, D., Pillet, P., Browaeys, A., and Grangier, P. *Nature Physics* **5**(2), 115–118 February (2009). 205

[305] Honer, J., Löw, R., Weimer, H., Pfau, T., and Büchler, H. P. *Physical Review Letters* **107**, 093601 Aug (2011). 205

[306] Firstenberg, O., Peyronel, T., Liang, Q.-Y., Gorshkov, A. V., Lukin, M. D., and Vuletic, V. *Nature* **502**(7469), 71–75 October (2013). 205

[307] Chang, D. E., Gritsev, V., Morigi, G., Vuletic, V., Lukin, M. D., and Demler, E. A. *Nature Physics* **4**(11), 884–889 11 (2008). 205

[308] Stanojevic, J., Parigi, V., Bimbard, E., Ourjoumtsev, A., and Grangier, P. *Physical Review A* **88**, 053845 Nov (2013). 205

[309] Kubler, H. Shaffer, P. J., Baluktsian, T., Low, R., and Pfau, T. *Nature Photonics* **4**(2), 112–116 February (2010). 205

[310] Demortier, L. *CDF Statistics Memo* **Version 2.10** (2005). 208, 209, 211

[311] Goldstein, M. *Bayesian Analysis* **1**, 403–420 (2006). 208, 211

[312] Feinberg, S. E. *Bayesian Analysis* **1**, 429–432 (2006). 208

[313] Gelman, A., Carlin, J. B., Stern, H. S., and Rubin, D. B. *Bayesian Data Analysis.* CRC Press, (2003). 211